An Optical and Infrared Analysis of Blue Compact Dwarf Galaxies

Bethan Lesley James

Thesis submitted for the Degree of Doctor of Philosophy
of University College London

Department of Physics & Astronomy
UNIVERSITY COLLEGE LONDON

August 2009

I, Bethan James, confirm that the work presented in this thesis is my own. Where information has been derived from other sources, I confirm that this has been indicated in the thesis. Specifically:

- The VLT-VIMOS data discussed and analysed in Chapters 2 and 3 were provided by the principal investigator of the ESO proposal, Y. G. Tsamis.
- The work presented in Chapter 2 has been published by James *et al.* (2009*a*) and incorporated comments from all co-authors. Figure 2.9 was created by Y. G. Tsamis (the second author of the publication), as were the final calculations of SFRs listed in Table 2.11.
- The work presented in Chapter 3 has been published by James *et al.* (2009*b*) and incorporated comments from all co-authors. Figure 3.19 was derived from helium abundance maps created by J. R. Walsh (the fifth author of the publication).

To my parents, whose endless love and support made this possible.

There is nothing in the dark that isn't there when the lights are on.

— Rod Serling (creator of The Twilight Zone, 1924-1975)

ABSTRACT

An understanding of Blue Compact Dwarf galaxies (BCDs) and the processes occurring within their chemically un-evolved environments is fundamental in our understanding of the early universe. This thesis presents an investigation into their physical conditions, kinematics, chemical abundances and dust compositions.

An optical integral field spectroscopy investigation of two perturbed BCDs, UM420 and UM462, is presented. Emission line maps show that both galaxies display signs of ongoing perturbation and/or interaction. Electron temperatures, densities and chemical abundances are computed from spectra integrated over the whole galaxies and for each area of star formation.

A similar yet more complicated analysis is undertaken of the BCD Mrk996, which displays multi-component emission lines. The high excitation energy [O III] λ4363 and [N II] λ5755 lines are detected only in the inner regions and purely in broad component form, implying unusual excitation conditions. A separate physical analysis of the broad and narrow emission line regions is undertaken, yielding a revised metallicity and N/O ratio typical for the galaxy's metallicity.

The mid-IR properties of 19 BCDs are studied through Spitzer spectral and imaging data. The depeletion of PAH emission in BCDs is investigated and found to be due to formation and destruction effects. The [S III] flux ratio is used as a density diagnostic, showing typically low-densities. Maps of PAH emission and radiation field hardness are derived from IRS spectral mapping data. Blackbody fits to IR photometric SEDs typically reveal two dust components.

The observed physical and chemical properties of Mrk 996 are successfully reproduced using the photoionisation code MOCASSIN. The best-fit model involved the inclusion of a filling factor and an amorphous carbon dust component with a two-zone dust distribution. A STARBURST99 input spectrum was used, yielding ages consistent with the known young WR stars and old super star clusters within Mrk 996.

CONTENTS

LIST OF FIGURES

LIST OF TABLES

CHAPTER 1

INTRODUCTION

1.1 What are blue compact dwarf galaxies?

Blue compact dwarf galaxies (BCDs) are thought to be the least chemically evolved galaxies in the local Universe. They are emission line galaxies that lie at the lower extremities of many galaxy scales; they are faint (having $M_B > -18$), have blue optical colours, are typically small (optical diameter < 1 kpc) and have low metallicities ranging from 1/3 to 1/41 $Z_\odot$ (Thuan & Martin 1981). They have blue UBV colors and strong narrow emission lines that are indicative of sites of intense star formation. The star formation sites are mostly seen to be practically devoid of dust (Houck *et al.* 2004*b*), thus they emit mainly in the blue at visual wavelengths due to the vast numbers of OB-type stars (Sargent & Searle 1970). They are mostly star-bursting galaxies, where star formation is dominated by a small number of short intense bursts of star formation separated by extremely long intervals of time (Searle & Sargent 1972).

Their massive stellar populations have properties intermediate between those of massive stars in solar-metallicity galaxies such as the Milky Way and those of the hypothesised first stars. Being nearby, BCDs serve as excellent laboratories to study the physical processes of galaxy and star formation, as well as chemical enrichment processes in often unblemished environments, in comparison to their high-redshift counterparts. The proximity of BCDs allows studies of their structure, metal content, and stellar populations with a sensitivity, precision, and spatial resolution that faint distant high-redshift galaxies do not allow (Thuan 2008).

1.1.1 The history of blue compact dwarf studies

The first studies of extragalactic very metal-deficient systems were carried out by Sargent & Searle (1970) and Searle & Sargent (1972). Whilst carrying out a spectroscopic survey of compact objects originally selected by Zwicky & Zwicky (1971) in a study entitled "Compact Galaxies and Compact Parts of Galaxies", they began to focus on two particularly interesting objects: I Zw 18 and II Zw 40. The spectra of these two galaxies were "strikingly different from those of galaxies of the Hubble sequence" and found to resemble in size, absolute magnitude and color the H II regions found in the spiral arms of giant Sc galaxies, resulting in them being dubbed as 'isolated extragalactic H II regions'. Measured abundances of both galaxies revealed sub-solar metallicities of 1/40 $Z_{\odot}$ and 1/4 $Z_{\odot}$ for I Zw 18 and II Zw 40, respectively, and thus the title of 'the first metal-poor systems of Population I[1] to be discovered'. Because of these low metallicities, Searle & Sargent (1972) argued that these galaxies are either young (in the sense that most of their star formation has occurred in recent times) or that the star formation in them occurs in intense bursts which are separated by long quiescent periods. Nearly a decade later, Thuan & Martin (1981) showed that I Zw 18 and II Zw 40 are part of a general class of dwarf extragalactic systems undergoing intense bursts of star formation, producing young massive blue stars in a localised compact region, which they called Blue Compact Dwarf (BCD) galaxies. The definition criterion for Thuan & Martin (1981)'s BCDs were the following: (1) a low luminosity ($M_B \geq -18$); (2) an optical spectrum exhibiting strong narrow emission line superposed on a blue continuum, similar to that of a H II region ; and (3) a compact appearance (D_{25} =1–2 Kpc, where D_{25} is the diameter within which 25% of the galaxy's light is held) and a high mean surface brightness ($S_B \leq 22$ mag arcsec^{-2}). The enforcement of criteria (1) ensures that the galaxies are dwarf in type, and excludes more massive emission-line galaxies with density waves such as Seyfert galaxies and ensures that the galaxy has a low metallicity.

The nomenclature or classification of BCDs often varies throughout the literature. They are often called H II galaxies, which nominally refers to galaxies with spectra reminicant of BCDs but with higher metallicities, such as luminous high-metallicity objects with spiral structure (Kunth & Östlin 2000). Other names exist such as 'Blue Compact Galaxies' and 'Blue Amorphous Galaxies' (Sandage & Brucato 1979), with each notation focusing on a separate aspect. Whilst Sandage & Binggeli (1984) extended their classification of dwarf galaxies to include BCDs, their relation to other dwarf types such as dwarf-irregular (dIs) or dwarf-elliptical (dEs) remains unclear. Kunth &

[1] Population I refers to Walter Baade's stellar systems containing many luminous blue stars.

Östlin (2000) discuss the overlapping classification of metal-poor galaxies; at low faint absolute magnitudes the dI and dE merge with low surface brightness galaxies (LSBGs) whereas BCDs to some extent overlap with actively star-forming dIs.

Loose & Thuan (1985) defined four subclasses of BCDs based on the morphology of their star-forming regions and the surrounding host galaxy: 1) iE BCDs - complex structure with several centres of star formation and irregular (i) isophotes in the central regions super posed on a LSB component with elliptical (E) isophotes, which they deem as the most interesting BCDs; 2) nE BCDs - a nuclear star-forming region a the centre of a LSB elliptical (E) component; 3) iL BCDs - irregular (i) star-forming regions superposed on a LSB component (L) with irregular outer isophotes; and 4) i0 BCDs - irregular (i) star-forming regions but no (0) evident underlying older stellar population. A similar conclusion was reached by Kunth *et al.* (1988), namely that BCDs consist of a "mixed bag" of morphologies, including objects that appeared to be isolated extragalactic H II regions, irregular morphologies and cases with symmetric outer envelopes that are suggestive of an older stellar population, throwing doubt on their classification as *truly* young systems.

1.1.2 Old or young?

In the hierarchical model of galaxy formation (White & Rees 1978), dwarf galaxies are deemed as the building blocks of large galaxies. They are the first structures to collapse, and form stars, and continue gaining mass via clustering and merging. At high-redshifts, the study of primordial dwarf galaxies, which BCDs may parallel, are beyond the capability of most current instruments and hence we stand a much better chance of understanding them by studying local BCDs. Galaxy formation is one of the most fundamental problems in astrophysics and BCDs provide us with an opportunity to unravel how stars form within primordial-like environments and how the first stars interact with their surrounding environments.

However, much debate has surrounded the true ages of BCDs. While their initial compact classification by Zwicky & Zwicky (1971) showed them to be "almost stellar in appearance, with no obvious underlying galaxy", later CCD studies (e.g. Thuan (1985); Telles (1995); Thuan *et al.* (1996); Papaderos *et al.* (1996); Doublier *et al.* (1997); Cairós *et al.* (2001*b*,*a*); Bergvall & Östlin (2002)) showed them to almost always (95% of the sample in Thuan (1985)) have an underlying extended red low-surface brightness (LSB) component, upon which are superposed high-surface brightness compact star-forming regions. This posed the question of whether they are undergoing their first burst of star formation, or are they old galaxies with an old underlying stellar population

and a presently/recently occurring starburst? The current conclusion is that BCDs are not the young systems once proposed. However, in contrast to this, two bona-fide I0-type BCDs, I Zw 18 and SBS 0335-052, do *not* appear to show an underlying old stellar component (Izotov & Thuan (1999); Thuan *et al.* (1996); Izotov *et al.* (2005)). The following section provides an overview of the two most metal poor galaxies known, I Zw 18 and SBS 0335-052, and the studies dedicated to the discovery of their true ages.

1.1.2.1 The lowest metallicity systems: SBS 0335-052 and I Zw 18

SBS 0335-052 and I Zw 18 are the most metal-poor and hence most famous BCDs, often thought of as the prototypes of star formation (SF) in BCDs. While SBS 0335-052 is in an 'active' mode with a relatively high star-formation rate (SFR) in compact dense regions, I Zw18's SF occurs in 'passive' mode in more extended regions with a relatively low SFR (Wu *et al.* 2007). Extensive study of both these systems has taken place, treating them as the 'youngest' galaxies within useful reach. Both systems are contained within the object list for this study. The readers attention should also be drawn to another extremely metal deficient galaxy, DDO 68 (with 12+log(O/H)=7.14$\pm$0.03 (Izotov & Thuan 2007)), which is discussed in more detail in Chapter 6.

I Zw 18:

The first known member of this class of emission line galaxies, I Zw 18, was identified by Zwicky (1966) and was the most metal-poor galaxy known for many years, with 12+log(O/H)=7.2 (Alloin *et al.* 1978) and later a revised 12+log(O/H)= 7.18 (Izotov & Thuan 1999) or 1/50 $Z_{\odot}$. As highlighted by Kunth & Östlin (2000), it is intriguing that despite being one of the first BCDs to be investigated (along with II Zw 40), it remained the most metal poor BCD known for over two decades (recently replaced by SBS-0335-052W in 2005 (Izotov *et al.* 2005)), despite extensive efforts in searching for more metal-poor galaxies.

HST imaging in the optical (Figure 1.1) shows that it possesses two star-forming regions in the main body; a brighter northwest (NW) component separated from a fainter southeast (SE) component by 8$''$.

The most recent oxygen abundance determinations for I Zw 18 are 12+log(O/H)=7.17$\pm$0.01 for its NW component and 7.22$\pm$0.02 for its SE component (Thuan *et al.* 2005), corresponding to $\sim$1/35 $Z_{\odot}$ and $\sim$1/30 $Z_{\odot}$ respectively (utilising a solar oxygen abundance of 8.71$\pm$0.10 (Scott *et al.* 2009)). Previous estimations of the oxygen abundance were lower, with values ranging from 1/30 – 1/60 being quoted over the last 20 years (Kunth & Östlin 2000), due to higher solar oxy-

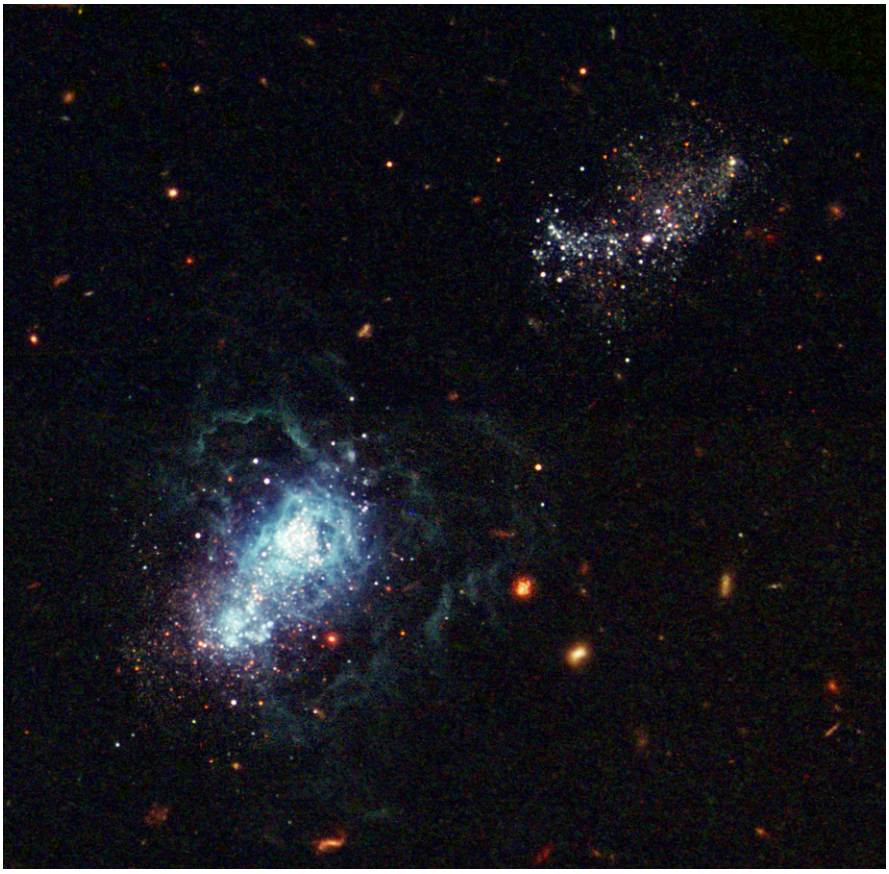

Figure 1.1: *HST* ACS and WFPC2 V- and I-band images of I Zw 18. Credit: NASA, Y. Izotov (Main Astronomical Observatory, Kyiv, UA) and T. Thuan (University of Virginia). North is up, east is left.

gen abundance estimations ($\sim$8.8–8.9), less accurate determinations of $T_{\rm e}$s and possibly a result of integrating the spectra over the entire galaxy rather than separated NW and SE components (Skillman & Kennicutt 1993).

Much debate has surrounded I Zw 18 regarding its true age. Izotov & Thuan (1999) came to the conclusion that any galaxy with 12+log(O/H)$<$7.6 must be younger than 40 Myr and thus a newly born galaxy. However, there are other interpretations of the abundance ratios of metal poor galaxies, which will be discussed later. At the time, the record low oxygen abundance of I Zw 18 and its lack of an outer regular envelope made it a promising candidate as a truly young system. Arguments surrounding its age from C/O and N/O ratios (Pantelaki & Clayton (1987); Garnett *et al.* (1997)) continued for over a decade, with values being revised and lowered by Izotov & Thuan (1999) in an attempt to strengthen the argument for a truly young galaxy. However, the clearest insight into the age of I Zw 18 has been through *HST* imaging studies that had the ability

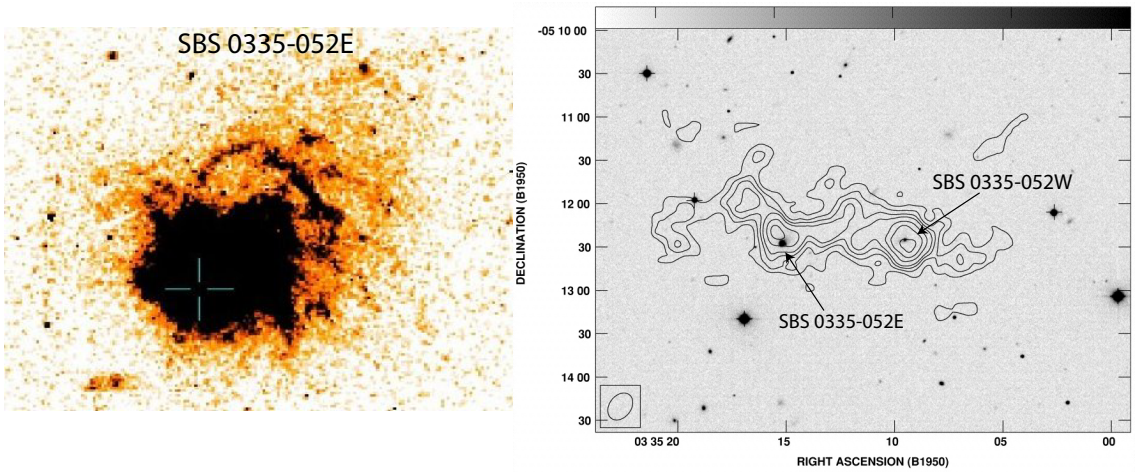

Figure 1.2: SBS 0335-052: left panel shows $20 \times 20''$ (5.2×5.2 kpc) *HST* WFPC2 V-band images of eastern component, cf. Thuan *et al.* (1997); the right panel shows Pustilnik *et al.* (2001)'s VLA H I image contours overlaid on B-band optical image from Papaderos *et al.* (1998), used to discover the western component of SBS 0335-052 - now the most metal poor BCD known in the Universe.

to resolve the galaxy's stellar population. Hunter & Thronson (1995) and Dufour *et al.* (1996) both resolved a population of young massive stars, but could not rule out an older population, as the images were not deep enough for its detection. The datasets were re-analysed by Aloisi *et al.* (1999) and, along with red AGB stars detected by deep NICMOS NIR imaging by Östlin (2000), support a stellar population age in excess of 1 Gyr. In addition to photometry of individual stars, surface photometry by Östlin (2001) also indicates that the galaxy is in fact old. However in a last attempt to resurrect its youth, Izotov & Thuan (2004) presented a new colour magnitude diagram (CMD) from *HST* ACS observations that showed no signs of an RGB (i.e. low-mass stars with ages $\sim$1–13 Gyr that are burning H in a shell around a He core) concluding that the most evolved (AGB) stars are not older than 500 Myr and that I Zw 18 is a bona fide young galaxy. This was later challenged by Momany *et al.* (2005) (using the same imaging data) and finally, again, by Aloisi *et al.* (2007) who presented new $V-$ and $I-$ band ACS photometry that strongly confirms the presences of an RGB, along with an accurate distance measurement (18.2 ± 1.5 Mpc, as opposed to $D \leq 15$ Mpc estimated by Izotov & Thuan (2004)) based on three classical Cepheids. At present, the strong evidence of an RGB population rules out the possibility that I Zw 18 is a truly

primordial galaxy formed recently in the local Universe.

SBS 0335-052(E & W):

For a while, the title of 'most metal poor' was held by I Zw 18 without any significant challenges from other BCDs. However, the discovery of SBS 0335-052E by the Second Byurakan Survey (SBS, Markarian & Stepanian (1983)) threatened this title. Studies of this galaxy from 1990 onwards have shown it to have an oxygen abundance comparable to and possibly lower than that of I Zw 18 (Izotov *et al.* 1990, 1997; Melnick *et al.* 1992).

A *HST* study by Thuan *et al.* (1997) found that star formation in SBS 0335-052E (Figure 1.2 (left panel)) occurs mainly in six superstar clusters (SSCs) roughly aligned in the SE-NW directions with ages $\leq$25 Myr, within a region of $2''$ in size. This work also presented $V - I$ colour maps of SBS 0335-052E, that showed clear evidence that dust is present and mixed spatially with the SSCs, which may be the cause of an increase in reddening of the clusters away from the brightest one or perhaps this is a colour evolution with time due to sequential propagating star-formation (Thuan 2008).

The first metallicity reports for this galaxy referred only to the eastern component, with an oxygen abundance of 12+log(O/H)=7.31$\pm$0.01 (Thuan & Izotov 2005), placing it in the same region as I Zw 18. However, a VLA H I imaging study by Pustilnik *et al.* (2001) (H I contours overlaid on B-band image are shown in the right panel of Figure 1.2) revealed that a huge H I complex is associated with SBS 0335-052E, with an overall size of $252'' \times 84''$ (66×22 kpc), along with two prominent H I peaks separated in the east-west direction by $84''$ (22 kpc). While the eastern part is coincident with SBS 0335-052E, the western peak is associated with a separate BCD, SBS 0335-052W. A recent study of SBS 0335-052W by Izotov *et al.* (2005) revealed a slightly lower metallicity (than its eastern counterpart) of 12+log(O/H)=7.12$\pm$0.03 (Z = $Z_{\odot}$ /41), confirming it as the most metal-poor emission galaxy known in the Universe. Hubble Space Telescope (HST) imaging of SBS 0335-052 by Thuan *et al.* (1996) suggests that this truly is a young galaxy, undergoing its first burst of star formation. This proof is based on its very blue colors and the irregular structure of the underlying extended low-surface-brightness component that suggests gaseous emission and no detectable underlying older stellar population. Recent stellar population ages for SBS 0335-052W are estimated as $<$500 Myr (Izotov *et al.* (2005)), with ages ranging from 3–12 Myr for the individual SSCs (Reines *et al.* 2008), making it a likely nearby young galaxy.

Regardless of its apparent young age, Thuan *et al.* (1999) estimated an optical depth of

A_V ∼19–21 mag from ISOCAM observations, implying a large fraction of the current star formation activity in SBS 0335-052 is hidden by an amount of dust comparable to those harboured by galaxies that are 10 times more metal-rich (3×10^3–5×10^5 $M_\odot$). The mid-IR observations also showed no detection of PAH emission (see below) which they attributed to the destruction of their carriers by the very high UV energy density in SBS 0335-052 ($\gtrsim 10$ eV cm^{-3}).

1.1.3 The spectra of BCDs

The first study by Zwicky (1966) provided evidence that BCDs are dramatically different from normal dwarf galaxies. This discovery sparked many observational studies that have allowed a compilation of their properties (an in-depth review of which is given by Kunth & Östlin (2000)). Their optical spectra are dominated by nebular emission lines similar to those of high-excitation giant H II regions in late spiral galaxies and consist of narrow emission lines superimposed on a blue stellar continuum. These lines are usually identified as helium and hydrogen recombination lines and several forbidden lines from elements such as O, N, S, Ar and Ne. These emission lines are essential in determining the physical (i.e. N_e, T_e, interstellar extinction) and chemical conditions (i.e. abundances) within BCDs (methods for which are described in Sections 1.4.1, 1.3 and 1.4.2, respectively)

Typically, in the mid-infrared, star-forming objects will show strong emission due to polycyclic aromatic hydrocarbons (PAHs) that lie in the photodissociation regions (PDRs) surrounding the massive star clusters. The PAHs absorb UV photons from the clusters and re-radiate at mid-IR wavelengths, thus highlighting the PDRs surrounding the H II regions (Lebouteiller *et al.* 2007). This morphology can be attributed to the hard radiation field inside the H II region dissociating the molecules while outside the PDR there are insufficient UV photons to excite the PAHs into emission (Jackson *et al.* 2006). PAHs can consist of tens to hundreds of carbon atoms and emit due to the fluorescence of aromatic C-C and peripheral C-H fundamental vibrational and bending modes (Lebouteiller *et al.* 2007). The strength of the PAH emission features is greatly dependent on the environmental conditions of the PDR, e.g. dust temperature, hardness of the radiation field and dust composition. It is due to this latter dependency that PAHs are expected to be depleted in low-metallicity environments such as BCDs.

1.1.4 Ionising Sources within BCDs

Massive stars (i.e. $M > 8$–$10 M_{\odot}$) are the dominant stellar population in young (<100 Myr) starbursts and provide the major source of UV ionising radiation in starburst galaxies such as BCDs. They are also the primary source of chemical and mechanical enrichment input into the interstellar medium through stellar winds and SNe. However, massive stars make up only a small fraction for the total stellar population due to the fact that the initial mass function (IMF)[2] of star formation is extremely biased towards low mass stars.

The young stellar populations of BCDs presented in this study are dominated by O and WR stars whose ionising UV radiation is the energy source for the emission lines observed within their spectra (Thuan & Izotov 2005). A description of the properties of these two types of ionising source follows, largely obtained from the review articles edited by Conti & Underhill (1988).

1.1.4.1 O stars

Being deemed 'young' galaxies, it is not surprising that the main sources of ionisation within BCDs are newly formed O stars (Cairós *et al.* (2001*b*,*a*, 2003) and references therein). O stars represent the earliest and rarest spectral type of all the main-sequence stars, with lifetimes of only a few ($\sim$1–10) million years (see e.g. Maeder & Meynet (1987)). This makes them excellent tracers of recent episodes of star formation. They are not only the most massive stars (20–120 $M_{\odot}$), but are also the hottest and most luminous of the main-sequence stars, with effective temperatures in the range of 25000-50000 K and luminosities of up to a few Solar luminosities ($L_{\odot}$). Their UV spectra is characterised by strong P-Cygni stellar wind lines as a result of their strong mass-loss rates of $\sim 10^{-6} M_{\odot}$ yr^{-1}.

1.1.4.2 Wolf-Rayet stars

Wolf-Rayet (WR) stars are the highly chemically evolved and short-lived ($t \sim 10^5$ yrs; Maeder & Meynet (1994)) descendents of the most massive O stars (Kunth & Östlin 2000). They experience intense mass-loss through strong stellar winds, stripping away their outer layers to reveal CNO cycle products at the surface. Thus, WR stars represent the bare-core remnants of what were once O stars.

WR stars can be classified into three spectral types based on the dominance of helium and

[2]The IMF represents the distribution fo the stellar mass at birth, i.e. the probability of obtaining a certain number of stars in a given mass bin once normalised to the total mass available for forming stars.

nitrogen (WN, nitrogen-rich), carbon (WC, carbon-rich) or oxygen (WO, oxygen-rich) emission lines within their spectra. WR stars can also be classified into numerical subtypes that follow an ionisation/excitation sequence in which the subtypes are defined by the intensity-ratios of different excitation lines. Briefly, in this sequence the WR stars with the lowest numerical subtype classification are commonly referred to as 'early' (E) WR stars (WNE, WCE) and those with the largest numerical designation (i.e. lowest excitation WR stars) are referred to as 'late' (L) WR stars (WNL, WCL). Late-type WR star are cooler and more luminous than their early-type counterparts. The strongest optical lines in WN and WC stars optical spectra are He II λ4686 (WN and WC) and C IV λ5808 (WC).

Many BCDs are also classified as WR galaxies; a subset of starburst galaxies that show the stellar signatures of WR stars in their integrated spectra. WR features have also been observed in the rest-UV frame spectrum of high-redshift Lyman Break galaxies (Steidel *et al.* 1996; Shapley *et al.* 2003). The number of known WR galaxies currently stands at 570, with an additional 1115 possible candidates, obtained through a dedicated search of the Sloan Digital Sky Survey (SDSS) by Brinchmann *et al.* (2008). Prior to the SDSS, only ~ 140 were known; a large number of which were identified through optical spectroscopic surveys of H II emission-line galaxies (Schaerer *et al.* (1999*b*); Pindao *et al.* (2002)). However, as detailed in Chapter 2, the detection of a 'WR galaxy' through the characteristic 'blue WR bump' at $\sim$ λ4680 and 'red WR bump' at $\sim$ λ5800 can depend on the aperture and integration time of the observation.

1.2 Physical processes in BCD H II regions

Emission lines arise when an excited atom or ion returns to a less excited or ground state by emitting a photon. Atoms/ions can achieve these excited states via three excitation mechanisms: photoexcitation, recombination and collisional excitation. While the first is associated with photoionisation, the dominant heating source in photoionised regions, the latter two are cooling mechanisms that balance the heating by photoionisation. This section provides a brief outline of the theory behind the observed emission lines and their diagnostic properties that are used in this thesis.

1.2.1 Photoexcitation

An atom may be excited to a higher energy level in two ways, radiatively or collisionally. Radiative or photoexcitation occurs when a photon is absorbed by the atom; where the photon's energy must equal that of the energy difference between the two energy levels of the atom. For excitation to an

excited level, the typical timescale that the atom remains in its excited state, i.e. the time it takes to decay back to the grounds state (e.g. n = 2→1, Ly-α), is typically 10^{-8} s, after which the electron cascades through several energy levels, emitting photons accordingly on its way to the ground state. The young stellar populations within BCDs emit copious amounts of UV photons and those photons with wavelengths below the Lyman limit (912 Å) have energies greater than 13.6 eV and are thus able to ionise hydrogen from its ground state. The ejected electron (photoelectron) will have a kinetic energy equal to the energy of the incident photon minus the electron binding energy of the state it left.

Depending on the size and density of the ionised region and the luminosity and temperature of the ionizing source, there are two possibilities for the ionization structure of hydrogen within a H II region. If there are sufficient photons to ionize all the hydrogen then we say that the ionised region is 'matter bounded', i.e. the limit to the size of the ionized region is determined by the amount of matter within it. However if there are not enough ionizing photons to ionise all the hydrogen in the region, then an ionisation structure will be set up, with material close to the ionizing sources ionized and material beyond the 'ionization front' predominantly neutral. This H II region is said to be 'ionization bounded', i.e. the number of ionizing photons determines the size of the ionized region (Strömgren 1939; Osterbrock 1989).

1.2.2 Radiative recombination and line emission

Radiative recombination is the free-bound recapture of an electron by an ion to a bound level. Following multiple downward cascades, the electron reaches the ground level of the atom of the next lower stage of ionisation. The transitions result in recombination lines from UV to radio wavelengths. The strongest recombination lines in H II regions are those of hydrogen and helium, e.g. the Balmer optical recombination lines (ORLs) such as Hα λ6563, Hβ λ4861, Hγ λ4340 etc, and also of He I (λ4471, λ5876, λ6678) and He II (λ1640, λ4686) (Seaton 1959; Hummer & Storey 1987). The heavy elements form much weaker recombination lines, which can be seen in sufficiently deep spectra.

While the typical timescale between photoionisations is of the order 10^9 s, the line transition probabilities following recombination are $\sim 10^4$–10^8 s^{-1}. Thus all ions can be considered to be effectively in their ground state, so that photoionisations occur from that level.

Relating to their ionisation structure, Baker & Menzel (1938) defined two recombination cases within H II regions; Case A, where the optical depths of all line and continuum radiation are small and thus all photons escape (i.e. an optically thin 'matter bounded' H II region); and Case B,

where the optical depths of Lyman photons (radiation corresponding to transitions to the $n = 1$ hydrogen level) are high and are thus absorbed 'on the spot' (i.e. an optically thick, 'ionisation bounded' H II region). Under the latter case, all radiation belonging to the Balmer series (and higher) is assumed to have a low optical depth and thus escapes the H II region.

In reality, Case B is always a more realistic approximation than Case A and under this assumption the hydrogen atom can be treated as though its ground state does not exist since every recombination directly to $n = 1$ is followed by an absorption and photoionisation from the ground state. An exception exists for the Ly-α photon ($n = 1 \rightarrow 2$), which is multiply scattered, diffusing slowly through outwards through the H II region. And so, Lyman continuum radiation from the ionising sources is converted into photons of the higher hydrogen series; Balmer, Paschen, Brackett etc, photons *plus* Ly-α photons. In ionisation equilibrium the number of ionising photons is equal to the number of recombinations, which for a pure-hydrogen H II region can be written as:

$$\int_{\nu_0}^{\infty} (L_\nu / h\nu) \mathrm{d}\nu = \int_V N(H^+) N_e \alpha_B \mathrm{d}V \tag{1.1}$$

where L_ν is the stellar luminosity, ν_0 is the photon frequency at the Lyman limit (i.e. at 912 Å) and $N(H^+)$ and N_e are the proton and electron number densities, respectively. α_B is the total recombination coefficient in units of cm^3 s^{-1} which represents the sum of the rates of direct recombination to the second and higher levels of the H^+ ion. Thus by measuring the luminosity of one of the hydrogen recombination lines, by using Equation 1.1 one can estimate the number of ionising photons emitted by the exciting stars within the H II region.

The intrinsic intensity of a recombination line due to an $i \rightarrow j$ transition, received at the Earth is given by:

$$I_{ij} = \frac{1}{4\pi D^2} \int_V N(X^{(i+1)+}) N_e h\nu_{ij} \alpha_{eff}(\lambda, T) \mathrm{d}V \tag{1.2}$$

where the ionised region is at a distance D, and $N(X^{(i+1)+})$ is the number density of the recombining ion in the state $X^{(i+1)+}$ and N_e is the number density of the electrons. The emissivity of the line (in units of erg cm^{-3} s^{-1}) can be written as

$$\epsilon_\lambda = N(X^{+i+1}) N_e \alpha_{eff}(\lambda, T) \frac{hc}{\lambda} \tag{1.3}$$

Here $\alpha_{eff}(\lambda, T)$ is the 'effective recombination line coefficient' given by

$$\alpha_{eff}(\lambda) = B(\lambda) \alpha_{eff}(X^{+i}) \tag{1.4}$$

which represents the probability for spontaneous radiative decay via a line of wavelength λ, or the branching ratio

$$B(\lambda) = A_{ij} / \sum_{k<i} A_{ik} \tag{1.5}$$

multiplied by the 'effective recombination coefficient' of a particular atomic state X^{+i}.

It should be noted, that unlike in the case of collisionally excited lines, radiative recombination coefficients and hence the emissivities of radiative recombination lines, have a weak temperature dependence, approximately proportional to ${T_{\rm e}}^{-\alpha}$, where $\alpha = 1$ (Osterbrock & Ferland 2006).

Another possible method of recombination in an ionised region is dielectronic recombination, where an ion captures a free electron which excites another electron in the ion. The excited ion can either ionise via autoionisation or decay via radiative cascades. Dielectronic recombination has a high temperature dependence, with $\alpha_D \propto T^{-3/2} e^{-f/T}$ where f is a coefficient that depends on the transition (Nussbaumer & Storey 1984). Dielectronic recombination can become the dominant recombination mechanism at high temperatures, such as in the solar corona, as well as being important at low temperatures, both for line emission and ionisation balance, as shown by Nussbaumer & Storey (1984).

1.2.3 Collisionally excited line emission

While the recombination lines of hydrogen can often be very obvious, they are not the dominant cooling mechanism in most ionised regions. Collisionally excited lines (CELs) are created following the excitation of an ion after collisions with, but not recombinations with, an electron. As mentioned previously, such lines are the major sources of cooling in ionised regions, in spite of the low abundance of heavy element ions, compared to that of H and He ions. Hydrogen and helium have energy levels with quite high excitation energies, $\gg$ kT, such that they are unlikely to be excited by electrons. The meta-stable levels (i.e. energy levels above that of the ground state and which can only decay via weak magnetic dipole or electric quadrupole transitions, rather than strong electric dipole transitions) of some heavy element ions, such as O^+ and N^+, have much lower excitation energies, of the order of a few kT or less and can therefore be strongly excited by electron collisions (Seaton 1968).

For heavy element ions, the excited level can arise from the same electron configuration as the ground state, and thus, according to dipole selection rules, a radiative transition back to the ground state is forbidden. However the transition may occur via much slower magnetic dipole or electric quadrupole transitions (Osterbrock & Ferland 2006). There are three types of collisionally excited

lines, each with a typical associated transition probability: forbidden, semi-forbidden ($10^2 s^{-1}$) and permitted ($10^8 s^{-1}$). These lines cannot be seen in laboratory conditions (hence the 'forbidden' nomenclature) because the competing process of de-excitation by collisions with electrons dominates, whereas this is prevented in H II regions due to the tenuous nature of the gas. Since the transition probabilities are low, the probability of the reverse process of radiative absorption (by an atom in the lower level) is also low and so the forbidden lines escape easily from the ionised region.

Due to the low density nature of astronomical H II regions, it is not possible to assume any kind of thermodynamic equilibrium (i.e. the relative populations in atoms cannot be obtained from the Boltzmann formula such as in a high density stellar interior that is in local thermodynamic equilibrium). Instead, a statistical equilibrium is assumed that considers all processes capable of populating or depopulating a level. For a multi-level ion the statistical equilibrium equations for each level that concerns only relative populations (i.e. neglecting 'weak' processes such as recombination) are (Osterbrock & Ferland 2006):

$$\sum_{j \neq i} N_j N_e q_{ij} + \sum_{j>i} N_j N_e A_{ji} = \sum_{j \neq i} N_i N_e q_{ji} + \sum_{j<i} N_i N_e A_{ij} \tag{1.6}$$

where q_{ij} and q_{ji} are collisional excitation and de-excitation rates per unit volume up to or down from level j, and A_{ji} and A_{ij} are the radiative transition probabilities for $i \rightarrow j$ (to all lower levels). In other words, the left part of Equation 1.6 gives the transitions that populate level i while the right part gives transitions that depopulate level i. Since $\sum_j N_j = N$, this equation may be solved to yield the population of each level relative to the ground state. The collisional de-excitation rate from level i to level j per unit volume is given by

$$q_{ij} = \left(\frac{2\pi}{kT}\right)^{\frac{1}{2}} \frac{\hbar^2}{m^{3/2}} \frac{\Omega(j,i)}{g_i} \tag{1.7}$$

$$= \frac{8.629 \times 10^{-6}}{T^{\frac{1}{2}}} \frac{\Omega(j,i)}{g_i} \tag{1.8}$$

and the collisional excitation rate from j to i is given by

$$q_{ji} = \frac{g_i}{g_j} q_{ij} e^{-E_{ij}/kT} \tag{1.9}$$

where $\Omega(j,i)$ is the collisional strength, g_i and g_j are the statistical weights of the levels

and E_{ij} is the energy difference between levels i and j. m refers to the mass of an electron (9.11×10^{-31} kg) and $\hbar$ is Planck's constant h (6.63×10^{-27} erg s) divided by 2π.

The emissivity of a line from a level i of ion X^{m+} that has been collisionally excited from the ground state is given by:

$$\epsilon_{ij} = N(X^{m+})n_i A_{ij} E_{ij} \tag{1.10}$$

where n_i is the fractional population of level i which may be determined from Equation 1.6. At low densities where collisional de-excitation is negligible, the level population is proportional to the collisional excitation rate, and a photon is emitted for every collisional excitation. At higher densities, where collisional de-excitation must be considered, a two-level approximation gives the following expression for the fractional population of n_i to n_j:

$$\frac{n_i}{n_j} = \frac{g_i}{g_j}\frac{e^{-E_{ij}/kT}}{1 + A_{ij}/(q_{ij}n_e)} \tag{1.11}$$

It can be seen that at high densities, the level population will no longer increase as n_e increases, and the line is collisionally suppressed.

As a result of the balance between radiative decays and collisions, a critical density (N_{crit}) arises for each level at which the rate of radiative de-excitation from a level is equal to the rate of collisional excitations and de-excitations from the level

$$N_{crit} = \frac{\sum_{i<j} A_{ij}}{\sum_{i\neq j} q_{ij}} \tag{1.12}$$

For $N_{\rm e} > N_{crit}$, collisions dominate and the population of level j is in Boltzmann equilibrium, i.e. determined by the Boltzmann equation, with the population of level j, and therefore the line emission rate, $N_j A_{ij}$, proportional to $N_{\rm e}$. For $N_e < N_{crit}$, every excitation of level j from level i will be followed by a radiative decay. In this density regime the upward collisional excitation rate will be proportional to $N_e N_i$, i.e. to the square of the density. The dominance of forbidden line emission as a cooling mechanism in H II regions and nebulae maintains a typical electron temperature in an ionised environment of the order of 10^4 K.

1.3 Interstellar Extinction

Before proceeding with the analysis of the spectra from H II regions, a correction must be made for the effect of interstellar extinction. Extinction is primarily caused by the preferential absorption

and scattering of light with decreasing wavelength by interstellar dust particles. The extinction increases towards shorter wavelengths, thus reddening the light from an emitting source; light which is propagating through the interstellar dust is reduced according to the equation

$$I_\lambda = I_{\lambda 0} e^{-\tau_\lambda} \tag{1.13}$$

where $I_{\lambda 0}$ is the intensity of the light observed at Earth had reddening not occurred, I_λ is the actual intensity observed and τ_λ is the optical depth at the wavelength of the observation.

Over the years, measurements of the interstellar extinction along the line of sight for many pairs of stars of the same spectral type have been made, by taking the ratio of their brightnesses. The results show that in the optical domain the wavelength dependence, $f(\lambda)$, of extinction is roughly the same along any direction of interstellar space, while the amount of extinction, c, varies such that it can be expressed as a reddening law;

$$\tau_\lambda = c f(\lambda) \tag{1.14}$$

It is common for the reddening functions to be normalised to Hβ such that

$$f(\lambda) = \frac{X(\lambda)}{X(H\beta} - 1 \tag{1.15}$$

As in this work and most H II studies, rather than referring to the total extinction in magnitudes (e.g. A_v), it is described by terms of the logarithmic difference between observed and intrinsic Hβ fluxes, c(Hβ). This is related to the total extinction A_λ and colour excess $E(B-V)$ of the B and V magnitudes by

$$A_{H\beta} = 2.13 c(H\beta) \tag{1.16}$$

and

$$c(H\beta) = 1.452 E(B-V) \tag{1.17}$$

for the Galactic reddening law of Howarth (1983)

Once c(Hβ) is derived using the method described below, the observed emission lines (often in units relative to Hβ=100) can be corrected for interstellar extinction by

$$I(\lambda) = F(\lambda) \times 10^{c(H\beta)f(\lambda)} \tag{1.18}$$

where $f(\lambda)$ is given by Equation 1.15.

1.3.1 Derivation of c(Hβ)

A common way to derive c(Hβ) in optical studies of emission line galaxies is from a comparison between the observed and predicted H I Balmer decrement, e.g. using observed and predicted Hα/Hβ and Hγ/Hβ line ratios. This is the method used in this work to deredden the optical spectra presented in Chapters 2 and 3. It involves two preliminary c(Hβ) values obtained from the above specified Balmer line ratios that are averaged with weights of 3:1, respectively, according to the relative intensities and wavelength separation of the lines. A comparison is then made against theoretical ratios from Hummer & Storey (1987) for suitable $T_{\rm e}$ and $N_{\rm e}$ estimates. For example, at $T_{\rm e} = 1 \times 10^4$ K and $N_{\rm e} = 100$ cm^{-3} the intrinsic Hα/Hβ and Hγ/Hβ ratios are 2.863 and 0.468, respectively. The main disadvantage of this method is the relatively small wavelength separation of the Balmer lines employed.

Although not attainable for work within this study, it should be noted that a more accurate estimate of c(Hβ) is possible through a comparison of the observed (optically thin) radio *free-free* continuum radiation of the ionised region, with the observed total Hβ flux (Osterbrock & Ferland 2006). Since the wavelength baseline involved is large, and the radio flux suffers virtually no extinction, this method can give highly reliable reddening estimates.

1.4 What can emission lines tell us about BCDs?

Emission lines are observed from many types of objects, at all scales and all wavelengths. They provide a diagnostic window into the regions from which they are emitted, allowing us to determine physical conditions and chemical compositions. This section describes how the emission lines can be used to determine the electron temperature ($T_{\rm e}$), electron density ($N_{\rm e}$) and chemical abundances within BCDs.

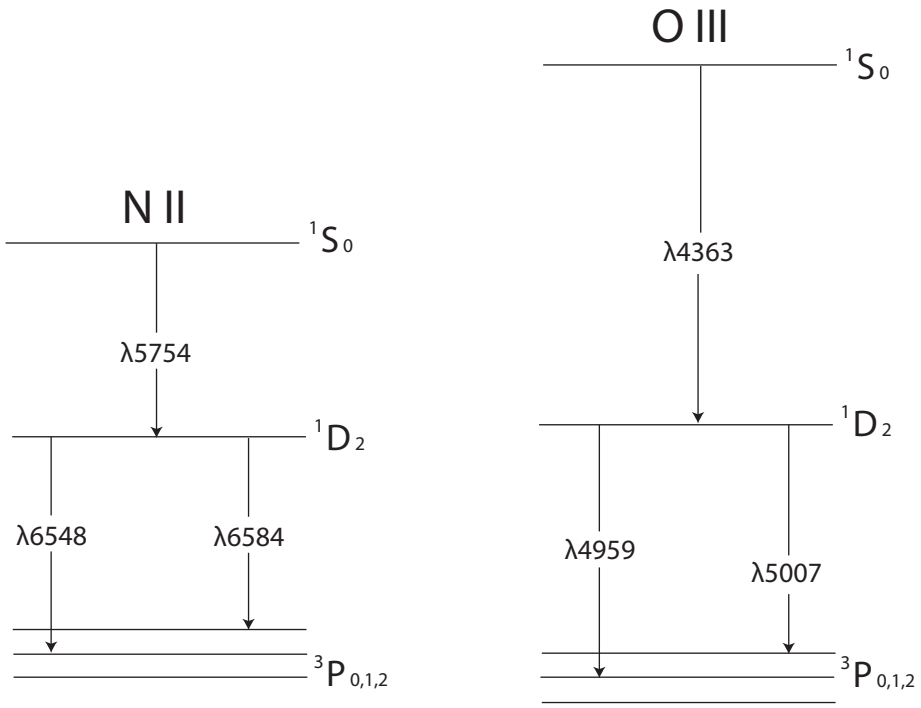

Figure 1.3: Energy level diagram for N^+ and O^{2+} showing the [N II] and [O III] auroral and nebular lines used for T_e determinations; see text for details. The fine-structure splitting of the ground terms has been exaggerated for clarity.

1.4.1 T_e and N_e determinations

To begin to understand the physics and chemistry within H II regions, it is first necessary to determine the temperature and density of the gas. Traditionally, determinations of physical conditions have relied on the bright and easily observable CELs in H II region spectra.

1.4.1.1 Electron temperature determinations

Some ions, such as [O III] and [N II] have energy level structures in which transitions giving rise to emission lines at optical wavelengths arise from upper levels with very different excitation energies. Energy level diagrams for [O III] and [N II] (Figure 1.3) make the picture clear, showing that, taking [O III] as an example, excitation to the $^1S_0$ level and subsequent emission of a λ4363 photon requires more energy than excitation to the $^1D_2$ level and subsequent emission of a λ5007 or λ4959 photon (a λ4931 photon may also be emitted, but the transition has a very low probability

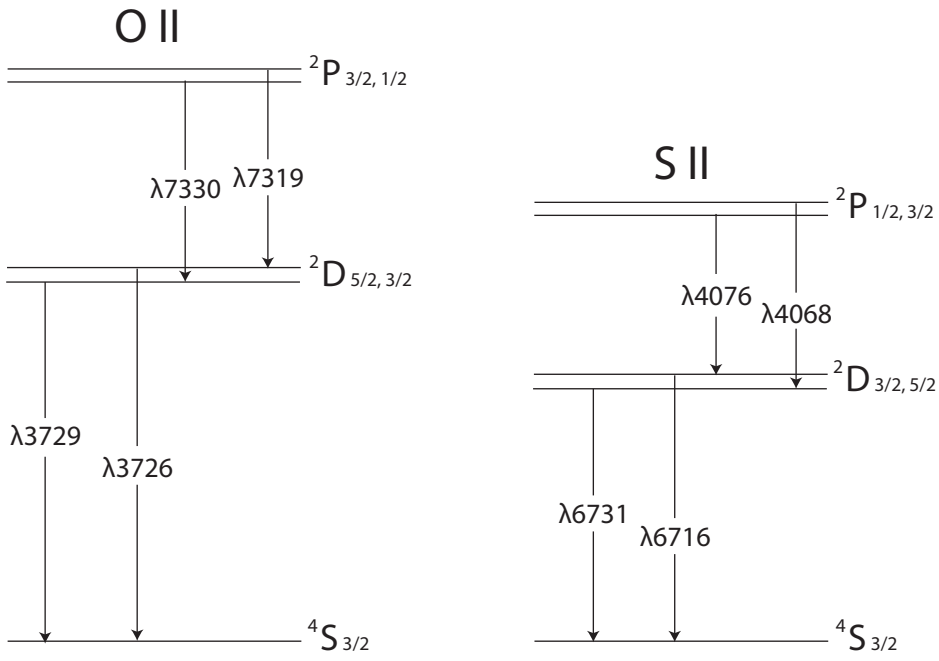

Figure 1.4: Energy level diagram for O^+ and S^+ showing the [O II] and [S II] lines used for T_e and N_e determinations; see text for details.

and can be ignored in this discussion). Therefore, the intensity ratio $I(\lambda 4959 + \lambda 5007)/I(\lambda 4363)$ depends strongly on temperature. Similarly for [N II] the ratio $I(\lambda 6548 + \lambda 6584)/I(\lambda 5755)$ can be used to measure the electron temperature. The dependence on temperature of this intensity ratio can be seen from equations 1.10,1.9 and 1.11 to be $\propto e^{\Delta E/kT_e}$.

Although not used in this work, the transition ratios [O II] (λ3726 + λ3729)/(λ7319 + λ7330) and [S II] (λ4068 + λ4076)/(λ6716 + λ6730) (both shown in Figure 1.4) are also potential electron temperature diagnostics. However, the usefulness of these diagnostics can be limited since the lines involved are often affected by processes other than simple collisional excitation/de-excitation and contributions from recombination excitation have to be accounted for in some cases.

1.4.1.2 Electron density determinations

CELs useful for measuring electron densities are those which have very similar excitation energies but widely differing collisional de-excitation rates, resulting in the line ratio depending very

weakly on temperature but strongly on $N_{\rm e}$. In the cases of [O II] , [S II] , [Cl III] and [Ar IV] the ratios of the $^2D - ^4S$ doublet transitions are useful density indicators (i.e. the doublet $\lambda\lambda$ 3726, 3729 for [O II] and $\lambda\lambda$ 6716, 6730 for [S II]). An energy level diagram for [O II] and [S II] is shown in Figure 1.4

The range of densities over which these diagnostics remain useful depends on the critical densities of the upper levels. For $N_{\rm e} << N_{crit}$, level populations are proportional only to the collisional excitation rate and not the electron density, while at $N_{\rm e} >> N_{crit}$, it can be seen from Equations 1.10 and 1.11 that the line ratio reduces to the ratios of the statistical weights and transition probabilities of the two levels. The critical densities of the upper levels of the [O II] and [S II] doublets are fairly low at $\sim 10^4$ cm^{-3}, while for [Ar IV] and [Cl III] the critical densities are higher at $\sim 10^5$ cm^{-3} and $\sim 3 \times 10^4$ cm^{-3}

1.4.2 Abundance determinations

1.4.2.1 Ionic abundance derivations using CELS

As the strongest lines in H II region spectra, CELs have long been used to derive abundances. The ratio of a CEL from level i to level j to Hβ can be used to derive an abundance for the parent ion X^{i+} using the following formula:

$$\frac{N(X^{i+})}{N(H^+)} = \frac{N_e h\nu \alpha_{eff}(H\beta)}{A_{ij} n_i E_{ij}} \frac{I(\lambda)}{I(H\beta)} \tag{1.19}$$

The presence in this equation of the level i population n_i means that the derived abundance has an exponential dependence on the adopted $T_{\rm e}$ (c.f. Equation 1.11). This extreme sensitivity to physical conditions is the chief disadvantage of using CELs as abundance indicators, and demonstrates that great care must be taken to obtain temperatures as accurate and appropriate as possible for the emitting regions. Any systematic under- or overestimate of the electron temperature will result in a considerable over- or underestimate of heavy element abundances.

Hence the ionic abundances of the CEL emitting ions (e.g. O^+, O^{2+}, N^+, S^+), relative to H^+, can be determined once the $T_{\rm e}$ and $N_{\rm e}$ of the ionised region has been measured using one of the methods described in Section 1.4.1. In order to subsequently derive the *total* abundance of a given element relative to hydrogen, one adds up the relative abundances of observed ionisation stages. Whenever important ionisation stages are not covered by the spectral observations, then the empirical approach makes use of ionisation correction factors (ICFs) and total abundances may

be found as:

$$\frac{N(X^0)}{N(H)} = ICF(X) \sum_i \frac{N(X^{i+})}{N(H^+)} \tag{1.20}$$

In this work, the ICF scheme of Kingsburgh & Barlow (1994) was used which is based on the similarity of ionisation potentials amongst various ions along with results from detailed photoionisation modelling of PNe, which included the effects of charge exchange, dielectronic recombination etc.

1.4.2.2 Ionic abundance derivations using ORLs

In comparison to their strength relative to Hβ, ORLs are generally much weaker than CELs, with strengths of $\sim 10^{-3}$–10^{-1} relative to H$\beta = 100$, while CEL line strengths may exceed 500 (e.g. [O III] λ5007). However, as they arise via the same process as the hydrogen lines, their ratios to Hβ are far less dependent on physical conditions than those of CELs, and so abundances derived from them should in principle be more reliable. However abundance discrepancies between ORLs and CELs have been found (Tsamis *et al.* (2003) for H II regions, Liu *et al.* (2000); Tsamis *et al.* (2004); Wesson *et al.* (2005) for PNe).

The abundance of an ion relative to hydrogen may be calculated from the following formula:

$$\frac{N(X^{i+1}+)}{N(H^+)} = \frac{I(X^{i+}, \lambda)}{I(H\beta)} \frac{\alpha_{eff}(H\beta)}{\alpha_{eff}(X^{i+})} \frac{\lambda}{4861} \tag{1.21}$$

where $I(\lambda)$ is the intensity of an emission line from the recombined ion X^{i+}.

Helium

Attention should be brought to helium; the only element within this work that make use of this abundance determination method. The abundance of helium is determined from observations of strong optical He I recombination lines, e.g. the λ4471, λ5876, λ6678 lines. The populations of the upper levels of these lines however are affected also by collisional excitation from the He^0 $2s^3S$ metastable level. This results in a non-negligible increase in the strength of the aforementioned He I lines that has to be allowed for, before deriving abundances via Equation 1.21.

The correction formulae, derived empirically by Kingdon & Ferland (1995) based on 29-state quantal calculations of the He atom by Sawey & Berrington (1993) , for each helium line used

in this work are listed below, where C/R is the ratio of the collisional component to that arising from recombination for a given line:

$$\frac{C}{R}(\lambda 4471) = (6.95t_4^{0.15}e^{-4.545/t_4} + 0.22t_4^{-0.55}e^{-4.884/t_4} + 0.98t_4^{-0.45}e^{-4.901/t_4})/D \quad (1.22)$$

$$\frac{C}{R}(\lambda 5876) = (6.78t_4^{0.07}e^{-3.776/t_4} + 1.67t_4^{-0.15}e^{-4.545/t_4} + 0.60t_4^{-0.34}e^{-4.901/t_4})/D \quad (1.23)$$

$$\frac{C}{R}(\lambda 6678) = (3.15t_4^{-0.54}e^{-3.776/t_4} + 0.51t_4^{-0.51}e^{-4.545/t_4} + 0.20t_4^{-0.66}e^{-4.901/t_4})/D \quad (1.24)$$

Where in all formulae, the denominator D is equal to $(1+3130t_4^{-0.50}n_e^{-1})$ and $t_4 = T/10000$. Corrections are thus made to the uncorrected helium abundances (y^+) by dividing by $(1 + \frac{C}{R})$, i.e.

$$y^+(\lambda) = \frac{y^+(\lambda, uncorrected)}{1 + \frac{C}{R}(\lambda)} \quad (1.25)$$

In order for the total He abundance to be obtained, one has also to add in the amount of He^{2+}. The He^{2+}/H^+ ionic fraction is usually derived from observations of the nebular He II λ4686 line, which is only rarely observed in H II region spectra.

1.5 Integral Field Spectroscopy

With our increasing desire and capability to observe and understand BCD galaxies, the requirement for spatially resolved spectroscopy has become very apparent. Since a significant part of this thesis is based on a number of observations making use of integral field spectroscopy (IFS), a short introduction into the technologies used is presented here.

IFS (also known as 3D spectroscopy or integral field unit (IFU) spectroscopy) is distinct from multi-object spectroscopy (MOS) by the fact that a continuous spatial area is observed, rather than discrete points across the field. IFS can be achieved using a number of instruments employing different techniques, including Fabry-Pérot devices or IFUs. An IFU is designed to split the field-of-view (FoV) into sections for re-imaging by a spectrograph and is described in more detail in the following section.

The resultant data product from IFS contains three dimensions, usually formated as a data-cube (two spatial dimensions for each slice, along with the wavelength dimension). The 'data-cube' is

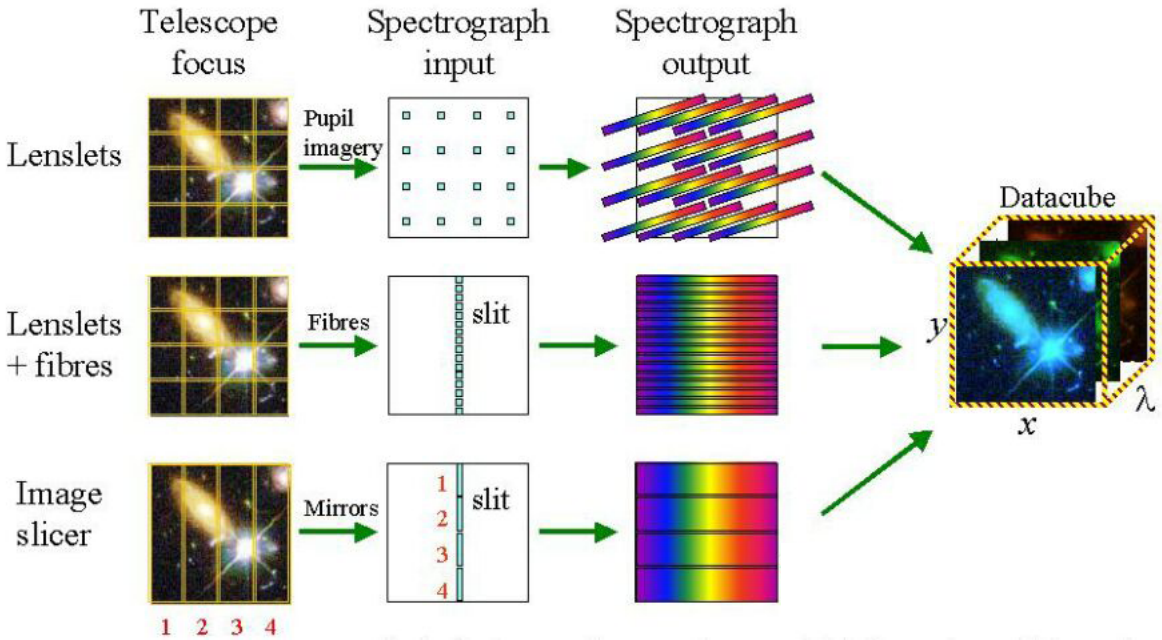

Figure 1.5: Cartoon diagram depicting the three main designs for integral-field units. *Top:* the FoV is split using a lenslet array, and through pupil imagery, the light is transmitted to the spectrograph. The individual spectra have to be tilted to avoid overlap on the detector. *Middle:* a lenslet array coupled to optical fibres reformats the FoV into a pseudo-slit at the entrance to the spectrograph. *Bottom:* a set of angled mirrors slices up the FoV and the subsequent optics reformat the slices into a pseudo-slit before the light enters the spectrograph. In all three methods, the information on the original spatial arrangement of the spectra can be used to reconstruct the data into a set of $x - y$ images for each wavelength unit (adapted from Allington-Smith *et al.* (1998))

not a revolutionary idea; the radio community have used data-cubes ever since detectors were developed with spatial resolution capabilities. Although existing techniques, such as stepping a longslit spectrograph or scanning a Fabry-Pérot device, can produce such a data cube, the IFS technique collects the data simultaneously, with obvious savings in observing efficiency.

1.5.1 Integral Field Units (IFUs)

An IFU is defined by the method it uses to split up the available FoV for re-imaging by a spectrograph. A cartoon representation of the three main techniques is shown in Figure 1.5 (Allington-Smith *et al.* 1998). What follows is a description of the middle panel of Figure 1.5, which represents the IFU techniques employed within VIMOS (VIsual Multi-Object Spectrograph) IFU, the instrument used to take the IFS observations presented in Chapters 2 and 3 of this thesis.

The lenslet+fibre method involves optical fibres used to image the FoV and transmit the light

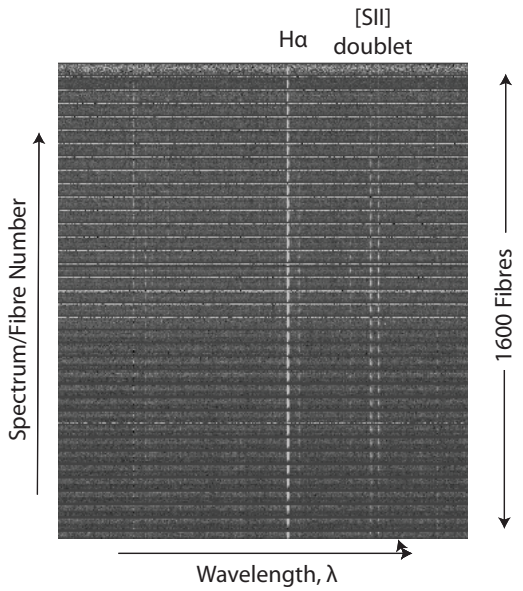

Figure 1.6: An example of the 3D data cube stacked into a 2D format, as imaged onto a CCD detector after having been re-formatted by a lenslet+fibre IFU array. Hα and [S II] doublet emission is evident, along with faint emission lines such as [N II] either side of Hα.

to the spectrograph. An array of lenslets in front of the fibres are used to increase the efficiency of both light collection and spatial sampling. The advantage of this technique is that the spatial format of the spectra can be re-formatted (in any order) by the fibres onto a pseudo-slit at the entrance aperture of the spectrograph (i.e. all the fibres are arranged such that they line up in a row forming the shape of a slit). Figure 1.6 shows an example of a CCD image showing a sub-set of spectra taken with the VIMOS-IFU, focusing on the Hα spectral region. As can be seen, a separation sufficient to avoid contamination between individual spectra and to enable them to be easily traced along the length of the detector must also be made when re-arranging the fibres into the pseudo-slit.

1.5.2 IFS and BCDs

In order to attempt to understand the complex H II regions within BCDs we require innovative and novel approaches to investigating their inner-workings. Long-slit spectroscopic studies of BCDs are hindered spatially, restricting information about an object's overall chemical, kinematical and physical structure. Since IFS provides both spatial and spectral resolution, it is ideally suited to

studying BCDs with the detail required for a true understanding of the overall nature of these systems, although IFS studies of BCDs are currently rather scarce. One recent study, by García-Lorenzo *et al.* (2008), involved a sample of five BCDs using the fibre system INTEGRAL on the 4.2 m William Herschel Telescope, in which maps of emission lines, radial velocity, $T_{\rm e}$ and $N_{\rm e}$ were presented, although abundance maps were not attempted. Two recent studies by Lagos *et al.* (2009) (GMOS-IFU observations of the BCD UM 408) and Kehrig *et al.* (2008) (PMAS-IFU observations of the BCD II Zw 70) have been published in which oxygen abundance maps are used to provide insight into the chemical recycling processes and massive star feedback within each galaxy. It is exactly this type of spatially resolved chemical and physical information that the observations in this thesis were designed to achieve. However, a plethora of studies *do* exist in which integral field spectrographs have been used to study emission line regions within planetary nebulae (Tsamis *et al.* 2006, 2008), nearby WR galaxies (Bastian *et al.* 2006), starbursts and superwind systems (Westmoquette *et al.* 2007*a*,*b*, 2009), and the methods and techniques employed by such studies are easily transferable to studies of BCDs.

1.6 Structure of this Thesis

Motivated by the topics presented in this introduction, the following chapters contain work based on approaches I have taken to investigate blue compact dwarf galaxies:

- The first two chapters concern an optical IFU study of three BCDs using VIMOS-IFU. A comparative study of UM 420 and UM 462 are described in Chapter 2 whereas Chapter 3 describes a more complex, multicomponent study of a highly anomalous BCD Mrk 996.
- Chapter 4 contains a mid-IR wavelength analysis of a sample of 13 BCDs using *Spitzer* spectroscopy and imaging data.
- The optical and infrared results from Chapters 3 and 4 are used in Chapter 5 to constrain a photoionisation model of Mrk 996.
- Conclusions derived from the whole body of work are presented in Chapter 6, together with possible future directions for research into blue compact dwarf galaxies.

Table 1.1 lists the all the targets involved in this study and their general properties, including redshift, metallicity and classification, and the references from which they are derived.

Object Name	RA (J2000)	DEC(J2000)	LOG(O/H)+12	Redshift	NED Type	Alternative Object Names	O/H References
SBS 0335-052E	03 37 44	-05 02 39	7.31	0.013486	BCG		Izotov *et al.* (2005)
II ZW 40	05 55 42	+03 23 32	8.13	0.00263	BCD;Sbc;merger H II	UCGA116	Thuan & Izotov (2005)
He 2-10	08 36 15	-26 24 32	8.93	0.00291	BCG ,sbrst,pec	ESO491-21	Kobulnicky *et al.* (1999)
Mrk 33	10 32 31	+54 24 04	8.42	0.00477	Im, pec, H II	UGC5720, HARO 2	Shi *et al.* (2005)
NGC 3353	10 45 22	+55 57 33	8.34	0.00315	BCD,Irr,H II	UGC5860, Mrk 35 ,HARO 3	Thuan & Izotov (2005)
UM 448	11 42 12	+00 20 03	7.99	0.01856	Sb pec,sbrst,H II	UGC6665, Mrk 1304	Izotov & Thuan (1998)
NGC 4670	12 45 17	+27 07 32	8.20	0.003566	Sb0,pec, BCD	UGC7930 ,HARO 9	Heckman *et al.* (1998)
NGC 5253	13 39 56	-31 38 42	8.51	0.00136	Im pec,H II,sbrst	UGCA369,Haro 1	Shi *et al.* (2005)
II ZW 70	14 50 56	+35 34 17	7.8	0.00394	pec, BCD, H II	UGC9560, Mrk 829	Shi *et al.* (2005)
NGC 6764	19 08 16	+50 55 54	8.86	0.008059	SBbc,LIN	UGC11407	Izotov & Thuan (1998)
NGC 7625	23 20 29	+17 13 33	?	0.005447	SAa pec,H II	UGC12529, III Zw 102	
NGC 7673	23 27 41	+23 35 20	8.50	0.011368	pec, H IIsbrst	UGC12607, Mrk 325	Shi *et al.* (2005)
III ZW 107	23 30 09	+25 32 00	7.9	0.019127	Im	IVZw 153	Gallego *et al.* (1997)
NGC 7714	23 36 14	+02 09 18	8.9	0.00933	SBb pec, H IILIN	UM 167, UGC12699, Mrk 538	Engelbracht *et al.* (2005)
I Zw 18	09 34 02	+55 14 28	7.12	0.002505	cI, BCD	UGCA166,Mrk 0116	Thuan & Izotov (2005)
Mrk 996	01 27 35	-06 19 35	8.37	0.00544	WR		This Work
UM 420	02 21 36.2	00 29 34.3	8.25	0.060604	BCG		This Work
UM 461	11 51 33.35	-02 22 21.9	7.78	0.003465	BCG/Irr ,H II		Izotov & Thuan (1998)
UM 462	11 53 18.5	-02 32 20.6	8.11	0.003527	Pec, H II	UGC 06850, Mrk 1307	This Work

Table 1.1: Notes: Units of right ascension are hours, minutes, and seconds, and units of declination are degrees, arcminutes, and arcseconds. The coordinates redshifts and classifications of the objectes are cited from the NASA/IPAC Extragalactic Database (NED), which is operated by the Jet Propulsion Laboratory, California Institute of Techonology, under contract with the National Aeronautics and Space Administration. Key for classification: BCG=Blue compact galaxy, BCD=Blue compact dwarf, H II= H II region, IG=Irregular Galaxy, sbrst=Starburst galaxy, EmG= Emission line galaxy, Irr=Irregular galaxy ,WR= Wolf-Rayet Galaxy, Pec= Peculiar Galaxy, cI=Compact Irregular, LIN=Liner, Sbc=Barred spiral type C.

CHAPTER 2

AN IFU STUDY OF PERTURBED BLUE COMPACT GALAXIES: UM 420 AND UM 462

The work described in this chapter, excluding Section 2.1, has been submitted for publication in MNRAS entitled "A VLT VIMOS integral field spectroscopic study of perturbed blue compact galaxies: UM 420 and UM 462" by B. L. James, Y. G. Tsamis and M. J. Barlow, 2009.

2.1 A VLT-VIMOS Investigation

A successful period 78A ESO proposal was made by PI Yiannis Tsamis (currently at Instituto de Astrofísica de Andalucía, Granada, Spain) entitled "Investigating the chemical homogeneity of the gas in H II galaxies with deep VLT-VIMOS integral-field spectroscopy". Chapters 2 and 3 are based on the reduction and analysis of the data obtained as a result of that proposal. The applicants proposed to investigate a sample of four BCDs with VIMOS IFU spectroscopy, concentrating specifically on their spatial He, N and O elemental abundances and any He/O or N/O spatial variations that might exist, as a function of metallicity. The four objects were chosen according to their nitrogen abundance properties. Two of the objects in the sample, Mrk 996 (Chapter 3) and UM 420 (this chapter), were selected from a group of BCDs with anomalously high N/O ratios and spatial nitrogen abundance variations. They are both relatively metal rich ($\sim$0.20 $Z_{\odot}$), and their N/O abundance ratios had been reported as being 0.3-1.4 dex higher than BCDs of similar metallicty (Pustilnik *et al.* 2004). The remaining two, UM 462 (this chapter) and Mrk 600 (not presented in this work) are utilised as comparisons, being of lower metallicity (0.10–0.20 $Z_{\odot}$), with *normal* N/O abundance ratios, i.e. close to the average observed at those metallicities.

2.2 Introduction

Blue compact dwarf galaxies (BCGs) offer a means of exploring star-formation in low-mass, low-metallicity (1/50–1/3 $Z_{\odot}$,Kunth & Östlin (2000)) systems and, by analogy, the chemically un-evolved systems in the high-z primordial universe. Typically, they are characterised by their strong emission lines superimposed on a faint, blue continuum, resulting from one or more recent bursts of star-formation. These compact, gas-rich objects are estimated to have high star-formation rates in the order of 0.1 to 1 $M_{\odot}$ yr^{-1} (Fanelli *et al.* 1988) with typical H I masses of $M_{HI} \sim 10^7 - 10^8\ M_{\odot}$ (van Zee *et al.* 1998), and are ideal laboratories for many topics related to star-formation, partly because they do not display more complicated phenomena, such as density waves, that operate in larger galaxies (Cairós *et al.* 2001*b*). This is a study of two BCGs, UM 420 and UM 462, first discovered by the University of Michigan survey for extragalactic emission-line objects (MacAlpine & Lewis 1978). Their individual properties may provide insights into the role of galaxy interactions in chemical recycling and starbursting episodes. Several studies have suggested that interactions with other systems are a contributing factor to large-scale starbursts in dwarf galaxies (Méndez & Esteban 2000; Iglesias-Páramo & Vílchez 2001; Verdes-Montenegro *et al.* 2002; Tran *et al.* 2003). Hence it may be no coincidence that both galaxies studied here display signs of interaction and/or perturbation in the form of tails, multiple nuclei, or disrupted morphology.

UM 420 was reported by López-Sánchez & Esteban (2008) as having an irregular and elongated morphology, with two long regions extending in different directions from the brightest central region. A bright spiral galaxy, UGC 1809, lies 16.5″ west of UM 420, but at less than half the redshift of UM 420 is not physically associated to it and cannot cause an effect. UM 420 was once thought to be a large H II region near the edge of UGC 1809's spiral arms, and as a result the SIMBAD data base currently incorrectly lists its RA and DEC as those of UCG 1809 (the correct RA and DEC for UM 420 are given in Table 2.1). Pustilnik *et al.* (2004) describe UM 420 as being a possible 'sinking merger', i.e. harbouring a satellite galaxy that is sinking into a larger, gas-rich companion.

UM 462 with UM 461 form part of an interacting binary pair separated by only ∼50″ (Taylor *et al.* 1995; Telles & Terlevich 1995). In a H I survey of H II galaxies[1] with companions (Taylor *et al.* 1995), UM 461 was observed to have a tidal arm extending in the direction of UM 462 and

[1] H II galaxies are galaxies with spectra similar to H II regions but more metal-rich than blue compact dwarfs (Kunth & Östlin 2000)

outer H I contours that are clearly disturbed by its nearby neighbour. Telles & Terlevich (1995) interpreted UM 462 as being part of a group of H II galaxies, UM 461, UM 463 and UM 465, whose star-bursting episodes are synchronised on time scales of less than 10^7 years, despite being separated by $\sim$1–2 Mpc. Following the classification system of Loose & Thuan (1985), Cairós *et al.* (2001*b*) classified UM 462 as being of 'iE' type, i.e. showing a complex inner structure with several star-forming regions superimposed on an extended regular envelope. This type of structure is commonly interpreted as a sign of interaction. Spectroscopically, both galaxies have been classified as Wolf-Rayet (WR) galaxies (this is however disputed in the present work; see Sec. 5.3), with broad He II λ4686 being detected in their spectra (Izotov & Thuan 1998; Guseva *et al.* 2000). Guseva *et al.* (2000) also claimed to see broad C IV λ4658 and C IV λ5808 emission in the spectra of UM 420, indicating the presence of WCE stars, although the detections were doubted by Schaerer *et al.* (1999*b*) on the basis of the S/N ratio of the Guseva *et al.* (2000) spectrum. The relative numbers of WR stars to O-type stars were estimated by Guseva *et al.* (2000) as 0.03 and 0.005 for UM 420 and UM 462, respectively. Schaerer *et al.* (1999*b*) have defined WR galaxies as being those whose ongoing or recent star formation has produced stars sufficiently massive to evolve to the WR stage. However, the same authors also note that the definition of a WR galaxy is dependent on the quality of the spectrum, and the location and size of the aperture.

UM 420 falls within a small sub-set of BCGs reported by Pustilnik *et al.* (2004) as having anomalously high N/O ratios ($\sim$ 0.5 dex) compared to BCGs of similar oxygen metallicity (12+log(O/H)=7.93; Izotov & Thuan 1998, IT98 hereafter). They attributed this over-abundance of nitrogen to the effects of N-rich winds from large numbers of Wolf-Rayet (WNL-type) stars. A previous IFU study by James *et al.* (2009*b*) (J09 hereafter and presented in Chapter 3) of another BCG in this 'high N/O' group, Mrk 996, derived a significantly higher O/H ratio than previously and an N/O ratio for its narrow-line component which is now typical for its metallicity. Mrk 996, however, was shown by J09 to also contain an extremely dense, extended broad-line component displaying a N/O ratio up to 20 times higher than the galaxy's narrow-line component; this large N/H and N/O enrichment was attributed to the cumulative effects of a large population of $\sim$2600 WNL-type stars whose number was estimated from fitting the broad emission features at 4640 and 4650-Å with theoretical WR spectral templates. By conducting a similar study of UM 420 I aimed to investigate its N/O ratio status, and to study potential effects to the gas abundance patterns due to WR stars. On the other hand, UM 462 provides a useful comparison, as it has been reported to have a rather normal N/O ratio close to the average observed for many BCGs at its published metallicity of $12 + \log(\mathrm{O/H}) = 7.95$ (IT98).

Table 2.1: General Parameters of UM 420 and UM 462

	Coordinates (J2000)				
Name	α	δ	z^a	Distance (Mpc)	Other Names
UM 420	02 21 36.2	00 29 34.3	0.060604	238	
UM 462	11 53 18.5	-02 32 20.6	0.003527	14.4	Mrk 1307, UGC 06850

[a] Derived from the present observations

In order to understand interaction-induced starbursts, it is essential to gain spatial information regarding the properties (e.g. physical conditions, chemical abundances) of the starburst regions and any spatial correlations that may hold. This type of information has been limited in previous long-slit spectroscopic studies of H II galaxies. In this chapter I present high resolution optical observations obtained with the VIMOS integral field unit (IFU, described in detail in Section 1.5.1) spectrograph on the ESO 8.2m Very Large Telescope UT3/Melipal. The data afford us new spatiokinematic '3-D' views of UM 420 and UM 462. The spatial and spectral resolutions achieved (Section 2.3.1) allow us to undertake a chemical and kinematical analysis of both systems, providing a clearer picture of the ionised gas within their star-forming regions. I adopt distances of 238 Mpc and 14.4 Mpc for UM 420 and UM 462, respectively, corresponding to their redshifted velocities measured here of +17,454 and +1057 km s^{-1} ($z = 0.060604$ and 0.003527, as given in Table 2.1), for a Hubble constant of H_o = 73.5 km s^{-1} Mpc^{-1} (DeBernardis *et al.* 2008).

2.3 VIMOS IFU Observations and Data Reduction

2.3.1 Observations

Two data sets for each galaxy were obtained with the Visible Multi-Object Spectrograph (VIMOS) IFU mounted on the 8.2m VLT at the Paranal Observatory in Chile. All data sets were taken with the high-resolution and high-magnification settings of the IFU, which resulted in a field-of-view (FoV) of $13'' \times 13''$ covered by 1600 spaxels (spatial pixels) at a sampling of $0.33''$ per spaxel. The data consist of high-resolution blue grism spectra (HRblue, $\sim$0.51 Å/pixel, 2.01$\pm$ 0.23 Å FWHM resolution) covering 4150–6200 Å and high-resolution orange grism spectra (HRorange, $\sim$0.6 Å/pixel, 1.92 $\pm$ 0.09 Å FWHM resolution) covering 5250–7400 Å. Spectra from both grisms for each galaxy are shown in Figure 2.1. The observing log can be found in Table 2.2. Four exposures were taken per grism, per observation ID. The third exposure within each set was dithered by $+0.25''$ in RA and by $+0.61''$ in DEC for both galaxies (corresponding to a 2 spaxel offset in

Table 2.2: VIMOS IFU observing log

Observation ID	Date	Grism	Exp. time (s)	Airmass range	FWHM seeing (arcsec)
			UM 420		
250536-9	14/11/2006	HR blue	4×402	1.11–1.40	0.85
250534,250535	14/11/2006	HR orange	4×372	1.13–1.36	0.79
			UM 462		
250563-6	22-23/03/2007	HR blue	4×402	1.60 – 1.10	1.02
250559,250562	22-23/03/2007	HR orange	4×372	2.16 – 1.73	0.74

the X-direction) in order to remove any broken fibres when averaging exposures. All observations were taken at a position angle of 20° for UM 420 and 22° for UM 462.

2.3.2 Data Reduction

Data reduction was carried out using the ESO pipeline via the GASGANO[2] software package and followed the sequence outlined by J09 (also detailed in Section 3.2.2). The reduction involves three main tasks: *vmbias*, *vmifucalib* and *vmifustandard*. The products of these were fed into *vmifuscience* which extracted the bias-subtracted, wavelength- and flux-calibrated, and relative fibre transmission-corrected science spectra. The final cube construction from the quadrant-specific science spectra output by the pipeline utilized an IFU table that lists the one to one correspondence between fibre positions on the IFU head and stacked spectra on the IFU (Bastian *et al.* 2006). A final data cube for each of the HRblue and HRorange grisms was then created by averaging over the final flux-calibrated science cubes created from each observation block. For a more detailed description of the data reduction and processing from science spectra to spatially reconstructed cube, see J09. A schematic representation of the data reduction processes performed within GASGANO is provided by Zanichelli *et al.* (2005). Sky subtraction was performed by locating a background region within each quadrant, summing the spectra over each of the spaxels in the reconstructed cube and subtracting the median sky spectrum of the region from its corresponding quadrant. Median combining was needed to ensure that any residual contamination from faint objects was removed. In the case of UM 420, the western edge of the IFU frame sampled the outermost faint regions of the unrelated foreground spiral galaxy UGC 1809 (e.g. López-Sánchez & Esteban (2008)), and this background subtraction procedure enabled the removal of any contaminating signal. Before averaging to produce a final data cube for each grism, each cube was corrected for differential

[2]http://www.eso.org/sci/data-processing/software/gasgano

atmospheric refraction (DAR). This correction accounts for the refraction of an object's spectrum along the parallactic angle of the observation as it is observed through the atmosphere. The cubes were corrected using an IRAF-based programme written by J. R. Walsh (based on an algorithm described in Walsh & Roy (1990)). The procedure calculates fractional spaxel shifts for each monochromatic slice of the cube relative to a fiducial wavelength (i.e. a strong emission line), shifts each slice with respect to the orientation of the slit on the sky and the parallactic angle and recombines the DAR-corrected data cube. For both galaxies a high S/N ratio fiducial emission line (He I λ5876) was available within the wavelength overlap of the HRblue and HRorange cubes. Although not essential, correcting multiple spectral cubes to a common emission line allows one to check that the alignment between them is correct.

2.3.3 Emission Line Profile Fitting

Taking into account that there are 1600 spectra across the FoV of each data cube, I utilized an automated fitting process called PAN (Peak ANalysis; Dimeo 2005). This is an IDL-based general curve-fitting package, adapted by Westmoquette *et al.* (2007*a*) for use with FITS data. The user can interactively specify the initial parameters of a spectral line fit (continuum level, line peak flux, centroid and width) and allow PAN to sequentially process each spectrum, fitting Gaussian profiles accordingly. The output consists of the fit parameters for the continuum and each spectral line's profile and the χ^2 value for the fit. It was found that all emission lines in the spectra of both UM 420 and UM 462 could be optimally fitted with a single narrow Gaussian profile. For high S/N ratio cases, such as Balmer lines and [O III] λ5007, attempts were made to fit an additional broad Gaussian profile underneath the narrow component. These fits were assessed using the statistical F-test procedure, a process that determines the optimum number of Gaussian profiles required to fit each line (see J09 for a more detailed discussion). I found that it was not statistically significant to fit anything more than a single Gaussian profile to the emission lines in the spectra of either object. Thus single Gaussian profiles were fitted to each emission line profile, restricting the minimum FWHM to be the instrumental width. Suitable wavelength limits were defined for each emission line and continuum level fit. Further constraints were applied when fitting the [S II] doublet: the wavelength difference between the two lines was taken to be equal to the redshifted laboratory value when fitting the velocity component, and their FWHM were set equal to one another. The fitting errors reported by PAN underestimate the true uncertainties. I thus follow the error estimation procedure outlined by J09, which involves the visual re-inspection of the line profile plus fit after checking which solution was selected by my tests, and taking into account the

S/N ratio of the spectrum. By comparing PAN fits to those performed by other fitting techniques (e.g. IRAF's SPLOT task) on line profiles with an established configuration (i.e. after performing the F-test) I find that estimated uncertainties of ∼5–10 per cent are associated with the single Gaussian profile fits. A listing of the measured flux and FWHM uncertainties appears in Table 2.3, where errors are quoted for individual component fits to emission lines detected on the integrated spectra from across all of UM 420 and UM 462. Errors correspond to the one sigma difference between the data and the optimised Gaussian fit and represent lower limits to the true uncertainty since they do not allow for the uncertainty in the placement of the continuum level.

2.4 Mapping Line Fluxes

2.4.1 Line fluxes and reddening corrections

Full HRblue and HRorange spectra for UM 420 and UM 462 are shown in Figure 2.1(a) and (b), respectively. Table 2.3 lists the measured FWHMs and observed and de-reddened fluxes of the detected emission lines within UM 420 and UM 462, respectively. The listed fluxes are from IFU spectra summed over each galaxy and are quoted relative to $F(\mathrm{H}\beta) = 100.0$. Foreground Milky Way reddening values of $E(B-V) = 0.04$ and 0.02 were adopted, from the maps of Schlegel *et al.* (1998), corresponding to $c(\mathrm{H}\beta) = 0.05$ and 0.03 in the directions of UM 420 and UM 462, respectively. The line fluxes were then corrected for extinction using the Galactic reddening law of Howarth (1983) with $R_V = 3.1$ using $c(\mathrm{H}\beta)$ values derived from each galaxy's Hα/Hβ and Hγ/Hβ emission line ratios, weighted in a 3 : 1 ratio, respectively, after comparison with the theoretical Case B ratios from Hummer & Storey (1987) of $j_{\mathrm{H}\alpha}/j_{\mathrm{H}\beta} = 2.863$ and $j_{\mathrm{H}\gamma}/j_{\mathrm{H}\beta} = 0.468$ (at $T_\mathrm{e} = 10^4$ K and $N_\mathrm{e} = 100$ cm^{-3}). The same method was used to create $c(\mathrm{H}\beta)$ maps for each galaxy, using Hα/Hβ and Hγ/Hβ ratio maps, which were employed to deredden other lines on a spaxel by spaxel basis prior to creating electron temperature, electron density and abundance maps. As stated in Table 2.3, overall $c(\mathrm{H}\beta)$ values of 0.25±0.08 and 0.19±0.04 were found to be applicable to the integrated emission from UM 420 and UM 462, respectively.

2.4.2 Hα line properties

Here I discuss the appearance of the targets in the light of the highest S/N ratio H I emission line, Hα. Figure 2.2 shows flux, radial velocity and FWHM maps for Hα from UM 420 and UM 462, respectively.

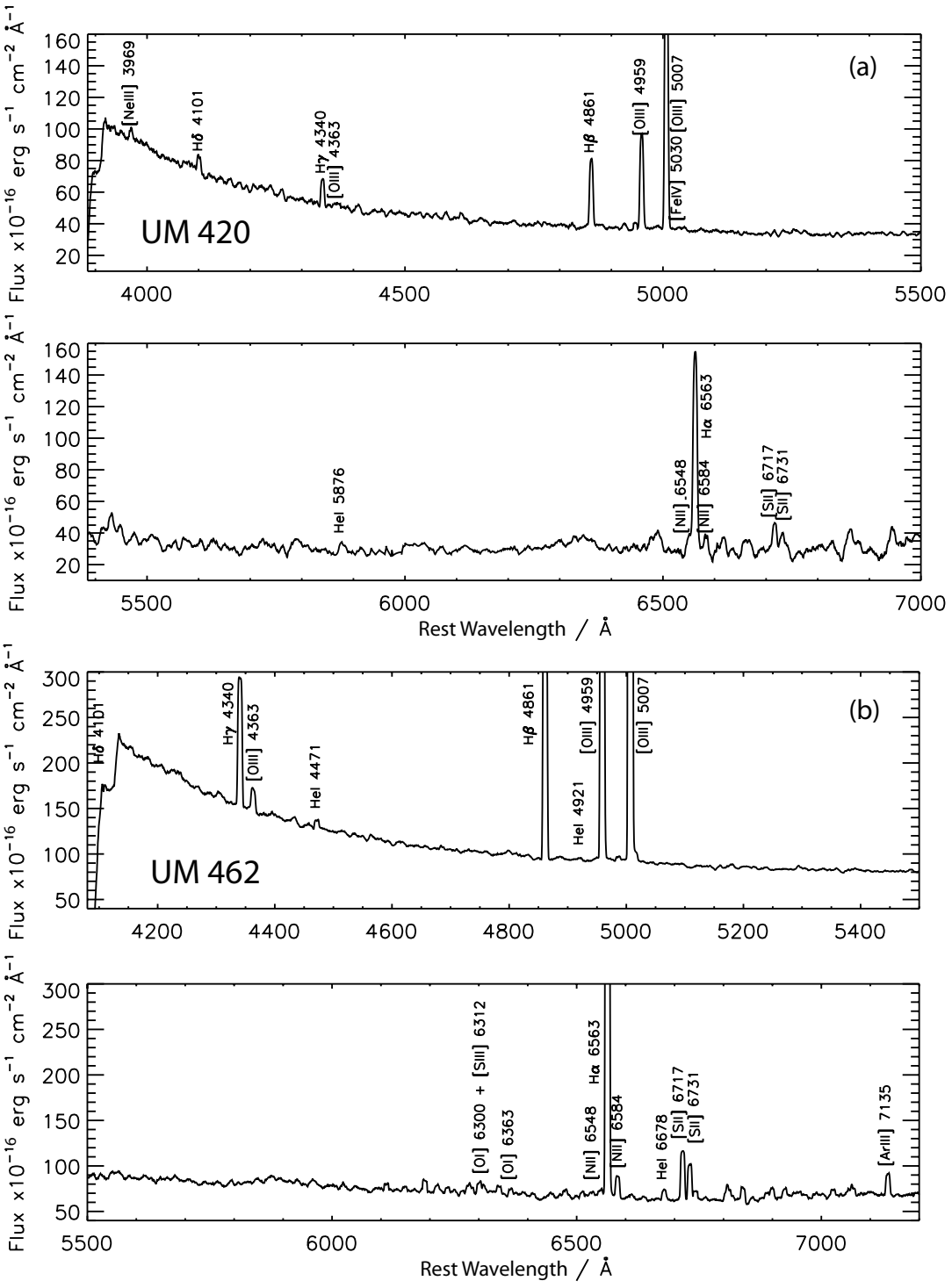

Figure 2.1: VIMOS IFU summed spectra of UM 420 after smoothing with a 5 pixel boxcar function: (a) UM 420, top panel: high resolution blue spectrum, bottom panel: high resolution orange spectrum. The spectra are integrated over an area of $7.6'' \times 6.3''$ (8.8×7.2 kpc^2) and correspond to exposure times of 4×402 s and 4×372 s for the HRblue and HRorange grisms, respectively; (b) Same as (a), for UM 462. Spectra are integrated over an area of $10.2'' \times 10.2''$ (714.1×714.1 pc^2).

Table 2.3: Emission line measurements for summed spectra of UM 420 and UM 462. Observed and de-reddened fluxes are relative to F(Hβ)=I(Hβ)=100. Line fluxes were extinction-corrected using the c(Hβ) values shown at the bottom of the table, calculated from the relative Hα, Hβ and Hγ fluxes. FWHMs have been corrected for the instrumental FWHM resolution (Section 2.3.1). F(Hβ) are in units of $\times 10^{-16}$erg s^{-1} cm^{-2}

	UM 420			UM 462		
Line ID	FHWM (km s^{-1})	F(λ)	I(λ)	FHWM (km s^{-1})	F(λ)	I(λ)
3969 [Ne III]	431.0± 52.2	27.1± 2.5	30.5± 2.8	—	—	—
4101 Hδ	205.7± 12.1	22.8± 1.2	25.3± 1.3	—	—	—
4340 Hγ	183.3± 5.3	42.0± 1.1	45.1± 1.1	143.1± 1.8	43.3± 0.5	45.7± 0.5
4363 [O III]	239.1± 64.0	6.3± 1.3	6.8± 1.4	156.6± 13.8	7.1± 0.5	7.4± 0.5
4471 He I	143.5±26.3	3.5±0.5	3.7±0.5	113.7± 12.4	3.1± 0.3	3.2± 0.3
4686 He II	—	—	—	175.4± 5.1	1.7± 0.1	1.7± 0.1
4861 Hβ	187.9± 2.0	100.0± 1.3	100.0± 0.9	123.4± 0.7	100.0± 0.7	100.0± 0.5
4921 He I	—	—	—	122.5± 7.3	0.9± 0.2	0.9± 0.2
4959 [O III]	182.3± 1.8	139.2± 1.7	137.3± 1.1	118.6± 1.2	164.6± 1.7	162.9± 1.5
5007 [O III]	181.4± 1.0	430.5± 4.5	421.9± 1.9	116.4± 0.7	477.4± 3.5	470.2± 2.5
5015 He I or [FeIV]	—	—	—	104.2± 6.6	1.8± 0.1	1.8± 0.1
5030 [Fe IV]	79.9± 15.2	3.5± 0.5	3.4± 0.5	—	—	—
5876 He I	184.0± 14.4	13.2± 0.9	11.7± 0.7	115.8± 11.6	12.1± 1.0	11.0± 0.9
6051 [Fe IV]	36.7± 7.2	6.8± 0.4	5.9± 0.3	—	—	—
6300 [O I]	—	—	—	116.8± 17.2	5.0± 0.6	4.4± 0.5
6312 [S III]	—	—	—	123.6± 21.9	1.9± 0.4	1.7± 0.3
6363 [O I]	—	—	—	150.9± 28.8	3.5± 0.7	3.1± 0.6
6548 [N II]	238.3± 56.6	10.9± 2.1	9.1± 1.7	127.3± 13.5	3.1± 0.3	2.7± 0.2
6563 Hα	178.8± 1.1	334.4± 3.6	279.1± 1.4	103.1± 0.6	323.4± 2.5	282.2± 1.6
6584 [N II]	189.7± 14.4	29.5± 1.8	24.6± 1.5	109.8± 4.2	8.5± 0.3	7.4± 0.2
6678 He I	135.7±105.2	4.7±1.6	3.8±1.3	127.6± 6.3	4.2± 0.4	3.7± 0.3
6716 [S II]	196.5± 9.3	33.9± 1.4	27.9± 1.1	101.0± 5.2	19.0± 0.8	16.4± 0.7
6731 [S II]	201.2± 12.6	26.9± 1.4	22.1± 1.1	105.9± 7.4	14.4± 0.8	12.4± 0.7
7136 [Ar III]	—	—	—	104.6± 8.9	9.2± 0.6	7.8± 0.5
c(Hβ) dex		0.25±0.08			0.19±0.04	
F(Hβ)		359.1±6.1			2660±14	

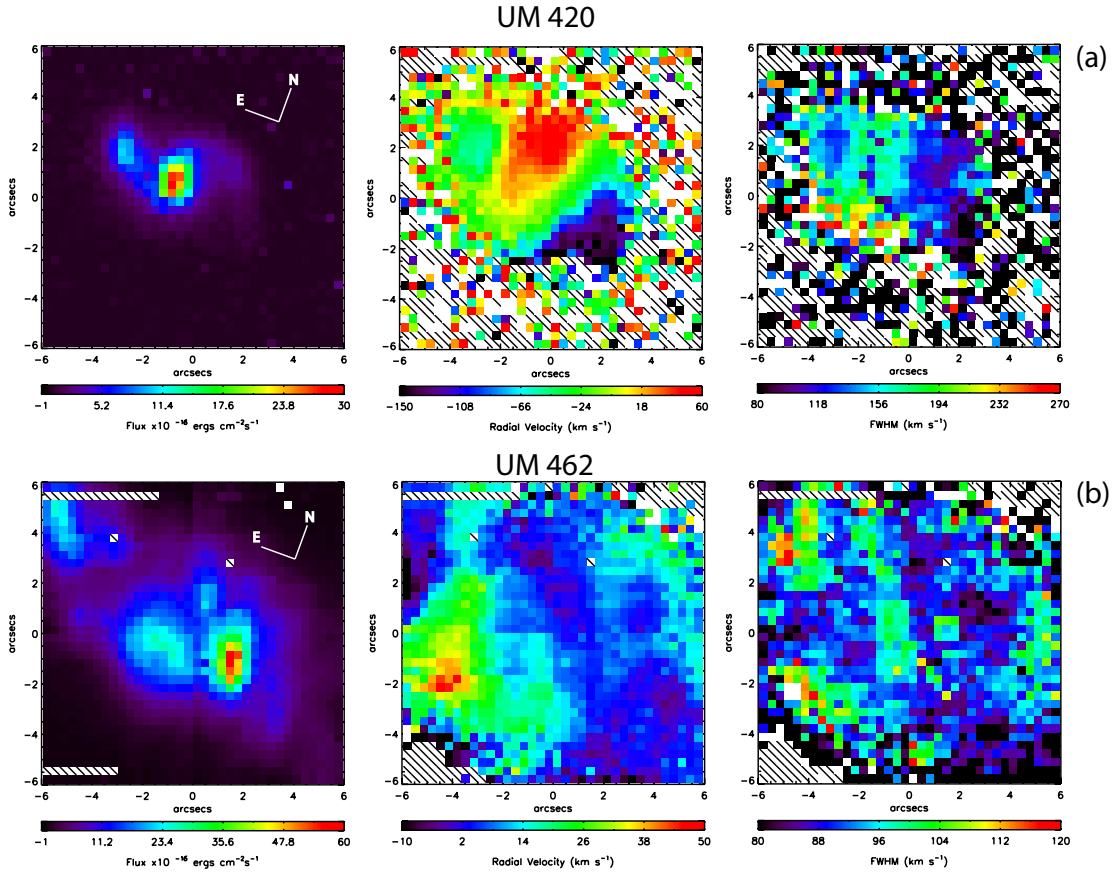

Figure 2.2: Maps of UM 420 (a) and UM 462 (b) in Hα; left column: flux per 0.33 arcsec^2 spaxel; centre column: radial velocity (relative to heliocentric systemic velocity of +17,545 and +1057 km s^{-1} for UM 420 and UM 462, respectively; right column: Hα FWHM corrected for the instrumental point spread function. See text for details.

2.4.2.1 UM 420

The Hα flux map shown in the left-hand panel of Figure 2.2(a) displays a double peak; the first peak is centrally located at the RA and DEC listed in Table 2.1, with a surface brightness of 2.75×10^{-14} erg cm^{-2} s^{-1} arcsec^{-2} and the second peak is located $\sim$2.2″ east of that central position, with a peak surface brightness of 9.72×10^{-15} erg cm^{-2} s^{-1} arcsec^{-2}. These two Hα peaks provide the basis for defining two main star-forming regions, as displayed in Figure 2.3. An arm-like structure can be seen north-west of the central peak, extending in a south-westerly direction; it could be the result of an ongoing merger or interaction between the two identified regions. A more luminous spiral galaxy, UGC 1809, lies 16.5″ westward of the galaxy, as noted by Takase & Miyauchi-Isobe (1986), but at less than half the redshift of UM 420 it cannot be

identified as an interacting companion. The VIMOS IFU Hα flux is a factor of 1.1 larger than the one measured by IT98 in a $3'' \times 200''$ slit and a factor of 1.8 times larger than that estimated by López-Sánchez & Esteban (2008) from broad band Hα + [N II] images. The Hα radial velocity map shown in the central panel of Figure 2.2 shows two separate velocity gradients. Firstly, there is a balanced velocity gradient at position angle (PA) 50° east of north (labelled as 'Position 1' on the central panel of Figure 2.4). This linear velocity gradient may be indicative of solid body rotation between the main emission peak (Region 1) and the 'arm-like' structure north-west of Region 1. Secondly, the main body of the galaxy, i.e. the double peaked emission structure, shows a velocity gradient at a PA of 110° east of north (labelled as 'Position 2' on the central panel of Figure 2.4).

Figure 2.4 shows position-velocity (P-V) diagrams along both these axes. These diagrams were created by placing a spaxel-wide (i.e. with a width of $0.33''$) pseudo-slit across the radial velocity map, and plotting the radial velocity as a function of distance from the slit's centre. The smooth and symmetrically structured velocity gradient along Position 1 suggests that the axis orthogonal to it could be adopted as a rotational axis for UM 420 (projected on the plane of the sky). From the top panel of Figure 2.4 I can then make a new estimate of the heliocentric systemic velocity of UM 420; a radial velocity of $+17{,}545 \pm 30$ km s^{-1} is needed to normalize the distribution along the proposed axis of rotation to zero (cf. the $+17{,}514 \pm 12$ km s^{-1} estimation of IT98). Thus a velocity gradient ranging from $\sim$-100 km s^{-1} to $\sim$+100 km s^{-1} is seen in the direction normal to the rotation axis, with the negative radial velocity of -100 km s^{-1} lying within the south-west arm of the galaxy. Also, a velocity gradient exists between Region 1 and 2, ranging from ~ -5 km s^{-1} to $\sim$+100 km s^{-1}. This velocity difference of $\sim$100 km s^{-1} between the two peaks in Hα flux may be evidence that Region 2 is a satellite galaxy falling into or merging with a larger companion, Region 1.

A FWHM map for Hα is shown in the right-hand panel of Figure 2.2(a). The highest measured FWHM is $\sim$270 km s^{-1}, located southwards of the central emission peak, along the southern edge of the galaxy. The central flux peak is aligned with a peak of $\sim$160 km s^{-1} whereas the second, easterly, flux peak is located within an area of decreased FWHM, $\sim$130 km s^{-1}, surrounded by a slightly higher FWHM area of $\sim$150 km s^{-1}. The south-western arm harbours the lowest line FWHM of $\sim$80–120 km s^{-1}.

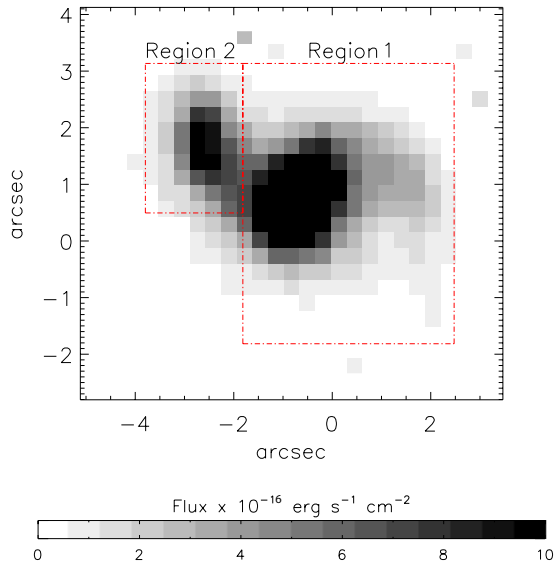

Figure 2.3: UM 420: Hα emission per 0.33×0.33 arcsec^2 spaxel. The two main areas of Hα emission have been used to define two main star-forming regions.

2.4.2.2 UM 462

UM 462 exhibits a far more disrupted morphology than UM 420. The left-hand panel of Figure 2.2(b) shows a peak in Hα flux located at $\alpha = 11^{\rm h}\,53^{\rm m}\,20.25{\pm}0.1^{\rm s}$, $\delta = -02^\circ\,32'\,19.62{\pm}0.1''$ (J2000), with a surface brightness of $5.34{\times}10^{-14}$ erg cm^{-2} s^{-1} arcsec^{-2}. Three additional flux peaks can be seen, located 2.5″ northeast, 3.05″ east and 8.9″ east of this central peak. These Hα peaks provide the basis for defining four main star-forming regions, as displayed in Figure 2.5. Three of the regions have a similar peak surface brightness of 2.0–2.4×10^{-13} erg cm^{-2} s^{-1} arcsec^{-2}. Region 4 lies farthest away from the brightest SF region (Region 1), at almost 9″; a large low surface brightness envelope ($\sim$5×10^{-14} erg cm^{-2} s^{-1} arcsec^{-2}) separates it from Regions 1–3. It could be the result of interaction with the nearby galaxy UM 461 (Taylor *et al.* 1995). Previous R-band imaging studies by Taylor *et al.* (1995) and H I imaging by Telles (1995) revealed only two star-forming regions within UM 462 which correspond to Regions 1 and 2 in Figure 2.5. The Hα flux measured by IT98 amounts to 35% of the corresponding VIMOS IFU flux, in accordance with the fraction of the galaxy's emitting area intercepted by IT98's slit. The radial velocity distribution of Hα, displayed in the central panel of Figure 2.2(b), shows no overall velocity structure through the galaxy. UM 462, being part of an interacting binary pair of

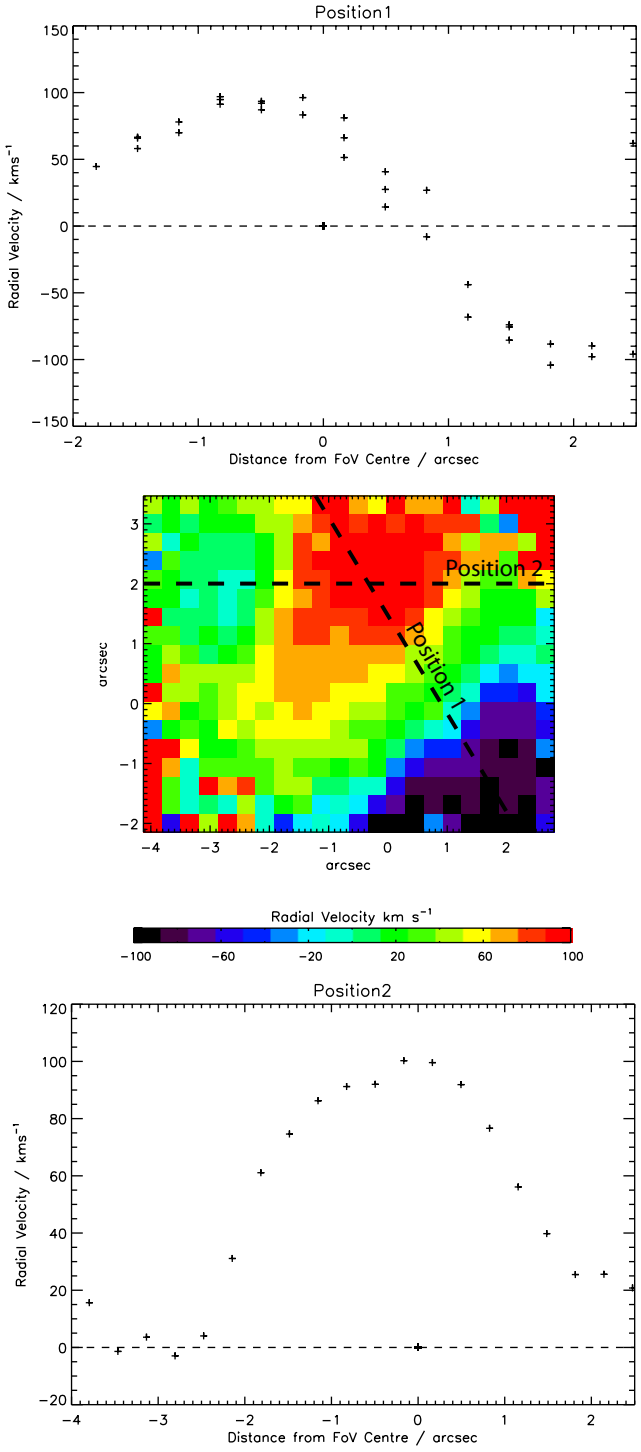

Figure 2.4: Position velocity (P-V) diagrams for UM 420 in Hα: central panel: radial velocity map of UM 420 (see Figure 2.2(a) for details) where the black dotted line overlaid on the map represents cuts orthogonal to the two proposed axes of rotation, as used for the P-V diagrams in the top and bottom panels; top panel: P-V diagram for Hα along Position 1, defined as 50° east of north; bottom-panel: P-V diagram for Hα along Position 2, at 110° east of north. Zero-point velocities are relative to a recession velocity of +17,514 km s^{-1}. Typical relative radial velocity errors are estimated as 30 km s^{-1}, with an estimated spatial uncertainty of 0.5 spaxels ($\pm 0.17''$).

galaxies, has a highly disturbed velocity distribution which shows no spatial correlation with flux (Figure 2.2(b): left-hand panel). The brightest region (Region 1) has a radial velocity of ∼0–10 km s^{-1}, as does the majority of the emitting gas. The largest radial velocity lies directly south-east of this region, with a magnitude of +50 km s^{-1}, in an area of low surface brightness emission. This velocity space extends into the envelope separating Region 4 from Regions 1–3. Region 4 itself lies within a space of negative radial velocity, where again the peaks in velocity and flux are spatially uncorrelated.

The Hα FWHM map of UM 462 (right-hand panel of Figure 2.2(b)) shows no spatial correlation with the flux distribution and only a minimal correlation with radial velocity (Figure 2.2(b):central panel). A peak in the FWHM of Hα is seen $\sim 1''$ south of the emission peak of Region 4, at 130 km s^{-1}, which aligns with the negative radial velocity peak.

2.4.3 [O III] and [N II]

Emission line maps of both galaxies in the light of [O III] λ5007 and [N II] λ6584 lines are shown in Figs 2.6 and 2.7. For UM 420 the morphology of [O III] is similar to that of Hα exhibiting two main starbursting regions along with the arc-like 'tidal arm' protruding from the brighter region. In UM 462, which is the nearest of the two objects, the [O III] map shows more structure that the corresponding Hα map with an additional area of compact emission to the south-west of Region 1 of Fig 2.5. According to the morphological criteria of Cairos et al. (2001) these maps support the designation of UM 462 as being of 'iI,C' type (irregular; cometary appearance) rather than of 'iE' type; UM 420 can be classified as 'iI, M' (merging). For both BCGs, the [N II] morphology is more diffuse and extended that that of [O III]. The wider distribution of [N II] is probably due to the effect of lower energy photons surviving farther away from the massive ionizing clusters and allowed to produce N^+ beyond the O^{2+} zone.

2.5 Electron Temperature and Density Diagnostics

The dereddened [O III] (λ5007 + λ4959)/λ4363 intensity ratios were used to determine electron temperatures within each galaxy. The $T_{\rm e}$ values were computed by inputting [O III] intensity ratios and an adopted electron density into IRAF's[3] `TEMDEN` task in the `NEBULA` package. Atomic transition probabilities and collisional strengths for O^{2+} were taken from Wiese *et al.* (1996) and

[3]IRAF is distributed by the National Optical Astronomy Observatory, which is operated by the Association of Universities for Research in Astronomy

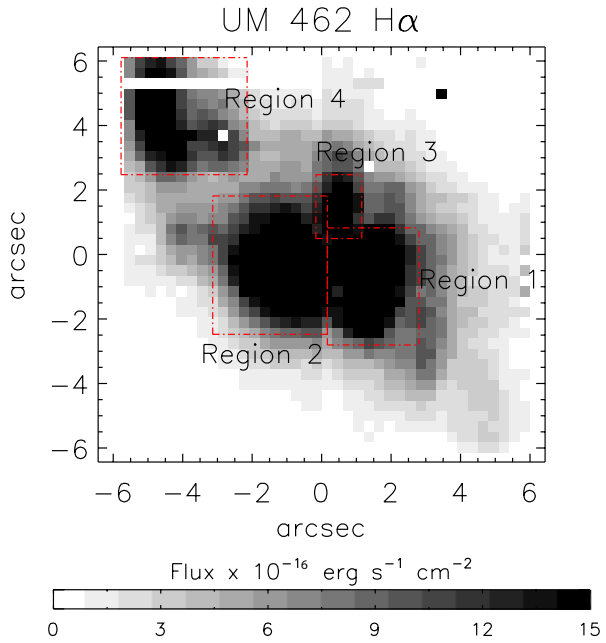

Figure 2.5: UM 462: Hα emission per 0.33×0.33 arcsec^2 spaxel. The four main Hα emission areas have been labelled Regions 1–4.

Lennon & Burke (1994), respectively. More recent and accurate atomic transition probabilities are known to exist, e.g. those given in Storey & Zeippen (2000), and the effects on the diagnosed electron temperatures were found to be negligible. From the summed spectra over each galaxy (Table 2.3) and adopting the electron densities quoted below we derived mean electron temperatures of ∼14,000 K and ∼13,700 K for UM 420 and UM 462, respectively (Table 2.4). Using the same method, $T_{\rm e}$ maps were derived using [O III] (λ5007 + λ4959)/λ4363 emission map ratios. Average $T_{\rm e}$ values for the regions corresponding to peaks in Hα emission for UM 420 and UM 462 are given in Tables 2.6 and 2.8, respectively, using the regionally integrated relative line intensities (Tables 2.5, 2.7). The $T_{\rm e}$ values from the summed spectra were adopted when computing $N_{\rm e}$ values from the [S II] doublet ratio λ6717/λ6731: I derived average $N_{\rm e}$ values of ∼170 cm^{-3} and ∼90 cm^{-3} for UM 420 and UM 462, respectively (Table 2.4). Similarly, the $T_{\rm e}$ maps were used to compute $N_{\rm e}$ maps from λ6717/λ6731 ratio maps, which were then adopted for the computation of ionic abundance maps discussed in the following Section. Average $N_{\rm e}$ values for the regions corresponding to peaks in Hα emission for UM 420 and UM 462 are given in Tables 2.6 and 2.8,

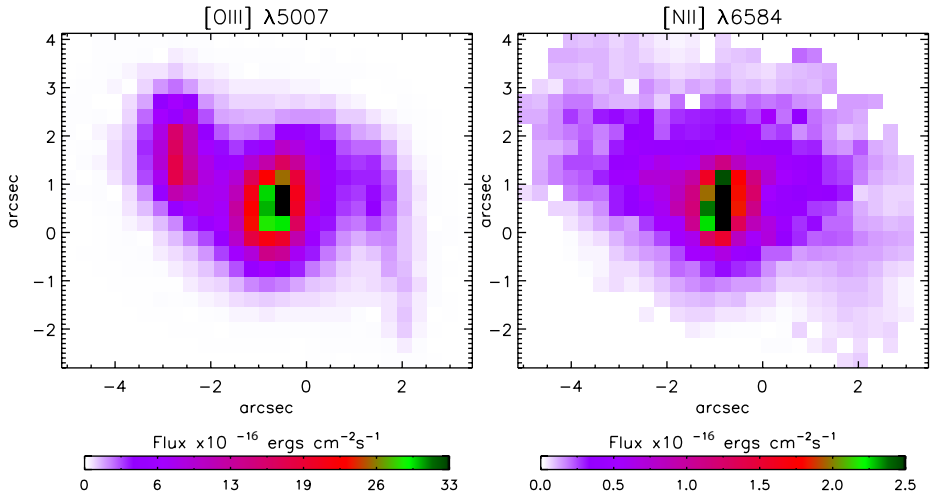

Figure 2.6: UM 420: The distribution of flux per 0.33×0.33 arsec^2 spaxels of [O III] λ5007 (left panel) and [N II] λ6584 (right panel)

respectively.

2.6 Chemical Abundances

Abundance maps relative to H^+ were created for the N^+, O^{2+}, S^+ and S^{2+} ions, using the $\lambda\lambda$6584, 5007, 6717+6731 and 6312 lines, respectively, when the appropriate line was detected. Examples of flux maps used in the derivations of these abundance maps can be seen in Figures 2.6 and 2.7, showing the distribution of flux in the [O III] λ5007 and [N II] λ6584 emission lines for UM 420 and UM 462, respectively. Since the [S III] λ6312 line was not detected from UM 420, its S^{2+}/H^+ abundance was estimated using an empirical relationship between the S^{2+} and S^+ ionic fractions (equation A38) from Kingsburgh & Barlow (1994). Ionic abundances were calculated using IRAF'S `IONIC` task, using each galaxy's respective T_e and N_e maps described above, with each VIMOS spaxel treated as a distinct 'nebular zone' with its own set of physical conditions. Ionic abundance ratios were also derived from the summed spectra fluxes, whose T_e's and N_e's are listed in Table 2.4, using the program EQUIB06 (originally written by I. D. Howarth and S. Adams). Table 2.4 also includes a Ne^{2+}/H^+ abundance ratio for UM 420, as the [Ne III] λ3969 line was redshifted into the HRblue spectral range, and an Ar^{2+}/H^+ ratio for UM 462. Abundance maps were however not created for either ion due to the low S/N ratio [Ne III] λ3969 and [Ar III]

Table 2.4: Ionic and elemental abundances for UM 420 and UM 462 derived, from summed IFU spectra over each galaxy. All ionisation correction factors (ICFs) are taken from Kingsburgh & Barlow, (1994).

Property	UM 420	UM 462
T_e (O III)/ K	14000± 1500	13700± 350
N_e (S II)/ cm^{-3}	170± 80	90± 75
c(Hβ)	0.25±0.08	0.19±0.04
He^+/H^+ (λ4471) $\times10^2$	7.65±1.03	6.68 ±0.62
He^+/H^+ (λ5876) $\times10^2$	9.07±0.54	8.63 ±0.71
He^+/H^+ (λ6678) $\times10^2$	10.6±3.6	10.4 ± 0.72
He^+/H^+ mean $\times10^2$	9.09±1.20	8.58 ±0.72
He^{2+}/H^+ (λ4686)$\times10^3$	—	1.45 ± 0.08
He/H $\times10^2$	9.09±1.20	8.73 ±0.72
O^+/H^{+a} $\times10^5$	$5.51\pm^{3.35}_{1.56}$	$4.32\pm^{0.43}_{0.36}$
O^{++}/H^+ $\times10^5$	$5.24\pm^{1.96}_{1.13}$	$6.30\pm^{0.50}_{0.44}$
O/H $\times10^4$	$1.08\pm^{0.53}_{0.27}$	$1.06\pm^{0.09}_{0.08}$
12+log(O/H)	$8.03\pm^{0.17}_{0.13}$	$8.03\pm^{0.04}_{0.07}$
N^+/H^+ $\times10^6$	$1.94\pm^{0.68}_{0.44}$	$0.61\pm^{0.05}_{0.05}$
ICF(N)	$1.95\pm^{2.12}_{1.04}$	$2.46\pm^{0.46}_{0.39}$
N/H $\times10^6$	$3.79\pm^{6.86}_{2.42}$	$1.50\pm^{0.43}_{0.33}$
12+log(N/H)	$6.58\pm^{0.45}_{0.44}$	$6.18\pm^{0.11}_{0.11}$
log(N/O)	$-1.45\pm^{0.57}_{0.62}$	$-1.85\pm^{0.14}_{0.15}$
Ne^{++}/H^+ $\times10^5$	$3.33\pm^{2.24}_{1.09}$	—
ICF(Ne)	$2.05\pm^{1.86}_{0.93}$	—
Ne/H $\times10^5$	$6.84\pm^{14.98}_{4.33}$	—
12+log(Ne/H)	$7.83\pm^{0.50}_{0.43}$	—
log(Ne/O)	$-0.20\pm^{0.63}_{0.61}$	—
S^+/H^+ $\times10^7$	$5.58\pm^{1.66}_{1.12}$	$3.30\pm^{0.33}_{0.30}$
S^{++}/H^+ $\times10^6$	$2.55^b\pm^{1.84}_{0.85}$	$1.20\pm^{0.34}_{0.29}$
ICF(S)	$0.81\pm^{0.19}_{0.49}$	$0.62\pm^{0.14}_{0.13}$
S/H $\times10^6$	$2.53\pm^{2.58}_{1.84}$	$0.96\pm^{0.51}_{0.35}$
12+log(S/H)	$6.40\pm^{0.31}_{0.56}$	$5.98\pm^{0.18}_{0.20}$
log(S/O)	$-1.63\pm^{0.43}_{0.74}$	$-2.05\pm^{0.22}_{0.24}$
Ar^{++}/H^+ $\times10^7$	—	$3.71\pm^{0.19}_{0.17}$s
ICF(Ar)	—	$1.07\pm^{0.05}_{0.03}$
Ar/H $\times10^7$	—	$3.98\pm^{0.38}_{0.31}$
log(Ar/O)	—	$-2.43\pm^{0.08}_{0.07}$

[a] Derived using [O II] λ3727 flux from IT98

[b] Derived using the relationship between S^{2+} and S^+ (Equation A38) of Kinsgburgh & Barlow (1994)

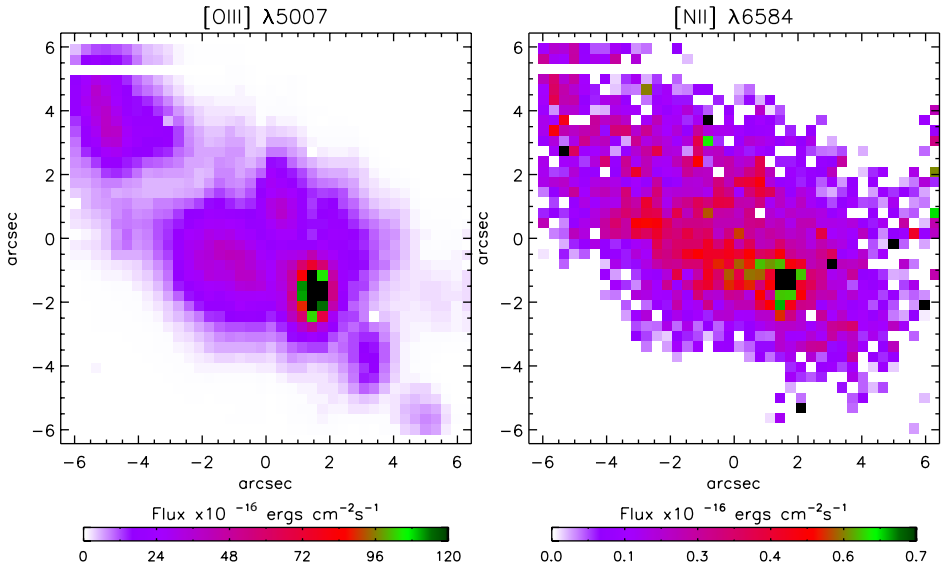

Figure 2.7: UM 462: The distribution of flux per 0.33×0.33 arsec^2 spaxels of [O III] λ5007 (left panel) and [N II] λ6584 (right panel)

λ7135 emission line maps, and the N/H and Ar/H listed in Table 2.4 have been computed from integrated line ratios across the IFU. Differences between abundances derived using the different atomic data tables utilized by IONIC and EQUIB06 were investigated by also using IONIC to compute abundances from the summed spectra. Typical differences were found to be ∼2% or less. Since [O II] λ3727 is not redshifted into the VIMOS spectral range for either galaxy I have to rely on published fluxes. I therefore adopted $F(\lambda3727)/F(\mathrm{H}\beta)$ values of 2.02±0.04 and 1.46±0.01 for UM 420 and UM 462, respectively (from IT98), and corrected them for reddening using the mean $c(\mathrm{H}\beta)$ values derived here (see Table 2.3). The spectra of IT98 were obtained using the 2.1-m Kitt Peak Observatory GoldCam spectrograph's 3″×200″ slit aligned to collect the maximum amount of flux from the targets. For UM 420, whose GoldCam and VIMOS Hα fluxes agree within 11 per cent, the adoption of [O II] fluxes from IT98 should introduce only minor uncertainties in my analysis; for UM 462 whose Hα flux measured by IT98 is 35% of the VIMOS flux, larger uncertainties might be expected. It is encouraging however that the *relative* line fluxes and intensities listed in Table 2.3 differ from those of IT98 by an average factor of only 0.96 for UM 420 and 1.09 for UM 462. Hence for the derivation of the O^+ abundance I adopted a constant $I(\lambda3727)/I(\mathrm{H}\beta)$ ratio for each galaxy. As a result I cannot, for instance, comment on the spatial variance of the N/O abundance ratio across the galaxies. An alternative method for deriving

an O^+ abundance map was investigated in which global O^+/N^+ ratios of 16.49 and 37.64 from IT98 for UM 420 and UM 462, respectively, were multiplied by the corresponding N^+/H^+ IFU maps. Overall it was found that maps derived using the 'global factor' method yielded elemental oxygen abundances $\sim$40% higher and nitrogen abundances $\sim$55% lower than those derived from a constant $I(\lambda3727)/I(\mathrm{H}\beta)$ ratio for each galaxy. However, by deriving an O^+ abundance map in this way I would be prevented from creating a meaningful N/H map since ICF(N) = O/O^+. I therefore opted to use the O^+ abundance maps derived from the constant $\lambda3727$ fluxes when creating ICF(N), ICF(S) and O/H abundance maps.

Ionic nitrogen, neon and sulphur abundances were converted into N/H, Ne/H and S/H abundances using ionisation correction factors (ICFs) from Kingsburgh & Barlow (1994). Average abundances from integrated galaxy spectra are listed in Table 2.4. Elemental O/H abundance maps for UM 420 and UM 462 are shown in Figure 2.8, while average ionic and elemental abundances derived from spectra summed over each individual star-forming region are listed in Tables 2.6 and 2.8 for UM 420 and UM 462, respectively.[4] Errors quoted for regional abundances are derived from the upper and lower regional estimates of T_e and N_e (also listed in Tables 2.6 and 2.8), combined with the uncertainty in the individual component fit to the respective line and thus reflect both the S/N of the individual emission line and the varying uncertainties in the regional T_es and N_es.

2.6.1 UM 420

The line fluxes for the summed spectra over Regions 1 and 2 of UM 420 are listed in Table 2.5 and the average physical properties from which they are derived are listed in Table 2.6. A graphical representation of the variations in elemental and ionic abundances between Regions 1 and 2 is shown in Figure 2.9.

The elemental oxygen abundance map shown in the left-hand panel of Figure 2.8 displays two peaks whose locations correlate with the two Hα peaks of UM 420 (marked in Figure 2.3). Minimal abundance variations are seen between Regions 1 and 2, whose average metallicity is $12 + \log(\mathrm{O/H}) \sim 8.25 \pm 0.07$. Adopting a solar oxygen abundance of 8.71 ± 0.10 relative to hydrogen (Scott *et al.* 2009), this corresponds to an oxygen abundance of $\sim$0.35 solar for Regions

[4]Regional abundances derived directly by taking averages over the abundance maps were found to be inaccurate due to occasionally large T_e uncertainties resulting from poor S/N ratio in some spaxels of the [O III] $\lambda4363$ maps. In contrast, summed regional spectra increased the S/N ratio for $\lambda4363$, allowing more reliable average line ratios and hence temperatures and abundances for each region to be derived.

Table 2.5: UM 420 regional fluxes and intensities used for regional T_e and N_e diagnostics and regional ionic abundance calculations.

	Region 1		Region 2	
Line ID	F(λ)	I(λ)	F(λ)	I(λ)
4340 Hγ	40.43± 0.49	45.05± 0.54	32.44± 1.15	35.86± 1.27
4363 [O III]	4.51± 0.31	5.00± 0.35	5.34± 0.78	5.88± 0.86
4471 He I	4.14± 0.33	4.49± 0.36	4.92± 0.59	5.30± 0.64
4861 Hβ	100.00± 1.04	100.00± 1.04	100.00± 1.80	100.00± 1.80
4959 [O III]	140.57± 1.47	137.72± 1.44	168.37± 2.69	165.20± 2.64
5007 [O III]	441.01± 4.40	427.64± 4.27	514.34± 8.13	499.91± 7.91
5876 He I	13.04± 0.31	10.86± 0.26	11.29± 0.79	9.53± 0.67
6563 Hα	366.84± 5.21	278.98± 3.96	296.63± 3.88	230.33± 3.01
6584 [N II]	29.66± 0.31	22.50± 0.24	16.80± 0.98	13.02± 0.76
6678 He I	2.24± 0.32	1.68± 0.24	—	—
6716 [S II]	30.15± 0.51	22.52± 0.38	24.11± 0.89	18.40± 0.68
6731 [S II]	23.31± 0.51	17.37± 0.38	20.81± 0.94	15.86± 0.72
F(Hβ)[a]	300.4± 3.330		48.414± 0.874	

[a] in units of 10^{-16}erg s^{-1} cm^{-2}

1 and 2. This is $\sim$0.2 dex higher than the value derived from the integrated spectrum of the whole galaxy. This could point to some limited oxygen enrichment in the areas corresponding to the peak Hα emission, that is the clusters associated with Regions 1 and 2. However, since all the oxygen abundances overlap within their 1σ uncertainties, I cannot conclude that this variation in oxygen abundance is significant. The nitrogen abundances of the two regions of star-formation are consistent within their uncertainties (Table 2.6). The N/O ratios for both regions are consistent with those of other metal-poor emission line galaxies of similar oxygen metallicity (Izotov *et al.* 2006), and do not show the nitrogen excess reported by Pustilnik *et al.* (2004). The S/O ratio for Region 1 is slightly higher than expected for BCGs, although Region 2 is closer to the average reported range of log(S/O) $\sim -1.4 - -1.7$ (Izotov *et al.* 2006).

2.6.2 UM 462

Table 2.6: Ionic and elemental abundances for UM 420, derived from summed IFU spectra over each region. All ionisation correction factors (ICFs) are taken from Kingsburgh & Barlow, (1994).

Property	Region 1	Region 2
T_e (O III)/ K	12300±330	12900±680
N_e (S II)/ cm^{-3}	120±55	300±160
c(Hβ)	0.37±0.04	0.34±0.08
O^+/H^{+a} $\times10^4$	0.95± 0.12	0.89± 0.25
O^{++}/H^+ $\times10^4$	0.79± 0.07	0.92± 0.18
O/H $\times10^4$	1.74± 0.19	1.81± 0.43
12+log(O/H)	8.24± 0.05	8.26± 0.09
N^+/H^+ $\times10^6$	2.67± 0.18	1.55± 0.22
N/H $\times10^6$	4.89± 1.60	3.15± 2.39
12+log(N/H)	6.69± 0.12	6.50± 0.25
log(N/O)	−1.55± 0.17	−1.76± 0.33
S^+/H^+ $\times10^7$	13.38± 0.92	11.26± 1.65
S^{++}/H^{+b} $\times10^6$	7.47± 0.49	6.39± 0.89
S/H $\times10^6$	7.58± 1.51	5.87± 2.62
12+log(S/H)	6.88± 0.08	6.77± 0.16
log(S/O)	−1.36± 0.12	−1.49± 0.24

[a] Derived using [O II] λ3727 flux from IT98

[b] Derived using the relationship between S^{2+} and S^+(Equation A38) of Kinsgburgh & Barlow (1994)

Table 2.7: UM 462 regional fluxes and intensities used for regional T_e and N_e diagnostics and regional ionic abundance calculations.

	Region 1		Region 2		Region 3		Region 4	
Line ID	F(λ)	I(λ)	F(λ)	I(λ)	F(λ)	I(λ)	F(λ)	I(λ)
4340 Hγ	40.92± 0.72	46.49± 0.49	45.97± 0.41	43.39± 0.54	45.98± 0.41	53.86± 0.48	43.39± 0.54	44.45± 0.56
4363 [O III]	8.61± 0.18	9.26± 0.19	7.27± 0.26	7.55± 0.27	9.17± 0.70	10.67± 0.82	6.62± 0.53	6.77± 0.55
4471 He I	3.01± 0.14	3.19± 0.15	3.51± 0.16	3.61± 0.16	3.66± 0.34	4.12± 0.38	3.63± 0.40	3.70± 0.40
4686 He II	—	—	1.21± 0.12	1.22± 0.12	—	—	—	—
4861 Hβ	100.00± 0.65	100.00± 0.65	100.00± 0.65	100.00± 0.65	100.00± 0.65	100.00± 0.65	100.00± 0.76	100.00± 0.76
4959 [O III]	218.90± 1.90	215.76± 1.87	169.17± 1.30	167.95± 1.29	182.95± 1.23	177.54± 1.19	174.63± 1.52	173.83± 1.51
5007 [O III]	630.70± 5.95	617.18± 5.82	503.02± 2.64	497.58± 2.61	564.84± 2.32	539.98± 2.22	507.96± 4.43	504.49± 4.40
5876 He I	14.47± 0.16	12.72± 0.14	9.77± 0.59	9.16± 0.55	15.02± 0.64	11.48± 0.49	—	—
6563 Hα	332.75± 0.98	274.41± 0.81	325.84± 2.44	295.81± 2.22	483.79± 3.16	324.20± 2.12	293.19± 4.92	275.84± 4.63
6584 [N II]	4.25± 0.11	3.50± 0.09	6.88± 0.23	6.24± 0.21	9.88± 0.48	6.60± 0.32	5.04± 0.42	4.74± 0.40
6678 He I	2.34± 0.10	1.91± 0.08	3.21± 0.13	2.90± 0.12	5.19± 0.44	3.41± 0.29	—	—
6716 [S II]	7.53± 0.10	6.13± 0.08	16.11± 0.20	14.53± 0.18	28.09± 0.72	18.32± 0.47	11.99± 0.38	11.23± 0.35
6731 [S II]	5.56± 0.10	4.52± 0.08	11.91± 0.20	10.74± 0.18	19.90± 0.73	12.95± 0.47	8.79± 0.40	8.23± 0.37
F(Hβ)[a]	1065.01± 6.32		594.32±6.03		96.24±2.33		275.04± 15.62	

[a] in units of 10^{-16}erg s^{-1} cm^{-2}

Table 2.7 lists the fluxes from summed spectra over Regions 1–4 of UM 462. The average ionic and elemental abundances, along with the average $T_{\rm e}$ and $N_{\rm e}$ values, derived from the summed spectra over the respective regions are listed in Table 2.8. A graphical representation of the variation in elemental and ionic abundances across Regions 1–4 is shown in Figure 2.9. .

The right-hand panel of Figure 2.8(a) shows the O/H abundance ratio map for UM 462. The oxygen abundance varies spatially across the different star-forming regions of UM 462 (as marked in Figure 2.5). Four maxima in oxygen abundance are seen across the map, all aligning spatially with peaks in Hα emission (shown as overlaid contours), with the exception of Region 1, where the maximum in oxygen abundance appears to lie $\sim$1.5$''$ south of the Hα peak of Region 1. A decrease in the oxygen abundance can be seen $\sim$1.0$''$ north-east of the peak in Region 1. Oxygen abundances for Regions 1–4 are listed in Table 2.8. A maximum variation of 40% is seen between Region 1 (displaying the highest metallicity) and Region 3 (displaying the lowest). The mean oxygen abundance of the four identified star-forming regions in UM 462 is 12 + log(O/H) = 8.08 $\pm$ 0.94, that is, $\sim$0.25 solar. This is in good agreement with the value derived from the integrated spectrum of the whole galaxy. Regional N/H and S/H abundance ratios are given in Table 2.8. Regions 2, 3 and 4 have the same nitrogen abundance within the uncertainties. The maximum difference (0.2 dex) is between Regions 2 and 1; the latter shows the lowest nitrogen abundance. In comparison with metal-poor emission line galaxies of similar metallicity (Izotov *et al.* 2006), UM 462 appears to be overall slightly nitrogen poor. The sulphur abundance across the galaxy is variable with Region 1 having the lowest, a factor of $\sim$ 2 below the other three regions. In comparison with other emission line galaxies, UM 462 displays a lower than average log(S/O) of $-$2.03 [typical values range from ~ -1.4 to -1.7; Izotov *et al.* (2006)].

2.6.2.1 Helium abundances

Following the method outlined by Tsamis *et al.* (2003) and Wesson *et al.* (2008), abundances for helium were derived using atomic data from Smits (1996), accounting for the effects of collisional excitation using the formulae in Benjamin *et al.* (1999). Ionic and total helium abundances relative to hydrogen derived from helium recombination lines measured from summed spectra over the entire galaxies are given in Table 2.4 (derived using the global $T_{\rm e}$ and $N_{\rm e}$ values from the same Table). Given that the reddening varies across the galaxies (predominantly in the case of UM 462), and in order to minimize the uncertainties, I have also computed helium abundances per each individual star forming region; these are given in Tables 2.9 and 2.10, for UM 420 and UM 462, respectively. These values are derived from summed spectra over each star-forming

Table 2.8: Ionic and elemental abundances for UM 462, derived from summed IFU spectra over each region. All ionisation correction factors (ICFs) are taken from Kingsburgh & Barlow, (1994).

Property	Region 1	Region 2	Region 3	Region 4
T_e (O III)/ K	13400±150	13500±230	15200±500	12800±440
N_e (S II)/ cm^{-3}	70±40	70 ±40	$20\pm^{70}_{10}$	60±50
c(Hβ)	0.26±0.03	0.13±0.03	0.54±0.03	0.08±0.08
O^+/H^{+a} $\times10^5$	4.85± 0.28	4.38± 0.33	3.91± 0.44	5.09± 0.81
O^{++}/H^+ $\times10^5$	8.86± 0.30	6.99± 0.34	5.58± 0.49	8.17± 0.88
O/H $\times10^4$	1.37± 0.06	1.14± 0.07	0.95± 0.09	1.33± 0.19
12+log(O/H)	8.14± 0.02	8.06± 0.02	7.98± 0.04	8.12± 0.05
$N^+/H^+\times10^6$	0.34± 0.01	0.60± 0.02	0.50± 0.03	0.51± 0.04
N/H $\times10^6$	0.97± 0.13	1.56± 0.28	1.22± 0.41	1.33± 0.56
12+log(N/H)	5.99± 0.05	6.19± 0.07	6.08± 0.13	6.12± 0.15
log(N/O)	−2.15± 0.07	−1.86± 0.10	−1.89± 0.17	−2.00± 0.21
S^+/H^+ $\times10^7$	3.01± 0.09	7.04± 0.28	7.06± 0.45	6.01± 0.51
S^{++}/H^+ $\times10^6$	0.96± 0.04	1.27± 0.08	1.37± 0.15	1.97± 0.26
S/H $\times10^6$	0.66± 0.12	1.15± 0.27	1.32± 0.51	1.49± 0.80
12+log(S/H)	5.82± 0.07	6.06± 0.09	6.12± 0.14	6.17± 0.19
log(S/O)	−2.32± 0.09	−2.00± 0.12	−1.86± 0.19	−1.95± 0.24

[a] Derived using [O II] λ3727 flux from IT98

region of the galaxy dereddened with the corresponding c(Hβ). My adopted mean values for He^+/H^+ were derived from the λ4471, λ5876 and λ6678 lines, averaged with weights 1:3:1. The helium abundances were calculated for the average temperatures and densities given in Tables 2.6 and 2.8. Regional helium abundances were not calculated for Region 4 of UM 462 because only one He I line was detected (see Table 2.7). It should be noted that whilst there appears to be a small variance (within the errors) of average the helium abundance across UM 462 (Table 2.10), it would be premature to conclude that this regional variation is real when considering the large variance in helium abundances derived from different lines for each respective region. The variation between the abundances derived from different lines suggests that the errors listed may be an under-estimation of the true uncertainties. Helium abundances derived from summed spectra are found to agree with those derived in IT98, within the uncertainties.

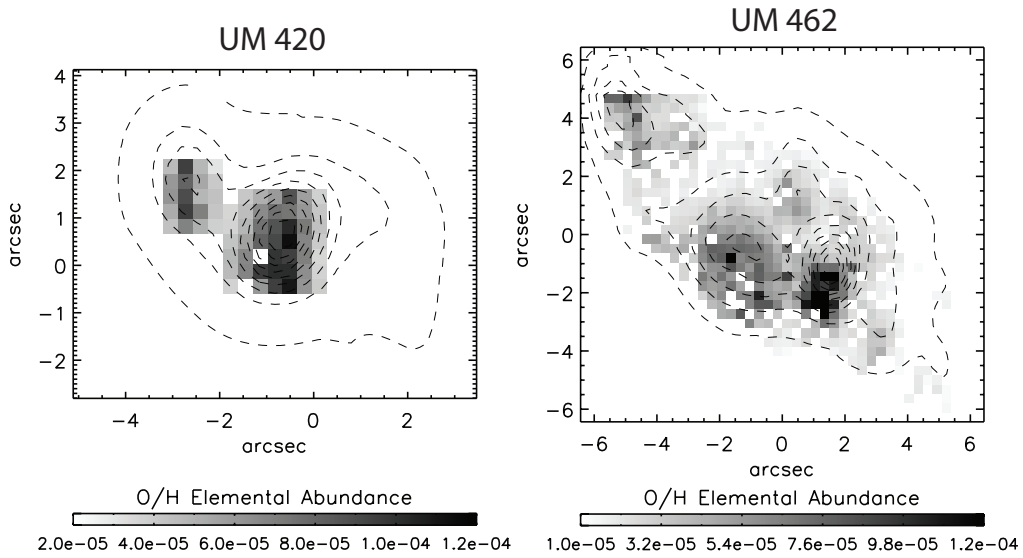

Figure 2.8: O/H abundance ratio maps of UM 420 (left panel) and UM 462 (right panel) derived from their respective O^{2+} and O^{+} ionic abundance maps and T_e and N_e maps, as described in Section 2.6. Overlaid are the Hα flux contours from Figure 2.2(a).

Table 2.9: Ionic and elemental helium abundances for UM 420 derived from summed spectra over each region.[a]

	Region 1	Region 2
He^+/H^+ (λ4471) $\times10^2$	9.23±0.73	10.77±1.23
He^+/H^+ (λ5876) $\times10^2$	8.31±0.20	7.15±0.52
He^+/H^+ (λ6678) $\times10^2$	4.56±0.66 :	—
He^+/H^+ mean $\times10^2$	8.54±0.33	8.05±0.70
He^{2+}/H^+ (λ4686)$\times10^3$	—	—
He/H $\times10^2$	8.54±0.33	8.05±0.70

[a] Entries followed by ':' were excluded from the final average.

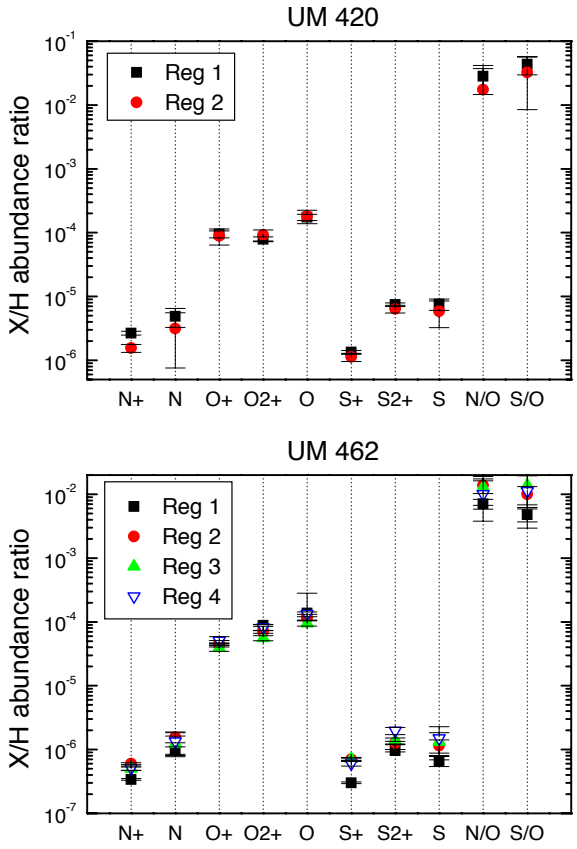

Figure 2.9: Graphical representation of the variations in ionic and elemental abundances across UM 420 and UM 462, as given in Tables 2.6 and 2.8, respectively.

Table 2.10: Ionic and elemental helium abundances for UM 462 derived from summed spectra over each Region (with the exclusion of Region 4, where only one He I line was detected).[a]

	Region 1	Region 2	Region 3
He^+/H^+ (λ4471) $\times10^2$	6.66±0.32	7.54±0.34	8.75±0.81
He^+/H^+ (λ5876) $\times10^2$	9.97±0.10	7.20±0.43	9.33± 0.40
He^+/H^+ (λ6678) $\times10^2$	5.34±0.23 :	8.11± 0.33	9.83±0.84
He^+/H^+ mean $\times10^2$	9.14±0.16	7.45±0.39	9.31±0.57
He^{2+}/H^+ (λ4686)$\times10^3$	—	1.04±0.11	—
He/H $\times10^2$	9.14±0.16	7.55±0.40	9.31±0.57

[a] Entries followed by ':' were excluded from the final average.

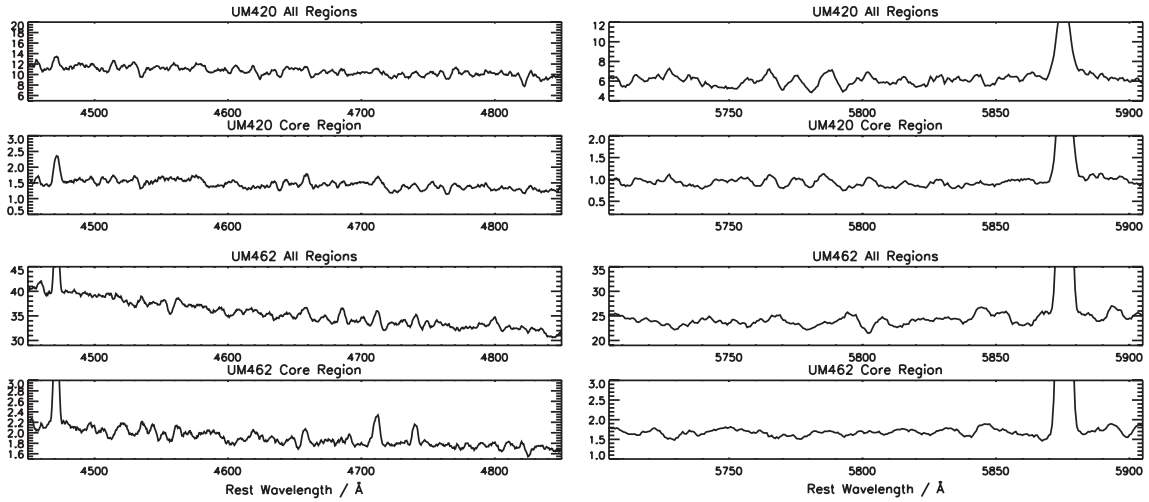

Figure 2.10: Sections of VIMOS IFU spectra, in flux units of $\times 10^{-16}$ erg s^{-1} cm^{-2}, where the WR 'blue bump' feature (left column) and C IV 'red' feature (right column) would be located within summed spectra over the core region (labelled Region 1 in Figures 2.3 and 2.5 for UM 420 and UM 462, respectively) and over the entire galaxy. There are no detections of WR emission features in any of the spectra.

2.6.3 Stellar Properties

2.6.3.1 Wolf-Rayet features?

Contrary to previous long slit studies (Izotov & Thuan 1998; Schaerer *et al.* 1999*b*; Guseva *et al.* 2000), which had limited spatial coverage, the VIMOS IFU spectra do not reveal any evidence for broad WR emission features at either ∼4686 Å or at ∼5808, 5812 Å. This is true for single spaxel spectra, summed spectra over Region 1 (the highest surface brightness SF region in both galaxies) or in the summed spectra over the whole of each galaxy, as shown in Figure 2.10. Hence this analysis does not support the classification of UM 420 and UM 462 as Wolf-Rayet galaxies. When searching for WR features one must consider the width of the extraction aperture, which can sometimes be too large and thus dilute weak WR features by the continuum flux (López-Sánchez & Esteban 2008). I therefore also examined the summed spectra over each individual star-forming region, with extraction apertures equal to those displayed in Figures 2.3 and 2.5 aiming to reduce the dilution of any WR features. However, those remained undetected. This supports the statement by Schaerer *et al.* (1999*b*) regarding the dependence of a object's classification as a 'WR galaxy' on the quality of the spectrum, and location and size of the aperture. Given that my spectroscopy was obtained with an 8.2 m telescope, with exposure times of ∼1500 s for each spectral region, I

conclude that the presence of WR stars in UM 420 and UM 462 is not yet proven.

2.6.3.2 Starburst ages and star formation rates

Luminosities of hydrogen recombination lines, particularly Hβ, can provide estimates of the ionizing flux present, assuming a radiation-bounded nebula (Schaerer & Vacca 1998). Thus, the equivalent width (EW) of Hβ is commonly used as an age indicator of the ionizing stellar population at a given metallicity. Maps of EW(Hβ) for UM 420 and UM 462 can be seen in Figure 2.11(a) & (b), respectively. I can use these maps, in conjunction with the metallicity maps described in Section 2.6, to estimate the age of the latest star forming episodes throughout UM 420 and UM 462 by comparing the regional observed average EW(Hβ) values with those predicted by the spectral synthesis code STARBURST99 (Leitherer *et al.* 1999). For the models I chose metallicities of 0.4 and 0.2 $Z_{\odot}$, representative of the average metallicities of UM 420 and UM 462 (derived from regional summed spectra), together with assumptions of an instantaneous burst with a Salpeter initial mass function (IMF), a total mass of $1{\times}10^{6}$ $M_{\odot}$ (the default mass chosen by Leitherer *et al.* (1999) to produce properties that are typical for actual star-forming galaxies), and a $100M_{\odot}$ upper stellar mass limit (which approximates the classical Salpeter (1955) IMF). Models were run for Geneva tracks with "high" mass loss rates (tracks recommended by the Geneva group) and Padova tracks with thermally pulsing AGB stars included. For each of these evolutionary tracks, two types of model atmosphere were used; firstly the Pauldrach-Hillier (PH, the recommended atmosphere) and secondly Lejeune-Schmutz (LS). The latter was chosen because it incorporates stars with strong winds, which would be representative of the WR population within each galaxy (if present). The stellar ages predicted by each model and the observed average EW(Hβ) within each peak emission region in UM 420 and UM 462 were derived from Figure 2.12 and are listed in Table 2.11. The difference between the ages predicted by the Geneva and Padova stellar evolutionary tracks is relatively small, with the Geneva tracks predicting lower ages by up to 20%. The difference in ages predicted by the PH and LS atmospheres are smaller still, with LS predicting lower ages by $\sim$6%. I cannot comment on which atmosphere model is more appropriate given that the existence of WR stars within each galaxy is questioned by the current study, hence I adopt average stellar ages from the four model combinations. It should also be noted that ages are predicted under the assumption that the stars are coeval, since the models concern an instantaneous burst where stars evolve coevally after formation. This approach, although unavoidable within the model parameters, overlooks the possibility that the stellar populations would involve a range of ages. The current (instantaneous) star formation rates (SFRs) based on the Hα luminosities were

Table 2.11: Age of the latest star formation episode and current star formation rates.

	Starburst ages (Myr)					
	UM 420		UM 462			
Model	Reg. 1	Reg. 2	Reg. 1	Reg. 2	Reg. 3	Reg. 4
Padova-AGB PH	4.51±0.21	5.26±0.19	4.85±0.32	5.45±0.13	5.85±0.13	5.90±0.27
Padova-AGB LS	4.24±0.34	5.16±0.19	4.66±0.36	5.31±0.10	5.66±0.07	5.76±0.24
Geneva-High PH	3.76±0.36	4.91±0.27	3.91±0.56	4.86±0.13	5.21±0.10	5.51±0.39
Geneva-High LS	3.50±0.34	4.71±0.22	3.76±0.48	4.61±0.10	5.01±0.10	5.21±0.33
	Star formation rates ($M_\odot$ yr^{-1})					
	UM 420		UM 462			
SFR(Hα)[a]	10.5	1.31	0.104	0.047	0.021	0.018
SFR(Hα)[b]	7.0	0.87	0.069	0.027	0.012	0.013

[a] Derived using the relationship between SFR and L(Hα) from Kennicutt (1998).

[b] Corrected for sub-solar metallicities following Lee *et al.* (2002).

calculated following Kennicutt (1998) and are given in Table 2.11. SFRs corrected for the sub-solar metallicities of these targets are also given, derived following the methods outlined in Lee *et al.* (2002).

UM 420: Regions 1 and 2 contain ionizing stellar populations with an average age of 3.94±0.31 and 4.99±0.21 Myr, respectively (Table 2.11). The difference in ages could imply that these were in fact once isolated bodies, and that star formation within Region 1 was triggered or is still a product of an ongoing merger with Region 2. Also in support of this are their respective SFRs which differ by almost an order of magnitude. Global SFRs derived by López-Sánchez & Esteban (2008) are 3.7 ± 0.2 $M_\odot$ yr^{-1} (based on an Hα flux estimated from broad-band photometry) and 1.9 ± 0.9 $M_\odot$ yr^{-1} (based on the 1.4 GHz flux), and are lower than my measurements which are based on the monochromatic Hα flux.

UM 462: Table 2.11 show average stellar population ages of 4.19±0.42, 5.07±0.11, 5.45±0.10 and 5.56±0.31 Myr for Regions 1–4, respectively. Since Region 1 shows the highest ionizing flux, I would expect it to contain the youngest stellar population. It is notable that the age of the stellar population increases through Regions 2–4 as the distance of separation from Region 1 increases and at the same time the SFR decreases. Our SFRs are comparable to previously published values of 0.13 (based on FIR fluxes), 0.00081 (blue) and 0.5 $M_\odot$ yr^{-1} (narrow-band Hα) from Sage

et al. (1992) and 0.36 (60 μm) and 0.13 $M_{\odot}$ yr^{-1} (1.4 GHz) from Hopkins *et al.* (2002). Evidence suggests that Regions 1–3 are linked in their SF properties, with decreasing metallicity and SFR and increasing stellar population ages as the distance from Region 1 increases. Region 4 breaks this pattern in metallicity harbouring a starburst which is coeval with that of Region 3.

2.7 Emission Line Galaxy Classification

It is useful to attempt to diagnose the emission line excitation mechanisms in BCGs using the classic diagnostic diagrams of Baldwin *et al.* (1981) (the BPT diagrams). These are used to classify galaxies according to the dominant excitation mechanism of their emission lines, i.e. either photoionisation by massive stars within H II regions or photoionisation by non-thermal continua from AGN. The diagrams consist of excitation-dependent and extinction-independent line ratios: log([O III] λ5007/Hβ) versus either log([S II] λ6716 + λ6731)/Hα) or log([N II] λ6584/Hα). Star-forming galaxies fall into the lower left region of the diagrams, AGN host galaxies fall into the upper right region and Low-Ionisation Emission Line Regions (LINERs) fall on the lower right. Here we adopt the 'maximum starburst line' derived by Kewley *et al.* (2001) from starburst grids defined by two parameters; metallicities Z = $\sim$ 0.05–3.0 $Z_{\odot}$ and ionization parameters $q = 5 \times 10^6$ – 3×10^8 cm s^{-1}, where q is the maximum velocity of an ionisation front that can be driven by the local radiation field and is related to the non-dimensional ionisation parameter $U = q/c$, (Dopita *et al.* 2001). This line defines the maximum flux ratio an object can have to be successfully fitted by photoionization models alone. Ratios lying above this boundary are inferred to require additional sources of excitation, such as shocks or AGNs. It is thus instructive to see what area of the BPT diagram UM 420 and UM 462 occupy as a whole, as well as their resolved star-forming regions which were defined in Figures 2.3 and 2.5.

UM 420: Figure 2.13(a) and (b) shows the BPT diagram locations of the two star-forming regions within UM 420. Although a large spread can be seen for both regions, Region 2 occupies the higher end of the [O III] λ5007/Hβ emission line ratio in both diagrams, and does not exceed the [O III] λ5007/Hβ values of Region 1. Some spaxels do cross the 'maximum starburst line', but are insufficient in frequency to be considered as evidence for substantial non-thermal line excitation. The [S II]/Hα ratios are generally lower than those predicted by standard predictions of shock models from the literature. There is a larger spread in [N II] λ6584/Hα as compared to [S II]/Hα which is probably due to the fact that the N^+/H^+ abundance ratio differential between Regions 1 and 2 is larger than the corresponding S^+/H^+ differential by 45 per cent. In relation

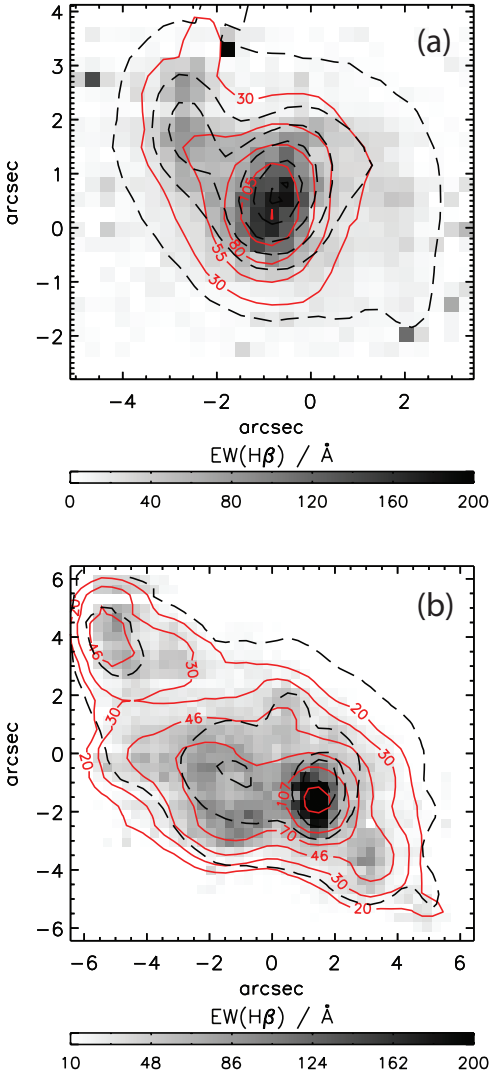

Figure 2.11: Maps of the equivalent width of Hβ across: (a) UM 420; (b) UM 462. Overlaid red solid lines are contours of EW(Hβ); black-dashed lines are Hα flux contours from Figure 2.2.

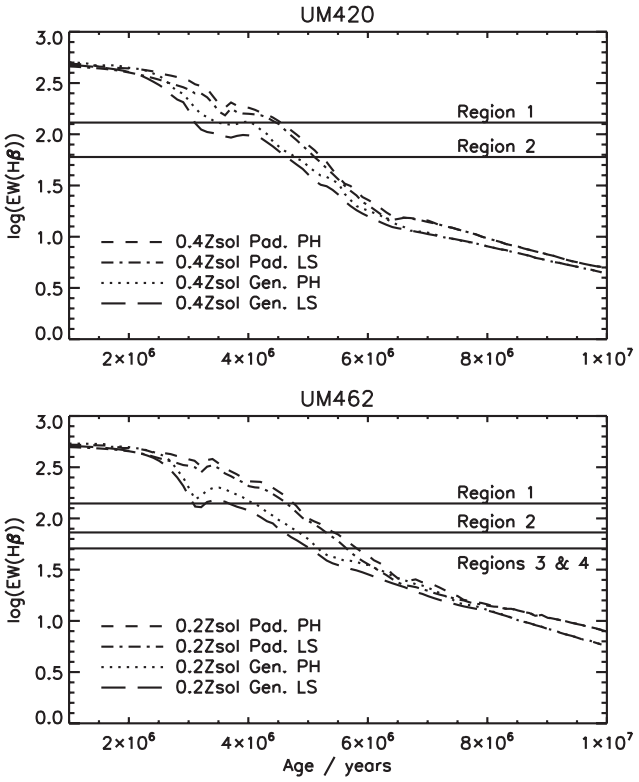

Figure 2.12: EW(Hβ) as a function of age, as predicted by the STARBURST99 code for metallicities of $0.4Z_{\odot}$ (UM 420) and $0.2Z_{\odot}$ (UM 462) using a combination of Geneva or Padova stellar evolutionary tracks and Lejeune-Schmutz (LS) or Pauldrach-Hillier (PH) model atmospheres. The observed average EW(Hβ)'s for each star forming region in UM 420 (top panel) and UM 462 (bottom panel) are overlaid (solid line).

to the grid of (Z, q) models of Kewley *et al.* (2001), UM 420 lies within a range of $Z = 0.4$–0.5 $Z_{\odot}$and $q \geq 3 \times 10^8$. This is consistent with the average metallicity of 0.35 ± 0.06 $Z_{\odot}$ for Regions 1 and 2 (Table 2.6). I conclude that photoionisation by stellar populations is the dominant line excitation mechanism within UM 420.

UM 462: The BPT diagnostic diagrams shown in Figure 2.14(a) and (b) show the emission line ratios for each spaxel within the four star-forming regions of UM 462 (as defined in Figure 2.5). As with UM 420 the [S II]/Hα diagnostic ratios tend to straddle the theoretical upper limit for photoionisation. Although their locations appear highly clustered, a slight distinction can be seen for Region 4 which lies slightly to the left of the diagram. The large spread in values can be seen more clearly in Figure 2.14(b), where the spread along the X-axis, i.e. [N II] λ6584/Hα, extends

on either side of the other three regions. This range in [N II] and [S II] excitation conditions is perhaps to be expected given the 9″ distance separating Region 4 from the central regions. Several spaxels' emission line ratios do spread into the locus of non-thermal excitation but their low occurrence renders them insignificant. In relation to the models of Kewley *et al.* (2001), UM 462 lies within a range of Z =0.2–0.5 $Z_{\odot}$and $q \geq 1.5 \times 10^8$. This is consistent with the average metallicity of $\sim$0.24$Z_{\odot}$ for Regions 1–4 (Table 2.8). I conclude that photoionisation from stellar sources is the dominant excitation mechanism within UM 462 as well. Comparing the two galaxies, the data points of UM 462 are more highly clustered than those of UM 420, despite the former system's disrupted morphology and are further to the left (smaller values) on the X-axis of both diagrams. The explanation probably lies in the higher S/H and N/H abundances of UM 420 compared to those of UM 462 (by corresponding factors of $\sim$ 2.5). Both galaxies display a similar level of [O III] λ5007/Hβ excitation.

2.8 Conclusions

I have analyzed VIMOS IFU integral field spectroscopy of the unrelated BCGs UM 420 and UM 462 and studied their morphology by creating monochromatic emission line maps. Both systems show signs of interaction and/or perturbation with the former galaxy currently undergoing a merger (type 'iI,M') and the latter displaying a highly disrupted irregular or cometary appearance (type 'iI,C'; probably due to interaction with a BCG which was not part of this study, UM 461). The spatially resolved emission line maps in the light of [O III] and Hα have revealed two main areas of massive star formation in UM 420 along with a tidal arm, and at least four such areas in UM 462. Current star formation rates were computed from the Hα line luminosities for each main starbursting region and the ages of the last major star formation episode were estimated by fitting the observed Balmer line equivalent widths with STARBURST99 models. The two merging components of UM 420 have SFRs that differ by a factor of $\sim$ 8 and starburst episodes separated by 1 Myr. The latest major star formation event took place $\sim$ 4 Myr ago in the largest merging component, and has been producing stars at a rate of 10 $M_{\odot}$ yr^{-1}. In UM 462 the last star forming episode was $\sim$ 4 – 5 Myr ago and has been producing stars at a rate which varies across the galaxy between $\sim$ 0.01 – 0.10 $M_{\odot}$ yr^{-1}, indicative of propagating or triggered star formation.

For both targets the abundances of He, N, O, and S were measured and O/H abundance ratio maps were created based on the direct method of estimating electron temperatures from the [O III] λ4363/λ5007 line ratio. The measured oxygen abundances (from integrated spectra over each

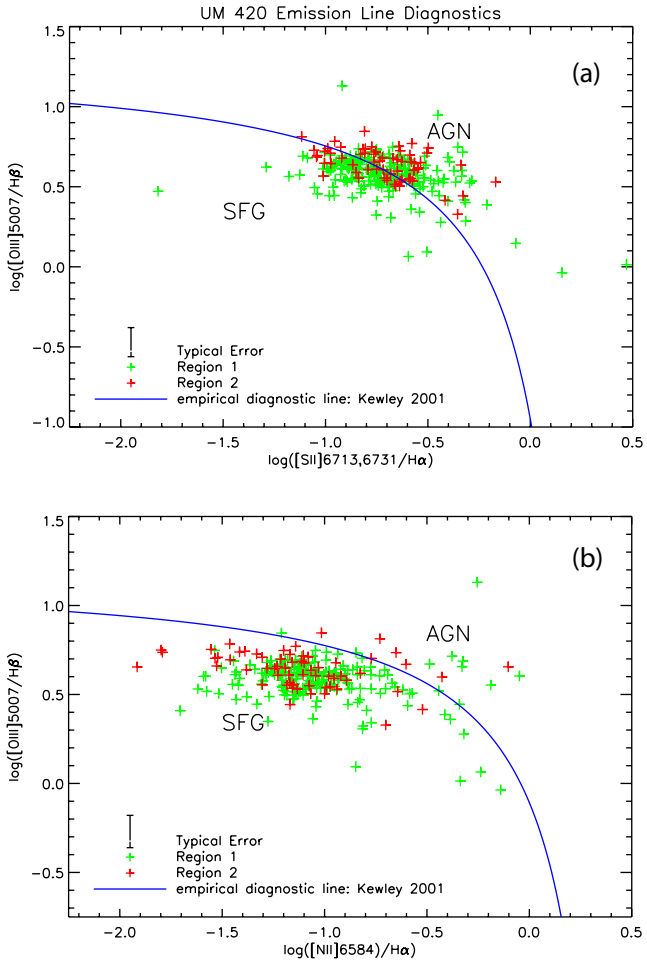

Figure 2.13: Emission line diagnostic diagrams for UM 420. Each data point represents a spaxel in the ratioed dereddened flux maps corresponding to [O III] λ5007/Hβ versus (a) [S II] λ6716 + λ6731/Hα and (b) [N II] λ6584/Hα. Spaxels corresponding to the two star-forming regions defined in Figure 2.3 are separated by colour. The empirical diagnostic 'maximum starburst' line from Kewley *et al.* (2001) is also shown, as are the positions of emission line ratios for star-forming galaxies(SFG) and active galaxies (AGN).

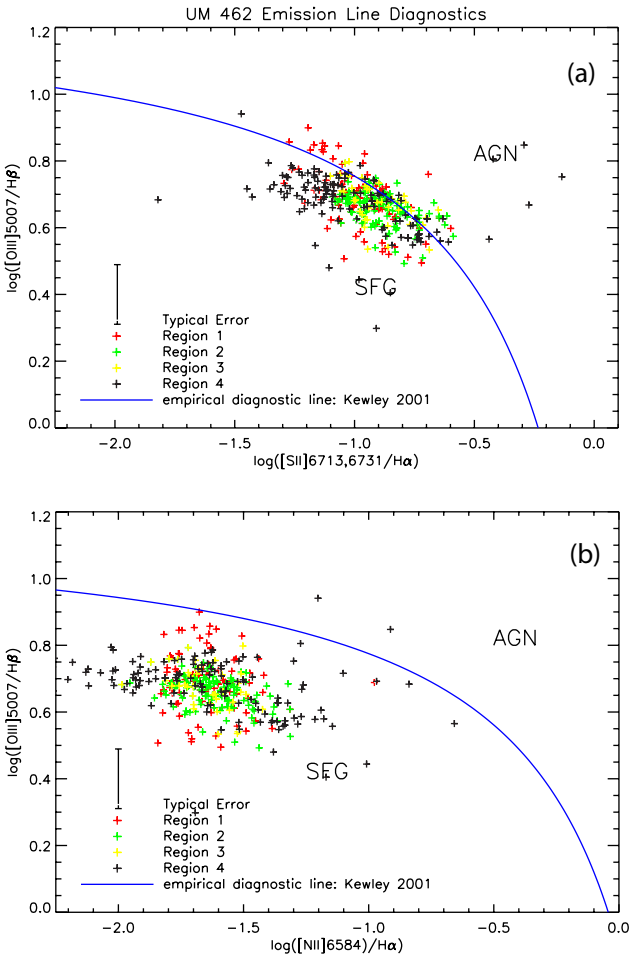

Figure 2.14: Same as for Figure 2.13, but for UM 462. Regions 1–4 correspond to the separate star-forming regions defined in Figure 2.5.

galaxy) are 12 + log(O/H) = 8.03 ± 0.20 for UM 420 and 8.03 ± 0.10 for UM 462 (20 per cent solar). I find no evidence for significant nitrogen or oxygen variations across the galaxies (at the 0.2 dex level), which would point to self-enrichment from nucleosynthetic products associated with the recent massive star formation activity. Helium abundances were also shown to show no significant variation across each galaxy. Regarding the abundance of nitrogen, and the N/O ratio, this result is in qualitative agreement with the finding that these BCGs cannot be classified as Wolf-Rayet galaxies as the characteristic broad-line stellar features have not been detected by VIMOS; the existence of WR stars in them is an open issue.

CHAPTER 3

AN IFU STUDY OF THE ANOMALOUS BCD MRK 996

The work described in this chapter has been accepted for publication in MNRAS entitled "A VLT VIMOS study of the anomalous BCD Mrk 996: mapping the ionised gas kinematics and abundances" by B. L. James, Y. G. Tsamis and M. J. Barlow, M. S Westmoquette, J. R. Walsh, F. Cuisinier and K. M. Exter, 2009 (arXiv;0903.2280).

3.1 Introduction

Blue Compact Dwarf (BCD) galaxies provide a means of studying chemical evolution and star formation in low metallicity environments in the nearby Universe. In general BCDs are faint ($M_B > 18$), have blue optical colours, are typically small ($\lesssim$1 kpc) and are thought to be experiencing bursts of star formation in relatively chemically un-evolved environments, ranging from 1/2–1/50 solar metallicity (Kunth & Östlin 2000), and are therefore good analogues to high redshift star forming galaxies.

The current study focuses on Markarian 996, a BCD whose properties are far from ordinary. Thuan *et al.* (1996) (TIL96 hereafter) presented a comprehensive *HST* study of Mrk 996 by analysing FOS UV and optical spectra and WFPC2 V- and I-band imaging. Their *HST* V-band image, shown in Figure 3.1, revealed that the majority of the star formation in Mrk 996 occurs within a bright, compact nuclear H II region of $\sim$3 arcsec angular radius ($\sim$315 pc for their adopted distance of 21.6 Mpc (TIL96)) surrounded by an extended elliptical low surface brightness component of $\sim$40.6 arcsec diameter. However, the remarkable nature of the galaxy was

exposed by the small-aperture ($\sim$1 arcsec) FOS spectra obtained from the nucleus of Mrk 996. Line widths increase with the degree of ionisation; lines from singly ionised species being narrow and typical of H II regions whereas lines from ions such as O^{2+} and Ne^{2+} are very broad, with FWHM widths up to $\sim$900 km s^{-1} (TIL96). Un-physically high [O III] electron temperatures are derived for the nucleus unless an electron density ($N_{\rm e}$) of at least $\sim 10^6$ cm^{-3} is adopted, several orders of magnitude higher than normal H II region electron densities (Izotov *et al.* 1994). In order to account for the observed line intensities, TIL96 applied a two-zone density-bounded H II region model, with an inner core density of $\sim 10^6$ cm^{-3} and an outer zone with a density of ~ 450 cm^{-3}. They suggested that this large density gradient is caused by a mass outflow driven by the large population of Wolf-Rayet stars found to be present in the galaxy.

Elemental abundances were also derived by TIL96, who estimated a metallicity of 0.22 $Z_{\odot}$, based on the abundance of oxygen. As a result of their study, Mrk 996 was placed in a small group of eight BCDs known to display a significant overabundance of nitrogen (Pustilnik *et al.* 2004), with derived N/O ratios that are 0.3–1.4 dex higher than for other BCDs of similar oxygen abundances. The enhanced nitrogen within this group has been suggested by Pustilnik *et al.* (2004) to be connected with merger events, in particular with a short phase of the consequent starburst, when many WR stars contribute to the enrichment of the interstellar medium (ISM). This was certainly the case for NGC 5253 (thought to be interacting with its companion galaxy NCG 5236 (Moorwood & Glass 1982)), where spatially resolved N/H and N/O enhancements were observed by Walsh & Roy (1987) to correlate strongly with WR star signatures. In support of this, a correlation was also found between spatial enhancements of He/H and N/O, attributed to helium enrichment of the ISM by WR stars (Walsh & Roy 1989).

The study of TIL96 showed that Mrk 996 has spatially varying physical properties. Spatially resolved kinematic and chemical abundance information across the galaxy is therefore crucial for understanding the nature of this system; such information can be readily obtained with integral field spectroscopy (IFS). In this chapter I present high resolution optical IFS observations obtained with the VIMOS integral field unit (IFU, described in detail in Section 1.5.1) spectrograph on the 8.2m Very Large Telescope UT3/Melipal. The data afford us a new spatiokinematic '3-D' view of Mrk 996. The spatial and spectral resolution achieved allows us to undertake a full multi-velocity-component analysis of this system, ultimately providing a more complete picture of its diverse ionised ISM.

I adopt a distance of 22.3 Mpc for Mrk 996, at a redshifted velocity of 1642 km s^{-1} (corresponding to $z = 0.00544$, this work), using a Hubble constant $H_{\rm o} = 73.5$ km s^{-1} Mpc^{-1} (De-

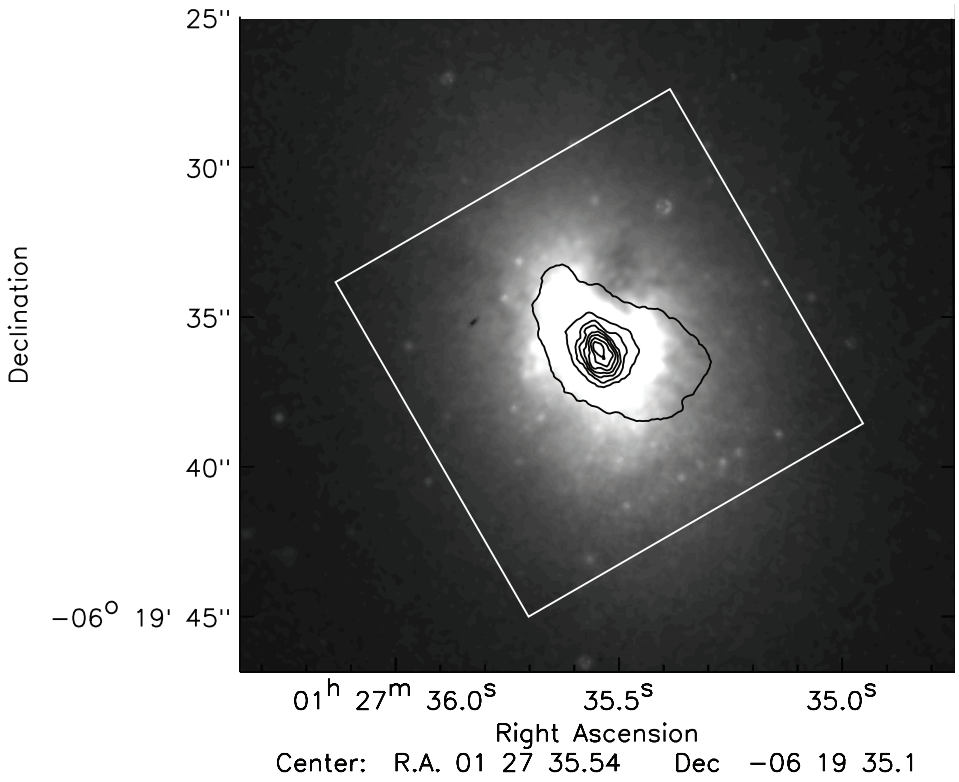

Figure 3.1: *HST* F569W WFPC2 image of Mrk 996 overlaid with the $13'' \times 13''$ VIMOS IFU aperture at a position angle of 30°, along with contours from the VIMOS IFU Hα narrow component emission line map (see Fig 3.4). North is up and east is to the left. Hα contours are shown for the range 24.8 – 899.9, in steps of 119, in surface brightness units of $\times 10^{-15}$ ergs cm^{-2} s^{-1} arcsec^{-2}.

Bernardis *et al.* 2008).

3.2 VIMOS IFU Observations and Data Reduction

3.2.1 Observations

Two data sets were obtained with the Visible Multi-Object Spectrograph (VIMOS) IFU at the 8.2m VLT at ESO's Paranal Observatory in Chile. The VIMOS IFU consists of 6400 (80×80) fibres coupled to microlenses and operates with four CCD detectors yielding four spectral and spatial quadrant samplings (Zanichelli *et al.* 2005). The spatial sampling is contiguous, with the dead space between fibres below 10 per cent of the inter-fibre distance. The data sets were taken with the high resolution and high magnification (i.e. a partially masked IFU head containing only

40×40 fibres) settings of the IFU, resulting in a field-of-view (FoV) of $13'' \times 13''$ covered by 1600 spatial pixels (spaxels) at a spatial sampling of $0.33''$ per spaxel. Two different grisms were used, high resolution blue (HRblue, ∼0.51 Å/pixel), covering 4150–6200 Å and high resolution orange (HRorange, ∼0.60 Å/pixel) covering 5250–7400 Å; spectra from both grisms are illustrated in Fig 3.2. The instrumental width delivered by the IFU HRblue and HRorange grisms was measured using arc lamp exposures. Gaussian profiles were fitted to a number of isolated lines within each extracted arc spectrum and were found to have FWHMs of 2.3 ±0.1 Å (113.5 ± 4.9 km s^{-1}) and 1.5 ±0.1 Å (72.3 ± 4.8 km s^{-1}) for the HRblue and HRorange grisms, respectively.

The observing log can be found in Table 3.1. Four exposures were taken per grism. The third exposure within each set was dithered by $+0.34''$ in RA and by $+0.58''$ in Dec (corresponding to a 2 spaxel offset in the X-direction) in order to remove any dead fibres when averaging exposures. All observations were taken at a position angle of $+30°$.

3.2.2 Data Reduction

The data reduction was carried out using the GUI-based pipeline software GASGANO[1] that allows the user to organise calibration files and run pipeline tasks. Three main tasks were used: (1) *vmbias* created the master bias frame; (2) *vmifucalib* determined the spectral extraction mask, wavelength calibration and the relative fibre transmission correction; (3) *vmifustandard* created flux response curves from a summed spectrophotometric standard star spectrum. Finally, the products of these tasks were fed into *vmifuscience* which extracted the bias-subtracted, wavelength- and flux-calibrated, and relative fibre transmission-corrected science spectra. Each VIMOS CCD quadrant is an independent spectrograph, therefore the IFU data processing was performed separately on each quadrant, creating four fully calibrated 3-D arrays per science exposure. The flux calibration was performed by multiplying the 2-D spectral frame for each quadrant by its relative response curve, derived from standard star observations in the same filter, grism and quadrant. The final data cube is produced by median-combining each exposure in a jitter sequence (i.e. re-aligning the dithered exposure with the other exposures of identical pointing), after all the individual data quadrants for each exposure had been reduced. Reconstructing the cube spatially utilises the IFU table that lists the one-to-one correspondence between fibre positions on the IFU head and stacked spectra on the CCD (Bastian *et al.* 2006). A schematic representation of the data reduction processes can be found in Zanichelli *et al.* (2005).

Unlike other IFU designs (such as VLT FLAMES/Argus), there are no 'sky-dedicated' fibres

[1] http://www.eso.org/sci/data-processing/software/gasgano

Table 3.1: VIMOS IFU observing log

Observation ID	Date	Grism	Exp. time (s)	Airmass range	FWHM Seeing (arcsec)
250520	13/10/2006	HR blue	4×402	1.135 – 1.097	0.72
250516	19/10/2006	HR orange	4×372	1.057 – 1.053	1.15

in VIMOS IFU mode. Sky subtraction was performed by locating a background region within each quadrant, summing the spectra over each of the spaxels in the reconstructed cube and subtracting the median sky spectrum of the region from its corresponding quadrant. Median combining was needed to ensure that any residual contamination from faint objects was removed. It should be noted that VIMOS IFU images are obtained as projections on the IFU CCD, i.e. they are mirror images to what is seen on the sky. Thus, all emission maps presented in this paper have been reflected about the Y-axis to obtain the correct orientation.

3.2.3 Emission Line Profile Fitting

The resolving power and signal-to-noise (S/N) of the data are high enough to allow the resolution of multiple components in the majority of the emission lines seen in the 1600 spectra across the FoV. In order to fit spectra of this quantity and complexity, I utilised an automated fitting procedure called PAN (Peak ANalysis; Dimeo 2005). This IDL-based, general-purpose curve-fitting package was adapted by Westmoquette *et al.* (2007*a*) for use with FITS format data by allowing multiple spectra to be read simultaneously in an array format. The user can interactively specify initial parameters of a spectral line fit (continuum level, line peak flux, centroid and width) and allow PAN to sequentially process each spectrum, fitting Gaussian profiles accordingly. The output consists of the fit parameters for the continuum and each spectral line's profile and the χ^2 value for the fit.

It was found that in the spectra of Mrk 996 most high S/N ratio emission line profiles consist of a strong, narrow central Gaussian component (hereafter C1), superimposed on a very broad component containing a substantial proportion of the flux (hereafter C2). In addition to this, in the core of the galaxy the C2 component of the Balmer line profiles splits into two broad Gaussian profiles of variable strength and velocity (hereafter C3 and C4, shifted towards the blue and red of the centroid of C1, respectively). The splitting of C2 into C3 and C4 and the region in which this occurs is discussed in Section 3.3.2. Fig 3.3 shows examples of fits to the Hα emission line from different regions of Mrk 996 in order to illustrate single, double and triple Gaussian fits, along with

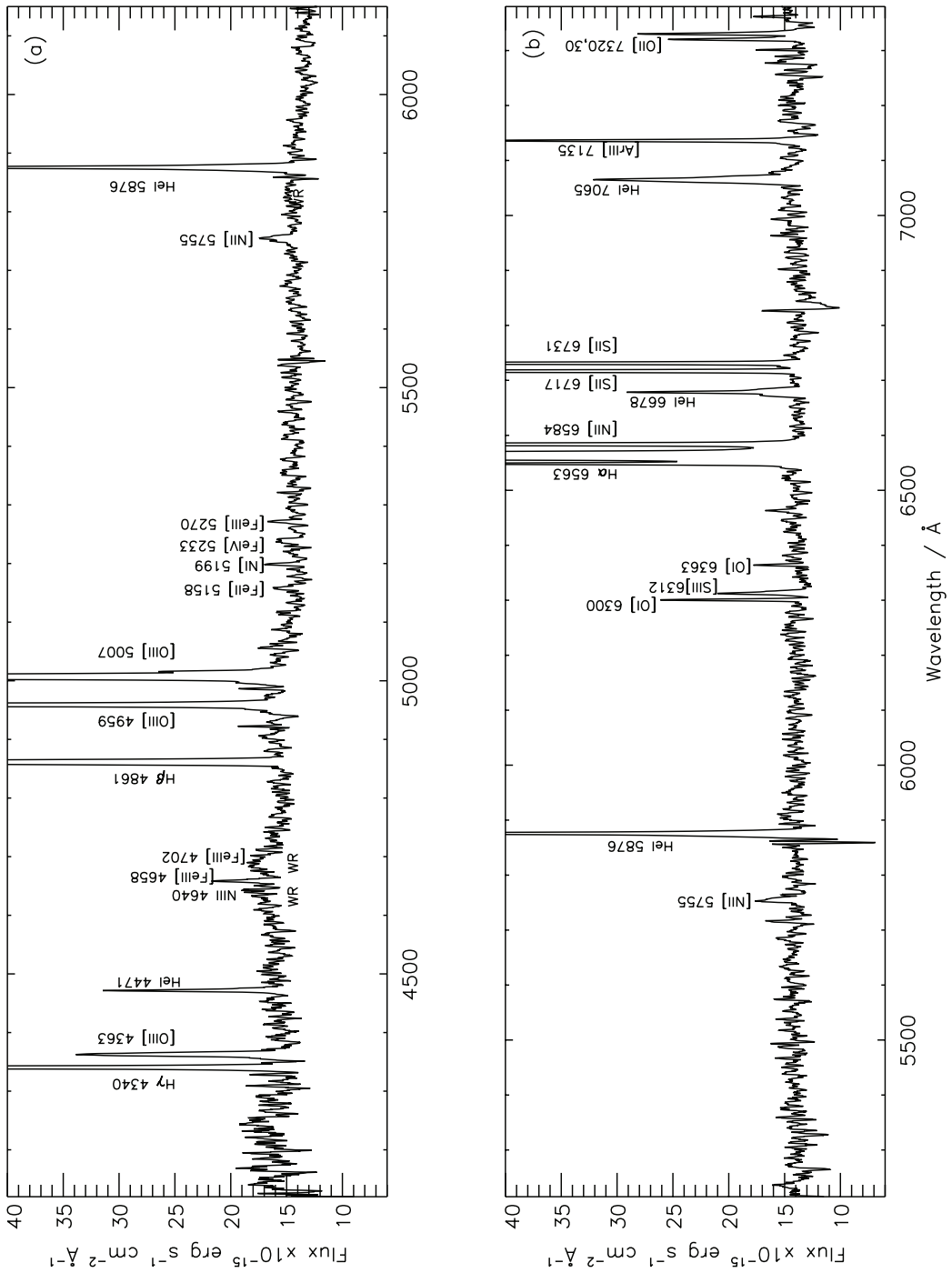

Figure 3.2: VIMOS IFU summed spectra of Mrk 996 after smoothing with a 5 pixel boxcar: (a) high resolution blue spectrum; (b) high resolution orange spectrum. Spectra are integrated over an area of 5.3×6.3 arcsec^2 (575×685 pc^2) and correspond to exposure times of 4×402 s and 4×372 s for the HR blue and HR orange grisms, respectively.

the corresponding fit residuals. In the same figure a double Gaussian fit to the [O III] λ5007 profile is also shown corresponding to the same central spaxel for which Hα requires a triple Gaussian fit, thus illustrating the difference between the Hα and [O III] line profiles. Where appropriate, single or multiple Gaussian profiles were fitted to the emission line profiles, restricting the minimum FWHM to be the instrumental width. Suitable wavelength limits were defined for each emission line and continuum level fit. Further constraints were applied when fitting the [S II] doublet: the wavelength difference between the two lines was taken to be equal to the redshifted laboratory value when fitting the velocity component, and their FWHMs were set equal to one another.

In order to rigorously determine the optimum number of Gaussian profiles required to fit each observed profile the statistical F-test was used. The F-distribution function allows one to calculate the significance of a variance (χ^2) increase that is associated with a given confidence level, for a given number of degrees of freedom. I note that even though many low S/N ratio lines may in reality be composed of multiple emission components, it is often not statistically significant to fit anything more than a single Gaussian profile. This is why the robust F-test method was chosen for objectively determining the optimum number of components to fit to each line. Resultant optimised fits for various line species are as follows:

Single narrow Gaussian fit (i.e. C1 component only) – [Fe III] $\lambda\lambda$4658, 4702, 4881, 4986, [O I] $\lambda\lambda$6300, 6364, [N II] λ6584, [S II] $\lambda\lambda$6717, 6731, and [O II] $\lambda\lambda$7320, 7330.

Single broad Gaussian fit (i.e. C2 component only) – [N II] λ5755, [O III] λ4363.

Double narrow/broad Gaussian fit (C1 and C2) – all Balmer lines (excluding the central spaxels), He I $\lambda\lambda$4471, 5876, 6678, 7065, [O III] $\lambda\lambda$4959, 5007, [S III] λ6312, and [Ar III] λ7136.

Triple narrow/broad Gaussian fit (C1, C3, and C4) – all Balmer lines (central spaxels only).

The errors reported by PAN during fitting underestimate the true uncertainties. I therefore followed an error estimation procedure which involves the visual re-inspection of the line profile plus fit after knowing which solution was selected by my tests, and taking into account the S/N ratio of the spectrum. The errors on the fits are minimised across the IFU's aperture varying S/N ratio during the F-testing procedure by selecting the number of components which best-fit the profile within that particular spaxel. It is further noted that the uncertainties associated with each individual line component are coupled to those of the other components within a given line profile. By comparing PAN fits to those performed by other fitting techniques (e.g. IRAF's SPLOT task) on line profiles with an established configuration (i.e. after performing the F-test) I found that uncertainties of $\sim$5–10 and $\sim$15–20 per cent are associated with the C1 and C2–4 fits, respectively. A listing of measured flux and FWHM uncertainties appears in Table 3.2, where errors are quoted

for individual component fits to emission lines detected on integrated spectra across the inner and outer regions of Mrk 996.

3.2.4 Cube alignment and correction for differential atmospheric refraction

Observations of an object's spectrum through the Earth's atmosphere are subject to refraction as a function of wavelength, known as differential atmospheric refraction, DAR. The direction of DAR is along the parallactic angle at which the observation is made. Each reduced data cube was corrected for this effect using the algorithm outlined by Walsh & Roy (1990); this procedure calculates fractional pixel shifts for each monochromatic slice of the cube relative to a fiducial wavelength (i.e. a strong emission line), shifts each slice with respect to the orientation of the slit on the sky and the parallactic angle and re-combines the DAR-corrected data cube. Having data cubes with different wavelength ranges would ideally involve a choice of fiducial wavelength that is common to both, e.g. He I λ5876 for these VIMOS data. However, the S/N ratio of this line is not consistently high across the IFU aperture, and pixel shifts for each cube relative to this line were found to be unreliable. Instead, I chose to correct each data cube using its strongest emission line: Hβ for the HRblue cube and Hα for the HRorange cube. The two cubes were then spatially matched by aligning the Hα and Hβ emission contours using a 2-D Gaussian fit. This involved a maximum shift of -0.73 spaxels in X and $+0.82$ spaxels in Y. Two effects can introduce minor errors when aligning monochromatic H I images: (i) an extinction gradient across the observed region disproportionately affecting the two lines, and (ii) the presence of a temperature gradient, since the H I lines have a very slightly different temperature dependence. However, both gradients would need to be significant for substantial errors to be introduced; the sub-spaxel shifts that were determined show that this is not the case here.

3.3 Mapping of line fluxes and kinematics

3.3.1 Line fluxes and reddening correction

Full HRblue and HRorange spectra are shown in Fig 3.2, with identified emission lines labelled. Table 3.2 lists the measured FWHM and observed and de-reddened fluxes for the main velocity components of the detected emission lines. The fluxes are from spectra summed over the core region and the outer annulus region, as defined in Section 3.3.4, and are quoted relative to the flux of the corresponding Hβ component. They were corrected for reddening using the Galactic reddening law of Howarth (1983) using c(Hβ) values derived from the Hα/Hβ and Hγ/Hβ line

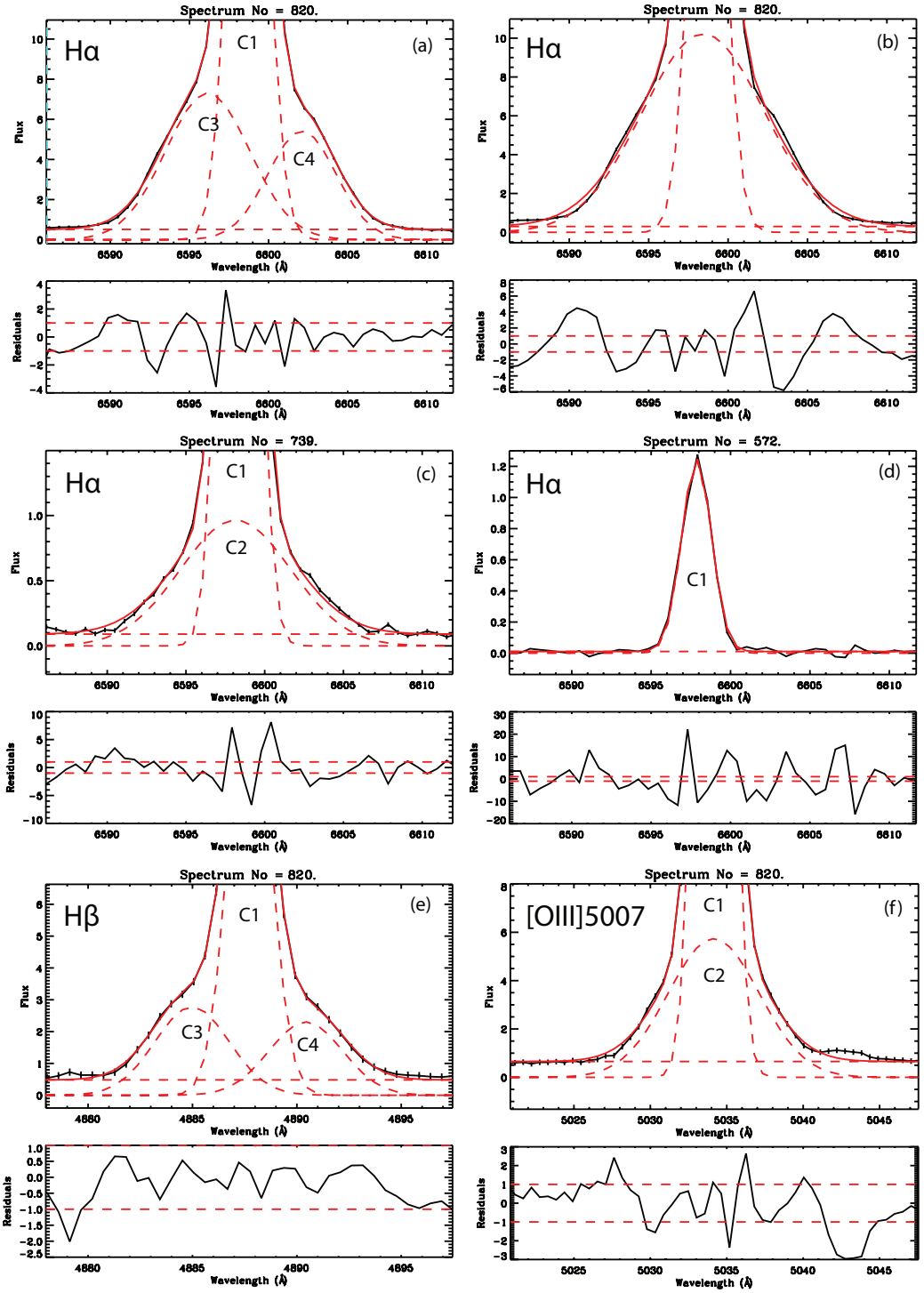

Figure 3.3: Example Mrk 996 emission line profiles and Gaussian fits: (a) a typical spaxel from the core region with a triple Gaussian fit to the Hα line; (b) the same spaxel spectrum shown in (a) but with a double Gaussian fit [note the larger residuals of the fit as compared to (a)]; (c) Hα emission line from a spaxel in the outer region which required a double Gaussian fit; (d) Hα emission line from the edge of the outer region where a single component fit is sufficient; (e) the Hβ emission line for the same core spaxel as that in (a), displaying the same triple component structure (Hγ also shows an identical structure in the core spaxels); (f) the [O III] λ5007 emission line for the same core spaxel as that of (a) and (b), illustrating an optimal double Gaussian fit (rather than the triple components required for the Balmer lines). The flux units are $\times 10^{-15}$erg s^{-1} cm^{-2} Å^{-1}. The fit residuals are plotted under each panel (in units of σ) with dashed guidelines at $\pm 1\sigma$. The wavelengths are not corrected for redshift.

		Core Region			Outer Region		
Line ID	Component	FWHM (km s^{-1})	$F(\lambda)$	$I(\lambda)$	FWHM (km s^{-1})	$F(\lambda)$	$I(\lambda)$
4340 Hγ	C1	145.1± 2.1	44.9± 0.5	46.3 ± 0.4	158.2± 6.2	54.4± 8.7	63.2 ± 2.2
4340 Hγ	C2	442.2± 15.9	42.6± 1.3	48.2 ± 1.4	–	–	–
4363 [O III]	C2	476.5± 14.4	20.2± 0.5	32.9 ± 0.8	–	–	–
4471 He I	C1	155.6± 14.8	3.8± 0.6	3.9 ± 0.6	260.2± 91.2	9.7± 2.9	10.8 ± 2.8
4471 He I	C2	540.6± 61.0	9.8± 1.0	10.7 ± 1.1	–	–	–
4658 [Fe III]	C1	277.5± 27.7	3.3± 0.2	3.3 ± 0.5	–	–	–
4702 [Fe III]	C1	274.3± 53.0	0.7± 0.4	0.7 ± 0.4	–	–	–
4861 Hβ	C1	130.8± 0.6	100.0± 1.0	100.0 ± 0.7	133.9± 0.6	100.0± 22.0	100.0 ± 15.6
4861 Hβ	C2	414.7± 4.3	100.0± 1.5	100.0 ± 1.0	308.5± 6.2	100.0± 21.5	100.1 ± 15.2
4881 [Fe III]	C1	313.4± 94.6	1.0± 0.4	1.0 ± 0.4	–	–	–
4959 [O III]	C1	131.2± 0.6	132.2± 1.3	131.7 ± 0.9	137.9±1.75	113.1± 2.3	109.9± 2.2
4959 [O III]	C2	392.0± 10.3	49.3± 1.4	48.2 ± 1.3	332.7± 3.6	58.32 ± 14.8	55.4 ± 14.08
4986 [Fe III]	C1	210.5± 54.8	1.5± 0.6	1.5 ± 0.6	–	–	–
5007 [O III]	C1	132.4± 0.6	399.6± 4.2	397.1 ± 3.2	130.6± 0.6	347.7± 54.3	333.4 ± 2.5
5007 [O III]	C2	415.2± 13.8	148.8± 4.7	143.8 ± 4.3	404.4± 38.9	133.9± 24.1	124.3 ± 11.9
5755 [N II]	C2	427.9± 74.5	3.3± 0.4	4.0 ± 0.5	–	–	–
5875 He I	C1	121.5± 2.5	11.3± 0.4	10.7 ± 0.4	147.0± 8.7	19.6± 3.2	15.2 ± 0.7
5875 He I	C2	425.8± 8.2	33.4± 0.7	27.2 ± 0.5	–	–	–
6300 [O I]	C1	128.0± 13.8	4.6± 0.4	4.3 ± 0.4	141.9± 22.9	7.6± 1.5	5.4 ± 0.7
6312 [S III]	C1	107.4± 13.8	1.2± 0.2	1.2 ± 0.2	133.0± 31.8	3.8± 0.8	2.7 ± 0.4
6312 [S III]	C2	403.0± 29.0	5.8± 0.4	4.4 ± 0.3	–	–	–
6363 [O I]	C1	153.2± 20.3	1.7± 0.2	1.6 ± 0.2	147.5± 38.2	4.0± 1.1	2.9 ± 0.6
6563 Hα	C1	116.5± 0.9	306.9± 4.4	285.6 ± 3.6	118.8± 0.4	418.9± 65.3	287.6 ± 1.6
6563 Hα	C2	420.5± 7.3	400.5± 7.5	294.0 ± 4.6	407.7± 9.6	555.5± 85.3	284.2 ± 0.8
6584 [N II]	C1	126.2± 4.1	38.0± 1.1	35.3 ± 1.0	123.4± 2.2	45.4± 7.1	31.1 ± 0.4
6678 He I	C1	112.7± 4.9	3.5± 0.2	3.2 ± 0.2	124.8± 14.8	6.8± 1.3	4.6 ± 0.5
6678 He I	C2	550.3± 28.8	9.2± 0.4	6.6 ± 0.3	–	–	–
6717 [S II]	C1	118.8± 1.8	30.9± 0.5	28.6 ± 0.5	117.4± 2.2	31.6± 5.0	21.2 ± 0.4
6731 [S II]	C1	118.5± 1.8	24.6± 0.5	22.8 ± 0.4	117.2± 2.2	22.4± 3.5	14.9 ± 0.4
7065 He I	C1	76.00± 65.4	1.1± 0.9	1.0 ± 0.8	217.8± 56.1	7.0± 1.9	4.4 ± 1.0
7065 He I	C2	425.4± 58.2	24.4± 2.8	16.8 ± 1.9	–	–	–
7136 [Ar III]	C1	127.3± 17.2	10.3± 2.3	9.4 ± 2.1	127.8± 11.4	13.5± 2.3	8.5 ± 0.7
7136 [Ar III]	C2	441.0± 213.9	8.2± 3.5	5.6 ± 2.4	–	–	–
7320 [O II]	C1	176.6± 11.9	6.1± 0.3	5.6 ± 0.3	219.2± 62.3	9.2± 2.3	5.6 ± 1.1
7330 [O II]	C1	165.3± 11.9	5.8± 0.3	5.3 ± 0.3	111.3± 21.3	10.8± 2.2	6.6 ± 0.8
c(Hβ)	C1		0.10±0.02			0.51±0.08	
c(Hβ)	C2		0.42±0.04			0.91±0.12	
F(Hβ)	C1		626.30±4.31			180.33±28.13	
F(Hβ)	C2		431.70±4.46			36.67±5.57	

Table 3.2: Emission line measurements for summed spectra of the inner core ($1.7'' \times 2.3''$) and an 'outer annulus' region whose extent is $5.3'' \times 6.3''$ but from which the inner core spectrum has been subtracted (see Section 3.3.4). Observed fluxes and dereddened intensities are given for the main two velocity components and are relative to Hβ = 100 (the corresponding velocity component of Hβ). The employed logarithmic extinction constants, c(Hβ), are quoted (see Section 3.3.1); integrated Hβ fluxes for the two main velocity components, in units of $\times 10^{15}$ erg cm^{-2} s^{-1}, are also listed.

ratios of their corresponding components, weighted in a 3:1 ratio, respectively, in conjunction with the theoretical Case B ratios from Hummer & Storey (1987). Following the same method, an average c(Hβ) map was also derived using ratioed Hα/Hβ and Hγ/Hβ emission line maps. The c(Hβ) map was used for correcting emission line maps for reddening in order to then create abundance maps. In the direction to Mrk 996 a foreground Milky Way reddening of $E(B-V) = 0.04$, corresponding to c(Hβ) $= 0.06$, is indicated by the extinction maps of Schlegel *et al.* (1998). Values of c(Hβ) of 0.10$\pm$0.02 and 0.51$\pm$0.08 are applicable to the narrow component emission in the inner and outer regions of Mrk 996, respectively, while values of 0.42$\pm$0.04 and 0.91$\pm$0.12 are applicable to the broad component emission for the inner and outer regions, respectively.

3.3.2 The Balmer line properties

All the Balmer lines detected from Mrk 996 (Hα, Hβ and Hγ) show a common multi-component velocity structure which in the innermost spaxels is exclusive to the Balmer lines, i.e. it is not seen in the forbidden lines. Here I present a discussion of the highest S/N ratio H I line, Hα. Maps of the individual Hα velocity components (flux, radial velocity and FWHM) are shown in Fig 3.4. As mentioned previously, up to three components are resolved in the Hα line profile in the nuclear region of Mrk 996:

(i) A central, narrow Gaussian profile (C1) is detected throughout the galaxy (see the flux map in Fig 3.4a), peaking at $\alpha = 01^{\rm h}\,27^{\rm m}\,35\overset{\rm s}{.}5 \pm 0.1$, $\delta = -06^{\circ}\,19'\,36\overset{''}{.}2 \pm 0.2$ (J2000), with a surface brightness of 10.1×10^{-12} erg cm^{-2} s^{-1} arcsec^{-2} in the central region, and gradually decreasing over a region with a major axis radius of 3$''$.84 (403 pc) and a minor axis of 2$''$.39 (251 pc); beyond this the Hα emission traces a very low surface brightness area (which TIL96 fitted with an exponential disk on their *HST* images). The galaxy does not show a smooth elliptical shape when viewed in Hα. Fig 3.1 shows the flux contours of the narrow Hα component (C1) overlaid on the *HST* F569W (*V*-band) image. The Hα emitting region imaged by VIMOS is mostly confined within the inner part of the F569W image but the major axes of the two are not aligned. A dust extinction feature is present in the north-west section of the inner star forming region that distorts the F569W flux isophotes (TIL96). The dust feature also distorts the outermost Hα contours of the VIMOS data.

(ii) In the very core of Mrk 996, over an area of $\sim$1$''$.5 in radius (162 pc), the narrow C1 profiles are accompanied by broad underlying components that are best fit with two Gaussian profiles (C3 and C4) to the blue and red of C1, respectively (Fig 3.4a). The significance of these features is discussed below.

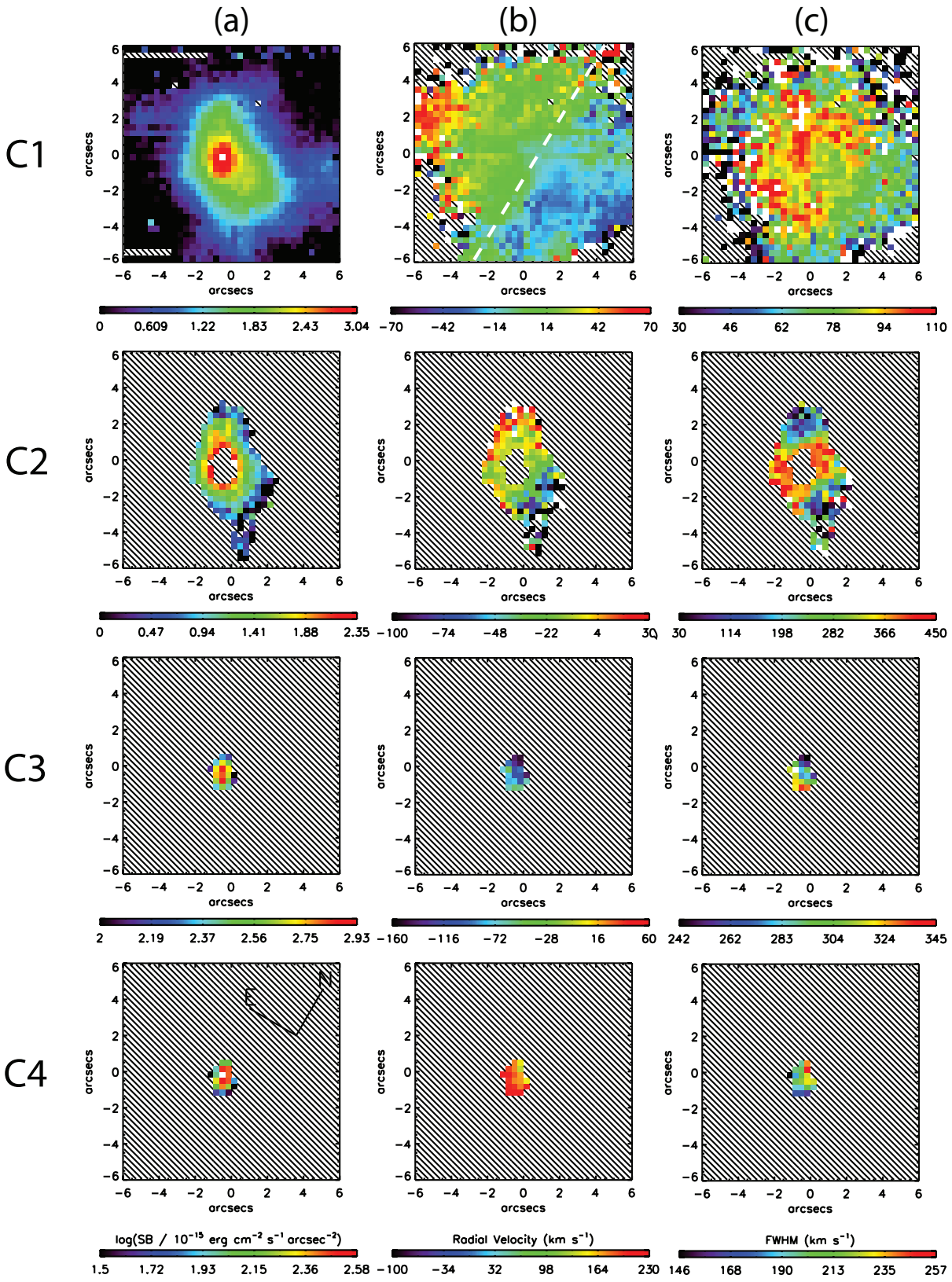

Figure 3.4: Maps of Mrk 996 in the Hα velocity components C1–4; (a) logarithmic surface brightness; (b) radial velocity (relative to the heliocentric systemic velocity of $+1642$ km s^{-1}), where the white dotted line overlaid on the C1 velocity map represents a cut along the rotational axis, as used for the position-velocity diagrams shown in Fig 3.5; (c) FWHM corrected for the instrumental PSF. See text for details.

(iii) Beyond a radius of $\sim$1″.5 from the core, C3 and C4 blend into a single broad Gaussian profile (C2) (Fig 3.4a). The region over which this component is seen is $\sim$2–4 arcsec in radius (216–432 pc); its outer boundary matches well that of the brightest portion of the C1 flux map.

The radial velocity map of component C1 (Fig 3.4b) shows a strong velocity gradient from west to east, with a definable axis of rotation at PA $= 5^{\circ}$ (marked by the dashed line across the C1 velocity map). Neither the rotation axis as revealed by VIMOS nor the axis normal to it are aligned with the apparent, i.e. photometric, major axis of the galaxy which lies at PA $\sim 23^{\circ}$ (TIL96). A velocity gradient in approximately the same direction is observed in the broad component C2, although in this case the negative velocity component is not exactly balanced by a positive counterpart. Fig 3.5 shows position-velocity (P-V) diagrams along the adopted axis of rotation (Fig 3.5a) and also perpendicular to this axis (Fig 3.5b). A new estimation of the heliocentric systemic velocity of Mrk 996 can be made using Fig 3.5a; a radial velocity of 1642 $\pm$ 10 km s^{-1} is needed to normalise the distribution of C1 velocities along the axis of rotation to zero (cf. the 1622 $\pm$ 10 km s^{-1} estimate of TIL96). The narrow line component C1 shows a velocity gradient along the direction normal to the rotation axis, with radial velocities ranging from ~ -50 km s^{-1} to $+50$ km s^{-1}, and the P-V diagram of component C1 shows a linear velocity gradient indicating solid-body rotation (Fig 3.5b). This type of structure is not uncommon for BCDs observed in the H I 21 cm line and has been used by van Zee *et al.* (2001) to constrain evolutionary scenarios.

Assuming a Keplerian velocity profile I have converted each radial velocity data point of component C1 (Fig 3.5b) into a mass within radius r, as shown in Fig 3.6. This plot shows dynamical mass growing at similar rates on either side of the centre, rising to a total mass of $\sim 5\pm1\times10^{8}$M$_{\odot}$ within a radius of $\sim$0.75 kpc. This is in good agreement with the total mass of 4.3×10^{8} $M_{\odot}$ estimated by TIL96 from H I emission features detected by Thuan *et al.* (1995). It should be noted that all previous kinematical studies of BCDs have been based on H I 21 cm observations (van Zee *et al.* 2001; Thuan *et al.* 2004).

The broad line component C2 also shows a velocity gradient roughly perpendicular to the rotation axis, (Fig 3.5b), aligned more closely with the major axis of Mrk 996, with radial velocities that merge with those of C1 2″ from the centre of the galaxy, but extending to larger negative values. No definite velocity structure can be seen along this axis for the C3 and C4 components; however, these show an opposing velocity gradient along the galaxy's rotation axis (Fig 3.5a). Their radial velocities lie much higher at -60 to -160 km s^{-1} for C3 and $+110$ to $+210$ km s^{-1} for C4, with the gradients in both showing a similar 'S' shape offset by 1″ from the dynamical

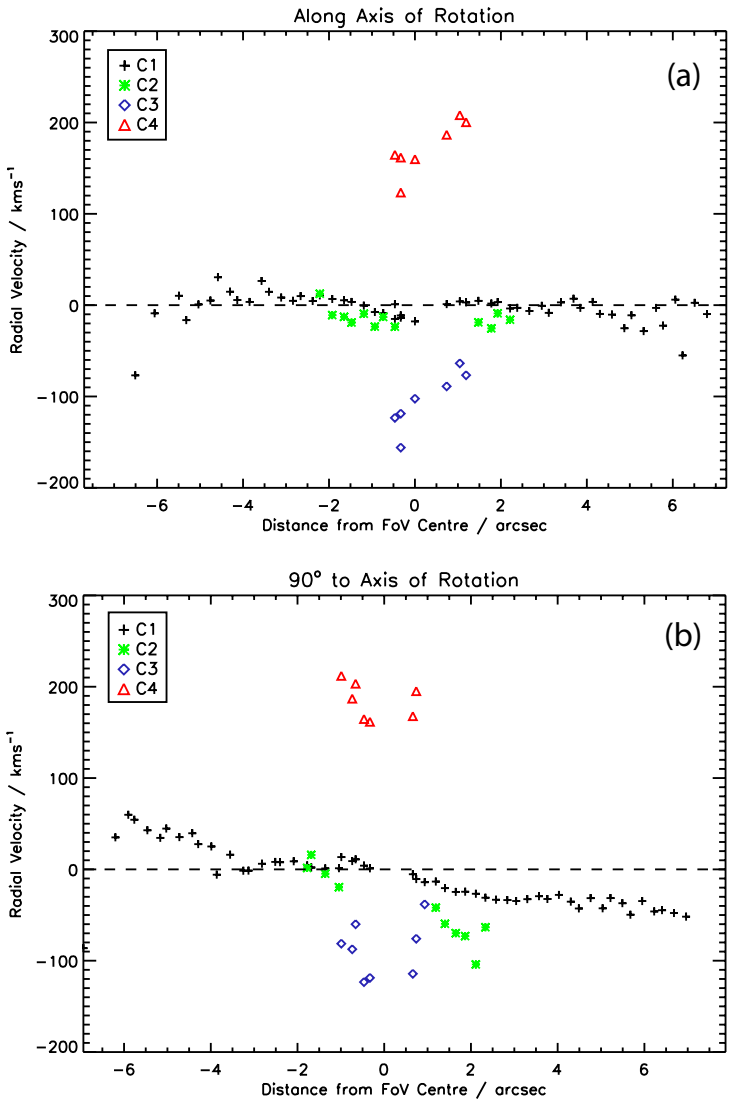

Figure 3.5: Position velocity diagrams for Hα: (a) along the axis of rotation, defined as 5° east of north, as indicated by component C1 in Fig 3.4b; (b) along the direction 90° to the rotation axis. Both diagrams are relative to a systemic velocity of $+1642$ km s^{-1}. Typical radial velocity errors are $<$3, 8–20, 12–15, and 7–11 per cent for C1, C2, C3 and C4, respectively, with a spatial error of 0.5 spaxels ($\pm 0.17''$).

centre of Mrk 996. It is further noted that the velocity centre of symmetry of the 'S' feature is offset by $+50\,\mathrm{km\ s^{-1}}$ from the heliocentric systemic velocity of Mrk 996 measured above. The 'S' kinematic feature can be attributed to a two-arm spiral structure located at the nucleus of Mrk 996, whose approaching and receding arms are respectively traced by the velocity distribution of the C3 and C4 components of Hα. Furthermore, my analysis reveals that the projected angular velocity vectors on the plane of the sky of the spiral and of the gas traced by the C1 narrow line component are at an angle of $<90^{\circ}$. In their WFPC2 images of Mrk 996, TIL96 identified a small spiral structure along the east-west direction (see their fig 4b) whose pivot is the nuclear star-forming region which is slightly offset from the centre of the outermost F791W image isophotes. The pivot of the spiral and the peak flux position on the VIMOS Hα C1 map coincide spatially. The $1''$ offset mentioned above for the spatial centre of symmetry of the 'S' feature (Fig 3.5a) is consistent with the asymmetry noted by TIL96. This fact, along with the $\sim$+50 km s^{-1} offset of the spiral's pivot with respect to the systemic velocity of the galaxy, indicates that the spiral-like nucleus of Mrk 996 is kinematically decoupled to some degree from the main ionised gas component. This could indeed be the fossil kinematic signature of a past merger event.

The FWHMs of C1–4 in Hα are shown in Fig 3.4c, corrected for the instrumental PSF (see Section 3.2.2). A peak in the FWHM of the narrow C1 component, $\sim$110 km s^{-1}, is seen at the nucleus of Mrk 996. This gradually, but not uniformly, decreases to $\sim$65 km s^{-1} towards the outer regions. The gradient in the FWHM of C2 is far stronger, peaking at $\sim$450 km s^{-1} at two positions northwest and southest of the nucleus and decreasing to $\sim$100 km s^{-1} elsewhere: the broader line widths along the former direction could be the signature of an expanding shell surrounding the inner star forming region, blown outwards by the stellar winds of the core cluster. Higher resolving power IFU spectroscopy is needed to disentangle the kinematics of this region. No significant gradient is seen in the FWHM of components C3 and C4, both remaining between 200–300 km s^{-1}.

3.3.3 The [O III] nebular line properties

As mentioned previously, the structure of the H I Balmer lines is not mirrored in the forbidden nebular lines. All the strong forbidden lines (with the exception of [O III] λ4363 and [N II] λ5755 discussed below) are comprised of a narrow, central Gaussian component (C1) with an underlying *single* broad Gaussian component (C2). An optimal fit, after applying the rigorous statistical F-test to a spaxel from the core of Mrk 996, can be seen in Fig 3.3f. For the spaxels in which the Balmer components C3 and C4 are detected, the FWHM of the [O III] λ5007 C2 component is $\sim$390–415

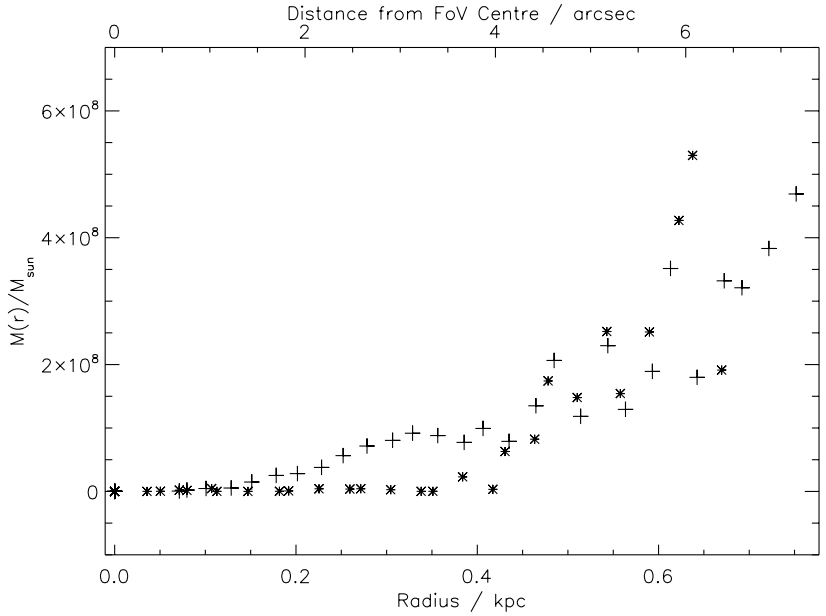

Figure 3.6: Dynamical mass as a function of radius, r, derived from the distribution of C1 radial velocities along the direction normal to Mrk 996's rotation axis: distance east from the centre represented by crosses and distance west from the centre represented by stars.

km s^{-1} and that of each of Hα C3 and C4 is $\sim$180–240 km s^{-1}. The occurrence of additional C3-4 components in the Balmer lines is in contrast to the non-occurrence of C2 splitting in the [O III] nebular lines and can perhaps be ascribed to a lower S/N ratio for the broad component of [O III] $\lambda\lambda$4959, 5007 compared to the C2 of H I lines: the observed C2/C1 flux ratios pertaining to the [O III] nebular lines in the inner core of Mrk 996 (as defined in the following subsection) are half of those observed in the H I lines (Table 2). However, from my analysis of the broad C2 component, I find log ($N_{\rm e}$/cm^{-3}) = 7.25 $\pm$ 0.25 from the [O III] lines (Section 3.4). This is high enough to collisionally suppress $\lambda\lambda$5007+4959 whose critical density for de-excitation is 6.4$\times$10^5 cm^{-3}. The distribution of flux in the C1 and C2 components of the [O III] λ5007 line is shown in Fig 3.7. The shape and extent of the emitting regions are similar to those of the corresponding Hα C1 and C2 components.

3.3.4 Broad emission lines: [O III] λ4363 and [N II] λ5755

My multi-component line analysis shows that only the broad (C2) components of the auroral [O III] λ4363 and [N II] λ5755 transitions are present, and only in the inner galaxy. The implications of this for the use of [O III] λ4363 as a temperature diagnostic are discussed in Section 3.4. For the

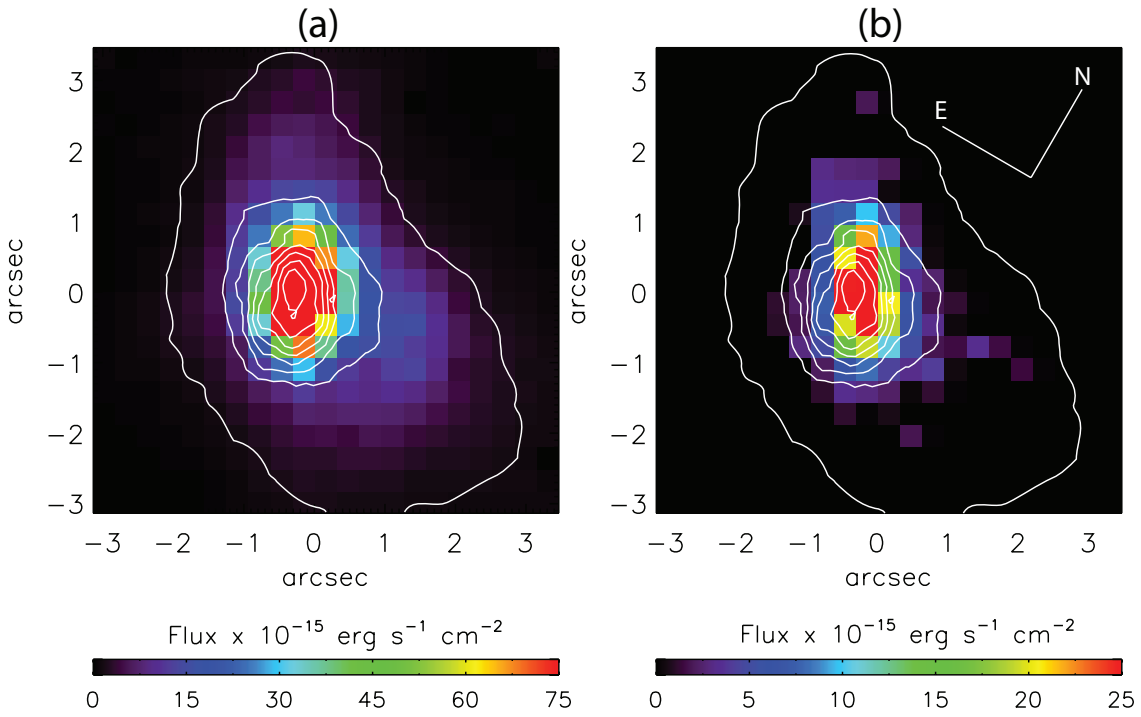

Figure 3.7: [O III] λ5007 emission line maps of Mrk 996 showing the flux distribution per 0.33×0.33 arcsec^2 spaxel: (a) in the narrow C1 component; (b) in the broad C2 component. Overlaid are the Hα narrow component contours (white), as shown in Fig 3.1.

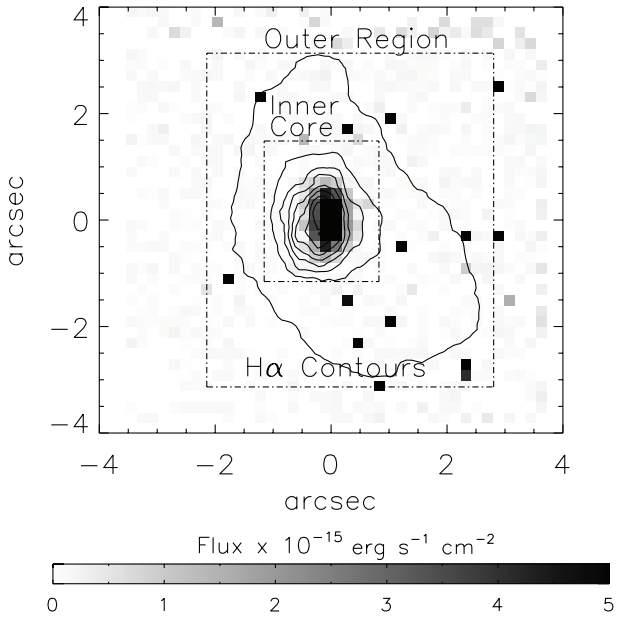

Figure 3.8: Flux distribution of [O III] λ4363 per 0.33×0.33 arcsec^2 spaxel with Hα contours overlaid. The area over which λ4363 is detected is used to define an 'inner core' region, with a surrounding 'outer region' covering the full extent of the Hα emission.

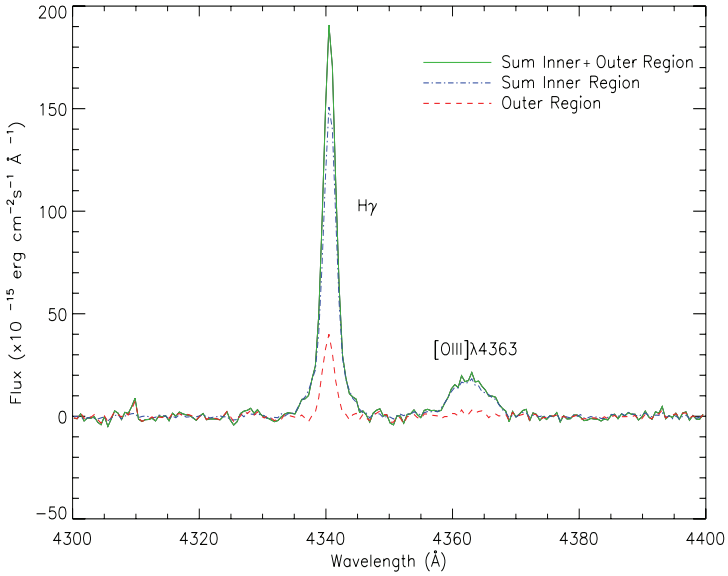

Figure 3.9: Summed spectra from the inner core and the outer region illustrating the lack of detectable [O III] λ4363 in the outer region of Mrk 996.

purpose of this study the λ4363 spectral map (Fig 3.8) is used to define a two-region model of Mrk 996: an 'inner core' region, defined by λ4363 emission extending over an area of 1.7×2.3 arcsec^2 (185×250 pc^2), and an 'outer region' large enough to incorporate almost the full extent of Hα emission over an area of 5.3×6.3 arcsec^2 (575×685 pc^2). The lack of any detectable [O III] λ4363 emission in the outer region is illustrated in Fig 3.9. Here I compare the summed spectrum of the outer region plus core with the summed spectrum of the core region, and also show the residual outer region spectrum. An emission line map of the broad [N II] λ5755 line is shown in Fig 3.10a; its flux distribution correlates strongly with that of the similarly broad λ4363, suggesting that the excitation of these lines is affected by processes that are particular to the inner core region of Mrk 996. In Fig 3.11 the velocity profiles of the broad C2 components of Hα, Hβ and [O III] λ5007 are shown, overlaid in velocity space with the profiles of the [O III] λ4363 and [N II] λ5755. Each spectral line has been summed over the inner core region and all show a FWHM of $\sim$300 kms^{-1}, suggesting that a common excitation mechanism is responsible for the emission of the broad component. The larger widths of [O III] λ4363 and [N II] λ5755 indicate that the physical conditions within the inner core are different from those in the outer region.

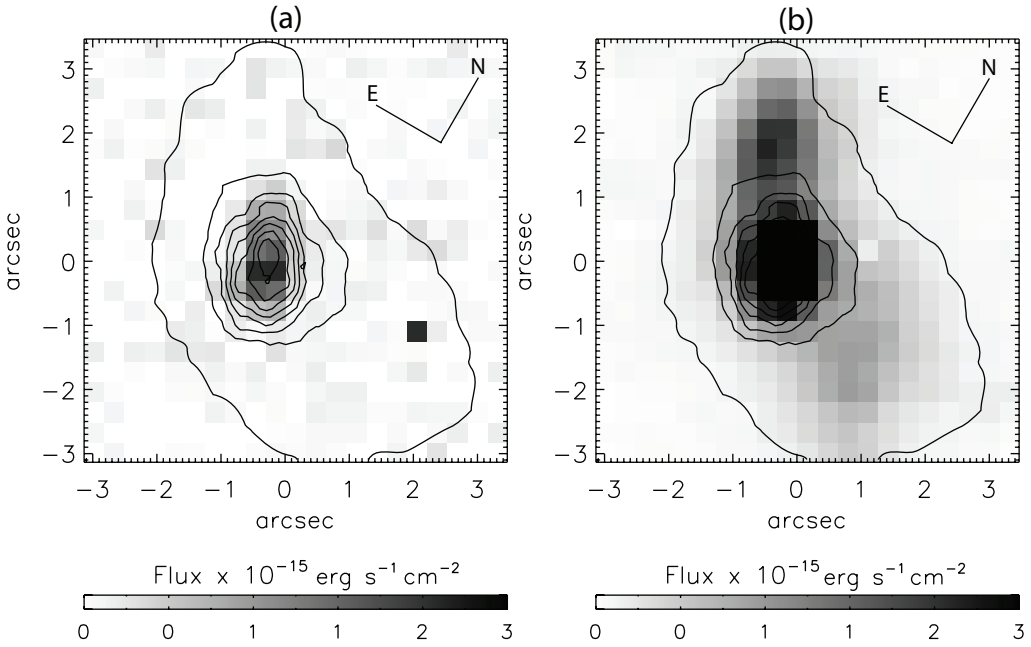

Figure 3.10: Flux distribution per 0.33×0.33 arcsec^2 spaxel of (a) [N II] λ5755 for which only a broad component is detected and which is seen only within the core region; (b) [N II] λ6584, whose flux distribution peaks in the core and towards the north-east; a fainter peak is seen west of the core. Overlaid are the Hα narrow component contours as shown in Fig 3.1.

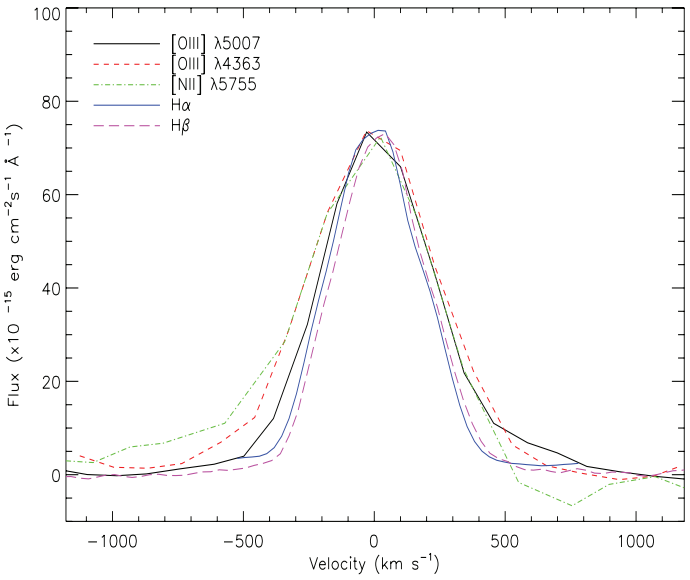

Figure 3.11: Velocity profiles of the broad C2 components of Hα, Hβ, [O III] λ5007, and of [O III] λ4363, [N II] λ5755 emission lines (relative to the heliocentric systemic velocity of +1642 km s^{-1}). Spectra have been summed over the inner core 1.7×2.3 arcsec^2 region of Mrk 996.

3.4 Multi-Component diagnoses: electron temperature and density

The multi-component nature of the emission lines from Mrk 996 must be taken into account when applying plasma diagnostic methods. For example, since [O III] λ4363 is only detected from the central region of Mrk 996 and completely lacks the narrow line component that [O III] $\lambda\lambda$4959, 5007 exhibit (see Fig 3.9), an integrated [O III] (λ5007+λ4959)/λ4363 ratio can not provide a useful temperature diagnostic; this would lead to incorrect results. Previous analyses lacked the spectral and spatial resolution needed to decompose the line profiles and were forced to assume a single density of $N_{\rm e} \sim 10^6$ cm^{-3} in order to match the anomalously low integrated [O III] (λ5007+λ4959)/λ4363 flux ratio (TIL96).

The detection of separate narrow and broad line components opens up the possibility of determining separate electron temperatures and densities and conducting a separate abundance analysis for each.

3.4.1 The Narrow Component Gas

In order to estimate the electron temperature ($T_{\rm e}$) from which the narrow line component C1 emission arises the following method was used. An upper limit to the $T_{\rm e}$ applicable to the H I and [O III] nebular C1 components can be obtained via the simulation of a narrow [O III] λ4363 component using the observed narrow λ5007 component. Predicted λ4363 C1 line intensities were obtained by multiplying the observed λ5007 C1 profile by the theoretical λ4363/λ5007 intensity ratio for a range of $T_{\rm e}$'s at $N_{\rm e} = 170$ cm^{-3}; the latter was measured from the [S II] doublet ratio as described below. It should be noted that the [S II] lines only show narrow C1 components (Table 3.2). The scaling factors were applied to both the inner core and outer region C1 component λ5007 absolute fluxes. Simulated narrow λ4363 profiles of decreasing intensity were then subtracted from the observed λ4363 line until the residual was no longer detectable, as shown for the core region λ4363 profile in Fig 3.12. It is found that a measurable narrow λ4363 C1 component would be detectable at an electron temperature of $>$10,000 K for both the inner core and the outer region. Thus I adopt an upper limit of 10,000 K to the electron temperature of the gas emitting the C1 component throughout Mrk 996. In Section 3.5.2 I argue that this limit is closer to 9200 K, based on the inference that these O/H abundance ratio across the narrow and broad line emitting regions is invariant.

The [S II] $\lambda\lambda$6717, 6731 lines, whose intensity ratio is a common electron density diagnostic for H II regions, show only the narrow emission component and were used to compute density

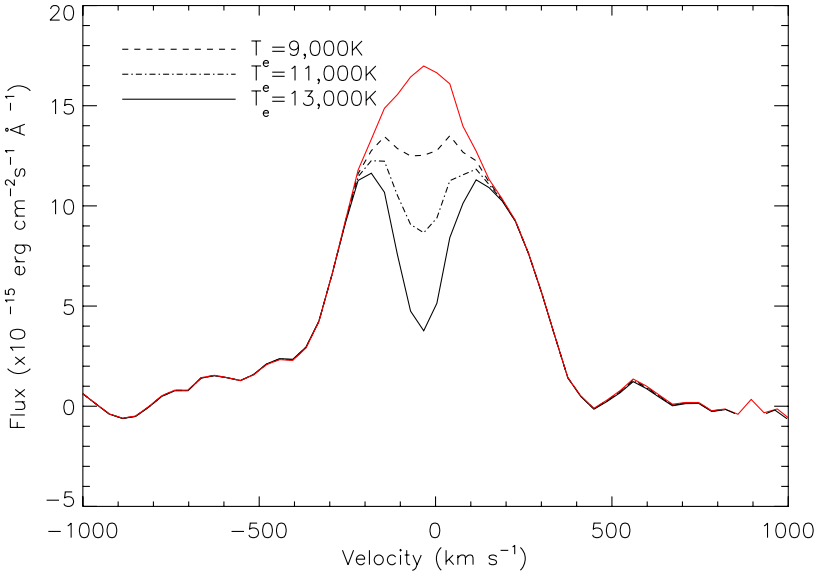

Figure 3.12: Inner core region dereddened [O III] λ4363 profile (solid red curve) with simulated narrow components subtracted from it, corresponding to the dereddened [O III] λ5007 narrow component profile, normalised to the different λ4363 flux levels that correspond to different adopted T_e values. The subtracted narrow component profiles correspond to electron temperatures of 9000 K, 11,000 K and 13,000 K for an electron density of 170 cm^{-3}. An upper limit of 10,000 K is estimated for the $T_{\rm e}$ of the gas emitting the narrow C1 component in the inner core region. See text for details.

Table 3.3: Electron densities derived from the narrow line [S II] λ6716/λ6731 intensity ratios (1.26±0.03 and 1.41±0.03, respectively for the inner core and outer region of Mrk 996).

Adopted $T_{\rm e}$ (K)	$N_{\rm e}$ (cm^{-3}) Core Region	$N_{\rm e}$ (cm^{-3}) Outer Region
9,000	170±40	$10\pm^{30}_{9}$
11,000	170±40	$10\pm^{30}_{9}$
13,000	170±40	$10\pm^{30}_{9}$

values for a range of electron temperatures for the inner and outer regions of the galaxy (Table 3.3, using the IRAF's[2] TEMDEN task of the NEBULA package). These densities are representative of conditions in the gas from which the narrow component emission arises. This propels us to use alternative methods to investigate the density of the gas emitting the broad line components in the inner core region of Mrk 996. With the electron temperature of $T_{\rm e} \leq$ 10,000 K obtained above, I find that electron densities of 170 cm^{-3} and 10 cm^{-3} are representative of the narrow C1 component gas in the inner and outer regions of Mrk 996, respectively.

3.4.2 [Fe III] line diagnostics

[Fe III] emission line ratios provide useful density diagnostics that can trace both high and low electron densities; see Keenan *et al.* (2001). The summed inner region spectrum of Mrk 996 (Fig 3.2) shows a few of the brightest transitions among the 3d^6 levels of Fe III; [Fe III] $\lambda\lambda$4658, 4702, 4881, 4986, and 5270. The flux in these lines above the continuum level was measured by integrating over the line profile. To maximise accuracy, the fluxes for λ4658 and λ4702 were measured after removing any contamination from Wolf-Rayet stellar features by subtracting the WR template fit derived in Section 3.6. Fig 3.13 shows the extinction corrected fluxes of λ4881 and λ5270 relative to λ4658 along with theoretical ratios as a function of $N_{\rm e}$, for $T_{\rm e}$'s between 7,000–20,000 K, from Keenan *et al.* (2001). Interpolating between the theoretical data for an adopted $T_{\rm e}$ of 10,000 K, the λ4881/λ4658 ratio indicates log ($N_{\rm e}$/cm^{-3}) = 5.7 $\pm$ 0.3, which falls within the somewhat larger range of log ($N_{\rm e}$/cm^{-3}) = $6.5^{+0.5}_{-1.5}$ implied by the observed λ5270/λ4658 ratio. These results indicate the presence of a very dense ionised medium throughout the inner core of Mrk 996.

In contrast to the above however, the [Fe III] λ4986/λ4658 ratio is a more sensitive tracer of low electron densities. Fig 3.14 shows that relative to λ4658 the λ4986 line should not be detectable at densities higher than $\sim$1,000 cm^{-3}; the fact that the line is detected from Mrk 996 indicates the presence of a low density gas component as well. This is not inconsistent with the high densities derived above for the inner core as the spatial distribution of λ4986 emission (not shown) contrasts strongly with that of the other [Fe III] lines – rather than peaking in the core of the galaxy, λ4986 is distributed throughout Mrk 996 and is not confined to the inner region defined by the broad [O III] λ4363 emission. There is a clear detection of λ4986 emission over a group of 8 spaxels extending $\sim$1$''$.6 east from the core. The λ4986/λ4658 and λ4702/λ4658 intensity

[2] IRAF is distributed by the National Optical Astronomy Observatory, which is operated by the Association of Universities for Research in Astronomy

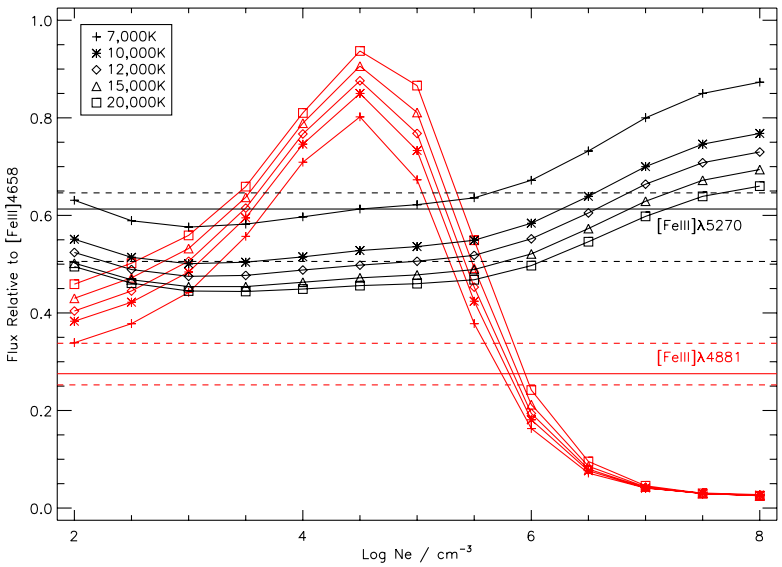

Figure 3.13: Theoretical [Fe III] line flux ratios, for λ4881 (red) and λ5270 (black), relative to λ4658 as a function of electron density for temperatures between 7,000 – 20,000 K. The horizontal lines denote the observed flux ratios (solid) and their uncertainties (dashed) from the summed spectra of the inner core region of Mrk 996.

ratios integrated over these 8 spaxels (Fig 3.14) confirm that this is a low density area ($N_{\rm e}\sim$100–1000 cm^{-3}), typical of normal H II regions. This emission could be tracing lower density ionised gas throughout Mrk 996. In a study of high excitation nebulae in the Magellanic Clouds by Nazé *et al.* (2003), [Fe III] λ4986 was only detected in the shell of the super-bubble surrounding the bright Hα nebula N44C. Due to the large distance of Mrk 996, I am unable to resolve any bubbles surrounding the central super-star cluster even though their presence in the galaxy is likely.

3.4.3 The Broad Component Gas

The [O III] (λ5007+λ4959)/λ4363 intensity ratio can be used to determine the electron temperature of the gas from which the broad component emission arises. Since, however, [O III] λ4363 is only detected as a broad line, this dictates that $T_{\rm e}$ estimates using [O III] can only involve the broad C2 components; moreover these will only be applicable to the inner core region of the galaxy where λ4363 is detected. The FWHMs of components C2 in $\lambda\lambda$4959, 5007 are very similar to that of λ4363, all being in the range of 320–515 kms^{-1} across the inner core region; their surface brightness distributions are also similar. Also in support of the suitability of the [O III] ratio involv-

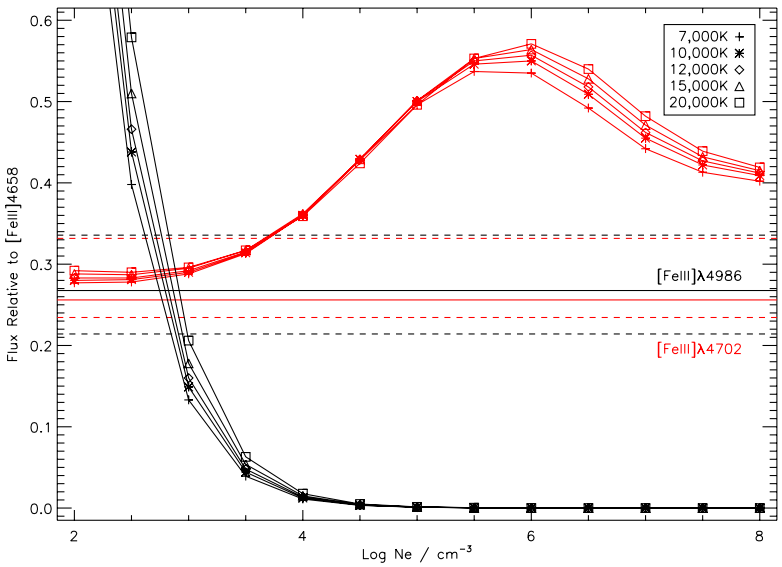

Figure 3.14: Theoretical [Fe III] line flux ratios, for λ4986 (black) and λ4207 (red), relative to λ4658 (in the region in which λ4986 is seen), relative to λ4658 as a function of electron density for temperatures between 7,000–20,000 K. The horizontal lines denote the observed flux ratios (solid) and their uncertainties (dashed) from the summed spectra of the region where λ4986 is detected.

ing the C2 components is that I do not find any indication of C3 or C4 components in the highest S/N emission line profiles of $\lambda\lambda$4959, 5007 (see Fig 3.3(f) for an optimised two-component fit to the λ5007 emission line from the inner core region). Even so, electron temperatures derived using only the broad line components are un-physically high (>30,000 K) until densities higher than $N_{\rm e}$ = 10^6 cm^{-3} are adopted.

I can attempt to constrain the electron temperature and density of the broad line component by using the λ1663/λ4363 and λ5007/λ4363 intensity ratios, which due to their considerably different O^{2+} upper level excitation energies can act as sensitive temperature and density diagnostics between the critical densities of each of these lines. The FOS UV spectra presented by TIL96 revealed a weak O III] λ1663 line detection which, due to its high excitation energy ought to originate from the same gas emitting the broad [O III] λ4363 that we detect. Using a simulated FOS aperture on my broad component flux maps for λ5007 and λ4363, fluxes of 39.6$\pm$6.3$\times10^{-15}$ ergs cm^{-2} s^{-1} for λ4363 and 214.1$\pm$14.2$\times10^{-15}$ ergs cm^{-2} s^{-1} for λ5007 are predicted to fall within the small FOS aperture centred on the nucleus of Mrk 996. Together with the λ1663

flux of $1.9^{+0.4}_{-0.2}\times10^{-15}$ ergs cm^{-2} s^{-1} measured from the FOS spectrum, these fluxes were then dereddened using an average c(Hβ) of 0.65 for a simulated FOS aperture on the broad component VIMOS c(Hβ) map, to yield λ4363/λ1663 and λ5007/λ4363 intensity ratios of 2.4 and 4.3, respectively. The theoretical λ4363/λ1663 and λ5007/λ4363 ratios for log($N_{\rm e}$) = 5.0–10.0 and $T_{\rm e}$ = 5,000–30,000 K are presented in Fig 3.15a, b and the resultant set of solutions are shown in Fig 3.15c. The two curves in Fig 3.15c overlap between log($N_{\rm e}$) = 6.5–8.5 and $T_{\rm e}$ = 7,000–14,000 K. I thus adopt $T_{\rm e}$ = 10,500 $\pm$ 3,500 K and log($N_{\rm e}$/cm^{-3}) = $7.25^{+1.25}_{-0.75}$ for the broad component emitting gas. The inferred density range is somewhat higher than the value derived from the [Fe III] λ4881/λ4658 ratio (Section 3.4.2) and supports the conclusion that the central regions of Mrk 996 contain very dense zones of ionised gas.

3.5 Chemical Abundances

3.5.1 Narrow Component Abundances

Abundance maps relative to H^+ were created for the N^+, O^+, O^{2+}, S^+, S^{2+}, Ar^{2+} ions, using the narrow $\lambda\lambda$6584, 7320+7330, 5007, 6717+6730, 6312, and 7136-Å lines respectively (via the ABUND task in IRAF). Each VIMOS spaxel was treated as a distinct 'nebular zone' with its own set of physical conditions. Ionic argon and sulphur abundance ratios were converted to total Ar/H and S/H using an ICF(Ar) = 1.87 and ICF(S) = 1.03 respectively (Kingsburgh & Barlow 1994). Very small changes were found by adopting the ICF prescriptions of Izotov et al. (2006). Since $T_{\rm e}$ maps are unattainable for the narrow component gas, we have adopted the upper limit of $T_{\rm e}$ = 10,000 K applicable throughout Mrk 996 (Section 3.4.1), together with the mean electron densities derived from the [S II] doublet ratios, of 170 cm^{-3} and 10 cm^{-3} for the inner core and outer region, respectively (Table 3.3). It is emphasised that since the adopted $T_{\rm e}$ for the narrow component gas is an upper limit, the abundances derived here are necessarily lower limits.

In Fig 3.16 abundance distributions are shown in the directions from north-east to south-west and south-east to north-west that pass through the centre of Mrk 996 (i.e. in the X and Y directions across the abundance maps, respectively, produced by averaging over a three spaxel-wide pseudo-slit). The variations in the abundances of O^{2+} and O^+ in Fig 3.16 mirror each other in their distribution. As expected, the more highly ionised species is dominant in the core region, where the UV radiation is expected to be harder. It should further be noted that these abundance trends are only correct if the temperature is constant throughout the gas emitting the narrow line component.

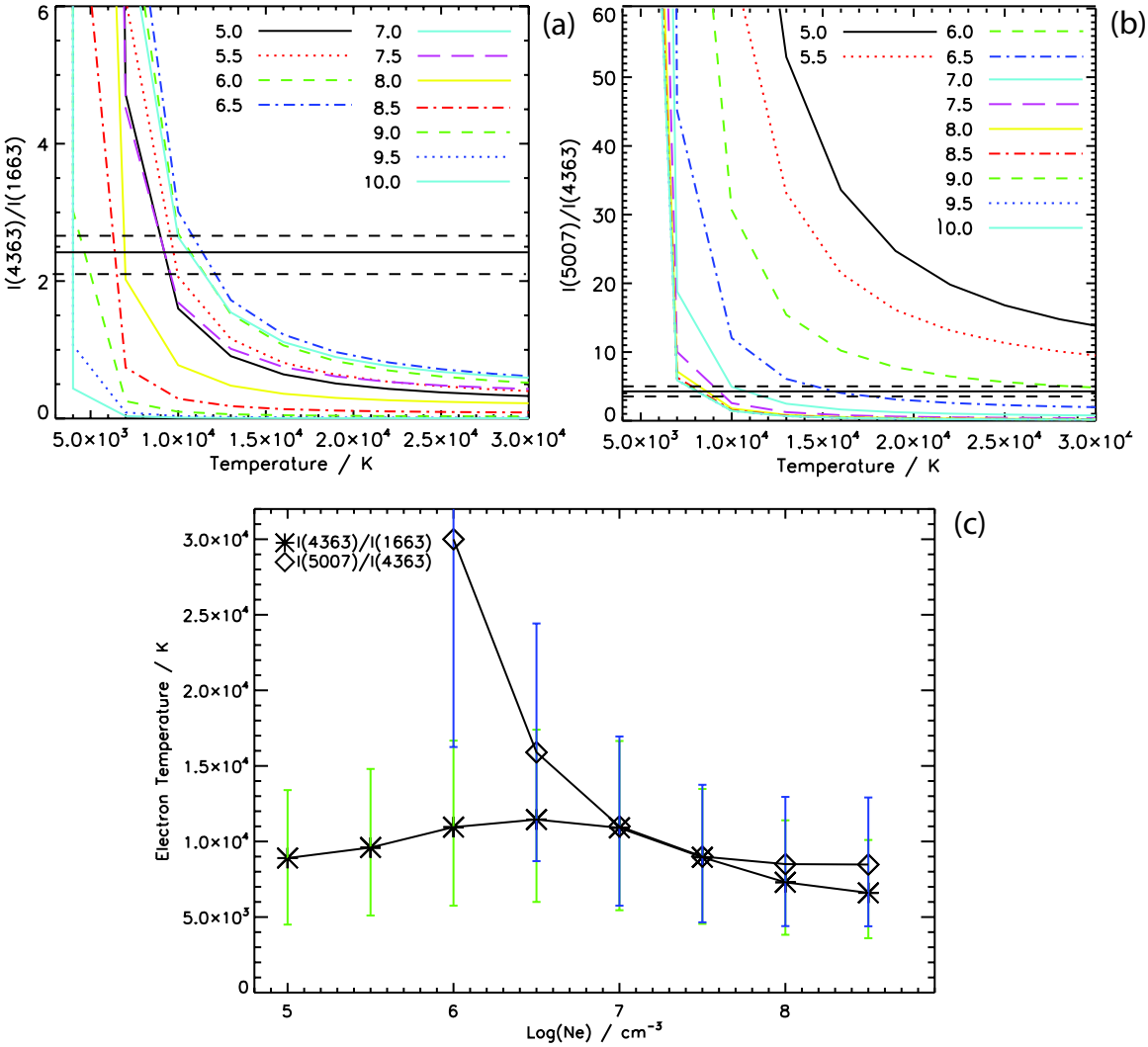

Figure 3.15: Broad component $T_{\rm e}$ and $N_{\rm e}$ diagnostic diagrams for (a) $I(\lambda4363)/I(\lambda1663)$, and (b) $I(\lambda5007)/I(\lambda4363)$, showing theoretical ratios for $T_{\rm e}$ = 5,000–30,000 K and $\log(N_{\rm e}/{\rm cm}^{-3})$ = 5.0–10.0. The horizontal solid lines in (a) and (b) denote the observed dereddened ratios and their uncertainties (dashed); (c) shows the ($T_{\rm e}$, $N_{\rm e}$) solutions applicable to Mrk 996 obtained from (a) and (b) and their uncertainties.

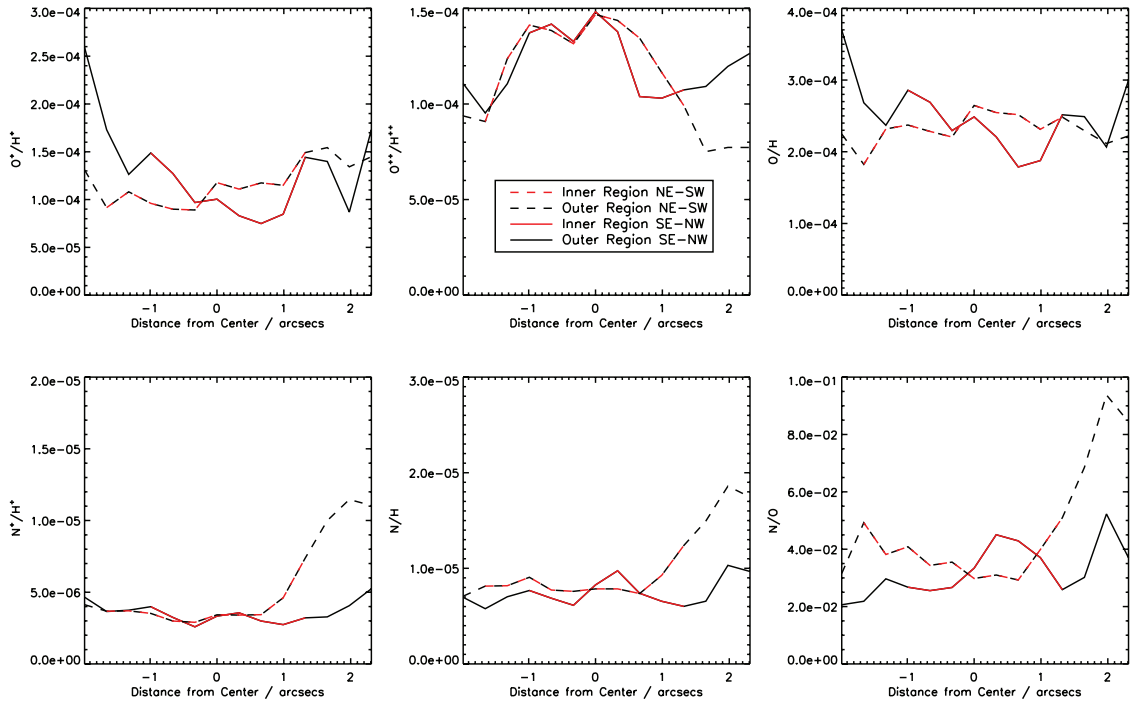

Figure 3.16: Spatial variations in narrow component ionic and elemental abundances across Mrk 996 obtained for $T_{\rm e}$ = 10,000 K and $N_{\rm e}$ = 170 cm^{-3}. The available $T_{\rm e}$ is an upper limit so the abundances shown are lower limits. The patterns should persist if $T_{\rm e}$ is constant across the emitting region. Three spaxel-wide averages were made across the IFU aperture in its X and Y directions, corresponding to south-east to north-west and north-east to south-west, respectively.

The O/H elemental ratio was derived by summing the O^+ and O^{2+} ionic abundance maps. Adopting a solar oxygen abundance of 4.9×10^{-4} relative to hydrogen (Allende Prieto *et al.* 2001), I find that Mrk 996 has an oxygen abundance of $\geq$0.50 solar throughout the inner core region and beyond. This is a significantly higher metallicity than the $\sim$0.2 solar derived previously by TIL96, which can be attributed to the high electron temperature of 15,000 K that they employed, based on CLOUDY models.

An N/H abundance ratio map (Fig 3.17) was created using an ionisation correction factor, ICF(N) = (O^++O^{2+})/O^+ (Kingsburgh & Barlow 1994). Again, very small changes were found by adopting the ICF prescriptions of Izotov *et al.* (2006). For a constant electron temperature, the N/H ratio, shown in Fig 3.17, remains constant throughout the core at $\geq 0.8 \times 10^{-5}$ but shows a two-fold increase north-east of the core region of Mrk 996. A cut across the N/O ratio map of Mrk 996, which is much less sensitive to the adopted electron temperature than either O/H or N/H, shows a similar trend, with log(N/O) $\simeq -1.5$ in the core, rising to $\simeq -1.2$ at a spot north-east of

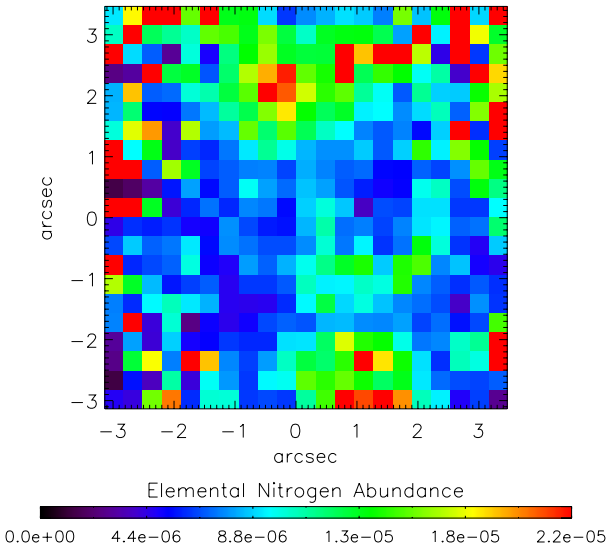

Figure 3.17: N/H abundance ratio map based on the narrow component emission across the region where [N II] λ6584 is seen. It should be noted that these abundances are lower limits since an upper limit to $T_{\rm e}$ was used for the calculation.

the core (Fig 3.16).

The mean abundances are listed in Table 5. For the revised oxygen metallicity of Mrk 996 the derived N/O, S/O and Ar/O ratios fall within the expected range for BCDs (e.g. Izotov *et al.* 2006).

3.5.2 Broad component abundances

In order to derive nitrogen elemental abundance for the broad component gas, we correct for the presence of N^{2+} using the N III] λ1750 line detected by *HST* FOS. This high excitation energy UV line was not used to correct the narrow emission component nitrogen abundances because it ought to originate from the high excitation gas responsible for the *broad* line emission. Table 3.4 lists the ionic abundances derived for the broad line emission gas derived from optical and UV lines. Fluxes are quoted relative to the broad Hβ flux within the simulated FOS aperture and are corrected for extinction using the average c(Hβ) value within that aperture in the reddening map derived from the broad components of Hα/Hβ, Hγ/Hβ ratios. The physical conditions adopted for these calculations are those derived from the broad component emission, i.e. $T_{\rm e} = 10{,}000 \pm 3{,}500$ K and $\log(N_{\rm e}/{\rm cm}^{-3}) = 7.25\ ^{+1.25}_{-0.75}$. I consider that the highest allowed $T_{\rm e}$ is 11,000 K with $\log(N_{\rm e}/{\rm cm}^{-3})$ = 7.00 being the lowest allowed density, based on Fig 3.15c. This latter density is consistent with

Table 3.4: Intensities of UV emission lines from *HST* FOS spectra and their optical broad component counterparts, measured within a FOS aperture superimposed on my broad component flux maps. All intensities are given relative to the broad component $F(\mathrm{H}\beta) = 122.1 \pm 11.1 \times 10^{-15}$ erg s^{-1} cm^{-2} within the simulated aperture.

			Abundance $\times 10^4$		
		T_e / K	9,000	10,000	11,000
		log(N_e/cm^{-3})	7.50	7.25	7.00
Line	100×I(λ)/I(Hβ)	Species			
5755 [N II]	7.1±1.9	N^+/H^+	1.9±0.5	0.9±0.2	0.4±0.1
1750 N III]	19.2±6.8	N^{2+}/H^+	7.5±2.6	3.0±1.1	1.3±0.5
		N/H	9.4±1.3	3.8±1.7	1.7±0.8
5007 [O III]	51.3±6.2	O^{2+}/H^+	12.6±1.5	4.8±0.6	2.0±0.2
		O/H	15.7±7.5	5.5±2.6	2.3±1.1

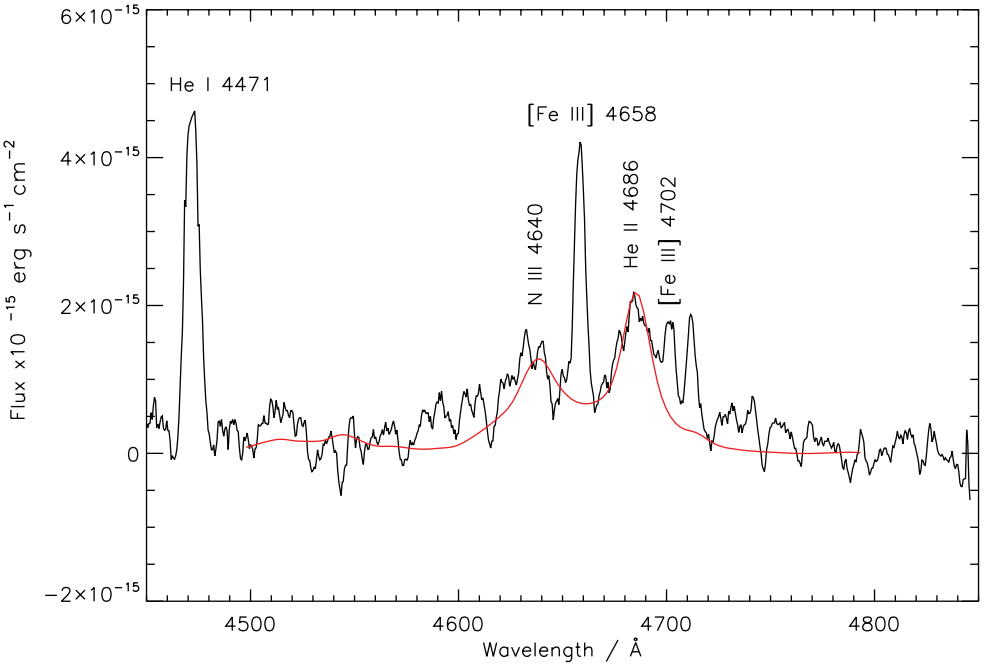

Figure 3.18: WR 'blue bump' feature summed over the inner core of Mrk 996. Overplotted is the combined fit for 2600 WNL stars and 400 WC stars, using the templates of Crowther & Hadfield (2006).

the upper density limit inferred from the [Fe III] diagnostics. For $T_{\rm e} = 11{,}000$ K and $\log(N_{\rm e}/{\rm cm}^{-3}) = 7.00$ the resulting broad-line O/H abundance ratio of 2.3×10^{-4} is consistent with being the same as for the narrow line emission regions (cf. Tables 3.4 and 3.5). As a consistency check, I determined the $T_{\rm e}$ for the narrow component VIMOS [O III] λ5007 and Hβ fluxes falling within the FOS aperture that would be required to match the above broad-line O/H ratio. This yielded a temperature of $\sim$9,200 K, reinforcing the upper limit of 10,000 K derived in Section 3.4.1 for the C1 emission. S/H abundances were computed using the [S III] λ6312 line and an estimated (minor) contribution from S^+/H^+ (in parentheses in Table 5) using equation A38 of Kingsburgh & Barlow (1994). Ar/H abundance ratios were derived using the [Ar III] λ7136 line with ICF(Ar)=1.87 as previously. The adopted mean values are listed in Table 5.

In contrast to the apparent lack of significant variation in the abundances of oxygen, sulphur, and argon between the two velocity components, it appears that the N/O ratio in the broad line region is enriched by a factor of $\sim$20 relative to the narrow line region, with the broad line region having $\log({\rm N/O}) \sim -0.13$. I conclude that the observations are consistent with the narrow and broad line regions both having an O/H ratio of $\geq$0.5 solar.

3.5.3 Elemental Helium Abundance

Narrow and broad component He^+/H^+ abundance maps were derived from He I λ5876 C1 and C2 maps. Abundances were calculated using the Case B He I emissivities of Porter *et al.* (2005) at the respective $T_{\rm e}$ and $N_{\rm e}$ of the broad and narrow emission components. Since these are only valid up to $\log(N_{\rm e}/{\rm cm}^{-3}) = 6$, a correction factor of 0.9543 was applied to the broad component emissivity to extrapolate up to $\log(N_{\rm e}/{\rm cm}^{-3}) = 7.25$. At these densities, collisional excitation from the He^0 $2s^3S$ metastable level by electron impacts contributes to the observed broad He I λ5876 component; this effect is accounted for by Porter *et al.* (2005). Fig 3.19 shows X and Y direction cuts across the broad and narrow component elemental He/H maps. I have assumed that the He^{2+}/H^+ fraction is negligible. Good agreement between the spatial variations in the He/H abundance for each component is observed. No relative He/H enrichment is seen across the components; within the uncertainties both fall between the pre-galactic He/H ratio of 0.08 (Luridiana *et al.* 2003) and the solar ratio 0.10 (Lodders 2003). This contrasts with the localised N/H enrichment north-east from the nucleus that spatially correlates with a peak in EW(Hβ) (see Section 3.6). The slight decrease in He/H in the core region might be attributable to the presence of He^{2+}. I find this unlikely, however, since no nebular He II λ4686 emission has been detected (none was reported in the recent study by Thuan *et al.* (2008)), and in addition, other similarly high

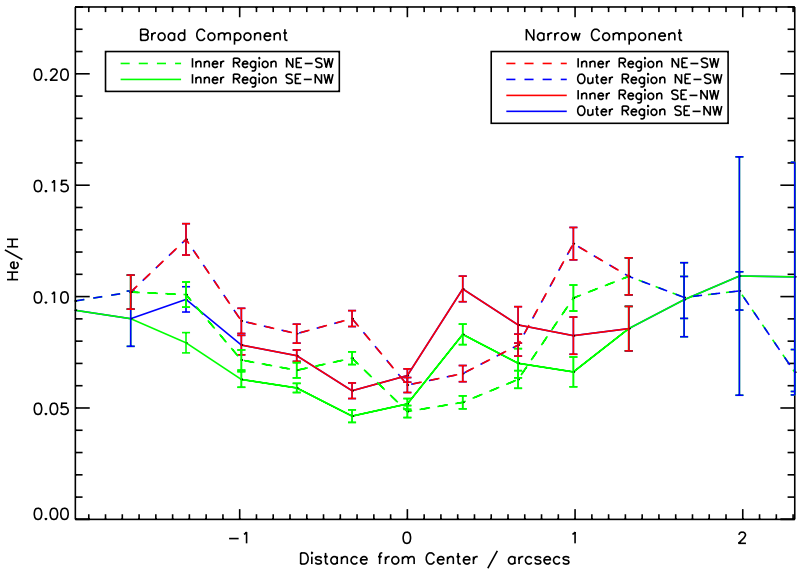

Figure 3.19: Spatial variations in the narrow (blue and red) and broad (green) component He/H elemental abundance across Mrk 996. Three spaxel-wide averages were made across the IFU aperture in its X and Y directions, corresponding to the south-east to north-west and north-east to south-west, respectively.

excitation lines such as [Ar IV] are not present in the spectrum of the galaxy. The derived He/H abundances at the centre of Mrk 996 agree well with those of TIL96 who calculated $He^+/H^+ \sim 0.09$ from the He I λ5876 emission within their FOS aperture.

Table 3.5 summarises the derived abundance for the narrow and broad line emission regions of the galaxy.

3.6 Wolf-Rayet Stars and Stellar Age

Wolf-Rayet (WR) features were identified in Mrk 996 by TIL96 in their single aperture FOS spectroscopy of a 0.″86 region at the centre of Mrk 996. The VIMOS IFU spectra also show a broad Wolf-Rayet (WR) stellar feature at 4650 Å, attributable to a mixture of late-type WN (WNL) and WC stars at He II λ4686 and N III λ4640 (with an additional weak WC stellar C IV feature at 5808 Å). The WR spectral signatures are seen to extend throughout the core region of Mrk 996 and show excellent agreement with the spatial extent of the broad [O III] λ4363 emission (Fig 3.8). A map of the 4650 Å WR feature is shown in Fig 3.20; this has been decontaminated from the emission by nebular [Fe III] λ4658 by fitting a Gaussian profile to the line and subtracting its flux

Table 3.5: Adopted abundances for the narrow (C1) and broad (C2) component emission regions throughout Mrk 996.

	C1	C2
Adopted $T_{\rm e}$ (K)	10,000[a]	11,000
Adopted $N_{\rm e}$ (cm^{-3})	170	10^7
He/H	0.091±0.017	0.072±0.018
$N^+/H^+ \times 10^5$	0.46±0.18	4.1±1.1
$N^{2+}/H^+ \times 10^4$	–	1.3±0.5
N/H $\times 10^5$	0.89±0.25	17.0±7.6[b]
$O^+/H^+ \times 10^4$	1.3±0.4	–
$O^{2+}/H^+ \times 10^4$	1.1± 0.2	2.0±0.2
O/H $\times 10^4$	2.4±0.4	2.3±1.1[b]
$S^+/H^+ \times 10^7$	10.3±1.8	(9.7±1.8)
$S^{2+}/H^+ \times 10^6$	4.7±0.9	5.4±1.3
S/H $\times 10^6$	5.9±1.6	6.6±1.6
$Ar^{2+}/H^+ \times 10^7$	8.19±1.8	12.0±2.8
Ar/H $\times 10^6$	1.5± 0.3	2.2± 0.5
log N/O	−1.43	−0.13
log S/O	−1.61	−1.54
log Ar/O	−2.20	−2.02

[a] Upper limit adopted $T_{\rm e}$ so that C1 abundances are lower limits.

[b] Applicable to a central 0.″86 (FOS) aperture; see the text for details.

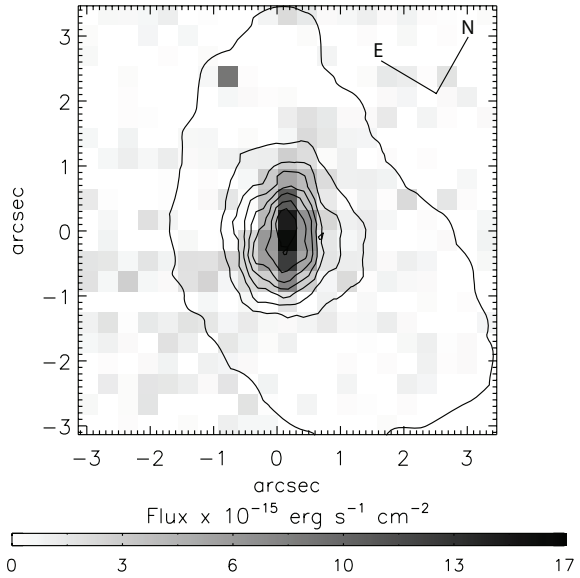

Figure 3.20: Emission map of the blue WR feature (created by integrating over the full emission feature and removing contaminant flux from [Fe III] λ4658), showing the distribution of WR stars in the inner core region of Mrk 996. Overlaid are the Hα narrow component flux contours from Fig 3.1.

from the integrated flux of the 4650 Å feature. After summing the spectra over the core region, LMC WR spectral templates from Crowther & Hadfield (2006) were used to fit both spectral features. Although the WC feature is weak, its contribution is essential in fitting the broad wings of the 4650 Å feature. At the distance of Mrk 996 (22 Mpc) the two WR features indicate the presence of $\sim$2600 WNL stars and $\sim$400 WC stars. Assuming a similar depth for the area over which these spectral features are summed, 1.7$\times$2.3 arcsec^2 (4.6$\times10^4$ pc^2), results in a volume density of 3×10^{-4} WR stars per pc^3 in the core region.

I can compare the WR number estimates with those of TIL96, who estimated that 600 late-type WN stars and 74 WC stars were responsible for the WR emission seen within their 0.″86 diameter FOS aperture. Scaling my own core region WR number estimates for the difference in aperture size would predict 390 WNL stars and 60 WC stars within the FOS aperture. While the agreement between the two estimates is quite good, the decrease in WNL star numbers for my scaled estimate can be attributed to the non uniform density of WR stars in the core region (see Fig 3.20). In contrast, the WC 5808 Å feature is very centrally peaked, thus giving a good agreement between the two estimates.

Luminosities of hydrogen recombination lines, particularly Hβ, can provide estimates of the ionizing flux present, assuming a radiation-bounded nebula (Schaerer & Vacca 1998). Thus, the

equivalent width (EW) of Hβ is commonly used as a stellar age indicator at a given metallicity. A map of EW(Hβ) across Mrk 996 (derived from integrating over the full emission line profile) is shown in Fig 3.21 and displays a surprising morphology compared to the central location of the ionizing sources in Mrk 996. A peak is seen directly NE of the centre of the galaxy, which correlates well with the peak in [N II] λ6584 emission shown in Fig 3.17. I can use the EW(Hβ) map, in conjunction with the metallicity map (described in Section 3.5.1), to estimate the distribution of stellar ages throughout Mrk 996. I find that the core region EW(Hβ) corresponds to a stellar age of 4.5 Myr whereas the EW(Hβ) peak NE of the core corresponds to a slightly younger stellar age of $\sim$3 Myr (cf. fig 7 of Schaerer & Vacca 1998); these ages are sufficiently long to allow for the presence of WR stars in the galaxy.

An estimation of the number of O-type stars was made, assuming that all ionizing photons, $Q_0^{\rm obs}$, are produced by O and WR stars and utilising the Hβ luminosity, L(Hβ), integrated over the whole galaxy (i.e. using the dereddened combined C1 and C2 Hβ flux from the inner and outer regions, and at a distance of 22.3 Mpc). The absolute number of O stars was derived using (e.g. Fernandes *et al.* (2004))

$$N_{\rm O} = N_{\rm OV} = \frac{Q_0^{\rm obs} - N_{\rm WR} Q_{\rm WR}}{\eta_0(t) Q_{\rm O7V}}, \tag{3.1}$$

where $Q_0^{\rm obs}$ is the emission rate of ionising photons, as derived from L(Hβ), and $Q_{\rm WR}$, $Q_{\rm O7V}$ are the emission rates of ionizing photons by WR stars and O7V stars, respectively, with $N_{\rm WR}$ being the total number of WR stars. $\eta_0(t)$ is a conversion parameter for the proportion of O7V stars relative to all OV stars and is estimated as being $\geq$0.2 by Schaerer & Vacca (1998) at the metallicity of Mrk 996 ($\sim$0.5 $Z_\odot$). Adopting $\eta_0(t)$ =0.2, $Q_{\rm WR} = Q_{\rm O7V} = 1.0 \times 10^{49}$ s^{-1} (Schaerer *et al.* 1999*a*), and $Q_0^{\rm obs}$(C1+C2)=3.36$\times$10^{53} photons s^{-1} I find $N_{\rm O} \lesssim$ 153,000 yielding $N_{\rm WR}/N_{\rm OV} \gtrsim 0.02$. As a lower limit, this ratio is in good agreement with those predicted by evolutionary synthesis models by previous studies; at the predicted age of $<$5 Myr for the Mrk 996 starburst, Cerviño & Mas-Hesse (1994) find that this $N_{\rm WR}/N_{\rm OV}$ fraction is typical at metallicities of 0.4 $Z_\odot$, while Schaerer & Vacca (1998) predict $N_{\rm WR}/(N_{\rm WR} + N_{\rm O}) = 0.04$ for a metallicity of 0.25 $Z_\odot$.

Using the Hα–SFR (star formation rate) relation of Kennicutt (1998) and the total Hα luminosity (C1+C2) of 4.83 $\times$10^{41} erg s^{-1} I obtain a global current SFR of 3.8 M$_\odot$ yr^{-1}. Taking into account the subsolar metallicity of Mrk 996 this can be reduced to 2.7 M$_\odot$ yr^{-1} (Lee *et al.* 2002). However, in the event that the C2 component emission is partly attributable to shock-excited gas

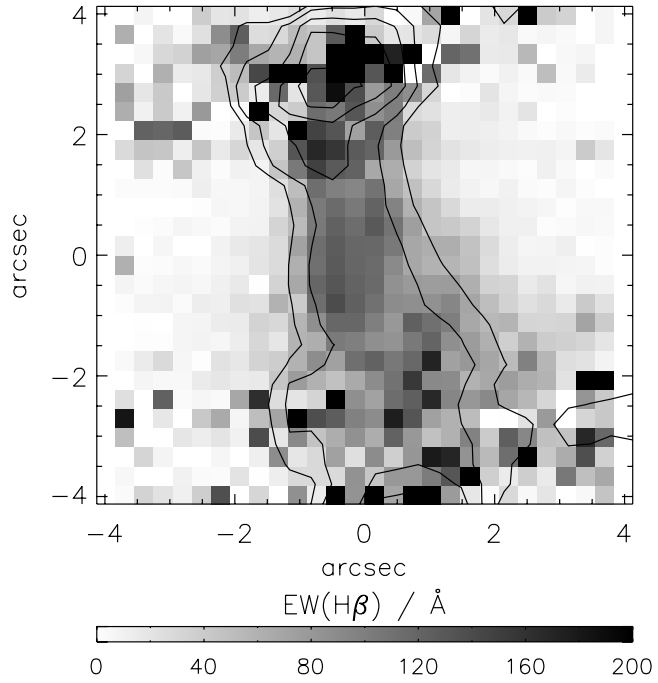

Figure 3.21: Map of the equivalent width of Hβ across Mrk 996, derived from the full emission line profile. Contours range from 70–180 Å in steps of 30 Å.

(see Section 3.7.1) so that it cannot be included in the estimate of $Q_0^{\rm obs}$, a SFR lower limit of $1.3\,{\rm M}_\odot\ {\rm yr}^{-1}$ is derived based on $\log({\rm Q}_0({\rm C1}) = 1.31\times10^{52}$ photons s^{-1} alone.

3.7 Discussion

3.7.1 Diagnosing the ionisation mechanisms

In order to gain insight into the mechanisms responsible for the multi-component line emission from Mrk 996, I made use of the classic diagnostic diagrams of Baldwin *et al.* (1981) (the BPT diagrams). These are employed to classify galaxies according to the dominant excitation mechanism of their emission lines, i.e. either photoionisation by massive stars within H II regions or photoionisation by non-thermal continua from active galactic nuclei (AGN). The diagrams consist of excitation-dependent, extinction-independent line ratios: log([O III] λ5007/Hβ) versus either log([N II] λ6584/Hα) or log([S II](λ6716,31)/Hα). Star-forming galaxies fall into the lower left region of the diagram, AGN host galaxies fall into the upper right region and Low-ionisation Emission Line Regions (LINERs) fall in the lower right region. The separation is not as clear, however,

for low metallicity AGNs (see e.g. Stasińska *et al.* (2006)), only a handful of which have been proposed to exist thus far (Izotov & Thuan 2008).

Kewley *et al.* (2001) calculated the first starburst grids that attempted to match optical diagnostic diagrams based on purely empirical data, by coupling the MAPPINGS III photoionisation code and STARBURST99 population synthesis models. Whereas previous semi-empirical studies involved only solar-metallicity calculations, their line ratios were computed for a range of metallicities (Z = 0.05–3.0 $Z_{\odot}$) and ionisation parameters ($q = 5 \times 10^6$–3×10^8 cm s^{-1}), where q is the maximum velocity of an ionisation front that can be driven by the local radiation field and is related to the non-dimensional ionisation parameter $U = q$/c, (Dopita *et al.* 2001). Utilizing these grids, Kewley *et al.* (2001) determined a 'maximum starburst line' (shown in Fig 3.22), above which the flux ratios of an object cannot be fitted by pure starburst models alone. Ratios lying above this photoionisation boundary require additional sources of excitation such as shocks or AGNs. As mentioned above, this picture has recently been revised and it is now believed that low-Z AGNs, should they exist, would occupy similar regions on the BPT diagram as normal H II galaxies; based on an analysis of a large sample of Sloan Digital Sky Survey galaxies, Stasińska *et al.* (2006) have found that composite AGN/H II region models with $Z < 0.4\ Z_{\odot}$ lie very close to and below the pure H II region sequence, whereas when considering also the regime of $Z > 0.6\ Z_{\odot}$ they established that the locus below the Kewley *et al.* (2001) line allows for an AGN-excited gas component of up to 20 per cent.

It is therefore instructive to see what area of the BPT diagram Mrk 996 occupies. Kewley *et al.* (2001) found that since the [S II](6716,31)/Hα ratio is affected by the density of the line emitting region and it is therefore less accurate as a diagnostic. Hence considering the large density difference between the narrow and broad component gas within Mrk 996 I only considered the [O III] λ5007/Hβ vs. [N II] λ6584/Hα ratios (Fig 3.22). Since no broad component is detected for [N II] λ6584 I have not been able to create separate broad and narrow diagnostic diagrams and instead present (i) a narrow component diagram (Fig 3.22 top panel), and (ii) ratios derived from the entire emission line profiles (i.e. integrated over broad and narrow component emission, where both exist; Fig 3.22 bottom panel). Spaxels corresponding to the core region of the galaxy are shown as red crosses, with outer region spaxels plotted as green crosses. Also shown is the maximum starburst line of Kewley *et al.* (2001).

The data points for the outer narrow line region of Mrk 996 mostly straddle the 'theoretical' upper limit for pure photoionisation. Based on the Kewley *et al.* (2001) grids, the flux ratios lie within a metallicity range of Z = 0.3–0.5 and along and above an ionisation parameter track for

$q = 3{\times}10^8$ (the maximum ionisation parameter computed). The narrow component emission in the core region occupies the top left of the distribution, which corresponds to a higher ionisation parameter and lower metallicity in the starburst grids, while a significant number of data points fall outside the SFG (star-forming galaxies) area of the plot. When the broad component is included in the diagnostics, the location of the outer region spaxels move to the left, whereas the core region spaxels move downwards and to the left for both ratios to occupy a lower ionisation parameter and metallicity region. This is most likely due to the suppression of the [O III] λ5007 broad component emission within the high density core region, which would lower the combined narrow plus broad [O III] λ5007/Hβ ratio.

As previously mentioned, exceeding the 'maximum starburst' line can also be indicative of a contribution to the ionisation by fast shocks. However, the amount by which this line can be crossed before shocks must be a substantial source of ionisation has not been established thus far. Similar diagrams were created by Calzetti *et al.* (2004) for four starburst (SB) galaxies using ratios from *HST* WFPC2 images, such as [O III] λ5007/Hβ vs. [S II] λ6716,31/Hα. They found that a number of regions in the SB galaxies lay above the maximum starburst line and as a result defined regions of non-stellar excitation as either lying above and to the right of it or where the [S II]/Hα ratio is high enough to be compatible with non-stellar sources, i.e. [S II]/H$\alpha > 0.7$–0.9 (Veilleux & Osterbrock 1987; Shull & McKee 1979). The log([S II] λ6716,31/Hα) ratio is traditionally used as a diagnostic for shock-excited gas because shock models predict that relatively cool high-density regions should form behind the shock front and emit strongly in [S II] (Dopita 1978). The [S II]/Hα flux ratios for the narrow component emission across Mrk 996 lie between 0.03–$6{\times}10^{-4}$, well below the high [S II]/Hα ratios predicted for shocks. On the other hand, Thuan *et al.* (2008) employed a model with shocks at a velocity of 250 km s^{-1} that reproduced the observed intensity of the high-ionisation potential [O IV] 25.9 μm line detected in the *Spitzer* spectrum of Mrk 996. In conclusion, Fig 3.22 by itself cannot provide firm evidence for or against the presence of AGN activity within Mrk 996 given the galaxy's rather low metallicity status, even though the integrated broad component Hα luminosity of $2.5{\times}10^{41}$ erg s^{-1} this at the lower limit of those measured from rare low-Z BCDs suspected of harbouring active galactic nuclei ($3{\times}10^{41}$ – $2{\times}10^{42}$ erg s^{-1} Izotov & Thuan 2008). Although photoionisation appears to be the dominant excitation mechanism, I cannot rule out a contribution from shocks, particularly with respect to the broad component emission. I draw attention to the significant bias inherent in BPT diagrams of galaxies whose analysis does not involve a separate consideration of narrow/broad line diagnostics.

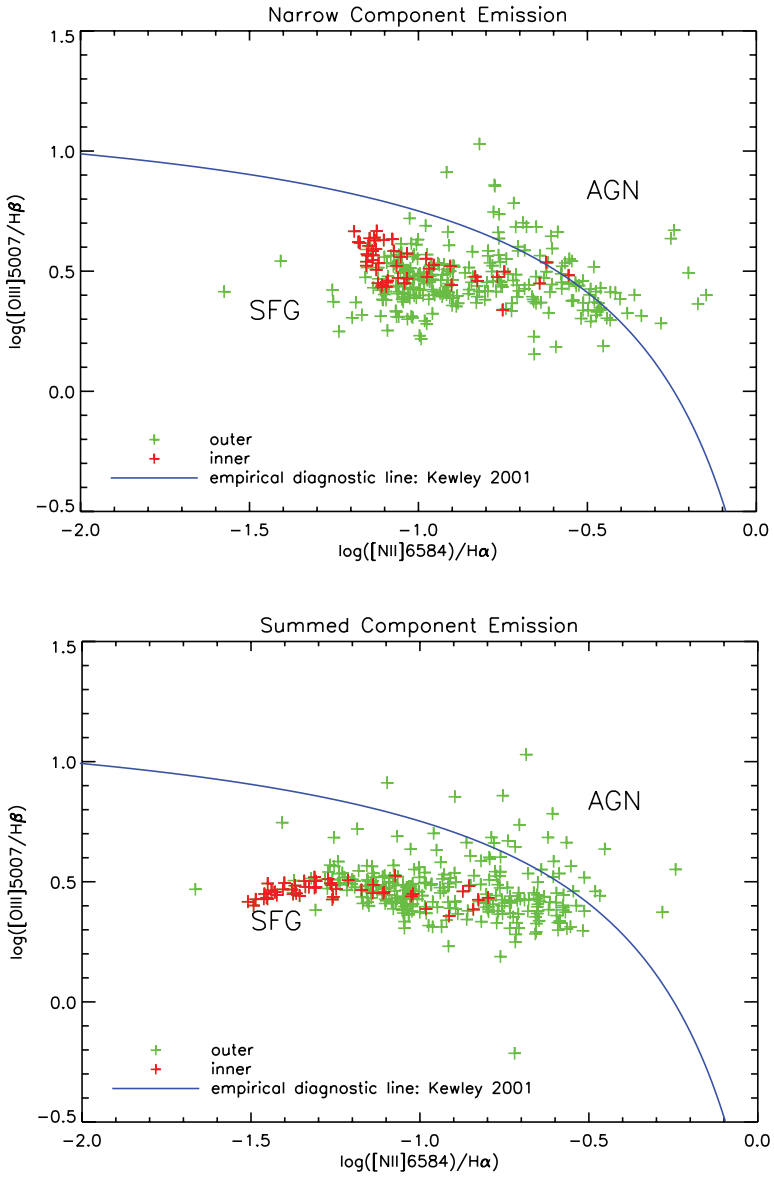

Figure 3.22: Emission line diagnostic diagram for Mrk 996. Each data point represents a spaxel in the ratioed dereddened flux maps corresponding to [O III] λ5007/Hβ and [N II] λ6584/Hα. The empirical diagnostic 'maximum starburst' line from Kewley *et al.* (2001) is also shown, as are the positions of emission line ratios for star-forming galaxies (SFG) and active galactic nuclei (AGN). The top panel represents narrow component emission line map ratios whereas the bottom panel shows ratios derived from the full emission line profile (i.e. narrow + broad component emission, where detected).

3.7.2 What is the origin of the broad line emission?

Mrk 996 is not the only BCD that shows evidence for large line widths. Izotov *et al.* (2007*a*) presented an analysis of a large number of low metallicity BCDs exhibiting broad emission lines with inferred gas expansion velocities of 1000–7000 km/s. WR stellar winds have been proposed as a possible mechanism for producing such broad line widths, but thus far no correlation between the presence of broad nebular lines and broad WR features have been found (Izotov *et al.* 2007*a*). I find that in Mrk 996 the surface brightness of the 4650Å WR feature does not correlate tightly with that of [O III] λ4363 (Fig 23), further indicating that the mechanism responsible for the broad line emission is not active only in the regions where WR stars are present.

Roy *et al.* (1991, 1992) investigated a variety of mechanisms to explain broad nebular gas components in H II regions, including electron scattering, stellar winds, supernova remnants and superbubble blowouts. However, each of these mechanisms was deemed unsatisfactory. An exploration of blowout mechanisms within low-metallicity H II regions was conducted by Tenorio-Tagle *et al.* (1997) using a hydrodynamical calculations to try to match a sample of low-metallicity H II regions with broad emission line components. They proposed that the absence of strong radiative cooling in the low-metallicity ISM within these regions could delay the action of Rayleigh-Taylor (RT) instabilities that can fragment the expanding shell within a blowout. However, this mechanism may not be applicable to Mrk 996, as one of the required conditions is a low-density environment, whereas I derive high densities for its broad component gas (log($N_{\rm e}$)$\sim$7).

Broad line emission (FWHM $\approx$ 400 km/s; C2) is detected throughout the central regions of Mrk 996, throughout the bright starburst region and out to $>5''$. Close to the nucleus of the galaxy the broad Balmer line component splits into two additional *broad* components (FWHM $\approx$ 200–300 km s^{-1}) which trace the kinematics of a two-armed mini spiral, but component C2 does not show evidence of velocity splitting at my level of spectral resolution farther out (Figs 3 and 4). Given the youth of the starburst region in Mrk 996 ($<$5 Myr) containing large numbers of young O and WR-type stars (Section 6), and presence of very dense zones of gas (Section 4.3), it is possible that the broad line emission partly originates from a turbulent mixing layer forming on the surface of dense cool clumps which are subjected to irradiation and hydrodynamic ablation from the hot winds from young massive star clusters (Begelman & Fabian (1990); Slavin *et al.* (1993)). Recent work on the nearby NGC 1569 and M82 has revealed that the broad line component observed in those starburst galaxies can be explained as originating within turbulent layers on the surface of the dense gas clumps (Westmoquette *et al.* 2007*a*,*b*). Motivated by this hypothesis, Binette

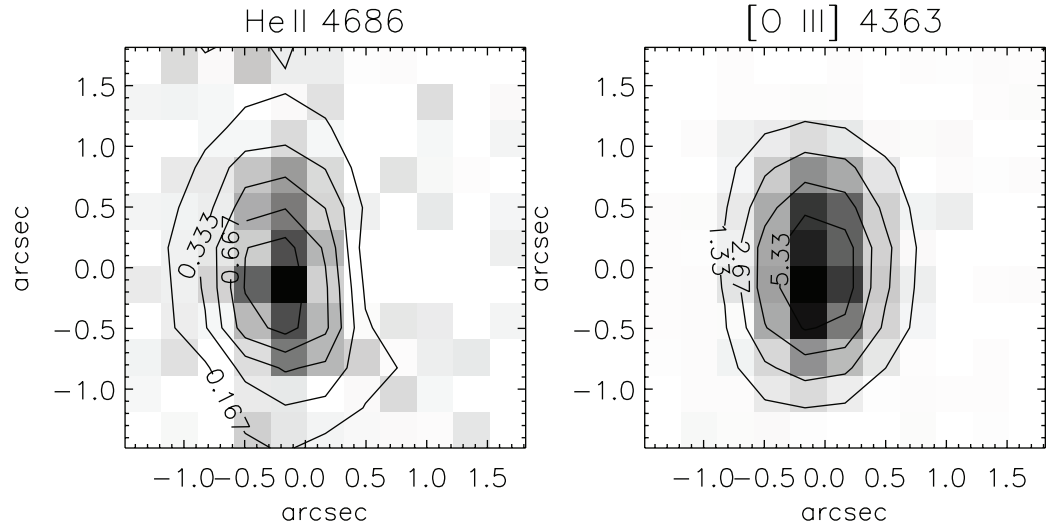

Figure 3.23: Grey scale and contour emission line maps of the He II λ4686 WR feature (left panel) and nebular [O III]4363 (right panel). Their contours suggest that the ionisation mechanism responsible for the broad emission line components (represented by [O III] λ4363) may not be strictly due to the WR stars. Flux contours are in units of $\times 10^{-15}$erg s^{-1} cm^{-2} per 0.33$\times$0.33 arcsec spaxel.

et al. (2009) have successfully modelled the broad underlying components seen in the Balmer and [O III] lines of NGC 2363 via the inclusion of a turbulent mixing layer and conclude that the broad profile results from radial acceleration of photoionised turbulent gas. Their models also correctly predict the absence of a broad component in [S II] and [N II] lines. Although the applicability of these results to Mrk 996 may be limited due to the high densities of Mrk 996's broad components ($N_{\rm e} = 100\,{\rm cm}^{-3}$ is adopted for NGC 2363) and their much broader predicted line widths ($\pm$3500 kms^{-1}), their results lend a great deal of weight to the turbulent mixing layer hypothesis.

This mechanism could also be at work here. It is probable that the central region of Mrk 996 consists of many small, dense clouds of relatively low volume filling factor dispersed within the young star clusters of the starburst. This results in a large cloud surface area with which the copious ionizing photons and fast stellar winds can interact. If the presence of broad emission indicates that strong wind-clump interactions are taking place, then by extension, material from these interaction sites must be being stripped off and entrained into the cluster wind flows contributing to the overall appearance of component C2.

3.8 Summary and conclusions

Mrk 996 is a complex system containing an extended starburst region (216–432 pc in radius) with a centrally concentrated Wolf-Rayet population in the nuclear regions ($\lesssim$200 pc). The young stellar population in the nuclear super-cluster contains $\sim$3000 WR stars and $\lesssim$150,000 O7V-type equivalent stars. The age of the nuclear starburst is estimated to be $\sim$4.5 Myr but there is evidence that the extended starburst is younger by $\sim$1 Myr. The presence of an old stellar population ($\gtrsim$1 Gyr) has been independently established (Thuan, Hunt & Izotov 2008). The current star formation rate is $\sim 2\,\mathrm{M}_{\odot}\,\mathrm{yr}^{-1}$. The spatially mapped ionised gas shows a composite emission spectrum consisting of narrow and broad lines. The Balmer line velocity structure close to the nucleus confirms the presence of a spiral structure confined in the inner 160 pc. The Hα broad component has a large integrated luminosity of 2.5×10^{41} erg s^{-1}; this is at the lower limit of those measured from the rare low-Z BCDs suspected of harbouring active galactic nuclei (Izotov & Thuan 2008). My VIMOS IFU analysis has enabled a separate analysis of the physical conditions and chemical composition of the narrow and broad emission line regions. The broad line region in the nuclear starburst is very dense ($10^7\,\mathrm{cm}^{-3}$) whereas the narrow line component is of lower density ($\lesssim 10^3\,\mathrm{cm}^{-3}$).

The upwards revised oxygen metallicity of Mrk 996 is $\geq 0.5\,Z_{\odot}$ (12 + log O/H $\approx$ 8.37). The broad line region is nitrogen-enriched compared to the narrow line region by $\lesssim$1.3 dex. However, no relative enrichment of He, O, S, and Ar is inferred. The S/O and Ar/O abundance ratios in the two components, as well as the N/O ratio in the *narrow* line component, are typical of those in H II galaxies and dwarf irregulars (e.g. van Zee & Haynes 2006; Izotov *et al.* 2006). The narrow-line N/O ratio in particular is exactly the value expected based on the galaxy's colour, and follows the metallicity-luminosity relationship for isolated dwarf galaxies (cf. figs 8, 9 of van Zee & Haynes 2006) for $M_B = -16.7$, $B-V = 0.44$, TIL96); its mean current value can be interpreted as the result of the slow release of nitrogen from the intermediate-mass stellar population over the last few Gyrs. On the other hand, the high N/O ratio in the broad line region of the inner galaxy is consistent with the presence of numerous evolved massive stars (e.g. WNL-type and Luminous Blue Variables) and can be attributed to the cumulative effect of their N-enriched winds. An elevated N/O could not in this case be due to the outflow of oxygen-enriched gas from supernova explosions: the absence of elevated (or suppressed) O/H, S/H and Ar/H ratios in the broad line gas implies that recent supernova ejecta are probably not implicated in its excitation; at the young age of the Mrk 996 starburst only a few very massive stars ($\gtrsim 50\,\mathrm{M}_{\odot}$) would have exploded as

supernovae (e.g. Woosley *et al.* 2002). The mild two-fold increase over the mean of the narrow-line N/H (Fig 3.16) spatially correlates with a local peak in $EW(\mathrm{H}\beta)$ in a region (Fig 3.21) where no WR stars are seen. This could mean that even though the narrow-line gas is fairly well mixed, some localised N-enrichment has already occurred in an area dominated by normal OB-type stars which is slightly younger than the nuclear starburst.

Finally, I would like to draw attention to the nature of the broad [O III] λ4363 line detected in Mrk 996. Even though this galaxy represents an extreme case in harbouring a very dense ionised component which dominates the excitation of this line, it is by no means unique (see e.g. Izotov *et al.* 2007*a*). In such cases where a substantial fraction of the [O III] 4363 and 4959, 5007 Å lines arise in different gas components, the integrated auroral to nebular ratio would *not* be representative of the electron temperature of the overall H II region; using it would result in biased physical conditions and chemical abundances. The problem would be aggravated in analyses based on low dispersion, low spatial resolution spectra and may therefore have implications for the so-called 'heating problem' of blue compact galaxies (e.g. Stasińska & Schaerer 1999; Péquignot 2008).

CHAPTER 4

INFRARED SPECTROSCOPIC AND PHOTOMETRIC ANALYSIS

This section will detail the IR spectroscopic analysis of the sample of blue compact dwarfs given in Table 1.1.

4.1 Spitzer Space Telescope

The mid-infrared analysis of the BCD sources presented within this thesis was undertaken with archive data obtained from the *Spitzer Space Telescope* (SST; Werner *et al.* 2004). Launched on 25^{th}August 2003 as NASA's Great Observatory for infrared astronomy, *Spitzer* incorporated a telescope with an aperture of diameter 85 cm and three cryogenically cooled science instruments that provided imaging and spectrocopy in the 3.6 to 160 μm wavelength range. Ground based IR observations are hindered by IR radiation of both the Earth's atmosphere and the instrument itself, as well as the atmosphere being opaque at many of these wavelengths. Thus, spaced-based IR observatories are essential for observing all of the IR emission from the nearby and distant Universe.

This study involves the use of Spitzer's three instruments; IRS, MIPS and IRAC (all detailed below). The chapter presents a detailed investigation of of a sample of BCDs' IR emission in order to diagnose their dust content.

4.1.1 The Infrared Spectrograph: IRS

The first of the instruments that I will describe is the Infra Red Spectrograph (IRS; Houck *et al.* 2004*a*). The optical train of the IRS is split into 4 separate spectrographs: short-low, short-high, long-low and long high (SL, SH, LL and LH respectively) that are split by wavelength coverage and resolution. The two low resolution modules were designed to optimise sensitivity to dust features in the near and distant Universe, whereas the 'high' resolution modules were to optimise the sensitivity to emission lines. Data from all modules are made use of within this work. There are two observing modes available for observing; mapping mode and staring mode. The latter was utilised for the majority of the observations in this study and corresponds to when the target is observed at 1/3 and 2/3 positions along the slit for a specified integration time. When observing in mapping mode, the slit is stepped parallel or perpendicular to the slit for a specified number and size of steps. Mapping mode is generally used for a spatial spectroscopic study of a source (analogous to the optical IFU data presented in Chapters 2 and 3). Background measurements are done automatically by the low resolution modules, where both on-source and off-source subslits are exposed simultaneously enabling a subtraction, whereas the high resolution modules are too short on the sky to subtract the background by differencing nod positions and separate off-source integrations must be used. The low resolution module has a spectral resolving power ($R = \lambda/\Delta\lambda$) between 64 and 128, whereas the high resolution module has a resolving power of 600.

4.1.2 Multiband Imaging Photometer: MIPS

The Multiband Imaging Photometer (MIPS; Rieke *et al.* 2004) had long wavelength imaging capability at 24, 70 and 160 μm, with bandwidths of 5, 19 and 35 μm respectively. There were four operating modes available, of which the 'Photometry' mode is utilised for the majority of sources. This operating mode involved the spacecraft pointing at the object of interest, and a combination of scan mirror motions and spacecraft small offsets were used to dither the image on the arrays (Rieke *et al.* 2004). When photometry mode data is not available, images taken in 'scan-map' mode are used - this involves the sky being scanned at a constant rate, and the scan mirror executing a reverse sawtooth motion to freeze the images on the arrays for an integration and then jumping forward for the next integration.

4.1.3 Infra-Red Array Camera: IRAC

Finally, the Infra-Red Array Camera (IRAC; Fazio *et al.* 2004) was primarily designed for the evolutionary study of galaxies to z>3 via deep surveying. The 3-10 μm range was chosen because stars have a peak emission at 1.6 μm at the minimum of H^- opacity. There are two focal plane arrays, each 256×256 pixels, with two channels within each array. The nominal channel wavelengths are 3.6, 4.5, 5.8 and 8.0 μm, which are suited to recognise the most common PAH bands (as detailed in Section 4.2.1).

4.2 What can Infrared data tell us about BCDs?

Dust is present in almost all astrophysical environments, ranging from circumstellar shells and disks, elliptical, spiral, starburst and active galaxies, to pre-galactic objects such as damped Ly-α systems (Dwek 2005*a*). A galaxy's IR spectrum can reveal the chemical composition of the dust contained within it and the resultant spectral features can be used to determine the physical properties of the galaxy such as metallicity and star formation rate. At optical wavelengths, BCDs are blue, as their name implies, emitting the light of the newly formed massive stellar populations that they host. When absorbed by dust, this starlight is reprocessed and emitted at far-IR wavelengths and as nebular emission lines. Hence, IR emission can be a tracer of star formation in galaxies. Broad emission features within the mid-IR wavelength range are thought to arise from polycyclic aromatic hydrocarbons (PAHs, detailed in Section 4.2.1) associated with interstellar dust. Emission from these macromolecules often highlights the photodissociation regions (PDRs) surrounding large H II regions (Giard *et al.* 1994). This morphology can be accredited to the UV radiation from the H II region dissociating the molecules in the transition zone (the PDR) between the H II region and quiescent molecular material, whereas outside the PDR there are insufficient UV photons to excite the PAHs into emission (Jackson *et al.* 2006). Studies using the Infrared Astronomical Satellite (IRAS) established that the LRS mid-IR spectra of star forming galaxies were interesting but had little diversity and confirmed that PAH emission is closely related to star formation (Cohen & Volk 1989).

The interstellar medium not only traces star formation but also obscures it. Studies of BCDs at optical wavelengths can be limited by dust extinction which makes some of the most obscured regions inaccessible. As an example, an ISO study of SBS 0335-052 by Thuan *et al.* (1999) revealed that there is an embedded super-star cluster (SSC) within its eastern component which remains invisible in the optical, although it contributes 75% of the bolometric luminosity. This

is despite its low metallicity of 12+log(O/H)=7.33 which ought to imply a low dust content. In addition to probing these dust-concealed regions, infrared emission allows access to lines that are less sensitive to any electron temperature fluctuations than the corresponding optical lines of the same ion.

4.2.1 Polycyclic Aromatic Hydrocarbons: PAHs

As previously mentioned, the mid-IR spectra of many objects – H II regions, reflection nebulae, diffuse interstellar clouds, galactic nuclei, the ISMs of galaxies as a whole and starburst galaxies – are dominated by strong, broad features which are thought to originate from PAHs. PAHs are aromatic hydrocarbons, i.e. hydrocarbons containing one or more planar sets of benzene rings (Figure 4.1). The broad mid-IR emission bands between 3–13 μm are believed to represent the vibrational relaxation process of FUV-pumped PAH species, which can contain from several tens up to a few hundred carbon atoms (Tielens 2005). The mid-IR features are believed to be due to the subsequent fluorescence of aromatic C–C (especially dominant at 6.2 and 7.7 μm) and peripheral C–H (3.3, 8.6, and 11.3 μm) fundamental vibrational and bending modes (Lebouteiller *et al.* 2007).

PAHs not only trace the star formation within galaxies, but can also reveal the physical conditions of their ISMs. As a result of their distribution throughout the PDR regions of the ISM (Leger & Puget (1984); Allamandola *et al.* (1989),Tielens:1999), it is hypothesised that PAHs can be observed in three states; neutral, ionic, radical. The strong UV radiation emitted from star forming regions is able to ionise the PAHs, while for weaker radiation fields PAHs can be seen as neutrals, or even negatively charged by accretion of a single electron (Bakes & Tielens 1994). It has been shown, from laboratory experiments, that the C–H emission modes of neutral PAHs are stronger relative to C–C modes, with the inverse being true for ionised PAHs (Kim *et al.* 2001; Szczepanski & Vala 1993). Therefore, the emission features at 3.3 and 11.3 μm are thought to originate mainly from neutral PAHs and those at 6 and 9 μm to arise from ionised PAHs.

Along with carbon grains, there is a silicate mineral component of interstellar dust that has strong vibrational resonances in the MIR. Amorphous silicates, the most common type of silicate, differ from crystalline silicates in that the tetrahedral shape of SiO_4 or SiO_3 is not directly repeated throughout the structure. They have a broad Si-O stretching resonance, peaking at about 9.8 μm and an even broader O-Si-O bending mode resonance, peaking at about 18.5 μm (Brandl *et al.* 2006).

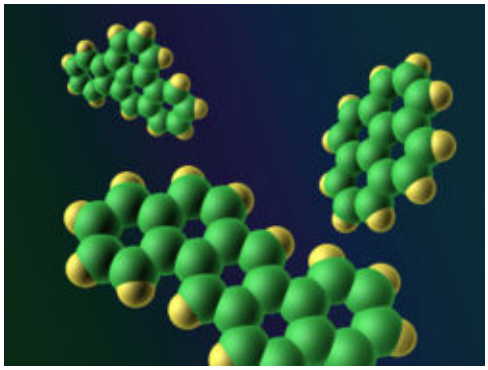

Figure 4.1: Three examples of PAH structures. Clockwise from top left:benzacephenanthrylene, pyrene and dibenzanthracene (CREDIT: Robert Hurt, *"Understanding PAHs"*, *Spitzer* Science Centre, 2005).

4.2.2 IR observations of PAHs within BCDs

Observations made with the *Infrared Space Observatory* (ISO) confirmed that low-metallicity galaxies are deficient in PAH emission in the mid-IR (Madden 2002). This was verified via *Spitzer* studies of low-luminosity galaxies (Engelbracht *et al.* 2005; Hunt *et al.* 2006; Rosenberg *et al.* 2006). The study of the spectral energy distributions of seven BCDs by Hunt *et al.* (2006) showed a significant difference from the standard templates of starburst galaxies since there was little or no PAH emission in their MIR spectra and their far-infrared spectra peaked at or below 60 μm. The PAH depletion could be due to a low carbon abundance, i.e. a low dust-to-gas ratio, that allows the hard interstellar radiation field (ISRF) to penetrate lower column densities, destroying the PAHs. Recent work by Galliano *et al.* (2005) has suggested that shock waves from supernovae (SNe) may be responsible for the small size of interstellar medium (ISM) dust grains that are emitting in the MIR and FIR, i.e. dust grains with radius a $\sim$3–4 nm that dominated the mass spectrum. The star formation in low metallicity systems is dominated by massive stars and high SN rates are expected in systems undergoing very recent massive star formation (Mas-Hesse & Kunth 1999). O'Halloran *et al.* (2006) proposed that this could be the reason behind the lack of PAHs in low-metallicity galaxies, i.e. destruction by strong SN shocks propagating through the ISM. They used the MIR emission line ratio of [Fe II]/[Ne II]as a tracer of SN activity (a high ratio being indicative of high SN activity), and found an anti-correlation with PAH strength. However, they do not claim that destruction by SNe is fully responsible, stating that the young age of the systems does not allow for a full PAH enrichment of the ISM. This links to a suggestion by Dwek (2005*b*) that the dust deficiency in chemically young systems is due to its late injection by long-lived low-mass

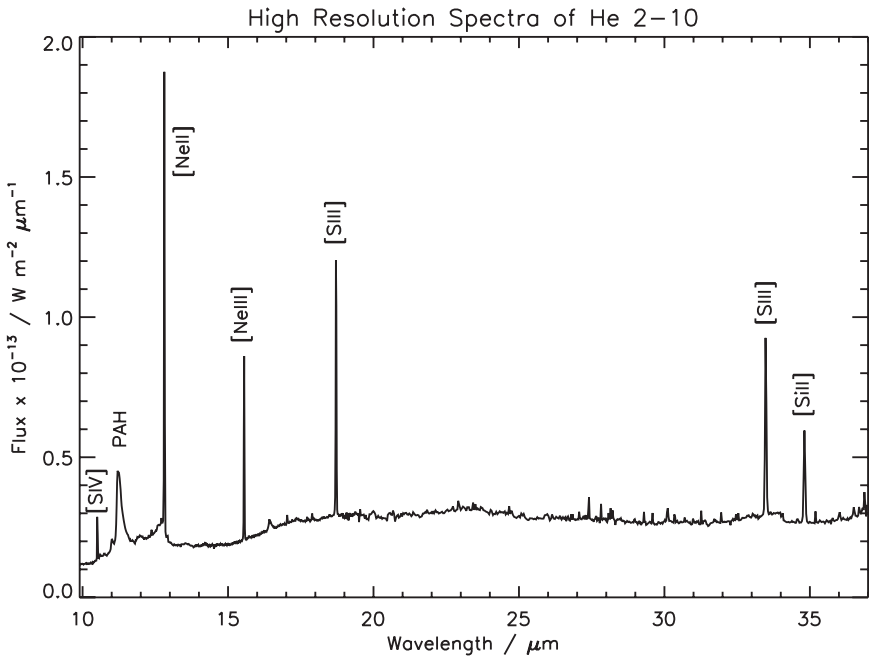

Figure 4.2: An example of *Spitzer* high resolution spectra of the BCD He 2-10.

stars. Galliano (2006) supported this, showing that PAH content is correlated with the rate of carbon dust production by AGB stars, since PAHs are believed to originate from the envelopes of AGB stars that are ejected into the ISM after they are fully evolved. It can be thus said that the issue of PAH deficiency in low metallicity environments is still open, and probably both chemical and radiative effects contribute.

4.2.3 Infra-Red Forbidden Lines

The 5-38 μm range contains numerous strong emission lines and it can be seen from the example spectra in Figure 4.2 and Figure 4.3 that there are many common forbidden transitions in both the high and low resolution spectra.

The energy levels responsible for infrared emission levels are low enough to allow their temperature dependence to be negligible, while some line ratios can be used as a density diagnostic. The dependence on electron density crosses from the low density limit when radiative transitions are dominant, to the high density limit where collisional transitions are dominant. Between these two limits lies the critical density, i.e. the density at which the collisional and radiative

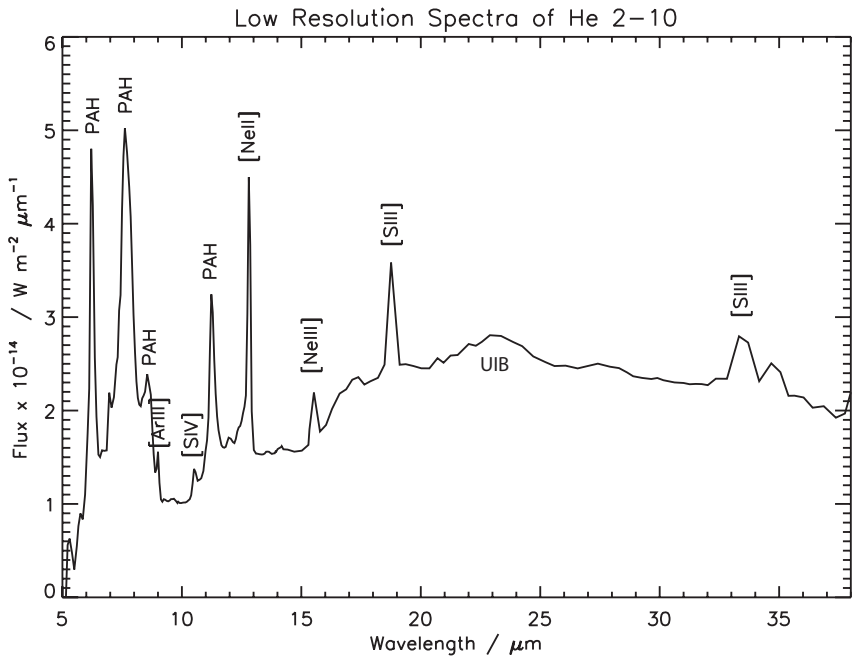

Figure 4.3: An example of *Spitzer* low resolution spectra of the BCD He 2-10. Different orders were stitched and scaled to match the flux density of the first-order LL. The identified forbidden lines are labelled, along with PAH features at 6.23, 7.6, 8.6 and 11.3 μm. The detection of a broad UIB (unidentified infrared band) feature at 23 μm should also be noted.

de-excitation rates from the upper level are equal.

The high energy photons that are produced by a young starburst can propagate large distances in a low metallicity environment before being absorbed by the atoms in the ISM. There is a large difference between the ionization potentials of Ne^{++} (41eV) and Ne^{+} (22eV), thus allowing the [Ne III]/[Ne II] ratio to be used as a tracer of radiation field hardness. Wu *et al.* (2006) discuss the use of the [S IV]/[S III] ratio as another indicator but conclude that the ratio of [Ne III]/[Ne II] is more reliable as it is less affected by silicate extinction.

4.3 IRS Spectroscopy

Where available, IRS data were obtained from the SST archive for each of the sources listed in Table 1.1. The observational details including date of observation, integration time and AOR key are given in Table 4.1. The sample listed in Table 1.1 is made up of 19 blue compact dwarf galaxies (BCDs); although a single catalogue of BCDs does not currently exist, all galaxies in Table 4.1

exist in selected BCD samples in the literature. The sample was chosen to provide a large cross-section across the BCD classification, including blue compact galaxies (BCGs, i.e. sources too large to be classified as dwarf galaxies), WR galaxies (e.g. NGC 5253, Mrk 996, UM 448), starbursting galaxies (e.g. II Zw 40, Hen 2-10, NGC 7673) and LINER (Low-ionisation Nuclear Emission Line Region) galaxies (NGC 6764, NGC 7714). A large range in metallicities exists within the sample, 12+log(O/H)=7.31–8.93, so that correlations with metallicity can be more fully explored. Based on the current estimation of the solar oxygen abundance (12+log(O/H)=8.71, Scott *et al.* (2009)), two galaxies within the sample (He 2-10 and NGC6764) have a super-solar oxygen abundance and were previously classified as BCDs according to the solar abundances available at that time. Although they would currently not be classified as BCDs based on their metallicity, they remain within my sample to give a more full metallicity range.

Object Name	RA (J2000)	DEC (J2000)	AOR key	OBS Date	Redshift	12+log(O/H)	On Source Time/s SL	LL	SH	LH
SBS 0335-052	03 37 44	-05 02 39	8986880	16/02/04	0.013486	7.31	840	420	...	...
			11769856	01/09/04			...	...	1440	960
II Zw 40	05 55 42	+03 23 32	9007616	01/03/04	0.00263	8.13	168	240	480	240
He 2-10	08 36 15	-26 24 32	4340480	18/04/04	0.00291	8.93	120	240	480	240
Mrk 33	10 32 31	+54 25 04	9481472*	15/04/04	0.00477	8.42	...	...	63	61
			9489920*	15/04/04			15	15	...	...
NGC 3353	10 45 22	+55 57 33	12556288	17/11/04	0.00315	8.34	...	...	240	224
			12710144	16/04/05			122	...	...	...
UM 448	11 42 12	+00 20 03	4342784	01/04/04	0.01856	7.99	168	240	480	240
NGC 4670	12 45 17	+27 07 32	4570880*	01/08/04	0.003566	8.20	...	...	31.5	14.7
NGC 5253	13 39 56	-31 38 42	4386304*	14/07/04	0.00136	8.51	32	19	44	44
II Zw 70	14 50 56	+35 34 17	12565760	14/01/04	0.00394	7.80	72	...	240	224
NGC 6764	19 08 16	+50 55 54	3858176	17/04/04	0.008059	8.86	48	48	...	...
NGC 7714	23 36 14	+02 09 18	3756800	17/12/03	0.00933	8.90	112	112	240	240
I Zw 18	09 34 02	+55 14 28	16205568	16/12/05	0.002505	7.12	4080	1680	5760	2880
Mrk 996	01 27 35	-06 19 36	12560896	03/01/05	0.005410	8.37	72	...	240	224
UM 461	11 51 33.35	-02 22 21.9	9006336	03/01/05	0.003465	7.78	168	240	480	240
UM 462	11 52 37	-02 28 09	4343040	03/01/05	0.003527	8.11	168	240	480	240

Table 4.1: Notes: Units of right ascension are hours, minutes, and seconds, and units of declination are degrees, arcminutes, and arcseconds. The coordinates and redshifts of the objectes are from the NASA/IPAC Extragalactic Database (NED), which is operated by the Jet Propulsion Laboratory, California Institute of Techonology, under contract with the National Aeronautics and Space Administration. All AORs (Astronomical Observation Request) with an asterix mark were observed in IRS spectral mapping mode rather than IRS staring mode. References for 12+log(O/H) values are given in Table 1.1.

4.3.1 Reduction and Analysis Techniques

The basic calibrated archive data were pre-processed by the *Spitzer* Science Center (SSC) data reduction pipeline version 11.0 (Spitzer Science Center 2004). This pipeline performs all the basic processing of the data, such as dark sky subtraction, ramp fitting, removal of cosmic rays, linearity correction, wavelength calibration etc. Reduction and exctraction of the spectra was done with the Smart Modeling, Analysis, and Reduction Tool (SMART) version 6.2.4, developed by Higdon *et al.* (2004).

The steps involved within the data reduction of the pipeline products follow a similar order as those given in Brandl *et al.* (2006); Lebouteiller *et al.* (2007); Wu *et al.* (2006). Firstly images with the same nod position, module and order are median combined. For the low resolution modules, a fixed column width extraction is used, i.e. a set extraction width at the central wavelength of each subslit, since all objects are extended sources that fill the slits. Thus the column width increases, along with the instrumental point-spread function (PSF), linearly with wavelength and recovers the same fraction of the diffraction-limited instrumental PSF. The high resolution modules can only be extracted via a 'full source extraction' from the median of the combined images. The sky emission was not subtracted from the high resolution data since no sky (off-position) measurements were taken. A local sky subtraction is selected for the low resolution data. The two nod position spectra for each module are averaged before combining the different modules. There is often a mismatch between the spectra from the modules, requiring a scaling process. Brandl *et al.* (2006) decided that this mismatch is more likely due to source flux that was missed in the narrower slits rather than *unrelated* flux that was picked up in the wider slits, thus they scale SL2 to SL1 and LL2 to LL1, then finally scale SL to LL. The choice of LL1 as the reference slit is supported by it being the widest slit and having the largest PSF. This approach of stitching together slit apertures of different widths assumes that the spectral properties are not changing within the region covered by the LL slit. However, as Brandl *et al.* (2006) note, the LL aperture size of 168×10.6 arcsec corresponds to 200 pc for the nearest BCDs - the average size of a circumnuclear starburst over which the spectral properties are assumed to not vary substantially. In a continuation of this approach, SH modules were scaled to match LH modules.

Flux calibration of the spectra was attained via multiplication by the relative spectral response function (RSRF). This consists of the IRS standard stars α Lac and ξ Dra for the low-resolution modules and high-resolution modules respectively, for which accurate template spectra were available (Cohen *et al.* 2003). The RSRF was created by firstly extracting the model spectra in the same

way as the source spectra (respectively of high/low resolution modules) and then dividing the template spectra of the stars by the spectra from the fixed column extraction. Each of the final source extractions was then multiplied by the respective RSRF.

4.3.2 Emission Line Measurements

Analysis of the emission lines was undertaken using *DIPSO* (created by I. D. Howarth et al., 1993 - Starlink User Note 50). After continuum subtraction using a cursor drawn continuum within close proximity of the emission line (typically 2 μm either side), a Gaussian profile was fitted to the line using DIPSO's *ELF* command that optimises Gaussian fit coefficients by minimising the sum of the squares of the deviations of the fit from the spectrum data. Outputs of the line fit consist of an optimised central wavelength, width, peak flux and integrated flux and their errors (calculated in the linear approximation, from the error matrix). However, in several cases, namely the unidentified infrared bands or PAH features, Gaussian profiles cannot be fitted and only the flux above a linear continuum can be measured, via the *FLUX* command. Uncertainties for these cases were estimated via a user-estimated max-min continuum level.

Following the method outlined in (Brandl *et al.* (2006) and Wu *et al.* (2006)), equivalent widths of the PAH features were measured on non-continuum subtracted spectra using the relation:

$$EW(\lambda) = \int \frac{I(\lambda)}{I_C(\lambda)} \mathrm{d}\lambda \tag{4.1}$$

where $I(\lambda)$ is the intensity of the line and $I_C(\lambda)$ is the average intensity in the integration range. Uncertainties on $I_C(\lambda)$ are calculated from maximum and minimum estimations of the continuum level on which the line lies. The wavelength limits for the integration of the features were approximately 5.95–6.55 μm for the 6.2 μm PAH, 7.15–8.20 μm for the 7.7 μm PAH, 8.2–8.90 μm for the 8.6 μm PAH and 10.80–11.80 μm for the 11.2 μm PAH feature.

Examples of high resolution and low resolution IRS spectra are shown in Figure 4.2 and Figure 4.3, respectively. Identified lines and dust features from all sources, along with their integrated fluxes, are listed in Tables 4.2 and 4.3 for high resolution and low resolution spectra, respectively, and the equivalent widths of selected PAH features are listed in Table 4.4.

Table 4.2: Forbidden line and PAH feature integrated fluxes from IRS high resolution data.

Object Name	Wavelength (μm)	Line ID	Flux (x10^{-15}W m^{-2})
SBS 0335-052	10.51	[S IV]	1.27±0.84
	12.81	[Ne II]	0.052±0.002
	15.55	[Ne III]	0.014±0.0004
	18.71	[S III]	0.003±0.0004
II ZW40	10.51	[S IV]	1.72±0.02
	12.81	[Ne II]	0.07±0.01
	15.55	[Ne III]	1.22±0.01
	18.71	[S III]	0.49±0.01
	33.5	[S III]	0.91±0.02
	34.8	[Si II]	0.38±0.07
	35.7	[Si VIII]	0.32±0.06
He 2-10	10.51	[S IV]	0.38±0.02
	11.2	PAH	7.24±0.31
	12.81	[Ne II]	3.61±0.10
	15.55	[Ne III]	1.35±0.02
	18.71	[S III]	2.55±0.03
	33.49	[S III]	3.83±0.12
	34.81	[Si II]	2.06±0.05
Mrk 33	11.2	PAH	0.37±0.02
	12.81	[Ne II]	0.12±0.01
	15.55	[Ne III]	0.08±0.004
	18.71	[S III]	0.09±0.005
NGC 3353	10.51	[S IV]	0.31±0.005
	12.81	[Ne II]	0.26±0.01
	15.55	[Ne III]	0.77±0.01
	18.71	[S III]	0.39±0.007
	33.5	[S III]	0.46±0.02
	34.8	[Si II]	0.24±0.09
UM 448	10.51	[S IV]	0.11±0.01
	11.3	PAH	1.08±0.03
	12.81	[Ne II]	0.23±0.02
	15.55	[Ne III]	0.41±0.01

cont. on next page

Table 4.2 cont.

Object Name	Wavelength (μm)	Line ID	Flux (x10^{-15}W m^{-2})
	18.71	[S III]	0.20±0.005
	33.5	[S III]	0.55±0.03
	34.8	[Si II]	0.50±0.01
NGC 5253	10.51	[S IV]	3.77±0.05
	12.81	[Ne II]	0.66±0.05
	15.55	[Ne III]	4.49±0.06
	18.71	[S III]	1.66±0.03
	33.48	[S III]	1.37±0.08
	34.8	[Si II]	0.84±0.04
II ZW70	10.51	[S IV]	0.047±0.003
	12.81	[Ne II]	0.028±0.005
	15.55	[Ne III]	0.095±0.005
	18.71	[S III]	0.049±0.002
NGC 7714	10.51	[S IV]	0.19±0.01
	11.26	PAH	3.45±0.12
	12.81	[Ne II]	1.19±0.06
	15.55	[Ne III]	0.77±0.01
	18.71	[S III]	0.74±0.01
	33.48	[S III]	1.10±0.07
	34.8	[Si II]	1.12±0.03
I Zw18	10.51	[S IV]	0.74±0.07
	12.81	[Ne II]	0.0026±0.0022
	15.55	[Ne III]	0.0059±0.0008
	17.22	[Si VIII]	0.0026±0.0007
	18.71	[S III]	0.0022±0.0007
Mrk 996	10.51	[S IV]	1.39±0.30
	11.2	PAH	1.69±0.06
	12.8	[Ne II]	0.69±0.26
	13.06	([ArV])	0.65±0.25
	15.55	[Ne III]	1.19±0.02
	18.71	[S III]	0.61±0.12
	33.48	[S III]	0.39±0.05
	34.81	[Si II]	0.14±0.08
UM 461	10.52	[S IV]	0.20±0.10

cont. on next page

Table 4.2 cont.

Object Name	Wavelength (μm)	Line ID	Flux (x10^{-15}W m^{-2})
	12.35	H(2-6)	0.15±0.05
UM 462	10.52	[S IV]	0.28±0.09
	11.25	PAH	0.82±0.48
	13.09	([ArV])	1.90±1.02
	34.8	[Si II]	0.31±0.11

Table 4.3: Forbidden line and PAH feature integrated fluxes from IRS low resolution data.

Object Name	Wavelength(μm)	Line ID	Flux(x$10^{-16}Wm^{-2}$)
II Zw40	6.2	PAH	0.84 ±0.09
	7.4	UIB	1.47 ±0.12
	8.5	PAH	1.30 ±0.10
	9.0	[Ar III]	1.27 ±0.07
	10.5	[S IV]	25.6 ±2.051
	11.3	PAH	0.78 ±0.10
	12.8	[Ne II]	1.17 ±0.15
	15.5	[Ne III]	14.3 ±0.76
	18.7	[S III]	10.2 ±0.64
	33.4	[S III]	5.98 ±0.43
He 2-10	6.2	PAH	84.5 ±3.96
	6.9	UIB	4.00±0.42
	7.6	PAH	154 ±5.08
	8.6	PAH	25.8 ±3.12
	9.00	[Ar III]	2.81±1.20
	10.5	[S IV]	4.34 ±0.10
	11.2	PAH	56.7 ±3.30
	12.8	[Ne II]	53.8 ±2.38
	15.5	[Ne III]	14.0 ±2.00
	18.7	[S III]	51.3 ±3.22
	23.0	UIB	65.0 ±5.10
	33.5	[S III]	45.2 ±95.5

cont. on next page

Table 4.3 cont.

Object Name	Wavelength(μm)	Line ID	Flux(x$10^{-16} Wm^{-2}$)
NGC 3353	5.6	He II	0.37 ±0.93
	6.2	PAH	5.31 ±0.25
	6.8	UIB	0.10 ±0.70
	7.6	PAH	10.1 ±0.43
	8.3	UIB	0.03±0.02
UM 448	5.6	[Fe II]	2.29 ±1.83
	6.2	PAH	17.6 ±0.61
	6.9	[Ar II]	0.66 ±2.16
	7.6	PAH	35.8 ±1.05
	8.5	PAH	5.64 ±1.14
	9.0	[Ar III]	0.79 ±2.04
	9.6	H (S3)	0.88 ±2.31
	10.4	[S IV]	3.57 ±1.11
	11.3	PAH	13.2 ±0.46
	12.7	[Ne II]	8.43 ±0.53
	15.5	[Ne III]	4.71 ±1.90
	18.7	[S III]	2.69 ±0.32
	33.5	[S III]	4.84 ±1.38
NGC 5253	5.6	[Fe II] /He II	0.34±0.16
	6.2	PAH	3.75 ±0.39
	7.6	PAH	7.82 ±0.54
	8.6	PAH	1.25±0.89
	9.0	[Ar III]	1.73 ±0.15
	10.5	[S IV]	16.1 ±2.54
	11.2	PAH	3.70 ±7.77
	12.7	[Ne II]	1.31±0.76
	15.5	[Ne III]	23.3 ±0.69
	18.8	[S III]	17.6 ±0.75
	33.5	[S III]	16.3 ±15.4
	38.0	[Si III]	17.4±8.30
II Zw70	7.5	UIB	0.63 ±0.10
	7.9	UIB	0.08 ±0.11
	8.1	UIB	0.23 ±0.12
	8.9	[Ar III]	0.13 ±0.11

cont. on next page

Table 4.3 cont.

Object Name	Wavelength(μm)	Line ID	Flux(x$10^{-16}Wm^{-2}$)
	10.5	[S IV]	1.33 ±0.05
	12.7	[Ne II]	0.27 ±2.55
NGC 6764	5.3	([FeII])	1.35 ±1.98
	5.7	PAH	0.99 ±2.28
	6.2	PAH	18.2 ±0.04
	6.9	UIB	4.59 ±0.49
	7.6	PAH	39.3 ±0.08
	8.5	PAH	1.38 ±2.52
	9.0	[Ar III]	0.446±0.25
	10.5	[S IV]	0.88±0.16
	11.2	PAH	17.8 ±2.79
	12.7	[Ne II]	11.5 ±2.85
	17.1	[SiVIII]	4.08 ±7.81
	18.7	[S III]	5.32 ±8.58
	23.0	UIB	2.64 ±4.570
	33.3	[S III]	7.41 ±4.14
	34.9	[SiII]	5.36 ±1.14
NGC 7714	5.676	PAH	1.19 ±3.93
	6.2	PAH	35.3 ±0.58
	6.6	UIB	0.69 ±0.12
	7.0	UIB	1.10 ±4.14
	7.6	PAH	65.7 ±1.16
	8.6	PAH	10.9 ±0.95
	8.9	[Ar III]	0.86 ±3.65
	10.5	[S IV]	3.19±0.85
	11.2	PAH	30.8 ±1.57
	12.7	[Ne II]	19.6 ±1.55
	15.5	[Ne III]	6.80 ±1.70
	18.6	[S III]	8.42 ±1.58
	23.0	UIB	17.8 ±7.47
	33.3	[S III]	19.9 ±7.09
Mrk 996	5.4	UIB	0.66 ±0.18
	5.7	[Ne III]	0.49 ±0.12
	6.2	PAH	0.70 ±0.20

cont. on next page

Table 4.3 cont.

Object Name	Wavelength(μm)	Line ID	Flux(x$10^{-16}Wm^{-2}$)
	7.7	PAH	0.40±0.16
	8.3	UIB	0.54 ±0.10
	11.2	PAH	0.27±0.13
	12.7	[Ne II]	0.67 ±0.13
UM 461	5.6	UIB	0.50 ±0.08
	6.4	UIB	0.65 ±0.13
	7.4	UIB	0.42 ±0.07
	7.9	UIB	0.11 ±0.07
	8.6	PAH	0.17 ±0.10
	10.5	[S IV]	0.59 ±0.43
UM 462	5.3	UIB	0.23 ±0.10
	5.6	[Ne III]	0.13 ±0.10
	6.0	UIB	0.36 ±0.13
	8.4	UIB	0.20 ±0.04
	8.6	PAH	0.16 ±0.05
	10.5	[S IV]	1.06 ±0.64
	12.7	[Ne II]	0.14 ±0.98
	15.5	[Ne III]	1.19±0.87
	18.7	[S III]	2.04 ±0.23
	33.6	[S III]	1.24 ±1.70
	36.0	[Ne III]	0.77±0.55
	38.0	[Si III]	4.42±1.52

The 5-38 μm range contains numerous strong emission lines and it can be seen from Tables 4.2 and 4.3 that there are many common forbidden transitions in both the high and low resolution spectra. Among those are the following, sorted by wavelength and with their ionisation potential ranges in parentheses: [Ar III] 8.99 μm (27.63–40.74 eV), [S IV] 10.51 μm (34.83–47.30 eV), [Ne II] 12.81μ (21.56–40.96 eV), [Ne III] 15.5 μm (40.96–63.45 eV) and [S III] 18.7 μm and 33.5 μm (23.33–34.83 eV). The flux measurements of the fine structure lines differ somewhat between the high and low resolution spectra. Since the line S/N is much higher in the high resolution data, it is these that are used as diagnostic tools below.

The program EQUIB (written by I. D. Howarth and S. Adams) was used to obtain electron

Object	6.2μm	7.7μm	8.6μm	11.2μm
IIZw40	0.023±0.003	0.034±0.003	0.030 ±0.002	0.012±0.001
He2-10	0.67±0.04	0.72±0.02	0.14 ±0.02	0.35±0.02
NGC3353	0.77±0.04	0.68±0.03	—	—
UM448	0.47±0.02	0.71±0.02	0.13 ±0.03	0.37±0.01
NGC5253	0.057±0.006	0.11±0.01	0.02 ±0.01	0.04±0.01
NGC6764	0.49±0.01	0.69±0.01	0.026 ±0.02	0.40±0.06
NGC7714	0.61±0.01	0.71±0.02	0.14 ±0.01	0.41±0.02
Mrk 996	0.20±0.06	0.10±0.01	0.13 ±0.02	0.079±0.009
UM462	—	—	0.090 ±0.029	—

Table 4.4: PAH equivalent widths measured from low resolution IRS spectra.

density estimates using the [S III] 33.5/18.7 μm doublet ratio that was measured for seven of the thirteen high resolution spectra, with the exclusion of UM 448, whose flux ratio far exceeded the low density limit. Using the flux ratio of the 33.5 μm transition and the 18.7 μm transition, and an adopted 10,000 K electron temperature, a range of densities corresponding to the flux ratio error limits was calculated for each object and these are given in Table 4.5. The low- and high-density limits for the [S III] 33.5/18.7 μm ratio are 1.75 and 0.082 respectively. The densities of H II regions are typically low, as can be seen in Table 4.5 where the derived densities range from $\sim$180–3000 cm^{-3}. When comparing with electron densities derived from the same [S III] ratio, for larger published samples of BCDs (e.g.Wu *et al.* (2007) and references therein) they appear to lie within a similar density regime (typically 10–3000 cm^{-3}). However, large uncertainties are involved in this method since the [S III]18.7μm/33.5μm ratios tend to lie on the flat part of the theoretical S-curve (see Herter *et al.* (1984)). Furthermore, as noted by Wu *et al.* (2007) the 33.5 μm [S III] line is located at the edge of the LH slit, where sensitivity drops dramatically, and considering that these emission lines are weak, the measured line flux for the 33.5 μm [S III] line has a large uncertainty. However, for the purpose of this work, these derived $N_{\rm e}$ values are sufficient for showing the typical low densities in BCDs.

The 11.2 μm PAH feature is present in several of the high resolution spectra, but it is the low-resolution spectra that show a plethora of unidentified infrared bands (UIBs) or PAH features. As previously noted by other authors, the spectral shape of starburst IR spectra is dominated by

Source	I(33.5)/I(18.7)	$N_{\rm e}$ (cm^{-3})
II Zw40	3.51±2.40	<500
He 2-10	0.15±0.01	$440\pm^{55}_{42}$
NGC 3353	0.79± 0.02	$860\pm^{95}_{93}$
NGC 5253	2.27±0.05	$1780\pm^{220}_{190}$
NGC 7714	0.26±0.01	$440\pm^{120}_{69}$
Mrk 996	0.65±0.15	$2820\pm^{600}_{570}$

Table 4.5: Estimated electron densities from the [S III] doublet ratio ($\lambda33.5/\lambda18.7$), for an adopted electron temperature of 10,000K.

strong emission features from PAHs (Brandl *et al.* 2006). In the current study, focus was put upon only the strongest of the features, namely those at 6.2, 7.7, 8.6 and 11.2 μm (the EWs of which are given in Table 4.4). Other PAH features are present in the spectra but have either low S/N or are not common throughout the sources and thus will be excluded from analysis. Special mention should be made, however, of the feature that is observed at 23 μm in three of the low resolution spectra (He 2-10, NGC 6764 and NGC 7714), shown in Figure 4.4. This feature is much wider than any of the usual PAH features and has not been reported for these objects in previous studies. A 23 μm band has been noted in two planetary nebulae (PNe) that Hony *et al.* (2002) identify with a form of iron sulphide, attributed to the ejecta of carbon-rich evolved stars. The same feature has also been detected in young stellar objects as a component of circumstellar dust (Keller *et al.* 2002). Spitzer observations of the Cassiopeia A SNe remnant by Rho *et al.* (2008) show a strong peak at 21 μm, which they attribute to Al_2O_3 and C grains, however due to the 2 μm-difference in peak centroid and also the relative strength of this peak in comparison to the 23 μm peak presented in this work, the relation between these two peaks is questionable. However, evidence does suggest that the 23 μm peak may indicate the presence of SNe within the H II regions of these BCDs.

4.3.3 Correlations with PAH emission

The responsibility for the suppression of PAHs within BCDs can either lie with formation effects, i.e. a *chemical* dependence, or destruction effects, i.e. an *energy* dependence, or a mixture of both. This section explores the current methods used to disentangle these two effects using correlations between metallicity and radiation field hardness and the strength of the PAH emission features.

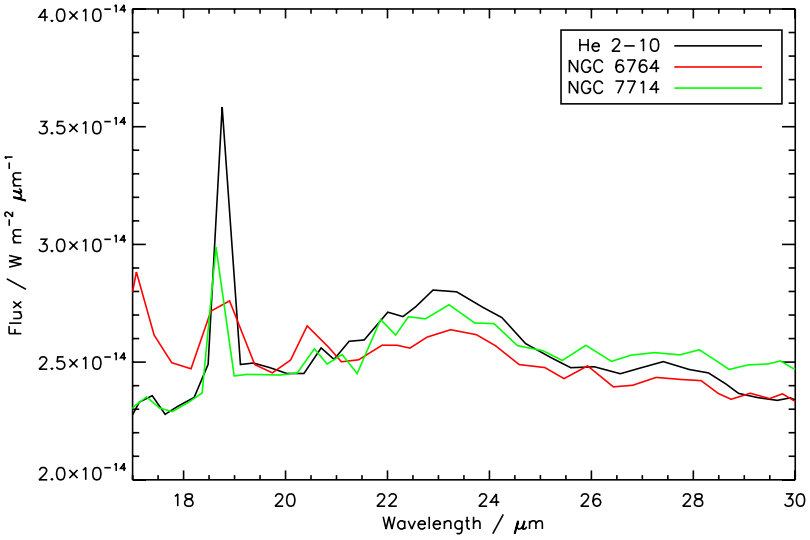

Figure 4.4: Low-resolution IRS spectra of He 2-10, NGC 6764 and NGC 7714 illustrating the wide 23 μm feature, common only to these three sources. The origin of this feature is unknown. Fluxes levels of NGC 6764 and NGC 7714 have been scaled up to those of He 2-10.

4.3.3.1 PAH and Metallicity

In Section 4.2.2 it was mentioned that the deficit of PAH emission in BCDs could be due to the low abundance of carbon grains. Madden *et al.* (2006) explored possible ISM enrichment sources for carbonaceaous particles (ignoring destruction effects), such as AGB stars and/or supernovae Type II (SN II), and ruled out SN II as large contributors to PAHs due to their relatively short life times. Dwek (2005*b*) and Dwek (2005*a*) also discussed this issue and noted that AGB stars begin to contribute to the carbon reservoir only when 4 $M_{\odot}$ stars have entered the AGB stage ($\sim$ 120 Myrs, Padovani & Matteucci (1993); Kodama (1997)). Therefore if we assume AGB stars to be the dominant source of PAHs it would explain why PAHS are under-abundant in low-metallicity systems. To examine the possible variation of PAHs with metallicity, the PAH 6.2, 7.7, 8.6 and 11.2 μm EWs of the sample were plotted as a function of their O/H abundance (relative to the solar 12+log(O/H)=8.71 (Scott *et al.* 2009)) in Figure 4.5. A list of all sources and their 12+log(O/H) values is given in Table 4.1 (the references from which the O/H values were obtained can be found in Table 1.1). A similar trend is seen for all PAH species, where a plateau of EW exists as metallicity decreases down to $\sim$0.4$Z_{\odot}$ and then a sharp decrease is seen. This is in contrast to previous studies by who report a smooth linear inverse relationship between PAH EW

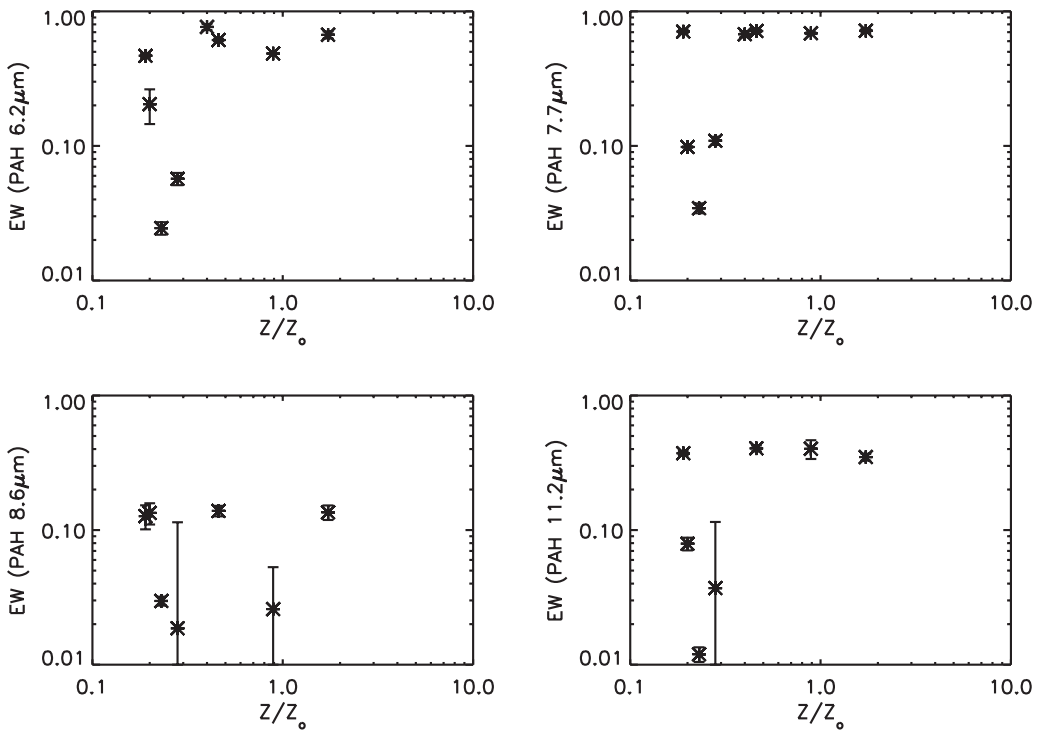

Figure 4.5: Plots of the 6.2, 7.7, 8.6 and 11.2 μm PAH EWs listed in Table 4.4 as a function of metallicity .

and metallicity (Wu *et al.* (2006), Madden *et al.* (2006), Engelbracht *et al.* (2005)). However, this result does continue to support the idea that PAH emission is suppressed in low metallicity environments.

4.3.3.2 PAHs and Radiation Field Hardness

As discussed previously, the large difference in the ionization potentials of Ne^{++} (41eV) and Ne^{+} (22eV), allows the ratio of the two to be used as a tracer of radiation field hardness. It is well known that EWs of PAHs are much reduced in AGN-dominated environments (Weedman *et al.* (2005), and references therein). PAHs are thought to be susceptible to destruction by UV-fields (Geballe *et al.* 1989), and *ISO* observations (e.g.,Cesarsky *et al.* (1996) have indicated that more intense far-UV radiation fields can lead to gradual destruction of PAHs around stellar sources (Brandl *et al.* 2006). The effect of the radiation field hardness on the PAH emission was investigated by plotting the PAH EWs as a function of [Ne III] 15.5 μm / [Ne II] 12.8 μm, as shown in Figure 4.6.

Although the anti-correlation is weak, in particular for the 8.6 μm feature, a suppression in EW of 6.2, 7.7 and 11.2 μm is observed as the ISRF hardens, as indicated by larger [Ne III]/[Ne II] ratios. This trend has also been observed by Madden *et al.* (2006) and Wu *et al.* (2006) who suggest that this is evidence that the deficiency in PAH emission may be related to the destruction of PAHs in the photodissociation region (PDR) by hard UV photons. As an additional check, Madden *et al.* (2006) also plotted the strength of the EW features as a function of the hardness of the interstellar radiation field (ISRF), quantifying this as the total energy divided by the total number of photons to give the mean energy per photon i.e.,

$$\frac{\int_0^\infty I_\nu \mathrm{d}\nu}{\int_0^\infty \frac{I_\nu}{h\nu} \mathrm{d}\nu} \tag{4.2}$$

which represents the relative hardness of the ISRF as measured from modeled SEDs by Galliano *et al.* (2003, 2005), where I_ν is integrated between $\sim$0.4–1 μm. This too increases as the PAH strength decreases and again supports the concept that hard radiation fields may be responsible for the destruction of PAHs.

4.3.3.3 Metallicity and Radiation Field Hardness

As pointed out by Brandl *et al.* (2006), lower metallicities and harder radiation fields go hand in hand in dwarf galaxies, and one cannot unambiguously distinguish between possibly suppressed PAH formation in low-metallicity environments and PAH destruction in harder UV fields. I studied the dependence of [Ne III]/[Ne II] on metallicity and the result is shown in Figure 4.7. A clear trend can be seen between radiation field hardness and an object's metallicity, confirming the opinion of Brandl *et al.* (2006). However, for some cases, a significant scatter is seen at a given metallicity which could be due to local variations or differential/patchy dust extinction in these systems (Wu *et al.* 2006). It also suggests that the metallicity may not be the only factor that affects the radiation field.

Conversely to the relation between these two parameters in dwarf galaxies, Dale *et al.* (2009) find that the metallicity of galaxies with AGN empirically plays little role in the radiation field hardness. Within AGN systems, including both Seyferts and LINERs, the radiation field hardness is likely to depend more on the temperature distribution within the X-ray emitting accreation disk, contributions from non-thermal process (e.g. synchrotron radiation) and the AGN/star formation luminosity ratio.

Overall, in low-metallicity systems such as BCDs, where the ISM is chemically unevolved and

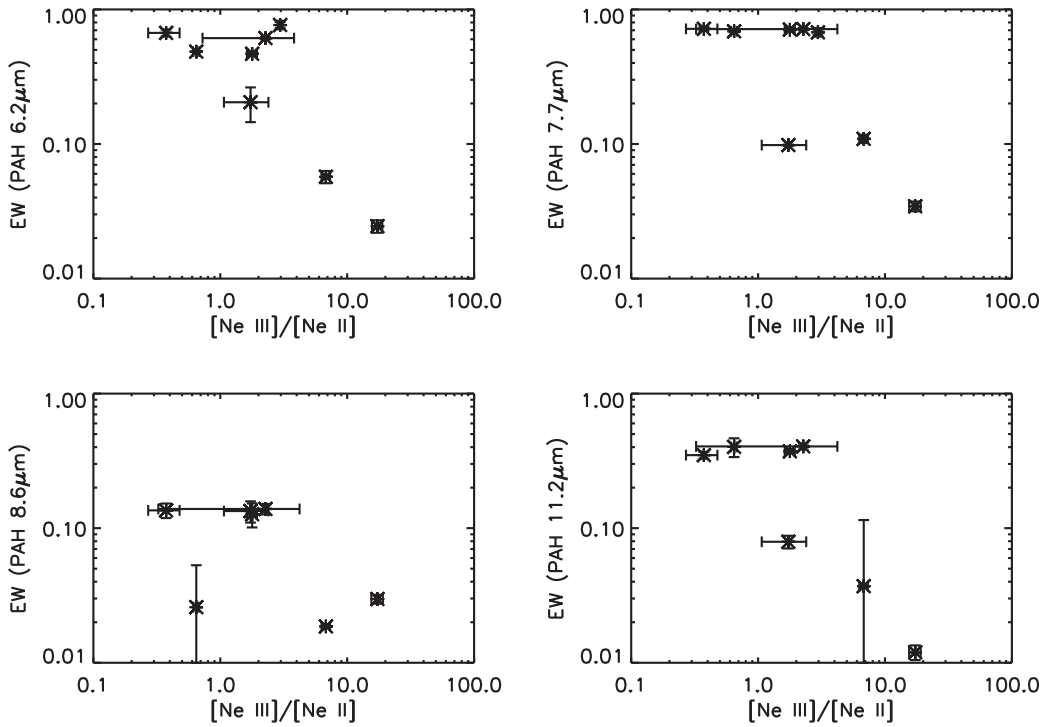

Figure 4.6: Logarithmic plots of PAH equivalent widths (6.2, 7.7, 8.6 and 11.2 μm) versus radiation field hardness (represented by the forbidden line ratio of [Ne III] 15.5μm / [Ne II] 12.8μm).

the low density dust abundance allows the hard UV photons to permeate through the surrounding environment with enough energy to dissociate PAHs, one cannot disentangle these effects. To conclude, as was found by previous studies, the photodestruction of PAHs as well as abundance effects are probably both playing important roles.

4.3.4 IRS Spectral Mapping

In addition to a low-resolution IRS staring mode analysis, I also made use of observations taken with the IRS spectral mapping mode. As detailed in Section 4.1.1, the IRS slit can be stepped parallel or perpendicular to the slit for a specified number and size of steps, providing a spatially resolved spectroscopic analysis. Archival spectral mapping data were available for three galaxies within the sample; Mrk 33, NGC 4670 and NGC 5253. Details of these observations, including AOR numbers, resolution modes and exposure times (calculated as the product of the number of cycles, ramp time, number of pointings in direction and number pointings perpendicular to that

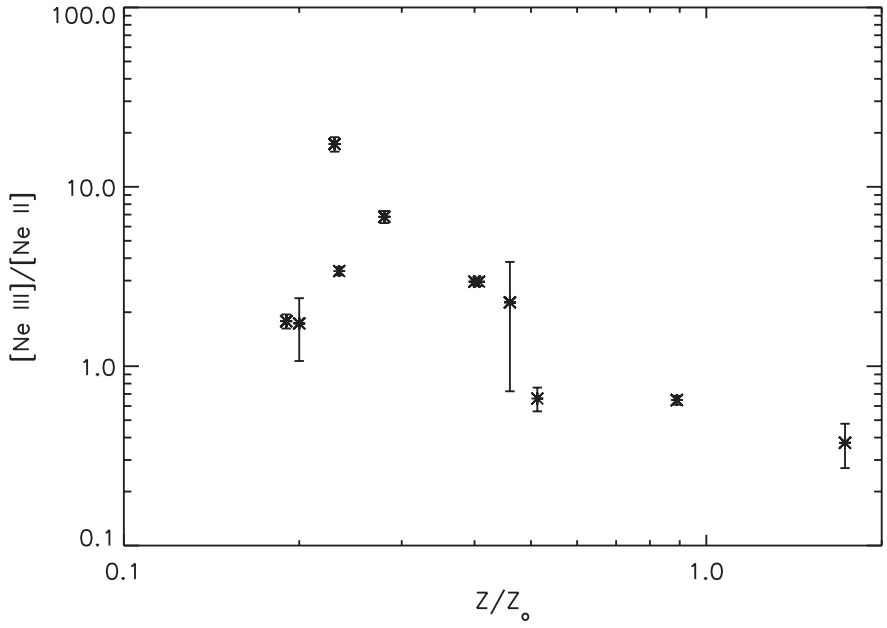

Figure 4.7: Logarithmic plot of [Ne III]/ [Ne II] ratio as a function of metallicity. The forbidden line ratio [Ne III] 15.5μm / [Ne II] 12.8μm is a representation of the radiation field hardness of the BCDs.

direction), are detailed in Table 4.6.

4.3.4.1 Reduction

The reduction and analysis of the spectral mapping data utilised the cube reconstruction algorithm within CUBISM (CUbe Builder for IRS Spectral Mapping) by Smith *et al.* (2007). CUBISM is written in Interactive Data Language (IDL) and is designed to combine sets of 2D IRS spectral images from mapping observations into single 3D spectral cubes. These cubes are parallel to those created in integral field unit observations, as detailed in Section 1.5.1; two spatial dimensions with a third spectral dimension.

The input data for CUBISM consists of basic calibrated data (BCD) spectral images that have been processed by the IRS pipeline (dark sky subtraction, ramp fitting, removal of cosmic rays, linearity correction, wavelength calibration etc). The cubes are constructed with a default pixel size identical to the sampling of the relevant spectrograph module (ranging from 1.85″ to 5.08″). Only one cube per sub-slit can be created, i.e. data must be of the same module. Six sub-slits

Object	AOR key	Obs Date	On Source Times / s					
			SL1	SL2	LL1	LL2	SH	LH
Mrk 33	9489920	15/04/2004	252	252	1200	...	...	...
Mrk 33	9481472	15/04/2004	...	...	...	...	900	900
NGC 4670	4570880	08/01/2004	...	...	...	...	750	350
NGC 4670	4570368	06/06/2005	...	...	...	...	252	...
NGC 4670	4570112	07/01/2004	...	588	...	...	...	...
NGC 5253	4386304	14/07/2004	600	600	36	36	504	252

Table 4.6: Details of IRS spectral mapping observations.

exist; two for each low resolution module (SL1, SL2, LL1, LL2) and two high resolution modules (SH, LH). For example, if SL2 module data are being used and SL1 data are subsequently read in, CUBISM will only extract the offset position of the SL1 data, which can then be used for the subtraction of astrophysical foreground and backgrounds. This option is not available for high-resolution modules and since only the low-resolution modules are used here, this is the method employed for background subtraction. Overlaying the mapped data on an IRAC image allows one to determine the on-source and off-source exposures and thus create background files (suffix –.bgl). Once created, the background spectra must be disabled to prevent them from being included within the cube. Subtraction of backgrounds also mitigates the effects of time varying warm or *rogue* pixels.

Bad-pixel masks are created by visualising the stack and selecting the brightest non-source pixels and can be marked globally (i.e. pixel $[x, y]$ is disabled in all input spectra) or on individual spectra. Alternatively, the bad pixel mask can be generated automatically during cube generation by computing outlier statistics. However, significant power at high spatial frequency (point sources, edges) results in a large natural range of contributing pixel values and care must be taken to ensure that valid data are not flagged (Smith *et al.* 2007).

CUBISM consists of three main components: the project window, a multipurpose viewer (*CubeView*) and a spectrum view and map creation interface (*CubeSpec*). When viewing full spectral cubes, *CubeView* provides an interface to scroll through the wavelength dimension and spectral extraction tool. Once extracted *CubeSpec* is used to view the resultant spectrum, and define wavelength limits and continuum regions for the creation of emission line maps. CUBISM

outputs maps in standard FITS and IPAC Table formats. Spectral extractions are reproduced in ASCII format and include units, labels and information describing the coordinates of the extraction rectangle. All products have associated WCS coordinate systems attached.

4.3.4.2 Spectral Mapping Results

The creation of monochromatic images, or emission line maps, allows spatially resolved insight into the physical and chemical conditions of the BCDs. For example, [Ne III] to [Ne II] or [S IV] to [S III] ratio maps can show the degree and spatial distribution of UV hardness within a source. Similarly, mapped PAH bands highlight the sites of star formation within BCDs (an example of these maps are shown in Figure 4.8). Unfortunately, ratio maps are limited to emission lines that fall within the same observing module, since different modules have different pixel sizes.

NGC 4670:

This galaxy is described in de Vaucouleurs & de Vaucouleurs (1964) as having a small, extremely bright nucleus, faint outer whorls and two faint, smooth arcs. A strong 0.55 arcmin x 0.08 arcmin bar with 'some structure' is noted, as is its non-interacting binary partner NGC 4673, 5.6 arcmin away. Although such internal structures are unresolvable with the IRS spectral mapping data, flux contours maps overlaid onto high resolution images provide information as to the location of the main sources of PAH emission and ionising radiation.

Maps were made of the main PAH bands; 6.2 μm (SL2 module) and 7.7, 8.6, and 11.2 μm (SL1 module) and are shown in Figure 4.8. All maps show two intensity peaks, north east and south west of the center. The NE peak remains brightest throughout all bands, increasing in intensity with wavelength, whereas the SW peak remains at a constant intensity. The suppressed PAH emission in the SW may be due to a harder UV field from a more recent starburst. This hard UV emission may be a result of a WR population, for which evidence in the form of a WR bump was reported by Mas-Hesse & Kunth (1991). Figure 4.9(a) shows the 11.2 μm flux contours overlaid on a *HST* WFPC2 F336W image. The strong SW peak in PAH emission is aligned with a super-star cluster (SSC) that lies SW of the galaxy centre and appears detached from the main, larger star-forming region extending E and NE of the centre. This region could be currently going through, or has recently gone through, a burst in star formation, emitting hard UV photons that could have dissociated the PAHs and caused a decrease in PAH emission. The stronger NE peak in PAH emission lies 0.2$''$ NE of the main star-forming body, hence the increased PAH emission. In support of this, UV spectra presented by Kinney *et al.* (1993) were reported to suggest a relatively

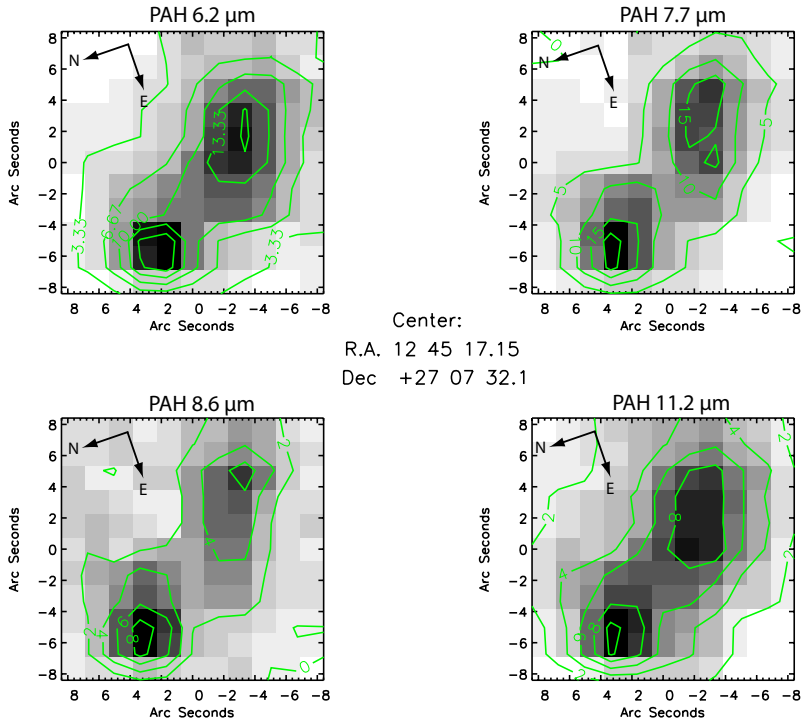

Figure 4.8: Maps of the main PAH features within NGC 4670 from IRS spectral mapping data. PAH flux contours corresponding to the grey scale images are overlaid in green. North and east are indicated by the compass points.

recent burst of star formation, with the young stars superposed on a much older population.

In order to sample the dust at a range of wavelengths, continuum maps were created between the low emission region at 7 μm (6.5–7.3 μm), 14 μm (13.0–14.5 μm) and 10 μm (9–10.3 μm) and are shown in Figure 4.10. As the continuum wavelength of NCG 4670 increases and the dust temperature decreases, only the SW star forming region is visible, another possible indication thta this region may be older with less active star formation than the NE region.

Huchra *et al.* (1983) describe NGC 4670 as an amorphous, metal-deficient blue galaxy whose central regions have a spectrum typical of an H II region (Huchra et al. 1983). The forbidden line emission maps of [Ne III] 12.8 μm, [Ne II] 15.5 μm, [S IV] 10.5 μm and [S III] 18.7 μm (not shown) all show centrally peaked emission with little variance in spatial distribution. Interestingly, ratio maps of [Ne III] /[Ne II] (contours shown in Figure 4.9, green) show a peak $\sim 4''$ south of the star-forming region. In order to verify this mis-alignment, ratio maps of [S IV] / [S III] were created (also shown in Figure 4.9, red contours) and found to show a similar location for their peak. Other than inaccurate WCS information, such a large offset from both star-forming regions is difficult

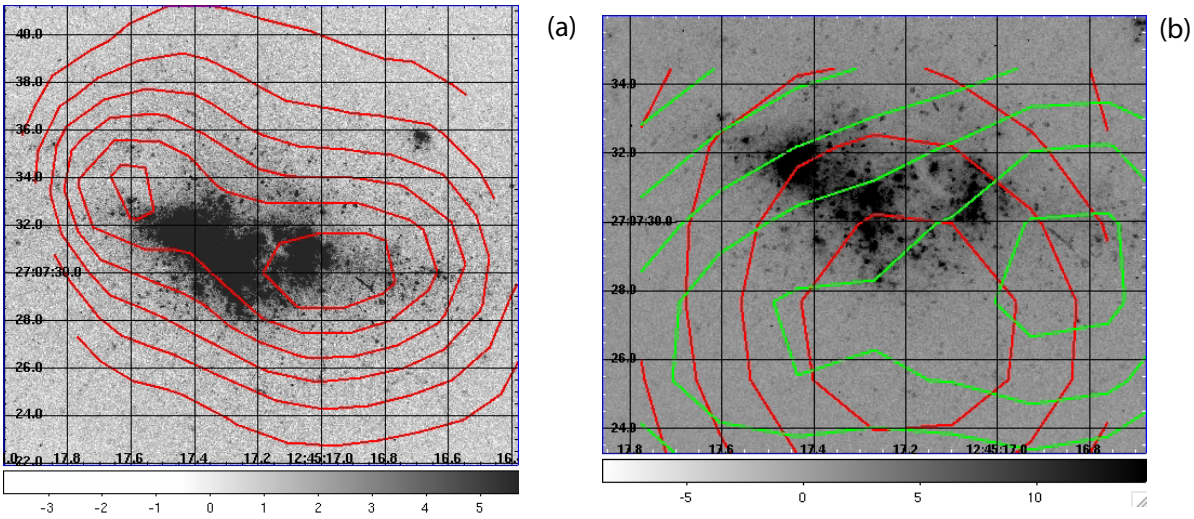

Figure 4.9: *HST* WFPC2 F336W greyscale image of NGC 4670 with: (a) flux contours of the 11.2μm PAH feature overlaid (red); (b) flux ratio map contours of [Ne III] /[Ne II] (green) and [S IV] / [S III] (red) overlaid. North is up, east is left.

to explain. The accuracy of the boresight for both images is 0.07″, which cannot account for the $\sim 0.2''$ offset between the peak in radiation field hardness and location of the SW SSC.

Mrk 33:

As with NGC 4670, maps were made of the main PAH bands and forbidden lines. Background subtraction was not possible for the forbidden line maps because the spectral steps were insufficiently far away from the source, and the source fills the slit throughout all steps. PAH maps, shown in Figure 4.11, show circular shaped contours centered on a singular star forming region in Mrk 33. Little or no variation is seen between the spatial distribution of the PAH emission bands.

Mrk 33, also known as Haro 2, is a much studied galaxy (Legrand *et al.* (1997) and references therein) and the archetypal example of a dwarf elliptical galaxy with a blue central starburst (B-V = 0.36, (Cairós *et al.* 2001*a*)) which sits inside a regular, extended elliptical envelope (this elliptical shape is clearly visible in the IRAC 3.6 μm image shown in Figure 4.12). V-I images presented by Cairós *et al.* (2001*a*) show several dust patches, three of them clearly visible in the S-SE; another, less clear, can be seen to the NW. The location of these dust patches may correlate with higher densities suppressing forbidden line emission SE and NW of the centre of the galaxy, thus resulting in the observed hour-glass shape of the radiation field.

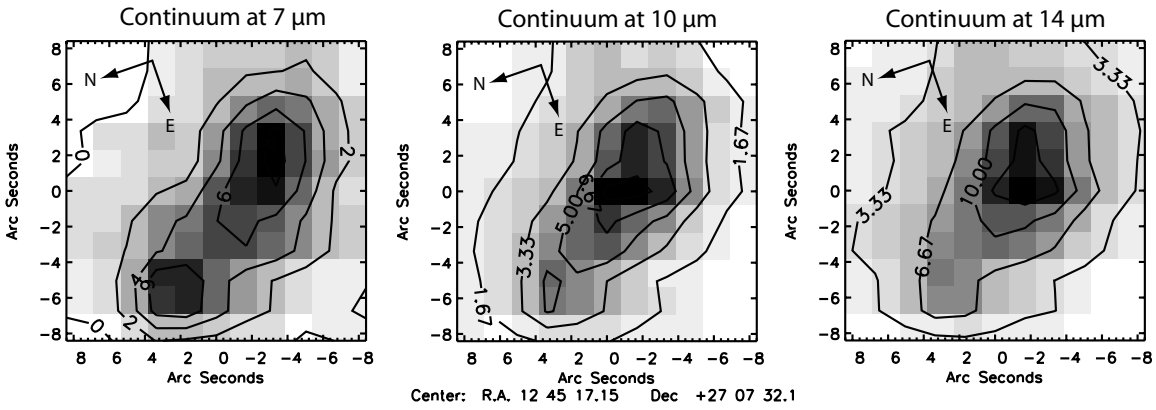

Figure 4.10: Continuum maps at 7, 10 and 14 μm of NGC 4670 from IRS spectral mapping data. Continuum flux contours corresponding to the greyscale images are overlaid. North and east are indicated by the compass points.

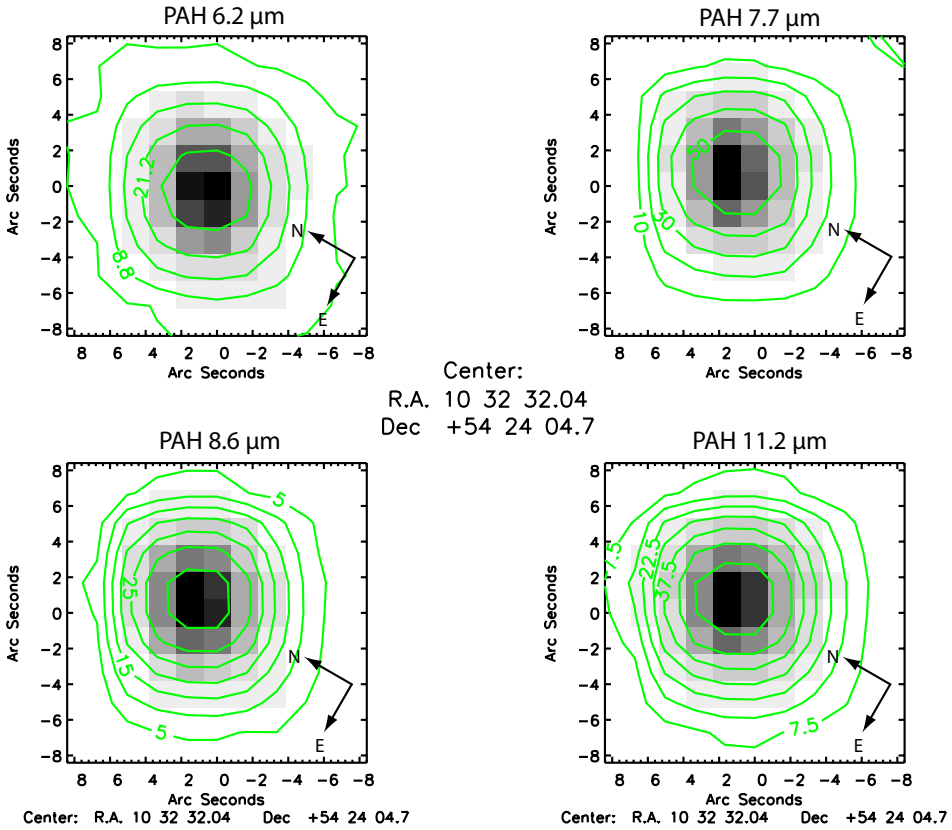

Figure 4.11: Maps of the main PAH features within Mrk 33 from IRS spectral mapping data. PAH flux contours corresponding to the greyscale images are shown in green.

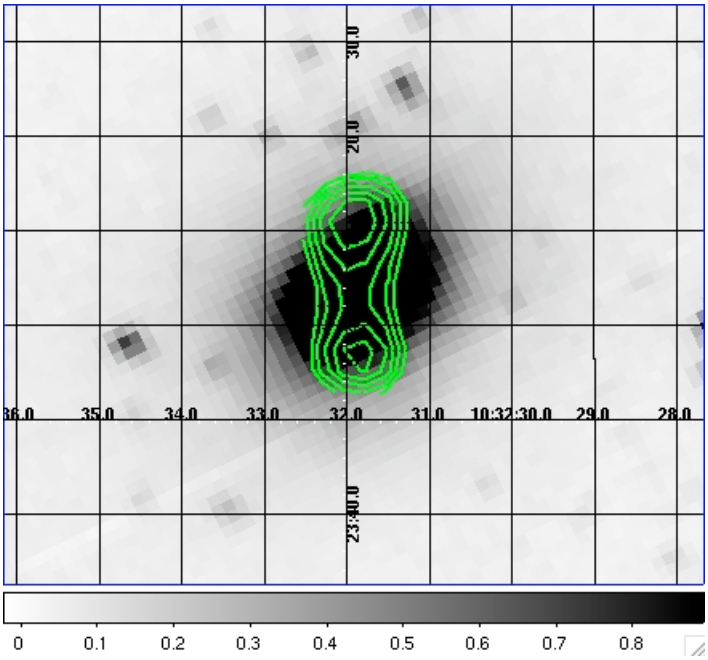

Figure 4.12: IRAC 3.6 μm image of Mrk 33 (greyscale) with map of [Ne III]/[Ne II]flux ratio contours overlaid. Contour levels range from 0.9–1.9 equally spaced by 0.16. North is up, east is left.

Forbidden line maps are centrally peaked with little or no difference in flux distribution between them. Interestingly however, the flux ratio map of [Ne III]/[Ne II] reveals two peaks north and south of the nuclear star forming region (displayed as green contours overlaid on a *Spitzer* IRAC 3.6 μm image in Figure 4.12). Unfortunately high resolution *HST* images are not available for this galaxy, but the 3.6 μm IRAC image (Figure 4.12) is of sufficient resolution to show the misalignment of the radiation field axis with the major axis of the galaxy. An increase in UV radiation hardness above and below the starburst may be an indication of an outflow, or perhaps a lower density region along the contour axis.

NGC 5253:

The quality of data in the low resolution modules for this galaxy is rather poor, showing minimal PAH emission due to a low S/N. However, PAH maps were still obtainable for three of the PAH bands, excluding 7.7 μm since it was not detected, and are shown in Figure 4.13. Minimal variation is seen spatially between the PAH bands, all are observed to have circular flux contours with a notable increase in emission at 11.2 μm which may indicate an abundance of neutral PAHs within this galaxy. The centroids of the PAH contours are well aligned with that of the galaxy.

Figure 4.14 shows the 11.2 μm contours (in green) overlaid on *HST* NICMOS F160W filter

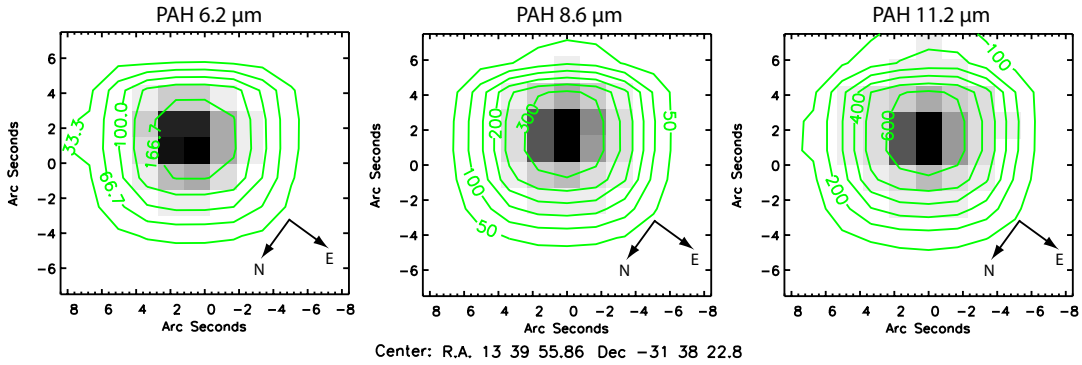

Figure 4.13: Maps of the main PAH features within NGC 5253 from IRS spectral mapping data.

image. The peak in PAH emission aligns reasonably well with that of a large super-star cluster (SSC). The high resolution NICMOS images show a double cluster in the nucleus of NGC 5253, separated by 6–8 pc. Approximately 115 star clusters are found within this galaxy in a report by Cresci *et al.* (2005), ranging from 3–19 Myrs in age.

Also overlaid on the NICMOS image are the [Ne III] / [Ne II] flux ratio map contours (in red). The peak in PAH emission is located $\sim$0.5″ east of the peak in radiation field hardness. However, the uncertainty in RA and DEC of the boresight is given as $\sim 0.7''$ (a factor of 10 higher than the uncertainty for the 11.2 μm image) which could suggest that both peaks might be aligned.

NGC 5253 is classified as a WR-galaxy, with strong WR features seen in its optical spectrum first reported by Walsh & Roy (1987). High S/N observations of Schaerer *et al.* (1997) reveal broad features of N III λ4640, He II λ4686, and C IV λ5808 in two spatial regions, indicating the presence of late-type WN and early-type WC stars (Schaerer *et al.* 1999*b*). Thus the peak in radiation hardness could be the centre of the combined photoionisation structure from the WR and O star population, which would not necessarily align with that of PAH emission since PAH molecules are prone to dissociation by hard UV photons. Beirão *et al.* (2006) have discussed these IRS spectral mapping observations and concluded that the flux within the central 2″ is a result of several thousand O7V stars (Crowther *et al.* (1999), Turner & Beck (2004)). Optical and NIR VLT observations by Cresci *et al.* (2005) detect 115 star clusters with a deduced age range of 3–19 Myr. Turner *et al.* (1998) found a compact radio source representing a hidden super star cluster (SSC) in one of the earliest phases of SSC formation ever observed with H II regions less than $\sim 10^6$ yr in age.

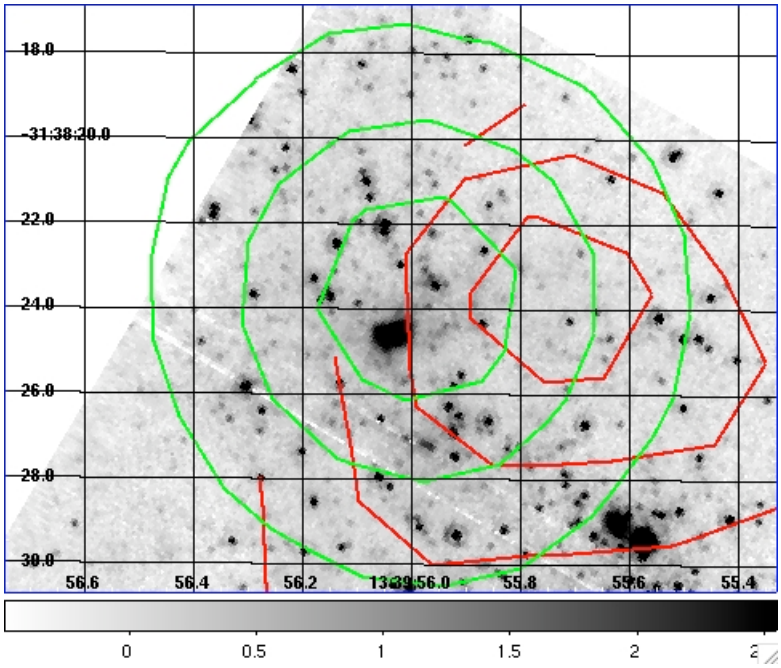

Figure 4.14: *HST* NICMOS F160W image of NGC 5253 (greyscale). Overlaid are 11.2μm PAH contours (green, levels approximately equal to those shown in Figure 4.13) and [Ne III] / [Ne II] flux ratio contours (red, levels range from 0.2–2.6 equally spaced by 0.4). North is up, east is left.

4.4 Infrared Photometry: MIPS & IRAC

Details of the *Spitzer* MIPS and IRAC instruments can be found in Sections 4.1.2 and 4.1.3, respectively.

Photometry was performed on post-basic-calibrated data that are products of a standard reduction pipeline, as well as advanced processing of IRAC and MIPS frames, (Spitzer Science Center 2004). For IRAC data, this extended pipeline refines the telescope pointing, attempts to correct for residual bias and produces mosaic images. For MIPS these data are the result of combining all individual BCD frames from a single AOR; in the case of the photometry mode, the product is an averaged and registered single image suitable for photometric measurements. Both IRAC and MIPS images are calibrated in MJy/sr.

Details of the IRAC and MIPS observations for each of the sources within the sample are given in Table 4.7.

Object Name	AOR keys		OBS date		On Source Time/s					
	IRAC	MIPS	IRAC	MIPS	3.6μm	4.5μm	5.8μm	8μm	24μm	70μm
SBS 0335-052	4327424	4345856	07/04/04	01/02/04	120	120	120	120	48	231
II Zw 40	4345856	4346368	07/03/04	15/03/04	120	120	120	120	48	126
He 2-10	4329472	4347904	20/04/04	08/04/04	48	48	48	48	48	126
Mrk 33	5539840	5559040*	23/11/04	12/04/04	120	120	120	120	42	42
NGC 3353	11180288	12564736	07/05/08	03/04/05	60	60	60	60	48	231
UM 448	4334848	4353280	20/12/05	29/05/04	120	120	120	120	48	126
NGC 5253	4386048	4356864	11/02/04	25/02/04	24	24	24	24	48	126
II Zw 70	10389248	12563456	21/01/05	30/01/05	120	120	120	120	48	231
NGC 7714	4339456	...	2/77/04	05/12/05	24	24	24	24	...	...
I Zw 18	4330752	4349184	03/04/04	07/04/04	120	120	120	120	48	231
Mrk 996	10391296	12555520	17/12/04	12/12/04	120	120	120	120	48	231
UM 461	4335360	4353536	20/12/03	28/05/04	120	120	120	120	48	231
UM 462	4335872	4354048	10/06/04	03/06/04	60	60	60	60	48	126

Table 4.7: Note: the MIPS data set that is asterixed was observed in MIPS Scanning Mode rather than MIPS Photometry Mode

4.4.1 Methods of Photometry

The IMEXAMIN and PHOT tools within the Image Reduction and Analysis Facility (IRAF) [1] were used to obtain photometric fluxes in each of the IRAC and MIPS channels. All of the sources are compact; apertures large enough to encompass all the flux were used. Suitable aperture radii were found using a radial light profile centered on the galaxy. Background flux measurements were taken in an annulus surrounding the source, at a sufficient distance from the galaxy, with the annulus typically 2 pixels in width. No colour corrections were applied, which should have negligible impact on the results, since the corrections listed in the IRAC and MIPS handbooks are typically only a few percent. Unfortunately all MIPS 160 μm data were deemed unusable.

4.4.1.1 IR SEDs

An example of MIPS and IRAC images, in all channels, is given in Figure 4.15. The photometric fluxes of the sample galaxies are given in Table 4.8 and are plotted in Figure 4.16. All SEDs either increase at 8μm or at 24 μm, the latter perhaps due to the presence of the 23 μm feature discussed in Section 4.3.2.

4.4.2 Blackbody Fitting

Within SMART a multiple blackbody fitting routine exists that can determine the temperature of the dust components responsible for the thermal infrared continuum. The user can dictate the number of summed blackbodies via the following summation:

$$Flux\ Density = (1 - e^{-\tau}) \sum_{i} \{\Omega_i B(\lambda, T_i)\} \tag{4.3}$$

where τ is the optical depth, incorporating the emissivity function explained below, Ω is the solid angle of the emission region in steradians, T is the temperature of the emitting region in Kelvin and $B(\lambda, T)$ is the Planck function:

$$B(\lambda, T) = \frac{2hc^2\lambda^{-5}}{exp(hc/k\lambda T) - 1} \tag{4.4}$$

$$= \frac{1.194\lambda^{-5}}{exp(14387.7/\lambda T) - 1} \quad [W/cm^2/\mu m/sr] \tag{4.5}$$

[1] IRAF is distributed by the National Optical Astronomy Observatory, which is operated by the Association of Universities for Research in Astronomy

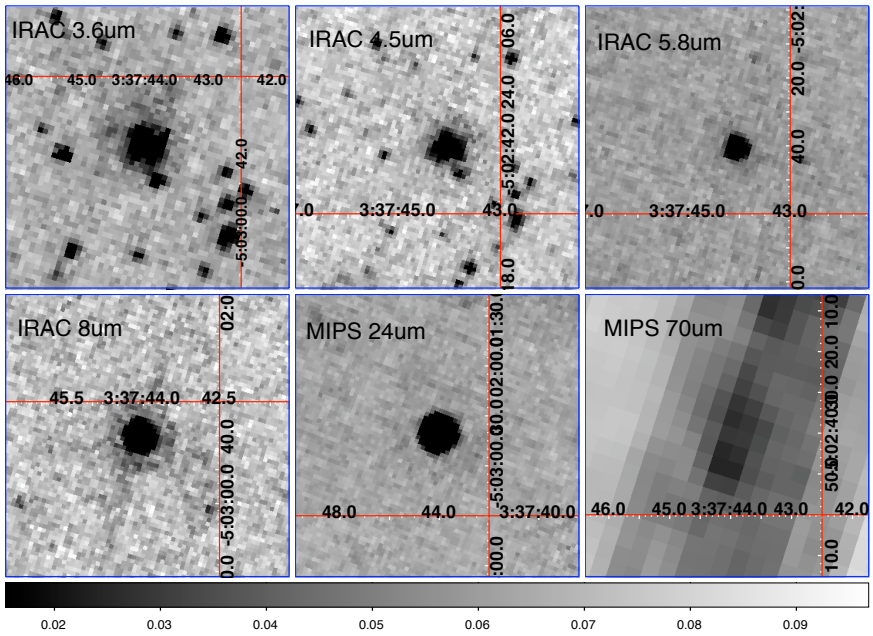

Figure 4.15: IRAC 3.6, 4.5, 5.8 and 8 μm and MIPS 24 and 70 μm images of SBS 0335-052. At a distance of 54 Mpc, 1$''$ corresponds to a linear size of 263 pc. The image is centered on the optical centroid of the galaxy($\alpha = 03^o37'44''$, $\delta = -05^o02'39''$).

where λ is the wavelength of the emission in microns. The dust emissivity law is a function of λ, ($\tau(\lambda) \propto \lambda^{-\alpha}$) where the coefficient α lies between 0 and 2 for warm dust. The blackbody profile will be shifted to shorter wavelengths when fixing α above zero, as this incorporates the emissivity law of the dust that will make it appear hotter. A pure blackbody can be fitted to the SED by fixing α to be zero.

Multiple black-body profiles were fitted to the infrared SEDs using SMART (detailed above). Modified black-bodies were fitted to the points (i.e. an emissivity law with $\alpha = 1$), as they are deemed more realistic in the sense that the emissivity of the dust will shift the profile to shorter wavelengths, making it appear hotter. The modified black-body temperatures are given in Table 4.9, along with the individual component's infrared luminosity relative to solar luminosity (3.83×10^{33} erg s^{-1}, Bradley & Dale (1996)) at the galaxy's respective distance (also given). All of the galaxies showed a two-component dust structure. In general the two components consist of a 160–450 K dust component and a separate 40–200 K component. In comparison with other studies that derive dust temperatures by modelling the SEDs of BCDs, the finding of a two to three component dust structure is typical of BCDs. Marshall *et al.* (2007) found temperatures ranging from 29–45 K, 5–150 K and 160–400 K for cold, cool and warm dust respectively and

when modelling the nuclear SED of a BCD galaxy, a fourth 'hot' dust component could also be observed with temperatures ranging from 1100–1500 K. Hunt *et al.* (2005) decomposed BCD SEDs using DUSTY (a code specifically designed to solve the radiative transfer equations within a dusty environment) and found an inner dust component with temperatures of 400-650 K and an outer, cooler dust structure at 20–70 K.

As a comparison, blackbody temperatures were derived from fits to the high resolution IRS spectral continua for each galaxy, and are also given in Table 4.9. Example fits to the spectra of II Zw 40, NGC 5253, NGC 7714 and UM 448 are shown in Figure 4.17. The wavelength range for these fits (9.9–37.2 μm) is more restricted than that of the photometric points and thus samples a smaller range in dust temperature. A two component fit is again optimal, with average temperatures of 60–90 K and 170–200 K. Overall, in relation to the findings of Marshall *et al.* (2007) the two temperatures obtained from the photometric data points appear to sample the warm and cold dust components, whereas the spectra sample the warm–cool dust components of each galaxy. SBS 0335-052, the lowest metallicity galaxy, was the only galaxy whose F-IR photometric data could not be fitted with a cold dust component.

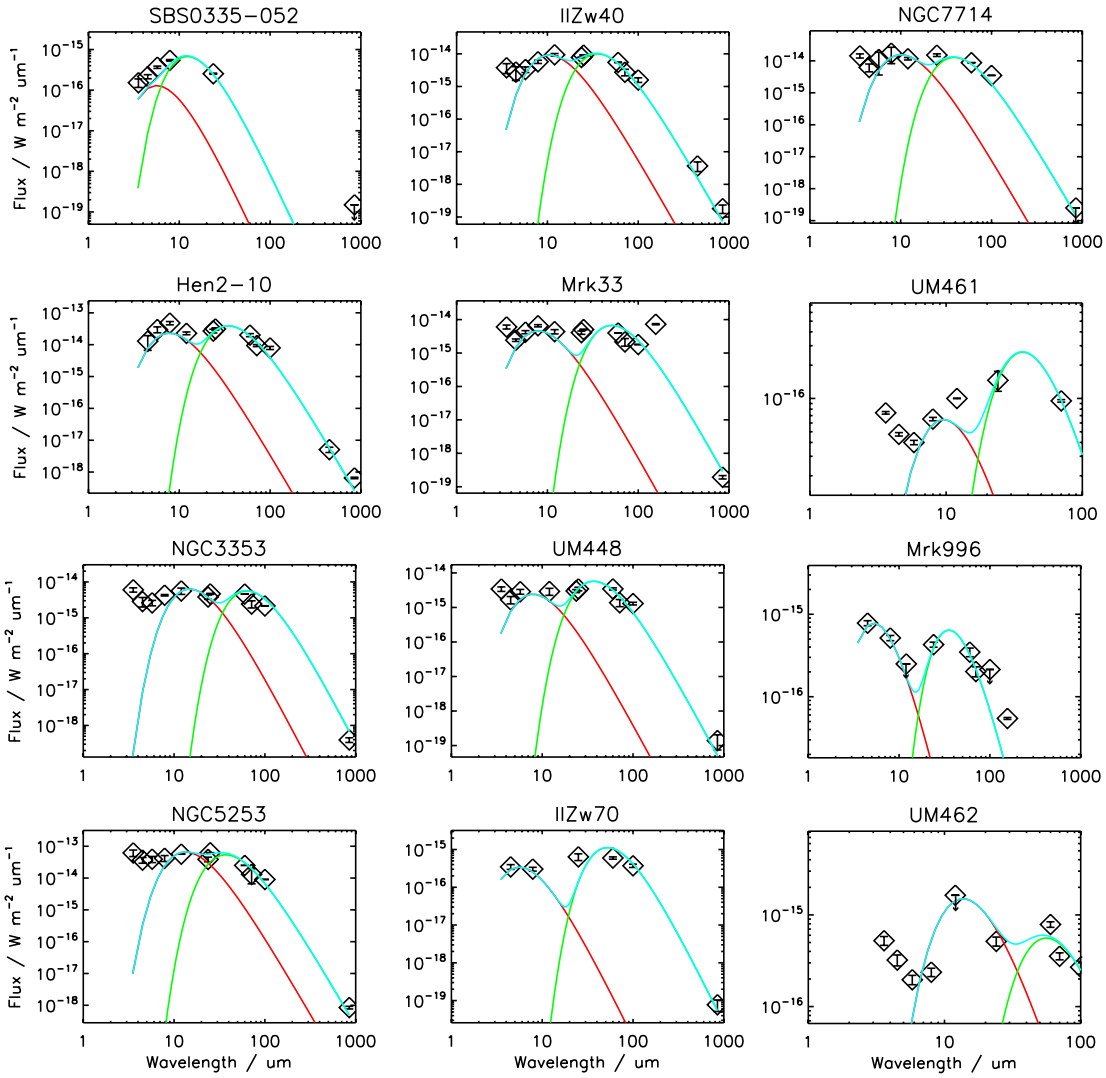

Figure 4.16: BCD spectral energy distributions from MIPS and IRAC aperture photometry of 12 BCDs, along with IRAS 12, 25, 60 and 100 μm data (from NED) and SCUBA 450 and 850 μm (from J. Fabbri, private communication). The blackbody fits for the hotter component are shown in red, the colder component in green and the sum of blackbodies is shown in blue.

λ/μm	SBS0335-052 ($\times10^{16}$)	II Zw40 ($\times10^{15}$)	He 2-10 ($\times10^{14}$)	Mrk 33 ($\times10^{15}$)	NGC 3353 ($\times10^{15}$)	UM 448 ($\times10^{15}$)
	IRS fluxes ($\times10^{-15}$W m^{-2} μm^{-1})					
3.6	15.2±3.60	3.74±1.25	...	6.03±0.81	6.04±0.82	3.42±0.51
4.5	21.5±2.50	2.77±1.15	0.12±0.06	2.42±0.21	2.84±0.85	1.66±0.40
5.8	36.7±2.40	3.32±0.65	0.29±0.06	4.22±0.45	2.61±0.45	2.86±0.46
8.0	54.3±2.30	5.71±0.75	0.47±0.06	6.55±0.50	4.27±0.20	...
24.0	25.3±0.80	7.75±0.21	0.26±0.04	4.07±0.45	3.82±0.54	2.99±0.30
70.0	...	2.73±0.62	0.09±0.07	2.16±0.55	2.43±0.55	1.37±0.32
	IRAS fluxes ($\times10^{-15}$W m^{-2} μm^{-1})					
12.0	...	9.37±0.83	0.23 ± 0.02	4.37 ± 0.64	5.62± 1.12	2.91 ± 0.66
25.0	...	9.16±0.15	0.31 ± 0.03	5.04 ± 0.14	4.65 ± 0.14	3.43 ± 0.41
60.0	...	5.47±0.13	0.20 ± 0.02	3.97 ± 0.04	4.61 ± 0.04	3.44 ± 0.24
100.0	...	1.58±0.25	0.08 ± 0.01	1.79 ± 0.04	2.14 ± 0.03	1.29 ± 0.12
	SCUBA fluxes ($\times10^{-19}$W m^{-2} μm^{-1})					
450.0	...	36.7±12.0	0.51 ± 0.10	...	...	...
850.0	≤149.0	1.80±0.52	0.07 ±0.01	1.93±0.22	3.94 ± 0.59	1.39 ± 0.65

λ/μm	NGC 5253 ($\times10^{16}$)	II Zw70 ($\times10^{14}$)	NGC 7714 ($\times10^{15}$)	MRK 996 ($\times10^{16}$)	UM 461 ($\times10^{16}$)	UM 462 ($\times10^{16}$)
	IRS fluxes ($\times10^{-16}$W m^{-2} μm^{-1})					
3.6	6.17± 1.43	...	1.43± 0.21	...	0.74±0.20	5.23±0.58
4.5	3.66± 0.75	0.03±0.01	0.62± 0.17	7.81±0.51	0.47±0.17	3.21±0.44
5.8	3.91± 0.85	...	1.11±0.75	...	0.39±0.18	1.96±0.23
8.0	4.20± 0.90	0.03±0.01	1.73± 0.92	5.15±0.38	0.65±0.23	2.37±0.25
24.0	3.88± 0.65	...	...	4.28±0.30	1.46±0.30	5.15±0.58
70.0	1.30± 0.65	...	...	2.02±0.28	0.95±0.25	3.54±0.31
	IRAS fluxes ($\times10^{-16}$W m^{-2} μm^{-1})					
12.0	5.66 ± 0.06	...	1.16 ± 0.10	≤2.50	...	≤16.3
25.0	6.26 ± 0.02	0.06± 0.01	1.51 ± 0.14	...	...	...
60.0	2.50 ± 0.04	0.06 ± 0.004	0.88 ± 0.002	3.47 ± 0.42	...	7.86 ± 0.55
100.0	0.902 ± 0.01	0.05 ± 0.01	0.35 ± 0.004	≤2.13	...	2.68 ± 0.43
	SCUBA fluxes ($\times10^{-20}$W m^{-2} μm^{-1})					
450.0	...	...	...	...	...	...
850.0	0.84 ± 0.08	0.08± 0.03	≤0.25	...	...	...

Table 4.8: Photometric fluxes of the sources measured from MIPS and IRAC data along with IRAS data from NED and SCUBA data obtained from J.Fabbri (private communication).

Table 4.9: Blackbody temperatures obtained from fits to the IRAC, MIPS, IRAS and SCUBA photometric spectral energy distributions and from fits to IRS high-resolution spectra.

Name	Distance / Mpc	T_1 / K	T_2 / K	$\log(L_1/L_{sun})$	$\log(L_2/L_{sun})$	$\log(L_{total}/L_{sun})$	$T_{1Spectra}$/ K	$T_{2Spectra}$/ K
SBS 0335-052	53.7	430	—	4.93	5.98	6.02	180	99
II Zw 40	11.1	230	68	5.68	6.24	6.35	170	76
He 2-10	10.4	310	69	5.89	6.77	6.83	180	82
Mrk 33	24.9	310	47	5.96	6.93	6.98	170	56
NGC 3353	18.5	160	38	6.11	6.69	6.79	94	38
UM 448	84.2	310	65	6.74	7.78	7.82	180	77
NGC 5253	2.5	180	65	5.36	5.71	5.87	190	79
II Zw 70	23.7	430	46	4.64	6.12	6.14	180	75
NGC 7714	38.5	240	62	6.97	7.47	7.59	190	83
Mrk 996	22.3	460	68	4.91	5.66	5.73	310	110
UM 461	12.7	250	66	3.60	4.79	4.82	320	110
UM 462	14.4	180	43	5.23	5.42	5.64	260	90

A study by Engelbracht *et al.* (2005) showed that the 8-to-24 μm flux density ratio depends strongly on metallicity in star-forming galaxies. Their results show a clear change in the 8-to-24 μm colour between one-third and one-fifth solar metallicity, between objects that show evidence of 8μm PAH emission, and those that do not. This result was confirmed by Wu *et al.* (2006) for a subset of galaxies that all show PAH emission (with the exception of SBS 0335-052). Both conclude that this is further evidence of PAH weakening at low metallicity. Figure 4.18 shows the plot of galaxy metallicity as a function of the 8-to-24 μm colour and it possibly confirms a steep transition in color at Z=0.2–0.3 $Z_{\odot}$ (boundaries labelled as dashed lines), although considering the lack of data points a linear rise between Z=0.1–0.4 followed by a plateau is equally plausible. All the galaxies, again with the exception of SBS 0335-052 (labelled and outlying from the general trend), show evidence of PAH emission. However, as Wu *et al.* (2006) comment, a lower F_8/F_{24} could also indicate increased emission at 24 μm as a result of warmer dust which would imply that lower metallicity galaxies have a warmer dust content. To investigate this hypothesis, I plotted dust temperatures as a function of metallicity using the black-body temperatures fitted to the high resolution IRS continua discussed in Section 4.4.2. Figure 4.19 shows that there is no correlation between the F_8/F_{24} colour ratio and dust temperature and for a given temperature there is a large range in F_8/F_{24}. I therefore conclude that the dependence of F_8/F_{24} colour ratio on metallicity can be interpreted as evidence in support of PAH suppression within low-metallicity environments and that emission from warm dust components has a negligible effect on the this dependence.

4.5 Summary

This chapter has described a mid-IR spectroscopic and photometric analysis of a subset of blue compact dwarf galaxies using *Spitzer* IRS, IRAC and MIPS archival data. A variety of methods and techniques were applied to the mid-IR spectra and photometric SEDs of each source in order to acquire information about its dust properties.

Emission line measurements of the forbidden lines and PAH features within the high and low-resolution IRS spectra were made and documented. The density diagnostic ratio [S III] 18.7 μm/33.5 μm, when available, was used to determine electron densities for seven BCDs. The range in $N_{\rm e}$ (400–3000 cm^{-3}) reflected the typically low density of the ISM in BCDs and was found to agree with previous optically derived densities.

The suppression of PAH emission in BCDs has been of some interest to the astrophysical

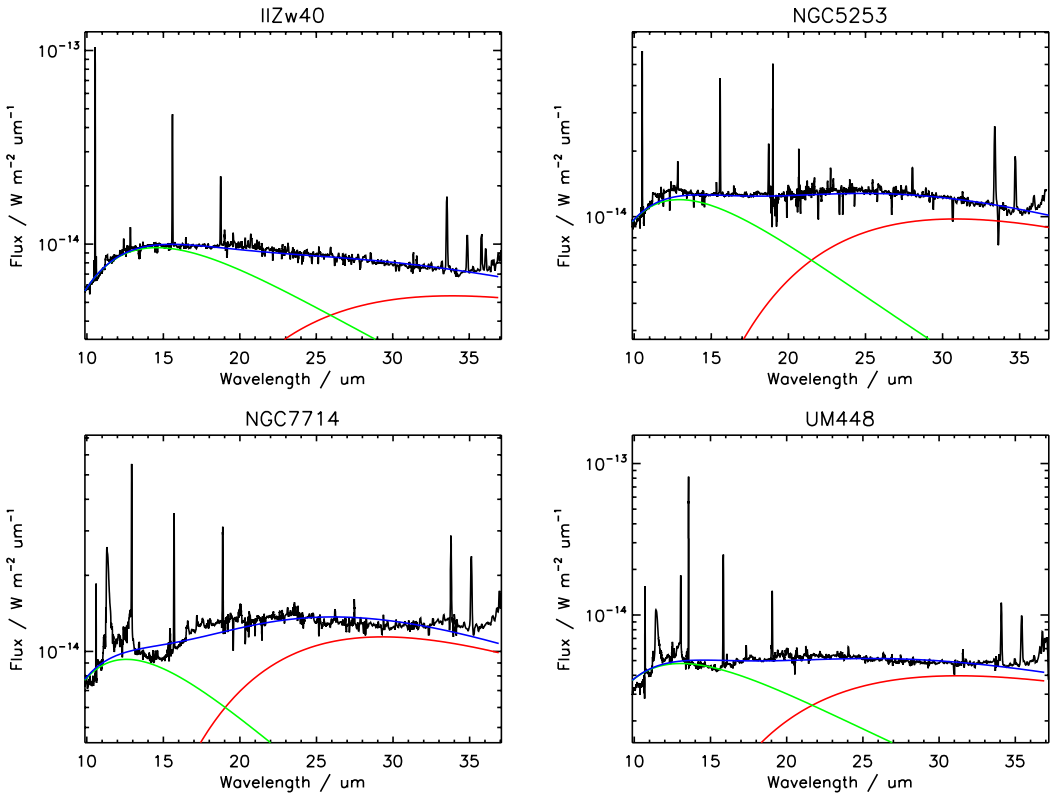

Figure 4.17: Four examples of BCD high resolution IRS spectra with two component modified blackbody fits. The blackbody fits for the hotter component are shown in green, the colder component in red and the sum of blackbodies is shown in blue. The temperatures of each component for those shown and for 8 more BCDs are given in Table 4.9.

community and the dominant mechanism responsible, i.e. whether it be destruction or formation effects, remains unknown. Several methods were used within this chapter to investigate this depletion of PAH emission, using equivalent width (EW) measurements of the four main PAH bands at 6.2, 7.7, 8.6 and 11.2 μm. Firstly, plots of PAH EW as a function of metallicity confirmed that the strength of PAH emission is dependent on an object's metallicity. Assuming that AGB stars are the main source of carbonaceous particles, this reduction is to be expected in low metallicty environments where AGB stars remain unevolved and have not yet contributed to the carbon reservoir. Secondly, PAH EWs were plotted as a function of radiation field hardness, as indicated by the large difference in ionisation potential between Ne^{2+} and Ne^{+}. This showed that PAH emission is

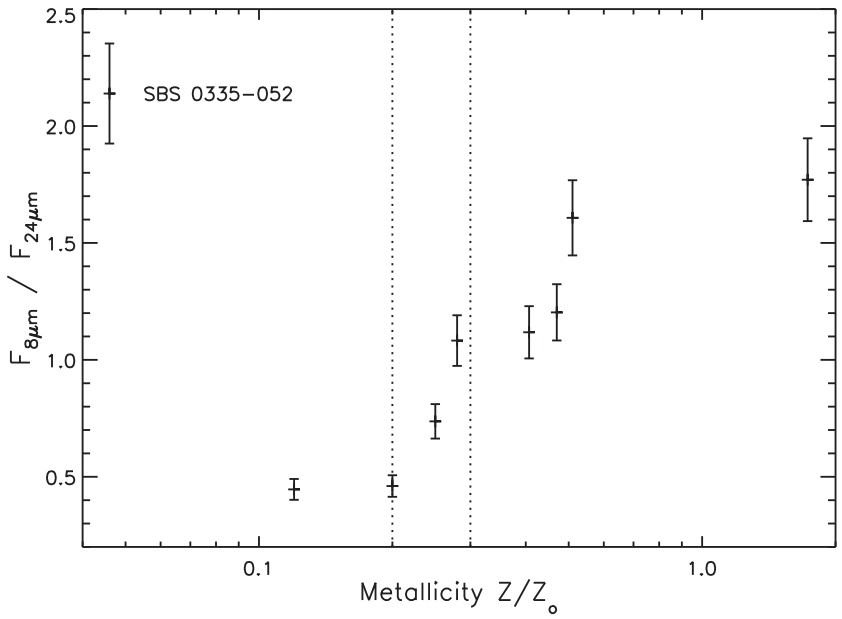

Figure 4.18: Galaxy metallicity as a function of the 8-to24 μ flux ratio. Photometric measurements were made directly from the IRAC and MIPS data respectively. Dashed lines represent the 1/5-1/3 $Z_{\odot}$ transition region reported by Engelbracht *et al.* (2005) and Wu *et al.* (2006).

dependent also on the strength of the UV photons propagating throughout the ISM. I thus conclude and agree with previous findings that photodestruction of PAHs as well as formation effects can be responsible for the lack of PAH molecules within these low-metallicity and relatively chemically unevolved systems.

IRS spectral mapping observations were presented for NGC 4670, Mrk 33 and NGC 5253. Stepping the IRS slit across the galaxy adds a spatial dimension to the IRS staring-mode spectroscopy that allows the creation of PAH maps and radiation field hardness maps using [Ne III]/[Ne II]. By overlaying the PAH map contours onto high resolution *HST* WFPC2 and NICMOS images (where available) it can be seen that the PAH emission is centrally localised to the main star-forming structures within each galaxy. The [Ne III]/[Ne II] ratio contours were also overlaid onto the images but did not show an expected alignment with the main SF regions. This is either due to inaccuracies in the WCS information in the LL modules or else the displacements could suggest the occurrence of outflow events.

Finally, 3.6–850 μm SEDs were derived from aperture photometry performed on MIPS and IRAC data and archive IRAS and SCUBA data. Multiple black-body profiles were fitted to the SEDs in order to assess the temperatures of the dust responsible for emission at these wavelengths.

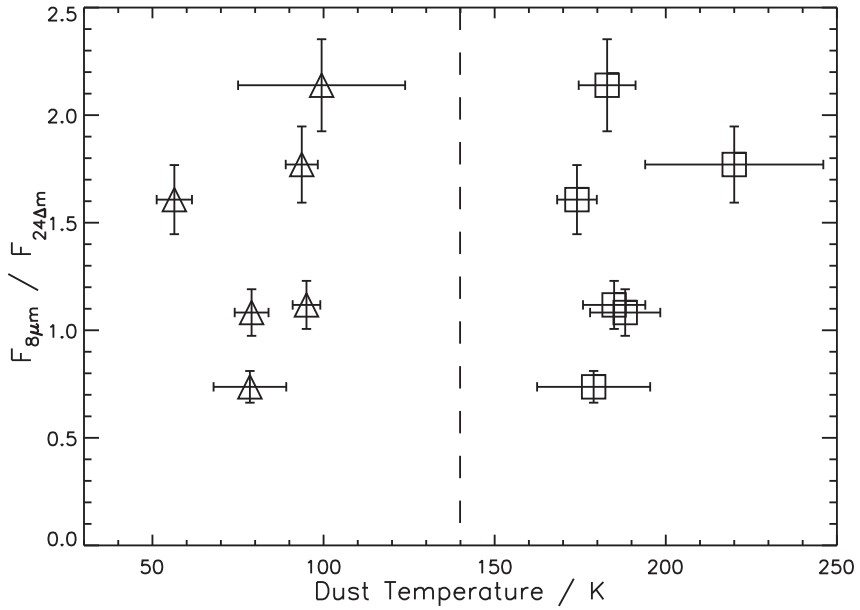

Figure 4.19: Blackbody dust temperature verses the 8–24 μm photometric flux ratio. The photometric flux-ratio measurements were made directly from IRAC and MIPS data. The dust temperatures were derived from black-body fits to IRS spectral continua, which typically revealed warm (squares) and cool (triangle) dust components.

All SEDs could be fitted with a two dust components; a cooler 40–70 K component and a warmer 160–460 K component. The cold dust component is typical of dust temperatures in the outer regions of BCDs or perhaps molecular clouds, whilst the warmer component is more reminiscent of the temperatures of dust in H II regions within the BCDs. Blackbody temperatures were also derived from fits to IRS high resolution IRS spectral continua. A two component fit was also optimal here with warmer average temperatures of 60–90 K and 170–200 K; a result of the shorter IRS wavelength limits of 9.9–37.2 μm. I was also able to confirm the metallicity dependence on the 8–24 μm colour ratio and found that there is a negligible contribution to this relationship from warm dust enhancing the 24 μm flux.

The IRS spectra of Mrk 996 presented here will complement the optical IFU data presented in Chapter 2 in the modelling of Mrk 996 using the 3D photoionisation code MOCASSIN that will be presented in the next chapter. The IRS spectrum provides constraints on the mid-IR SED of the galaxy and allows one to constrain the dust grain composition and grain size distribution in Mrk 996.

CHAPTER 5

3D PHOTOIONISATION MODELLING OF MRK 996

5.1 Modelling BCDs

Blue compact dwarf galaxies can be simplified structurally as having multiple ionised sources in the form of star-forming or star-bursting regions, distributed throughout gas which is photoionised to give H II regions, some with photodissociation reggions (PDRs). Often classified as giant/irregular H II regions, these galaxies are often far from symmetric in shape with some undergoing mergers or interactions with other H II regions or with larger, more gaseous galaxies. Their stellar populations are complex, usually consisting of young and powerful (e.g. WR) stars, superimposed on an older, underlying population (Kunth & Östlin 2000). Consequently, the modelling of BCDs is unavoidably a highly asymmetric, non-symmetric, multi-dimensional problem.

Several studies have been devoted to understanding the stellar features (continuum and lines) in BCDs in terms of stellar population synthesis models, with the aim of understanding the true ages of the stellar populations within BCDs, whose stellar populations are usually unresolvable (e.g. Raimann *et al.* (2000)). However, there is a lack of spatially resolved studies of the ionising sources and their links to the properties of the surrounding gas. This can be approached by means of photoionisation models that can be used to reproduce the integrated line fluxes and equivalent widths of observed lines emitted by the ionised gas, under various assumptions about the objects geometry, metal content, gas density and ionising radiation.

Previous attempts to model BCDs have mostly involved the use of 1-D photoionisation codes such as CLOUDY (Ferland 1993), PHOTO (Stasińska 1984) and NEBULA (Rubin 1968). The input parameters consist of the intensity and spectral distribution of the ionising radiation field, the chemical composition of the nebular gas and its density distribution. BCDs are treated as giant H II regions and it is generally supposed that the radiation field originates from a compact cluster of stars; one simply adds up the radiation from the different stars composing the cluster. As noted by Stasińska (2000*b*) if the typical separation between the exciting stars is an appreciable fraction of the size of the giant H II region, the validity of this assumption breaks down. The radiation field is constructed using stellar population synthesis codes (a review of which is given by Stasińska (2000*a*)) and a specific model atmosphere is adopted for the appropriate combination of metallicity, effective temperature and gravity. One of the major problems can be the geometry of the H II region itself. The above 1-D photoionisation codes are constructed for simple geometries (plane parallel or spherical), in which the gas density can vary only along one dimension. In reality, inhomogeneities within BCDs show up on every scale, and there is often no obvious symmetry characterising these objects.

Detailed photoionisation analyses have been undertaken for only a few BCDs. Three such studies are of NGC 7714 (modelled by Garcia-Vargas *et al.* (1997) and whose mid-IR spectra are presented in Chapter 4), NGC 2653 (by Luridiana *et al.* (1999)) and I Zw18 (modelled by Stasińska & Schaerer (1999)). In all of them, the predicted [O III] λ5007/λ4363 ratio was far higher than the observed value; this is discussed in more detail in Section 5.2.6. Possible explanations for this discrepancy include density enhancements and over-simplification of the nebular geometry, causing an underestimation of the electron temperature.

When modelling complex photoionised structures such as BCDs, one must ask 'How realistic can a model be?'. Here I attempt to model the BCD Mrk 996, for which the spatially resolved spectroscopic observations presented in Chapter 3 show evidence of multiple ionisation sources distributed throughout a core ionised region, along with a density distribution that is highly inhomogeneous. This chapter details the first stages of modelling Mrk 996 using the 3-D photoionisation model MOCASSIN (Ercolano *et al.* (2003, 2005, 2008)), a code designed to encompass asymmetric geometries and chemical and density inhomogeneities.

5.2 Modelling Mrk 996

5.2.1 Previous Attempts at Modelling Mrk 996: CLOUDY modelling

As part of the first study of Mrk 996, Thuan *et al.* (1996) (TIL96 hereafter), attempted to model it as a H II region using the photoionisation code CLOUDY (Ferland 1993) which has been used to simulate emission-line regions ranging from the intergalactic medium to the high-density local thermodynamic equilibrium (LTE) limit (Ferland 1990). It predicts the thermal, ionization, and chemical structure of a cloud and its spectrum. Failing to satisfactorily reproduce both the high and low-excitation line intensities with an ionisation-bounded, low-density H II region model, TIL96 adopted a density-bounded model, which required the specification of an outer radius, R_{out}, beyond which the electron density drops to zero. Input parameters for each model include $Q(H)$, the logarithm of the number of ionising photons emitted per second, T_{eff}, the effective temperature of the ionising stars and R_{in}, the inner radius (chosen to be 1 pc to account for the finite size of the ionising star cluster). They adopted a two-zone model, with an inner high-density zone with density log(N_e/cm^3)=6.66 and a low-density zone with density log(N_e/cm^3)=2.65 derived from the [S II] doublet ratio λ6716/λ6731. Other input parameters included a filling factor,f, and helium and heavy element abundances relative to hydrogen. Since the purpose of this model was to compute abundances for Mrk 996, they adopted starting abundances observed in low-metallicity BCDs by Thuan *et al.* (1995).

Their two best fit model parameters that gave line intensities closest to the observed ones and yielded the correct total dereddened Hβ luminosity were almost identical, apart from the nitrogen abundance which was increased by a factor of 6 in the first model. Interestingly, the best fitting filling factor, f = 2.63E-05, was several magnitudes lower than those typically found for H II regions (Kennicutt 1984), possibly due to the compact nature of Mrk 996. Overall, both models run by TIL96 successfully reproduced all the observed emission line intensities, apart from He I λ4471 and λ5876. Their second model, with an increased nitrogen abundance, was necessary to correctly predict the [N III] λ1750 line intensity. However, this over-predicted the line intensity of nebular [N II] λ6584, produced in the lower-excitation outer zone, by a factor of $\sim$5.6. The second model successfully reproduced all other high-excitation nebular lines, as well as [O III] λ4363 and [N II] λ5755. They concluded that in order to correctly predict all the nitrogen line intensities, both for the semiforbidden and auroral lines in the high-excitation region and for the nebular lines in the low-excitation region, a hybrid model was required. Such a model would feature a high nitrogen abundance in the high density, high-excitation inner region and a low nitrogen abundance

in the low-density, low-excitation outer region.

A nitrogen abundance gradient throughout Mrk 996 would also be consistent with the detection of WN stars within the central region of the galaxy, as discussed in Section 3.6, since WN stars could pollute the inner regions with their nitrogen-rich stellar winds. All TIL96 CLOUDY models involved $R_{out} = 300$ pc, which they estimated as containing the nuclear star forming region of Mrk 996. In comparison to my Hα flux contours overlaid on the [O III] λ4363 emission line map shown in Figure 3.8, their adopted $R_{out} = 300$ pc is a fair estimate, given that the defined 'outer region' is 5.3×6.3″ (575×685 pc^2) in size, with an 'inner region' of 1.7×2.3″ (185×250 pc^2). However, the difference in radius between the inner high-excitation region and the outer low-excitation region was not specified, it is only said that a transition radius of ∼100 pc exists between the high- and low-excitation zones. In my nitrogen abundance map for the narrow component flux, shown in Figure 3.17, it can be seen that N/H remains constant throughout the core but shows a two-fold increase north-east of the core region. I derived large nitrogen abundances from the broad component fluxes, showing an enrichment of $\lesssim$19 in the core region compared to those derived from the narrow component fluxes. Therefore a gradient of nitrogen abundance from the core outwards is an over-simplification and is a result of integrating over the entire line velocity profile rather than deconvolving the velocity components.

5.2.1.1 A new approach

Other than the obvious restrictions of a 1-D code such as the inability to treat asymmetries and inhomogeneous distributions of clumps/condenstations, additional drawbacks exists for 1-D codes when attempting to model complex H II regions such as Mrk 996. A realistic 3-D model of the electron density structure within Mrk 996 would require pockets of high electron density ($\sim 10^7$ cm^{-3}) immersed within a lower density region of $\sim$ 100 cm^{-3}, as observed for the spatially co-existing broad and narrow component emission lines. Also, an accurate treatment of a filling factor (essential in modelling H II regions) and defined as a fraction of total volume occupied by density condensations (see Section 5.2.3) cannot be attained without using a 3-D code. 1-D analytical codes treat filling factors by approximation, i.e simulating an overall lower density rather than having empty cells.

Therefore, in order to remedy the shortcomings of the previous modelling's one-dimensional approach, I decided to attempt a 3-D approach. Here I describe an investigation which aims at a representation using the 3-D photoionisation code, MOCASSIN. Whilst a model of Mrk 996's narrow component emission was achievable using a 1-D approach, an attempt to model both the

narrow and broad component emission required the code's 3-D capabilities.

5.2.2 MOCASSIN: a 3-D Photoionisation Code

Computational models of photoionised regions are sometimes limited because of the necessity of assuming spherical symmetry when solving the equations of radiative transfer. It can be seen from numerous HST and *Spitzer* imaging studies that this is often not a realistic assumption to make, since a nebula is often ionised by multiple non-centrally located sources. Also, the gas within these systems is inhomogeneous, containing clumps and condensations that are optically thick to ionising radiation that will produce shadow regions, where the ionic and temperature structure is determined by diffuse fields that can only be self consistently treated within a 3-D framework. These shortcomings have been remedied with the development of MOCASSIN (MOnte CArlo SimulationS of Ionised Nebulae, Ercolano *et al.* (2003, 2005, 2008)), a 3-dimensional photoionsation code using a Monte Carlo approach to the radiative transfer problem. The basic idea behind a MC treatment of radiative transfer is to simulate the individual processes of absorption, re-emisssion and scattering of photons as they leave the ionisation sources and diffuse through the nebula. Contrary to classical analytical approaches to the solution of radiative transfer (RT) equations, the MC method uses a discrete description of the radiation field consisting of enegry packets (i.e. monochromatic bundles of photons) to represent the simulation quanta.

The code was designed to build realistic models of photoionised nebulae with arbitrary geometries and density distributions and allowing the secondary radiation field to be accurately treated. Multiple non-central ionising sources and multiple gas chemistries are allowed within the grid, along with subgrids to resolve detail in areas of the grid.

A further development of this code was the inclusion of a fully self-consistent treatment of dust RT within a photoionised region, including all the microphysical processes, including gas-grain collisions, coupling of the gas and dust phases and photoelectric heating from the grain surface (Ercolano *et al.* 2005).

This code is ideally suited for the modelling of ionised regions within BCDs, since it allows for the presence of dust grains within the gas, which can potentially affect the RT and the physical conditions of the gas as both components compete to absorb the UV continuum photons. Furthermore, this version of MOCASSIN also treats discrete grain sizes and different species separately, enabling an accurate determination of dust temperatures and spectral energy distributions (SEDs) (Ercolano *et al.* 2005).

5.2.2.1 The Model Grids

The volume of space to be modeled is represented by a 3-dimensional cartesian grid where the gas and dust physical properties are constant within each grid cell. Defined properties within each cell are: the number density of the gas and dust (n_H, n_D), the electron temperature and density ($T_{\rm e}$ and $N_{\rm e}$), the dust temperature (T_D) and the frequency-dependent gas and dust opacities and emissivities (κ_ν and j_ν). The strict conditions of thermal balance and ionisation equilibrium are imposed in each grid cell in order to obtain the physical conditions in the local gas and dust.

A model is specified to the code via a 3-dimensional cartesian grid (defined in physical size units of cm) with the $N_{\rm e}$ (or N_H) and chemical abundance specified for each cartesian grid point i.e. each grid cell. Input files containing a three dimensional density distribution and chemical abundance sets and their specific abundance grid indices are specified to the code, allowing the user to accurately simulate inhomogenous chemical and physical conditions in the object being studied.

If desired, subgrids can be specified within the mother grid, to increase the resolution of particular elements of the grid. These are particularly useful when defining clumps of gas with more intricate density and/or composition. A single grid cell can contain its own three-dimensional grid, which is treated identically by the code since the passage of an energy packet between grid and subgrid is treated exactly as that between normal grid cells. Therefore, with a potentially unlimited mother grid size, and a number and size of subgrids within it, a MOCASSIN model may be adapted to efficiently treat any 3-dimensional density distribution (Ercolano *et al.* 2003). The detail of the model is thus limited only by the available memory and processing power of the computer system.

5.2.2.2 Dust

MOCASSIN includes a fully self-consistent treatment of dust radiative transfer (RT) within a photoionised region (Ercolano *et al.* 2005). The inclusion of dust within a H II region is essential when attempting to recreate radiative transfer and physical conditions within it. Dust grains compete with the gas for absorption of the UV photons, whose energy they reradiate in the infrared, contibuting to the observed SED. The code successfully establishes the dust and gas phase coupling by incorporating interactions in the RT such as scattering, absorption and re-emission.

In addition to the emission line spectrum, ionisation, $T_{\rm e}$ and $N_{\rm e}$ structure of the H II region, the code can also determine accurate dust temperatures and spectral energy distributions (SEDs). This is achieved by allowing the specification of discrete grain sizes and different grain species

separately, rather than having a single grain as a representative of an ensemble of grains (as in e.g. DUSTY, Ivezic & Elitzur (1997)). Firstly a dust composition is specified, consisting of a set of optical constants which encompass the wavelength range from the UV to the FIR where dust absorption, emission or scattering are important. Secondly, the grain size distribution is supplied, derived from a_{min} and a_{max}, the minimum and maximum grain radii in μm, and ρ the power-law exponent of the size distribution found by Mathis *et al.* (1977) to lie typically between -3.3– -3.6. Mie scattering is used to calculate the absorption and scattering efficiencies, $Q_{abs}(a, \lambda)$ and $Q_{sca}(a, \lambda)$, at each wavelength λ and grain radius a. Separate temperatures are derived for each grain radius and species. The neccessity for the independent treatment of all grain sizes and species was demonstrated by van Hoof *et al.* (2004) who showed using CLOUDY that approximating a grain mixture with a composite grain species can yield misleading results.

5.2.3 Modelling the Narrow Component Flux

Rather than adopting the hybrid two-zone model proposed by TIL96, I adopted a two-component model to attempt to reproduce the narrow and broad component fluxes seen throughout Mrk 996. With this approach I hoped to create two independent models that would recreate the two separate gas components responsible for the narrow and broad component emission within Mrk 996. This approach allowed high and low density gas to co-exist spatially throughout the model, in comparison to a hybrid two-zone model that restricts the low density gas to the outer regions of the galaxy. This section describes the method and parameters involved in reproducing the narrow component emission, using the observed chemical and physical conditions derived from the narrow emission line components (derived in Sections 3.5.1 and 3.4.1, respectively). Although this model could have been achieved with a 1-D code, a 3-D code was used in the hope of also simulating the high-density clumps in order to try to match the broad line component (discussed in Section 5.2.6)

It was decided that initially a simple gas-only model should be constructed, with dust to be added when the model was firmly established. Structurally, this gas-only model consisted of an ionising source that aimed to be representative of the stellar population of Mrk 996, at the center of a symmetrical grid. The size and resolution of the grid must be of sufficient resolution not to cause loss of detail via blending across the grid cells but is limited computationally. The ionising continuum was a blackbody of a temperature representative of the stellar population within Mrk 996, i.e. the ionising stellar continuum is approximated by a Planck function. As an input parameter, along with T_{eff}, either the luminosity of the central star, $L_\star$, in units of 10^{36} erg s^{-1}, must be specified, or the number of hydrogen-ionising photons per second, $Q(H^0)$, in units of $10^{36} s^{-1}$

(input parameter LPHOT, then used to derive $L_\star$). If $L_\star$ is defined, $Q(H^0)$ is then derived from it by the code.

As a first approach, a feasibility check was made for a model grid consisting of parameters derived from the narrow component gas properties derived in Chapter 3 via a calculation of the Stromgren radius using:

$$R_s = \Big(\frac{3Q(H^0)}{4\pi(n_H)^2\alpha_B}\Big)^{\frac{1}{3}} \tag{5.1}$$

(Osterbrock & Ferland 2006), where the hydrogen density, n_H, is related to n_e by $n_e = 1.08n_H$ (from ionised hydrogen plus the fraction of singly ionised helium). There are thought to be 3000 WR stars within the core region of the galaxy (Section 3.6), with a corresponding luminosity of $L_\star$=1140$\times10^{36}$ erg s^{-1} (using $L_{WR} = 3 \times 10^5 L_\odot$) and a typical WR stellar temperature of 6$\times10^4$ K (Crowther 2007). An initial grid size of 59^3 cells was chosen, and a uniform n_e=170 cm^{-3} was adopted (equal to the mean electron density observed for the narrow component gas). This gave $R_s = 1.1 \times 10^{19}$ cm.

Since this R_s is far less than the radius of the galaxy ($R_{out} = 1 \times 10^{21}$ cm, see Chapter 3), i.e. smaller than a grid cell unless dimensions of $> 50^3$ were used, this would result in gas which would remain mostly neutral. In order to obtain $R_s = R_{out}$, the luminosity of the central source needed to be 2.5$\times10^6$ larger than that of 3000 WR stars.

Therefore, rather than using the luminosity of 3000 WR stars, a better approach is to calculate the number of ionising photons using the observed Hα emission. Narrow component Hα emission in Mrk 996 is seen out to a radius of $\sim$600 pc ($\sim 1\times10^{21}$ cm), which was set to the R_{out} parameter. The number of ionising photons, $Q(H^0)$, in units of s^{-1} can be calculated using:

$$Q(H^0) = \frac{N(H\alpha)\alpha_B}{\alpha_{eff}^{H\alpha}} \tag{5.2}$$

where α_B is the Case B recombination coefficient summed over all levels above the ground level ($= 2.59 \times 10^{-13}$ at T_e=10,000 K) and $\alpha_{eff}^{H\alpha}$ is the effective recombination coefficient for emission of a Hα photon ($= 1.167 \times 10^{-13}$ at T_e=10,000 K, Storey & Hummer (1995)). The number of Hα photons, $N(H\alpha) = L(H\alpha)/E(H\alpha)$, the H$\alpha$ luminosity divided by the energy of a Hα photon.

In order to better match R_S with R_{out}, I employed a filling factor within my model. The filling factor is defined by Osterbrock & Ferland (2006) as the fraction of total volume occupied by density condensations, and typically falls within the range 0.01–0.5 for H II regions. It can be

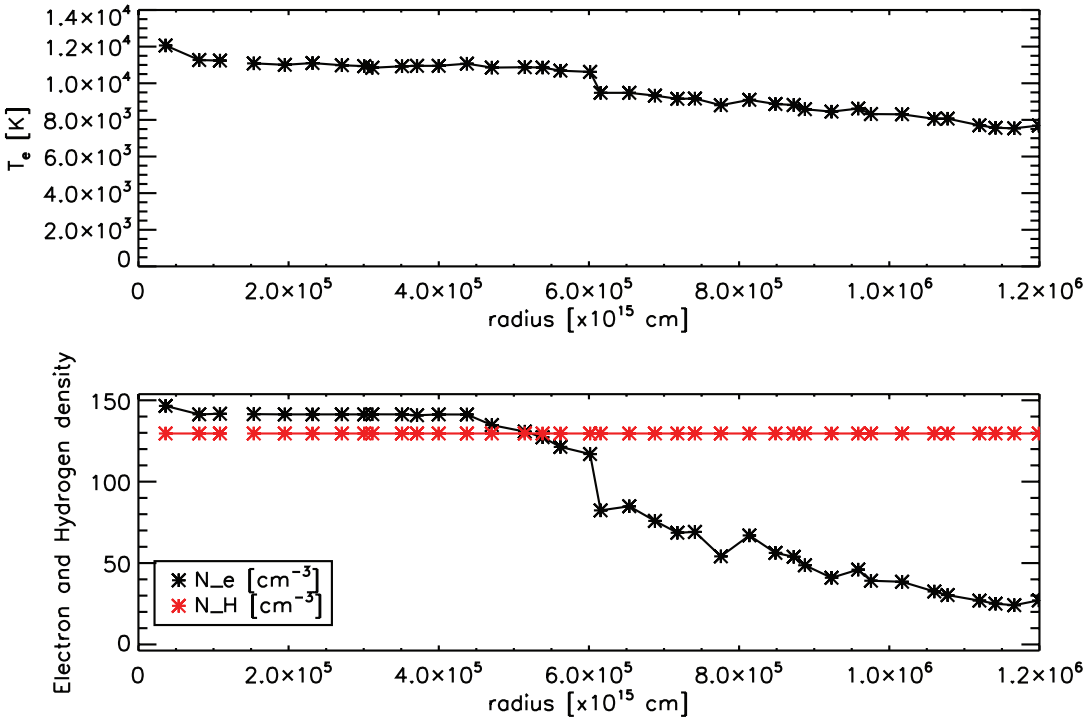

Figure 5.1: Electron temperature and electron density as a function of radius for a gas-only model of Mrk 996. Model parameters are listed in Table 5.2

calculated by comparing the number of recombinations expected at a specified $N_{\rm e}$, $T_{\rm e}$ and radius, with the observed number of ionising photons, e.g. for Hα photons:

$$\frac{4\pi}{3}R^3 n_e n_H \alpha_{H\alpha}^{eff}\epsilon = Q(H\alpha) \tag{5.3}$$

where here R would be equal to the observed R_{out}, $\rm n_e$ is the fobidden line electron density and $\rm n_H$ the corresponding hydrogen density, respectively.

5.2.3.1 Results

After exploring the parameter space, I found a best fit model consisting of the parameters given in Table 5.2. The total narrow component Hα luminosity observed within the outer radius of 1×10^{21} cm is equal to $L_{H\alpha} = 5.19 \times 10^{41}$ erg s^{-1} for a distance of 22.3 Mpc, which gives $Q(H^0) = 3.8 \times 10^{53}$ ionising photons per second, calculated using Equation 5.2. $\rm R_{\mathit{in}}$, the inner

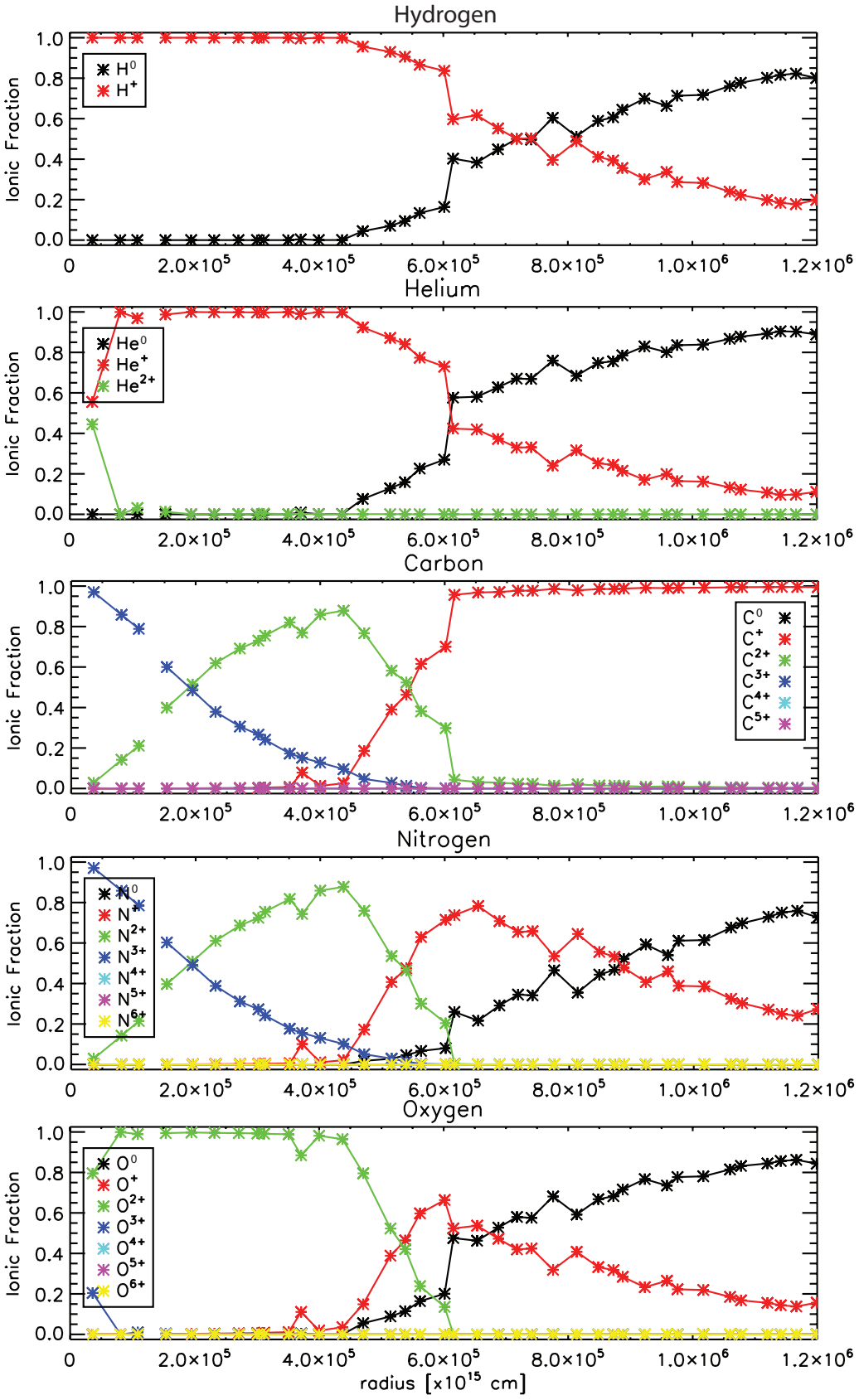

Figure 5.2: Ionic fractions of H, He, C, N and O as a function of radius for a gas-only model of Mrk 996. Model parameters are listed in Table 5.2

radius of the ionised region, was increased from zero to $\sim 0.09''$ corresponding to a radius of 10 pc at the distance of Mrk 996. This size is unresolvable with the spatial resolution of VIMOS-IFU at the distance of Mrk 996, and is a realistic assumption of a shell surrounding the central source whose material has been blown away. Rather than using an $N_{\rm e}$ derived from the summed spectra over the inner core ($\sim$170 cm^{-3}), it was more accurate to adopt an average $N_{\rm e}$ derived from the total dereddened [S II] λ6716/λ6731 ratio summed over the entire galaxy of $\sim$140 cm^{-3}, corresponding to $\rm n_{\it H} = 130$ cm^{-3}. This corresponded to a filling factor of $\epsilon = 0.037$ (derived using Equation 5.3) for the narrow component emission of Mrk 996. With the inclusion of a filling factor, over-ionisation of the grid was prevented by decreasing the temperature of the black-body input spectrum from an implausible 80,000 K (which most closeley matched the line strengths before inclusion of a filling factor) to 50,000 K. This temperature is also a more representative temperature of the WR+O star population at the center of Mrk 996 although still rather high. It should be noted that without the inclusion of a filling factor, the code could not recreate a match with the observations.

$T_{\rm e}$ and $N_{\rm e}$ as a function of radius are shown in Figure 5.1 and the ionic fractions of H, He, C, N and O as a function of radius are shown in Figure 5.2. Each value is binned radially, averaging along one slice of the grid without the inclusion of cells devoid of gas due to the filling factor. It can be seen that the distributions of electron temperature and electron density with radius match well those derived in Chapter 3. $T_{\rm e}$ starts at 12,000 K and decreases to 8,000 K as it approaches R_{out}, consistent with the derived C1 upper limit to $T_{\rm e}$ of 10,000 K throughout the inner and outer regions of Mrk 996 (c.f. Section 3.4.1). The $N_{\rm e}$ distribution starts at $\sim$175 cm^{-3} at R_{in} and decreases to $\sim$20 cm^{-3} at R_{out}, in excellent agreement with the derived C1 component electron densities of 170 cm^{-3} and 10 cm^{-3} for the inner and outer regions of Mrk 996 (c.f. Table 3.3). The top two panels of Figure 5.2 provide insight into the ionisation structure of the model. It can be seen that the ionisation front is located at $\sim 0.5R_{out}$, a realistic estimation within a H II region of this sort. The extended transition zone seen in the bottom panel of Figure 5.1, from 6×10^{20} cm to 1.2×10^{21} cm, may be related to the low filling factor utilised in the model which increases the overall column density by effectively decreasing the average density. A more sharp transition zone may have been achieved by having a non-uniform, 'clumpy' gas density in the outer regions which would provide a more sharp transition between H^+ and H^0 within the clumps, thus reducing the amount of neutral H (and O, shown in Figure 5.2). MOCASSIN predicts that double and triply ionised carbon should be observed within $r = 130$ pc ($1.2''$); although no strong carbon emission lines fall within the IFU spectra, TIL96 observe C III] λ1909 and CIV λ5808 within the central

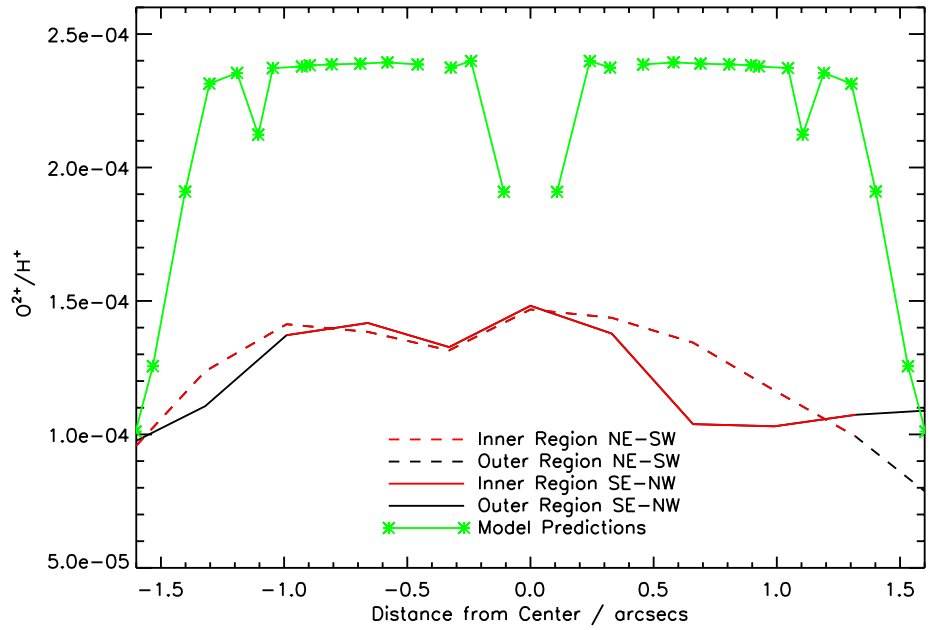

Figure 5.3: Observed and predicted O^{++}/H^{+} as a function of angular radius. The observed values are shown and derived in Chapter 3, Section 3.5.1. The absence of data points within the central $0.09''$ corresponds to the inner radius of the ionised region, R_{in}.

$0.86''$ (FOS) aperture. The radial distribution of ionic fractions of nitrogen predicts that N^{3+} and N^{2+} should be visible out to $r = 130$ pc ($1.2''$) but no strong [N III] or [N IV] lines fall within the IFU spectral range, although TIL96 do observe N III] λ1750 which we assumed to originate from the high-excitation gas responsible for the *broad* component emission. A rise in the N^{+} fraction just outside the central region, peaking at 195 pc ($1.8''$),is correctly predicted and can be seen in Figure 3.16 as an observed rise in N^{+}/H^{+} abundance 1–$2''$ from the center of Mrk 996. The model correctly predicts that nothing higher than doubly ionised oxygen should be seen. O^{2+} is dominant out to a radius of $1.4''$ ($\sim$150 pc) where there is a steep decline over a distance of 70 pc while O^{+} rises. The distributions in ionic fractions of oxygen are correctly predicted, as can be seen in the ionic abundance ratios of O^{+}/H^{+} and O^{++}/H^{+} shown in Figure 3.16. A comparison between the predicted O^{++}/H^{+} structure and radial cuts across Mrk 996's O^{++}/H^{+} abundance map (shown in Figure 3.16 and derived in Section 3.5.1) is shown in Figure 5.3. A similar structural shape can be seen, however differences observed and predicted values exist because the model-view is a radial cut along the x-axis, whereas the observations consist of averages over parallel chords through the

galaxy.

Once the ionisation structure was acceptable, I began to compare the predicted line fluxes (integrated over the volume of the grid and relative to H$\beta = 1$) with those observed. The observed line intensities used for comparison are those derived from summed spectra over the inner and outer regions of Mrk 996. For a black-body temperature of $T_{eff} = 4 \times 10^4$ K, the high-ionisation lines such as [O III] and He II were under-predicted by a factor of $\sim$0.5, as well as low-ionisation lines such as [S II] . Increasing T_{eff} by increments of 1000 K up to $T_{eff} = 5 \times 10^4$ K allowed me to successfully reproduce the emission line intensities relative to Hβ, as seen in Table 5.1. Increasing the temperature beyond $T_{eff} = 5 \times 10^4$ K caused over-prediction of the [O III] line strengths. A list of input parameters for the best-fit model to the narrow component emission is given in Table 5.2. The Hβ luminosity of this model was predicted to be 1.32×10^{41} erg s^{-1}, corresponding to a Hβ flux of 2.21×10^{-12} erg s^{-1} cm^{-2} for Mrk 996's distance of 22.3 Mpc. This is consistent with the total de-reddened narrow component Hβ flux of 1.37×10^{-12} erg s^{-1} cm^{-2} and the total (narrow plus broad component) Hβ flux of 2.03×10^{-12} erg s^{-1} cm^{-2}.

5.2.4 Modelling with STARBURST99

In the *Spitzer*-based study of Mrk 996 by Thuan *et al.* (2008), a compilation of photometric fluxes was presented and is shown here in Table 5.3. These fluxes, apart from those given as upper limits, were used to constrain the model SED, as shown in Figure 5.4. The SEDs shown in Figure 5.4 illustrate that the optical-to-mid-IR wavelength photometric points cannot be fitted accurately with the best-fit gas-only blackbody model due to neglecting emission from an older stellar population in the red and near-IR, since the blackbody model only incorporated the ionising photons emitted by the young, WR+O star population observed in Mrk 996. The model thus requires an input spectrum representative of the whole stellar population within Mrk 996, i.e. a spectrum produced by a stellar population synthesis code such as STARBURST99 (SB99, Leitherer *et al.* (1999)). This code consists of a comprehensive set of model predictions for the time-dependent spectrophotometric and related properties of galaxies that have undergone active star formation. Using a web-based interface, a user can run specific stellar population models using the latest set of stellar evolution models and atmosphere grids for a range of metallicities, initial mass functions and ages and retrieve a wide range of model outputs including spectra, stellar yields, ionising quanta and equivalent widths of spectral features.

In order to correctly match the observed optical-to-mid-IR photometric points, a 2 component SB99 input spectrum was created based on a *young* $\sim$3 Myr old WR population (as esti-

Table 5.1: Table of observed narrow component emission line intensities and their best-fit ratios from a MOCASSIN pure-gas model with a blackbody input spectrum ($T_{eff} = 5 \times 10^4$ K). Both the inner and summed inner and outer regions fluxes are listed, relative to Hβ=1.0. See Table 5.2 for model parameters.

Line ID	Obs Flux IN	Pred/Obs IN	Obs Flux Total	Pred/Obs Total
4341 Hγ	0.463	1.01	0.535	0.876
4363 [O III]	0.0341	0.892	0.0318	0.956
4959 [O III]	1.32	0.886	1.22	0.956
5007 [O III]	3.97	0.877	3.70	0.942
5876 He I	0.107	0.954	0.126	0.810
6300 [O I]	0.0430	15.6	0.0477	14.0
6312 [S III]	0.0120	0.122	0.0184	0.0798
6563 Hα	2.87	1.00	2.87	0.999
6584 [N II]	0.353	1.10	0.335	1.15
6678 He I	0.0320	0.904	0.0380	0.762
6717 [S II]	0.286	0.760	0.255	0.855
6731 [S II]	0.228	0.699	0.194	0.820
7065 He I	0.01000	1.83	0.0245	0.747
7319 [O II]	0.0560	0.683	0.0560	0.683
7330 [O II]	0.0530	0.588	0.0585	0.533

Table 5.2: Parameters for the narrow component best-fit gas-only model. These parameters (excluding CONTSHAPE) were subsequently used for the narrow component dust+gas model.

Parameter	Value
$N_{\rm e}$ (cm^{-3})	140
N_H (cm^{-3})	130
QPHOT(photons s^{-1})	3.8×10^{53}
ϵ	0.037
T_{eff} (K)	5×10^4
R_{in} (cm)	3.10×10^{19}
R_{out} (cm)	1.25×10^{21}
CONTSHAPE	Bbody
grid	59^3

Table 5.3: IRAC and MIPS photometric fluxes from THI08, with other published photometry.

Telescope/Instrument	Wavelength (μm)	Total flux (mJy)
Spitzer/IRAC	4.51	5.8±0.29
″	7.98	12.7±0.64
Spitzer/MIPS	23.7	84±4
″	71.0	381±10
″	156.0	442±12
IRAS[a]	12	<108
″	25	<159
″	60	417±50
″	100	<713
Optical[b]	0.36	2.1±0.2
″	0.44	3.7±0.3
″	0.55	4.7±0.4
″	0.64	6.9±0.6
″	0.79	6.6±0.6
IRCAM/UKIRT[c]	1.26	9.6±0.5
″	1.65	10.8±0.5
″	2.12	8.9±0.4
2MASS[a]	1.2	10.2±1
″	1.6	12.6±1
″	2.2	9.6±1

[a] From NED.

[b] From TIL96, colours defined within a 9″ aperture centered on the nucleus of *HST* WFPC2 images.

[c] In an aperture of 20″ diameter.

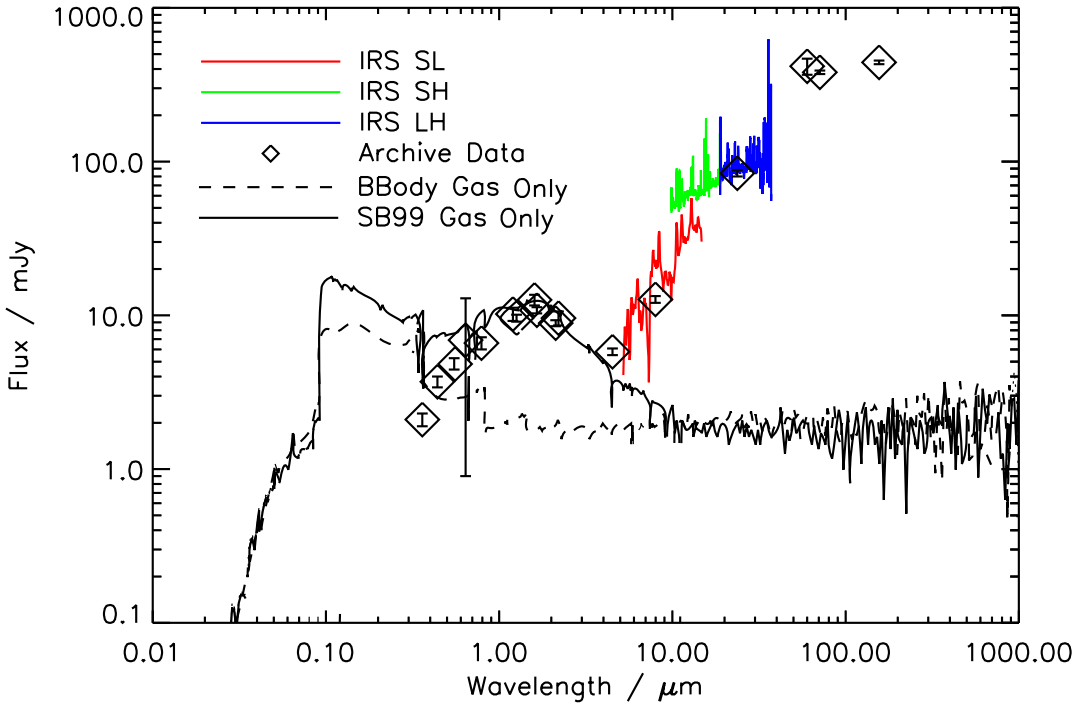

Figure 5.4: Spectral energy distribution produced by a gas-only model of Mrk 996 with a SB99 model input spectrum (solid line, $L_\star = 3.6 \times 10^{43}$ erg sec^{-1}) and a blackbody input spectrum (dashed line, $L_\star = 2.15 \times 10^{43}$ erg sec^{-1} with $T_{eff} = 5 \times 10^4$ K). Overlaid are the IRS SL, SH and LH spectra (described in Section 5.2.5) and the photometric fluxes listed in Table 5.3.

mated in Section 3.6) and an *old* ∼10 Gyr population of super-star clusters (SSCs) in and around Mrk 996, as estimated by Thuan *et al.* (1996) by comparing the visual absolute magnitudes of the observed SSCs with those of the globular clusters ω Cen and NGC 6752. The parameters of the model input spectrum were as follows; a metallicity of 0.4 $Z_\odot$ was chosen (the closest available match to the ∼0.5 $Z_\odot$ metallicity estimated for the narrow component gas), together with assumptions of an instantaneous burst with a Salpeter initial mass function (IMF), a reference stellar mass of 1×10^6 $M_\odot$ (this mass can then be scaled to match the observed spectrum and is the default mass chosen by Leitherer *et al.* (1999) to produce properties that are typical for actual star-forming galaxies) and a 100 $M_\odot$ stellar upper mass limit (which approximates the classical Salpeter (1955) IMF). The models contained Padova tracks with thermally pulsing AGB stars included and Lejeune-Schmutz model atmospheres, chosen since they incorporate stars with

strong winds, i.e. a stellar population representative of the WR population within Mrk 996. Once read in, MOCASSIN normalises the input spectrum to the specified $L_\star$ and calculates QPHOT - therefore, $L_\star$ must be changed accordingly until the observed number of ionising photons (i.e. $Q(H^0) \sim 3.8 \times 10^{53}$ s^{-1}) is matched and consequently the observed line ratios are correctly predicted.

Firstly the young stellar population was fitted using $Q(H^0)$ as a constraint and a range of 0.1–10 Myr populations. It was found that in order to correctly match the height of the SED *and* correctly predict the observed line fluxes, a 1$\pm$0.5 Myr young population is required. Figure 5.5 shows example best-fit model SEDs produced by a 0.5 and 1 Myr spectrum. Also shown is the model SED produced by a 3 Myr spectrum that over-predicts the optical photometric points by a factor of $\sim$5 because the $L_\star$ required to match $Q(H\alpha)$ was too high. A negligible difference is seen in the predicted SEDs between 0.5 and 1 Myr. Unfortunately the young population input spectra were unable to correctly match the photometric points at $\lambda < 0.6$ μm, which were previously correctly matched by the best-fitting blackbody model with $T_{eff} = 5 \times 10^4$ K (as shown in Figure 5.4). The emission at these wavelengths would be reminiscent of hot, young O-stars, which would certainly be accounted for in the 0.1–1 Myr populations and thus this discrepancy cannot be due to the age of the ionising spectrum. Alternatively, it could be because the current model is tailored to recreate the *narrow* component emission lines by matching the *total* (narrow+broad) Hα luminosity, with the reasoning that the broad component emission result from excitation by non-photoionisation (i.e. shocks, stellar outflows etc). Thus, one way in which to reduce the level of the SED would be to decrease $L_\star$ by attempting to match only the narrow component Hα luminosity. However, this would provide a decrease by a factor of only $\sim$2 rather than a required decrease by a factor of $\sim$4. Finally, the discrepancy could be the result of an aperture effect; if the photometric fluxes were derived from apertures that do not fully encompass the galaxy they would be an under-representation of the entire stellar population. However, all the optical fluxes listed by THI08 were defined within a 9$''$ aperture centered on the nucleus of *HST* WFPC2 images, which, as can be seen in Figure 3.1, should fully cover the extent of Mrk 996.

Secondly, the old stellar population was fitted. The addition of this population has no effect on the $L_\star$ required to match $Q(H^0)$ since the stars no longer emit ionising photons. Thus, the age and relative quantity of this stellar population component was governed by the shape of the SED between 1–5 μm and also the total mass and luminosity of the population. The young stellar population component corresponded to a total mass of $\sim 8 \times 10^6$ $M_\odot$, only a fraction of the $\sim 5 \times 10^8$ $M_\odot$ dynamical mass within a 6$''$ radius of the galaxy centre deduced from rotational

velocity curves (Section 3.3.2). Using an age range of 0.5–10 Gyr, the age and quantity of the old population, in relation to the younger 1Myr population, was varied until 1) the mass of the population correctly matched that of the dynamical mass and 2) the shape of the SED was sufficiently matched. It was found that an older population of 1.5±0.5 Gyr, in a ratio of 40±10 by mass to the younger population, was required to satisfy both these conditions. Figure 5.6 shows the best-fitting cases of a 1 Myr + 1 Gyr population combined in a 1:30 mass ratio (total stellar mass of $4.3 \times 10^8 M_\odot$), along with a 1 Myr+2 Gyr population in a 1:50 mass ratio (total stellar mass of $7.3 \times 10^8 M_\odot$). Also shown in Figure 5.6 is the predicted SED from a 1 Myr + 4 Gyr population in a 1:50 mass ratio (total stellar mass of $7.6 \times 10^8 M_\odot$), illustrating that in order to match the dynamical mass within a reasonable (e.g. 20%) limit, the predicted SED between 1–5 μm is too shallow and falls below the uncertainties of the photometric points within this wavelength range. Similarly, a population younger than 1 Gyr that is within 20% of the dynamical mass estimate produced an SED shape that would be too steep in the 1–5 μm region.

To conclude, I find that the best fitting stellar population consists of a 1±0.5 Myr population, combined with a 1.5±0.5 Gyr population in a mass ratio of 1:40±10, giving a combined stellar mass of $\sim 5.8 \pm 1.5 \times 10^8\ M_\odot$. In order to stay below the dynamical mass and to thus allow for additional mass attributable to gas and dust, I chose to use the $4.3 \times 10^8 M_\odot$lower mass limit to the stellar population corresponding to 1 Myr + 1 Gyr population combined in a 1:30 mass ratio for the dust+gas modelling described in the following section.

5.2.5 The Addition of Dust

As mentioned previously, the inclusion of dust within a photoionisation model for a nebula, a H II region in this case, is essential to gain an accurate view of the radiation transfer processes occurring within it. Incorporating a dust component into the gas model enabled me to recreate the IR portion of the spectral energy distribution shown in Figure 5.4 that is a product of the re-radiation of the energy of absorbed UV photons by the dust grains. In addition to the photometric fluxes in Table 5.3 described in Section 5.2.4, also used for comparison are the *Spitzer* IRS spectra of Mrk 996 presented in Chapter 2. The IRS modules available for Mrk 996 are SL (low-resolution, 5.2–14.5 μm), SH (high-resolution, 9.9–19.6 μm) and LH (high-resolution,18.7–37.2 μm). In order to correct and scale for slit losses after extraction, the SL 8.0 μm continuum level was scaled to the 7.98 μm IRAC photometric flux and similarly the LH spectrum was scaled to the 23.7 μm IRAC flux (both given in Table 5.3). The SH spectrum was consequently scaled to the LH using the 18.8 μm [S III] emission line which is present in their overlapping wavelength regions. Forbidden

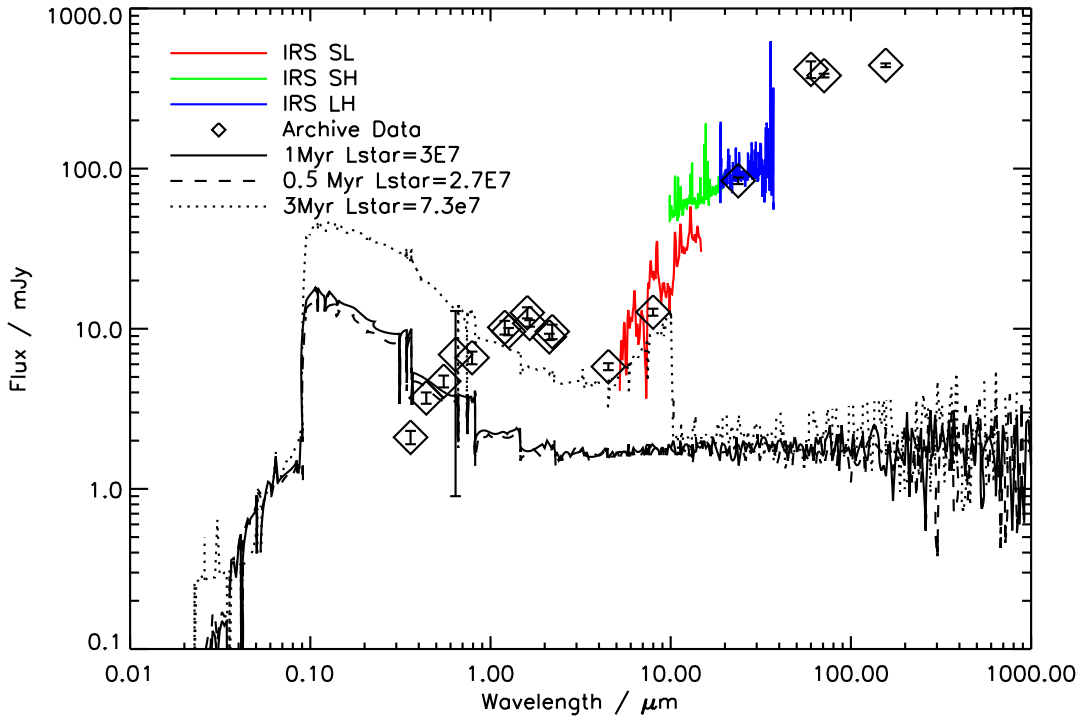

Figure 5.5: Spectral energy distribution produced by a gas only models of Mrk 996 with SB99 model input spectra for 0.1–3 Myr stellar populations. Each population has an $L_\star$ (in units of erg s^{-1}) that is required to produce the observed $Q(H\alpha)$ ($\sim 3.8 \times 10^{53}$ s^{-1}). Overlaid are the IRS SL, SH and LH spectra (described in Section 5.2.5) and the photometric fluxes listed in Table 5.3.

line integrated fluxes measured from the SH and LH spectra are listed in Table 5.5.

The most influential parameter on the level of IR emission by the dust is the dust to gas mass fraction, $\frac{M_d}{M_g}$. By constraining this parameter, an estimate can be made of the dust mass required to match the IR flux levels. Following the specifications outlined in Section 5.2.2.2, I used a dust composition with a constant $\frac{M_d}{M_g}$ throughout the grid, consisting of an amorphous carbon dust grain species with the standard grain size distribution of Mathis *et al.* (1977). This 'MRN' grain size distribution has dust parameters of a_{min}= 0.005 μm, a_{max}= 0.20–1.00 μm and a power-law size distribution exponent of -3.5. An amorphous carbon grain species was chosen since no silicate features were detected in the IRS spectra shown in Figure 5.7. Figure 5.8 shows the best-fitting SED from a gas+dust model, consisting of a constant $\frac{M_d}{M_g} = 1.7 \times 10^{-4}$ with a maximum grain size of a_{max}=1.0 μm that was required to fit the far-IR wavelengths. The total dust mass produced

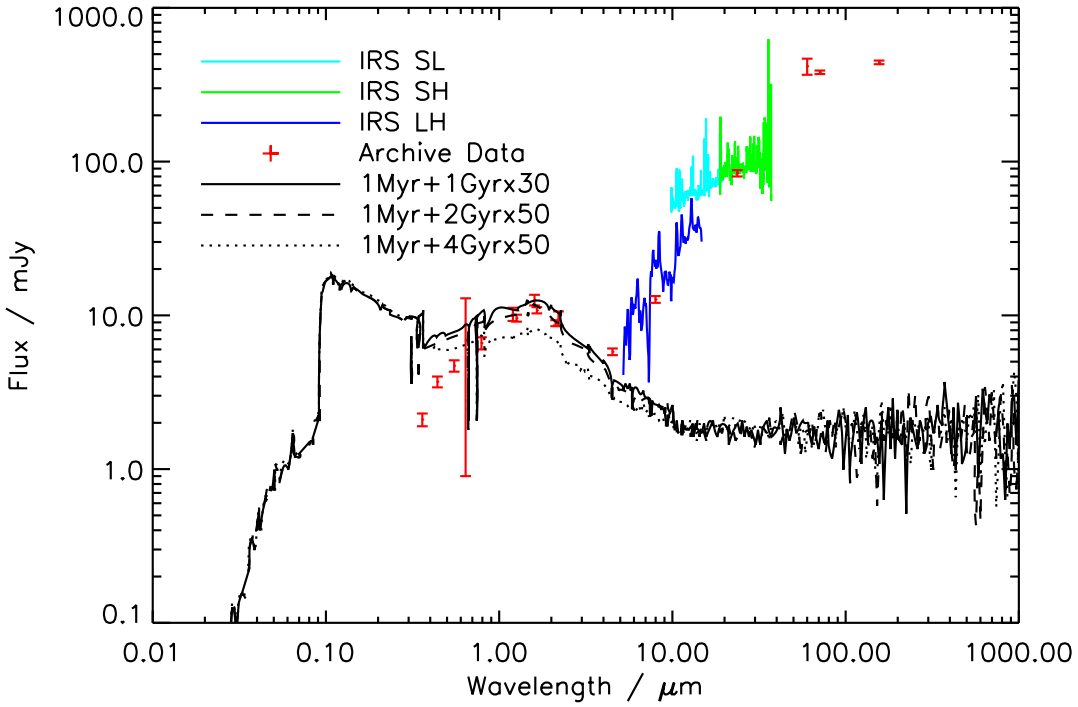

Figure 5.6: Spectral energy distribution produced by gas-only models of Mrk 996 with SB99 model input spectra, for a 1 Myr population combined with 1, 2 and 4 Gyr populations in respective mass ratios of 30, 50 and 50. Overlaid are the IRS SL, SH and LH spectra (described in Section 5.2.5) and the photometric fluxes listed in Table 5.3.

in this model was 7,200 $M_{\odot}$ corresponding to a total gas mass of $4.2{\times}10^{7}$ $M_{\odot}$ and a total stellar mass of $4.3{\times}10^{8}$ $M_{\odot}$. Thus, this best-fit gas+dust model with a 1 Myr + 1 Gyr (1:30) stellar population yields a total mass of $4.7{\times}10^{8}$ $M_{\odot}$, which is within 6% of the dynamical mass of 5×10^{8} $M_{\odot}$ derived in Section 3.3.2.

The 160 μm MIPS flux cannot be fitted with this model, presumably because it is produced by much colder grains than those in our models. Such cold grains are likely to be present in cold molecular clouds, which were not simulated by our photoionisation model.

The predicted to observed line intensities for the SB99 gas+dust model are listed in Table 5.4. For comparison, Table 5.4 also lists the line intensities predicted by the best-fit gas-only blackbody input spectrum model detailed in Section 5.2.3.1, and a comparison between the two models. Reasonably good agreement is seen between the observed and predicted line intensities, apart from

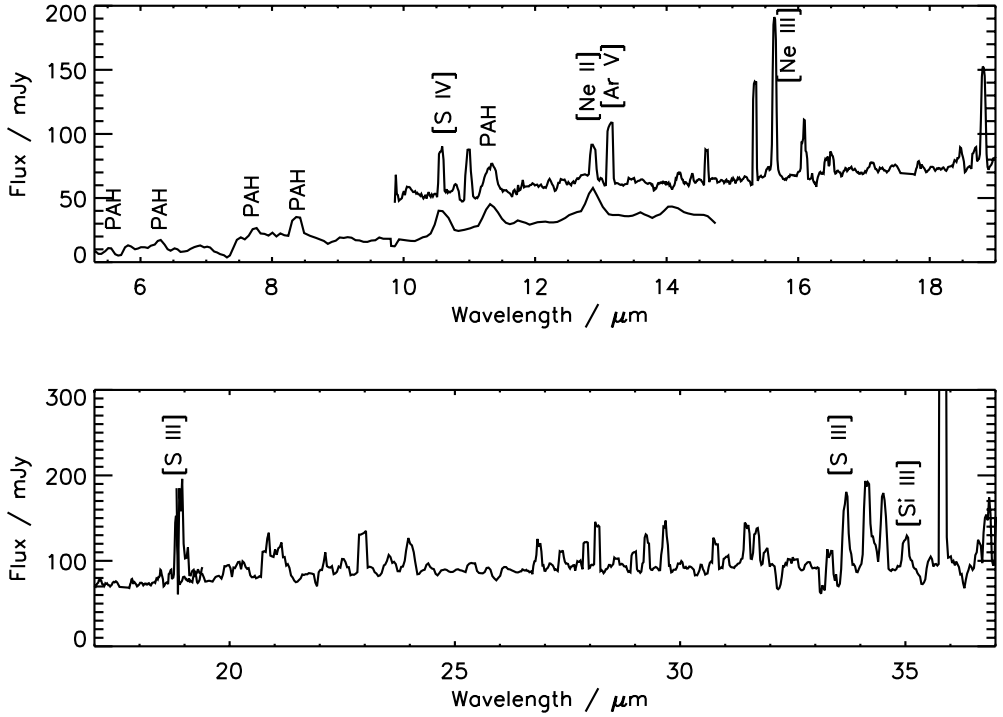

Figure 5.7: The IRS spectrum of Mrk 996 taken in short-wavelength low-resolution mode and in both high-resolution modes: SL+SH spectra are shown in the upper panel and the LH spectrum in the lower panel. Detected PAH features (5.7, 6.2, 7.7, 8.6 and 11.2 μm) and fine-structure emission lines are labeled.

[S III] λ6312, which is significantly under-predicted, possible due to the fact that this line has 66% of its flux in broad component form. There is also a significant over-prediction in [O I] λ6300 which may be linked to the extended ionisation zone of partial H and O ionisation extending from 6×10^{20} cm to 1.2×10^{21} cm (as seen in Figures 5.1 and 5.2 and discussed in Section 5.2.3.1). Table 5.5 lists the IR forbidden line fluxes obtained by THI08 from IRS SH and LH spectra as well as their values relative to the narrow component Hβ flux within the corresponding SH or LH aperture. Also listed are the ratios between the MOCASSIN predicted line fluxes and the observed values listed by THI08; a relatively good agreement is seen for the [S IV] and [O IV] lines, while the predicted [S III] IR fine structure lines fluxes are 49–65% of those observed. It should be noted that the gas+dust model IR fluxes are identical to those produced by the gas-only model.

Table 5.4: Line comparison for gas-only (blackbody input spectrum) and dust+gas (SB99 input spectrum) best fit models. 'Observed' correspond to dereddened fluxes on a scale where Hβ=1.00.

Line ID	Obs Flux Total	Pred/Obs Gas-Only	Pred/Obs Gas+Dust	Pred Gas-Only/Gas+Dust
4341 Hγ	0.535	0.876	0.876	0.999
4363 [O III]	0.0318	0.956	1.20	0.794
4959 [O III]	1.22	0.956	1.09	0.879
5007 [O III]	3.70	0.942	1.07	0.879
5876 He I	0.126	0.810	0.867	0.933
6300 [O I]	0.0477	14.0	14.9	0.940
6312 [S III]	0.0184	0.0798	0.0892	0.895
6563 Hα	2.87	0.999	0.997	1.00
6584 [N II]	0.335	1.15	1.18	0.981
6678 He I	0.0380	0.762	0.816	0.934
6717 [S II]	0.255	0.855	0.876	0.976
6731 [S II]	0.194	0.820	0.840	0.977
7065 He I	0.0245	0.747	0.807	0.926
7319 [O II]	0.0560	0.683	0.710	0.961
7330 [O II]	0.0585	0.533	0.554	0.961

Table 5.5: Table of observed IR line intensities from high-resolution IRS spectra, given by THI08, and relative to line intensities predicted by the best-fit MOCASSIN dust+gas model. Lines are also given relative to the dereddened narrow component Hβ flux within the IRS SH aperture ([S IV]) or LH aperture ([S III] 18.70μm , [O IV] and [S III] 22.38μm), obtained by superimposing tje IRS apertures onto the VIMOS IFU narrow component Hβ flux map. See Table 5.2 for model parameter details.

Line ID	Obs IR Flux[a] (THI08)	I(λ)/I(Hβ)	Pred/Obs
10.5 [S IV]	3.40	0.071	1.25
18.7 [S III]	7.40	0.056	0.49
25.9 [O IV]	1.20	0.0091	0.92
33.5 [S III]	10.85	0.082	0.65

[a] F(λ) $\times 10^{17}$ W m^{-2}

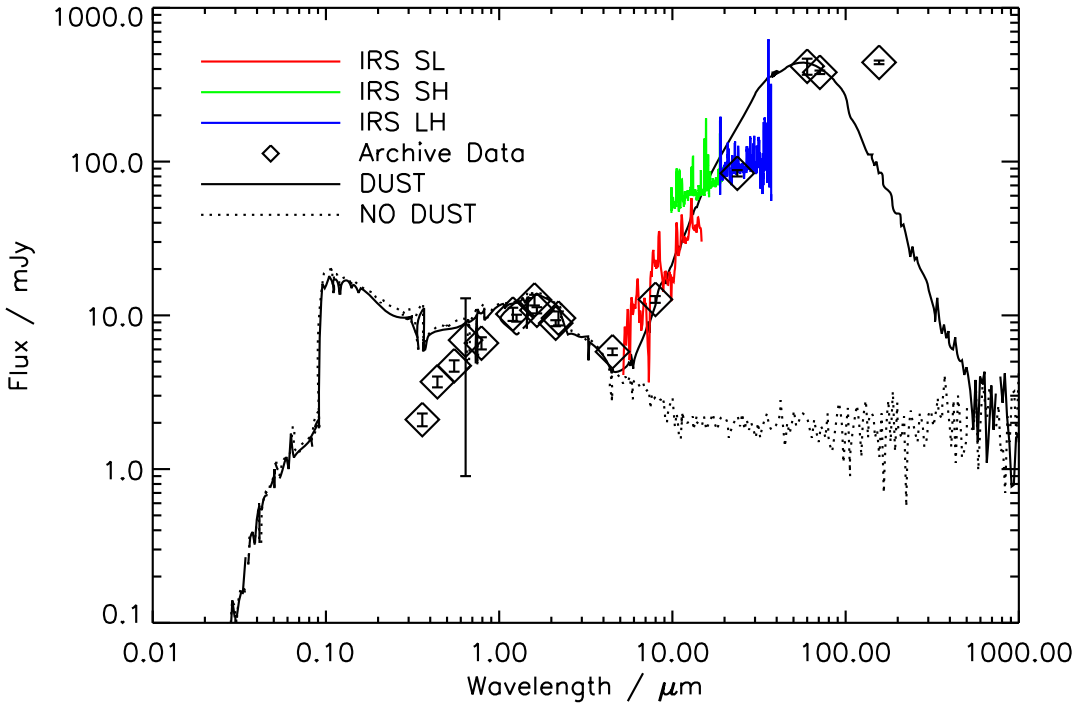

Figure 5.8: Spectral energy distributions produced by a gas-only (dashed) and gas+dust model (solid) of Mrk 996 with a SB99 input spectrum of 1 Myr+1 Gyr population combined in a 1:30 ratio. The dust model consists of a constant $\frac{M_d}{M_g} = 1.7 \times 10^{-4}$ distribution, an amorphous carbon grain species and an MRN grain size distribution with a_{max}=1.0 μm (see text for details).

5.2.6 Modelling the Broad Emission Line Component Flux

The broad component emission within Mrk 996 is discussed in Section 3.4. To summarise, a broad emission component is seen in most high S/N lines, and is seen *only* in the broad component form in the forbidden lines [O III] λ4363 and [N II] λ5755. As discussed in Section 3.4.3, the [O III] broad component line ratios can only be matched when densities of $N_{\rm e} \sim 10^7$ cm^{-3} are used. The origin of the broad component emission remains elusive. An AGN mechanism was suggested by THI08, but with a lack of high ionisation lines and excessively broad line widths, this is deemed unlikely. Another more likely possibility is emission resulting from the outflows/shocks propagating throughout the gas from the population of WR stars located within the core region. However, BPT diagnostic diagrams (see Figure 3.22) show that the broad component emission straddles the upper limit for excitation by photoionisation and is neither clearly within the shock-excited region

nor the photoionisation region. Sub-solar metallicity complications also exist for this diagnostic method. This section documents an attempt to model the broad component emission with a photoionisation model, in the hope of gaining a better understanding of the mechanisms behind the emission.

If I were to model the broad component emission region using a 3-D grid, one approach would be to have high density clumps/knots of $10^7 \mathrm{cm}^{-3}$, immersed in a low density (i.e. narrow component emission) gas $\sim$170 cm^{-3}. A calculation of the required filling factor, ϵ, for the broad component gas was made using Equation 5.3 and was found to be of the order $\sim 10^{-10}$. For a H column density of $\sim 10^{20}$ cm^{-2}, an eUV photon would be able to penetrate $\sim 10^{13}$ cm into such a high density knot. If we take this as the minimum permitted radius, R_k of a knot and $\mathrm{R}_{out} = 4 \times 10^{20}$ cm, i.e. the radius to which we observe the broad component emission ($\sim$130 pc), we can estimate N_k, the number of knots needed within our model using:

$$\frac{4\pi}{3} R_{out}^3 \epsilon = \frac{4\pi}{3} R_k^3 N_k \tag{5.4}$$

This gives $N_k = 10^{13}$, which is extremely computationally intensive.

Also, before running a full 3-D simulation in which knots of high density were distributed throughout the core region of Mrk 996 (i.e. fully utilising the capacity of MOCASSIN), I performed a feasibility study by running a large number of plane parallel models in order to verify that the line ratios found by the broad component could be reproduced at all. The model entailed a slab of high density material whose thickness of R_k (derived above) is small enough such that the ionising photons will be approaching parallel to one another. The slab was placed at D=10 pc out to 130 pc (R_{out}), at 10 pc intervals, by altering the luminosity of the central source according to:

$$N(H^0, D) = \frac{Q(H^0)}{4\pi D^2} \tag{5.5}$$

where $Q(H^0)$ is the total number of ionising photons and $N(H^0, D)$ is the number of ionising photons at distance D. To ensure the slab remained optically thick at each iteration of the code (i.e. as D increased), the length of the slab was made equal to that of the ionisation front. This also ensures that we only sample the photoionised region of the slab. Input abundance were those derived from the broad component intensities, as given in Section 3.5.2.

Comparing the volume weighted averages of the line ratios as the slab moved away from the ionising source, i.e. throughout the region of observed broad component emission, we found that for reasonable densities and ionisation parameters the line fluxes could not be reproduced. Figure 5.9 shows the volume weighted average [O III] λ4363 and [N II] λ5755 predicted and observed

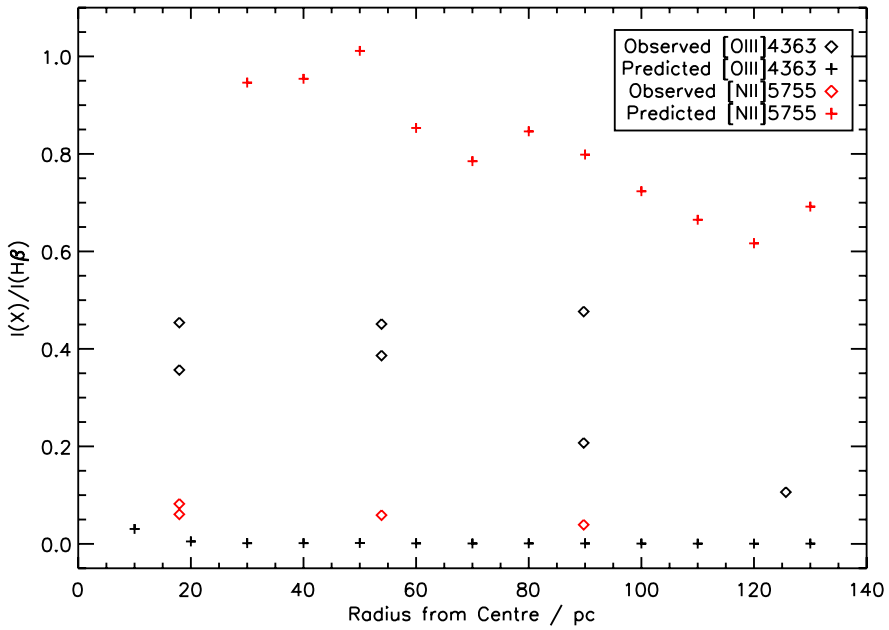

Figure 5.9: [O III] λ4363 and [N II] λ5755 volume weighted predicted line intensities, along with observed broad component intensities, as a function of radius.

intensities relative to Hβ=1 as a function of radius. Despite line of sight effects, which could potentially make this comparison ineffective, Figure 5.9 shows that these *broad only* lines are either severely under predicted (λ 4363) or over predicted (λ 5755). Given the high temperature sensitivity of the [O III] λ4363 line, the under prediction may be due to temperature effects. Although the electron temperature of the gas ranges from 12,000 K at 10 pc to 8900 K at 130 pc, this is similar the derived broad component electron temperature of 10,000$\pm$500 K (derived in Section 3.4.3). Using the summed spectra ionic intensities for Mrk 996, a broad-line [O III] λ5007/λ4363 ratio of 4.34$\pm$0.17 is obtained. The slab model predictions for this line intensity ratio lie between 13.9–78.6 as the slab moves from 10 pc out to 130 pc.

As mentioned in Section 5.1, detailed photoionisation analysis studies of NGC 7714, NGC 2653 and I Zw18 all resulted in predicted [O III] λ5007/λ4363 ratios far higher than the observed ones. Attempts made to remedy the discrepancy for this ratio included exciting stars with a range of effective temperatures and/or strong density enhancements towards the centre. In the case of I Zw18, Stasińska & Schaerer (1999) noted that *HST* images show that the global geometry of the nebula is not that of a spherical bubble, as might first appear, but is closer to a ring seen face on. In that

case, photoionsation models using spherical symmetry overestimate the role of the diffuse radiation field produced by the nebular gas, and thus underestimate the electron temperature. Other explanations invoked to explain this 'electron temperature problem' involve multi-density models, shocks (since they can heat the compressed gas to very high temperatures) and conductive heating or turbulent mixing with a very hot gas, expected to be present inside stellar bubbles (Weaver *et al.* 1977).

This under-prediction of the λ4363 line, despite sensible temperatures, strongly indicates that the origin of the broad component emission may not be photoionised gas. While further studies are needed to rule the photoionisation option out completely, my current investigation strongly suggests that other processes (e.g. shocks, turbulent mixing layers) may be at work.

5.3 Summary

This Chapter presented the first stages of a modelling study of Mrk 996, whose multi-component emission properties were presented in Chapter 3.

The narrow component fluxes were successfully reproduced using the observed physical and chemical parameters derived from optical IFU observations. The best fit model consisted of a central blackbody ionising source with an effective temperature 5×10^4 K and a stellar luminosity of 5.19×10^{41} erg s^{-1} (1.4×10^8 $L_\odot$), with the inclusion of a filling factor of 0.037, which correctly predicted most line fluxes. A fit to the optical photometric points was achieved by using an SB99 model input spectrum consisting of 1.0$\pm$0.5 Myr and 1.5$\pm$0.5 Gyr stellar populations, combined in a 1:40$\pm$10 mass ratio, which provides a more accurate representation of Mrk 996's stellar population than the initial blackbody. The inclusion of dust in this gas-only model provided insight into the dust population present within the galaxy. The best-fitting model to the mid-IR spectrum of the galaxy resulted from amorphous carbon dust with an MRN grain size distribution between 0.005–1.0 μm and a constant dust-to-gas mass distribution with $\frac{M_d}{M_g} = 1.7 \times 10^{-4}$. This final best-fit gas+dust model corresponded to a total stellar mass of 4.7×10^8 $M_\odot$, a total gas mass of 4.2×10^7 $M_\odot$ and a total mass which is within 6% of the dynamical mass of 5×10^8 $M_\odot$.

I was unsuccessful in reproducing the broad component line fluxes using a simple plane-parallel high-density slab model, used as an over simplification of the high density knots/clumps thought to exist throughout the core region of Mrk 996. I interpret this as evidence that other excitation mechanisms, such as shocks/turbulent mixing layers, may be responsible for the broad component line emission.

Further work is needed to use the full 3-dimensional capabilities of MOCASSIN, for both the narrow component and broad component models. This would include accurately recreating the geometry of the ionised gas (i.e. not spherically symmetric) and superimposing a VIMOS IFU sized aperture on the MOCASSIN output to allow a direct comparison with the nebular line emission maps derived in Chapter 3.

CHAPTER 6

CONCLUSIONS & FUTURE WORK

6.1 Conclusions

This thesis has presented an in-depth optical and infrared analysis of a sample of blue compact dwarf galaxies (BCDs). An optical integral field spectroscopy (IFS) analysis of three BCDs, UM 420, UM 462 and Mrk 996 enabled a spatially resolved analysis of their chemical, physical and kinematical properties. This work has provided detailed insight into the physical processes, e.g. chemical enrichment, propagation of star-formation, outflows etc, that occur within BCDs and demonstrated the importance of IFUs in diagnosing the chemical inhomogeneities that often occur in H II regions (Tsamis *et al.* 2006). An infrared analysis was performed on a subset of BCDs with a large range in metallicity that enabled a statistically-sound investigation of their dust component properties and the cause of the PAH depletion often seen within BCDs (Hunt *et al.* 2005; Madden *et al.* 2006; Wu *et al.* 2006). Finally, the optical and infrared data compiled in this work regarding the anomalous BCD Mrk 996 was used to constrain a photoionisation model of this galaxy, providing further insight into its dust-grain properties and old, underlying stellar population. What follows is a concise conclusion of the work presented in each chapter.

Chapter 2 concerned the analysis of VIMOS IFU integral field spectroscopy of two unrelated BCGs UM 420 and UM 462 and the study of their morphology from monochromatic emission line maps. Both systems show signs of interaction and/or perturbation with the former galaxy currently undergoing a merger (type 'iI,M') and the latter displaying a highly disrupted irregular or cometary appearance (type 'iI,C'; probably due to interaction with a BCG which was not part of this study, UM 461). The spatially resolved emission line maps in the light of [O III] and Hα revealed two

main areas of massive star formation in UM 420 along with a tidal arm, and at least four such areas in UM 462. Current star formation rates were computed from the Hα line luminosities for each main starbursting region and the ages of the last major star formation episode were estimated by fitting the observed Balmer line equivalent widths with STARBURST99 models. The two merging components of UM 420 have SFRs that differ by a factor of ~ 8 and starburst episodes separated by 1 Myr whereas in UM 462 the last star forming episode has been producing stars at a rate which varies across the galaxy between ~ 0.01 – $0.10\,M_{\odot}$ yr^{-1}, indicative of propagating or triggered star formation. For both targets the abundances of He, N, O, and S were measured and O/H abundance ratio maps were created based on the direct method of estimating electron temperatures from the [O III] λ4363/λ5007 line ratio. The measured oxygen abundances are 12 + log(O/H) = 8.03 $\pm$ 0.20 for UM 420 and 8.03 $\pm$ 0.10 for UM 462 (20 per cent solar). I found no evidence for significant nitrogen or oxygen variations across the galaxies (at the 0.2 dex level), which would have pointed to self-enrichment from nucleosynthetic products associated with the recent massive star formation activity. Regarding the abundance of nitrogen, and the N/O ratio, this result is in qualitative agreement with the finding that these BCGs cannot be classified as Wolf-Rayet galaxies since the characteristic broad-line stellar features have not been detected by VIMOS; the existence of WR stars in them is an open issue.

A third, and far more anomalous BCD, Mrk 996 was analysed in Chapter 3. It is a complex system containing an extended starburst region (216–432 pc in radius) with a centrally concentrated Wolf-Rayet population in the nuclear regions ($\lesssim$200 pc). The spatially mapped ionized gas showed a composite emission spectrum consisting of narrow and broad lines. My VIMOS IFU analysis has enabled a separate analysis of the physical conditions and chemical composition of the narrow and broad emission line regions. The broad line region in the nuclear starburst was found to be very dense (10^7 cm^{-3}) whereas the narrow line component is of lower density ($\lesssim 10^3$ cm^{-3}). I derived an upwards revised oxygen metallicity of Mrk 996 of $\geq 0.5\,Z_{\odot}$ (12 + log O/H $\approx$ 8.37). The broad line region was found to be nitrogen-enriched compared to the narrow line region by $\lesssim$1.3 dex. The N/O ratio in the *narrow* line component, is typical of those in H II galaxies and dwarf irregulars (e.g. van Zee & Haynes 2006; Izotov *et al.* 2006) and its mean current value can be interpreted as the result of the slow release of nitrogen from the intermediate-mass stellar population over the last few Gyrs. On the other hand, the high N/O ratio in the broad line region of the inner galaxy is consistent with the presence of numerous evolved massive stars (e.g. WNL-type and Luminous Blue Variables) and can be attributed to the cumulative effect of their N-enriched winds. A mild two-fold increase over the mean of the narrow-line N/H (Fig 3.16) was found to

spatially correlate with a local peak in $EW(\mathrm{H}\beta)$ in a region (Fig 3.21) where no WR stars are seen. This could mean that even though the narrow-line gas is fairly well mixed, some localized N-enrichment has already occurred in an area dominated by normal OB-type stars which is slightly younger than the nuclear starburst. A particularly interesting and important discovery was the broad-*only* [O III] λ4363 line detected in Mrk 996. In such cases where a substantial fraction of the [O III] 4363 and 4959, 5007 Å lines arise in different gas components, the integrated auroral to nebular ratio would *not* be representative of the electron temperature of the overall H II region; using it would result in biased physical conditions and chemical abundances. The problem would be aggravated in analyses based on low dispersion, low spatial resolution spectra and may therefore have implications for the so-called 'heating problem' of blue compact galaxies (e.g. Stasińska & Schaerer 1999; Péquignot 2008).

Chapter 4 described a mid-IR spectroscopic and photometric analysis of a subset of blue compact dwarf galaxies using *Spitzer* IRS, IRAC and MIPS archival data. A variety of methods and techniques were applied to the mid-IR spectra and photometric SEDs of each source in order to acquire information about its dust properties. Firstly, emission line measurements of the forbidden lines and PAH features within the high and low-resolution IRS spectra were made and documented. The density diagnostic ratio [S III] 18.7 μm/33.5 μm, when available, was used to determine electron densities for seven BCDs were found to agree with previous optically derived densities. Secondly, the suppression of PAH emission in BCDs was investigated using equivalent width (EW) measurements of the four main PAH bands at 6.2, 7.7, 8.6 and 11.2 μm as a function of metallicity and as a function of radiation field hardness, as indicated by the large difference in ionisation potential between Ne^{2+} and Ne^{+}. I conclude and agree with previous findings that photodestruction of PAHs as well as formation effects can be responsible for the lack of PAH molecules within these low-metallicity and relatively chemically unevolved systems. Secondly, IRS spectral mapping observations were presented for NGC 4670, Mrk 33 and NGC 5253. Stepping the IRS slit across the galaxy adds a spatial dimension to the IRS staring-mode spectroscopy that allows the creation of PAH maps and radiation field hardness maps using [Ne III]/[Ne II]. Overlaying the PAH map contours onto high resolution *HST* images showed centrally localised PAH emission that aligns with the main star-forming structures within each galaxy. The [Ne III]/[Ne II] ratio contours were also overlaid onto the images but did not show an expected alignment with the main SF regions. This is either due to inaccuracies in the WCS information in the LL modules or else the displacements could suggest the occurrence of outflow events. Finally, 3.6–850 μm SEDs were derived from aperture photometry performed on MIPS and IRAC data and archive IRAS and SCUBA

data. Multiple black-body profiles were fitted to the SEDs in order to assess the temperatures of the dust responsible for emission at these wavelengths. All SEDs could be fitted with a two dust components; a cooler 40–70 K component and a warmer 160–450 K component. The cold dust component is typical of dust temperatures in the outer regions of BCDs or perhaps molecular clouds, whilst the warmer component is more reminiscent of the temperatures of H II regions. I was also able to confirm the metallicity dependence of the 8–24 μm colour ratio and found that there is a negligible contribution to this relationship from warm dust enhancing the 24 μm flux, confirming the suspicions expressed by Wu *et al.* (2006).

Drawing from the optical and infra-red data detailed in Chapters 3 and 4, the final Chapter presented the first stages of a modelling study of Mrk 996. The narrow component fluxes were successfully reproduced using the observed physical and chemical parameters derived from optical IFU observations. The best fit model consisted of a central blackbody ionising source with an effective temperature 5×10^4 K and a stellar luminosity of 5.19×10^{41} erg s^{-1} (1.4×10^8 $L_{\odot}$), with the inclusion of a gas filling factor of 0.037, which correctly predicted most line fluxes. A fit to the optical photometric points was achieved by using an SB99 model input spectrum consisting of a 1.0$\pm$0.5 Myr and a 1.5$\pm$0.5 Gyr stellar population, combined in a 1:40$\pm$10 mass ratio, which provides a more accurate representation of Mrk 996's stellar population than the initial blackbody. The inclusion of dust into this gas-only model provided insight into the dust population present within the galaxy. The best-fitting model to the mid-IR spectrum of the galaxy resulted from amorphous carbon dust with an MRN grain size distribution between 0.005–1.0 μm. The final best-fit gas+dust model corresponded to a total stellar mass of 4.7×10^8 $M_{\odot}$, a total gas mass of 4.2×10^7 $M_{\odot}$ and a total mass which is within 6% of the dynamical mass of 5×10^8 $M_{\odot}$ derived in Chapter 3. I was unsuccessful in reproducing the broad component line fluxes using a simple plane-parallel high-density slab model, used as an over simplification of the high density knots/clumps thought to exist throughout the core region of Mrk 996. I interpret this as evidence that other excitation mechanisms, such as shocks/turbulent mixing layers, may be responsible for the broad component line emission.

6.2 Future Work

The True Age of BCDs

A current and long-standing issue in the study of metal-poor galaxies is the question of their true age. In the last decade, the advent of high resolution and high sensitivity spectrographs has

allowed more accurate estimations of the metallicities of BCDs, allowing us to determine, with increasing certainty, which BCDs are truly metal-poor.

However, are the metal-poor BCDs truly young? Despite gaining more accurate ionised gas abundances, the question posed by Searle & Sargent (1972) over three decades ago still remains unanswered: are the metal-poor dwarf galaxies truly young systems (forming stars $\leq$1 Gyr ago) or are they actually young systems whose current starburst is superimposed on older underlying population (formed several Gyr ago)? As discussed in Chapter 1, past CCD imaging studies, combined with spectral population synthesis models have shown that for the majority of BCDs the second scenario is true. These imaging studies, namely using high resolution observations by *HST*'s WFPC2 and ACS cameras, enable the most direct way to determine the true age of a stellar population: by constructing a colour magnitude diagram (CMD). However, this relies on the source being near enough for resolved stellar photometry and of the extremely metal poor sources known, only I Zw 18 and DDO 68 are close enough for this to be possible. Obtaining an accurate distance to the target is crucial in this method since ages rely on theoretical isochrones, the location of which in the CMD depends on the adopted distance to the galaxy. Accurate distances are either determined from high-resolution spectroscopy or (preferentially) from the photometry of variable Cepheid stars, as was the case for the most promisingly young BCD, I Zw 18 (Aloisi *et al.* 2007). However, the period-luminosity relations of Cepheids at low-metallicities are currently not well known and, as a consequence, Thuan (2008) find the distance calculation of I Zw 18 unreliable (along with it being based on a single Cepheid variable). Presently, the argument concerning the true age of I Zw 18 remains ongoing due to this fact. With the hope of remedying this situation, one of my future projects involves a similar ACS imaging investigation of the remaining nearby low-metallicity system, DDO 68 (detailed below).

Another way of investigating their true age is to probe the *neutral* gas component within BCDs, i.e. that which is responsible for feeding their star-formation (Thuan & Martin 1981). If they are truly young systems, then the H I gas component within BCDs is likely to be primordial - i.e. devoid of any heavy elements. Previous work regarding this issue involved FUSE UV spectroscopy of 8 BCDs by Lebouteiller *et al.* (2009) and revealed that a metallicity floor exists in neutral gas of $12+\log(O/H)_{neutral}$ $\sim$0.7 for BCDs with $12+\log(O/H)_{ionised}$ $\leq$8.0. This supports the suggestion of Thuan *et al.* (2005) that the matter from which dwarf emission-line galaxies formed was pre-enriched to a common level of about 2% of the abundance of the Sun, possibly by Population III stars. However, this work was limited by the modest S/N of the FUSE spectrograph and the low number of BCDs in the sample. Future work concerning a more in-depth investigation

into the neutral gas abundances of BCDs with low-metallicities is essential in understanding the enrichment processes within the ISM of BCDs. Such work is intended with the recently mounted Cosmic Origin Telescope (COS) on *HST* (described in further detail below).

A New Technological Era

We currently enter an era of technologically advanced instruments such as Herschel, JWST (James Webb Space Telescope), ALMA, SMA, SOFIA etc whose far-IR, sub-mm and mm wavelength observations will likely provide substantial advances due to improvements in spatial resolution and sensitivity.

The JWST 6.6 m IR space observatory, due to be launched early next decade, has one of four main science goals dedicated to the assembly of galaxies. This theme seeks to determine how galaxies and the dark matter, gas, stars, metals, morphological structures, and active nuclei within them evolved from the epoch of reionisation to the present day. As an example, one study under this theme involves observing sites of extreme star formation (SF) in local universe extragalactic objects such as low-metallicity H II regions. Sites of extreme SF, i.e. violent luminous SF that occurs in starburst galaxies (such as BCDs) and luminous IR galaxies, are sources of galactic winds and metal enrichment of a galaxies ISM. With the refurbishment of the *HST* and the development of ground-based adaptive optics systems, combined with the JWST, fundamental contributions to our understanding of extreme SF sites and their stellar content are highly likely.

Observations of metal-poor dwarf galaxies will also continue to advance with far-IR and sub-mm observations from the recently launched 3.5 m Herschel telescope. With a principal goal of furthering our understanding of galaxy evolution, one particular large scale Herschel project aims at observing 55 metal-poor dwarfs. According to the hierarchical model (White & Rees 1978), dwarf galaxies are thought to be their crucial building blocks of larger galaxies despite evidence of nearby dwarfs having younger populations than their larger cousins. This ambiguity may be due to inaccurate measurements of dwarf galaxies' ISM or poorly-understood star formation histories. By obtaining a large statistically sound sample of low-metallicity dwarf galaxies, something that was not achieved by ISO and Spitzer, the Herschel observations hope to provide an opportunity for the community to perform dust and gas analyses in unprecedented detail in low-metallicity galaxies. Their primary goal is to further our understanding of the physical processes at play within the ISM of low-metallicity environments and how other factors, including SF activity and has mass fractions, affect these processes.

Cosmological Implications: The Primordial Helium Abundance

With their ever-increasing accuracy, the observations of metal-poor dwarf galaxies will begin to play a fundamental role in cosmology. In addition to the role they play in the hierarchical structure of galaxy formation, BCDs are also relevant to cosmic metal enrichment, the study of the yield of heavy elements and the derivation of the primordial helium abundance (Kunth & Östlin 2000). In the standard Big Bang nucleosynthesis model, helium was produced during the first few minutes of the observable Universe, while subsequent nucleosynthesis has added 10–20% to its primordial value. Cosmologically, the primordial helium abundance, Y_p, has profound importance as it determines the nucleon density parameter in the early Universe. At present, the most accurate way of measuring Y_p is by measuring the elemental helium abundance, Y, in BCDs, and extrapolating the He/H versus O/H relation down to Y_p as the oxygen abundance approaches zero (Peimbert & Torres-Peimbert 1974; Lequeux *et al.* 1979). The current measurement stands at 0.2477$\pm$0.0018 (Peimbert 2008). However, further work is required in assessing firstly the importance of stellar absorption lines that may weaken the observed He I emission lines and secondly the discrepancies in $T_{\rm e}$ calculations. The latter issue is one of the major current hindrances in this work - at present T([O III]) values are used, which weight preferentially regions of higher temperature than the average. In order to investigate the difference between T([O III]) and $T(He^+)$, a significant amount of further work is needed to understand the temperature structure in H II regions (Izotov *et al.* 2007*b*). Further improvements to the accuracy of this parameter will also follow from high-resolution 2D spectroscopy of the most metal poor BCDs (such as I Zw 18, SBS 0335-052 and DDO 68) which will help tackle the stratification effects in H II regions and localise possible contaminations due to WR stars and supernovae.

6.2.1 VLT-FLAMES 3D Spectroscopy of UM 448 & Haro 11

Following the detailed IFU studies of UM 420, UM 462 and Mrk 996 presented in Chapters 2 and 3, and the insights that I have gained into their chemical, physical and kinematical properties, I would like to continue to investigating BCDs using integral field spectroscopy. This will begin with 2009 VLT-FLAMES observations (for which I am principal investigator (PI)) using the GIRAFFE IFU to obtain IFS of two BCDs: UM 448 and Haro 11. The proposal was awarded a Grade A classification for the ESO period 83A and will be taken in service mode (the prime targets cannot be observed in a single run). Observations of UM 448 were due to be taken between April-June 09, however only 2 out of 7 OBs were taken at the time of writing and are currently being considered for carry-over into the next useful semester. Haro 11 is was successfully ob-

served in July 2009 and reduction of the data (received August 2009) will commence following the submission of this thesis.

GIRAFFE is a medium-high resolution spectrograph (R=7500-30000) for the entire visible range (3700–9000 Å) and is one of three components of the FLAMES spectrograph mounted on the VLT in Paranal, Chile. My observations will make use of the ARGUS IFU mode of GIRAFFE, that consists of a rectangular array of 22×14 microlenses and a sampling of $0.52''$/microlens ($0.3''$/microlens sampling is also available).

The two galaxies are part of a group of eight BCDs thought to contain anomalously high nitrogen abundances, suggested to be connected with merger events, in particular with a short phase of the related powerful starburst, when many WR stars can contribute to the ISM enrichment (Pustilnik *et al.* (2004),Mallery *et al.* (2007)). The two target BCDs have a common high N/O and spatial nitrogen variations but are at a different evolutionary stage. They will also complement the VIMOS-IFU sample of objects presented in Chapters 2 and 3; Mrk 996 and UM 420 were also thought to contain N/O anomalies whereas UM 462 had been diagnosed as having a more *normal* N/O ratio and was used for comparison purposes. As a result of work presented in this thesis, Mrk 996 and UM 420 now have derived N/O ratios that are normal for their metallicities and are no longer part of the group with enhanced N/O ratios. UM 448 exhibits N/O excesses of a factor 3 or larger, relative to typical N/O values for its O/H (Pustilnik *et al.* 2004), whereas Haro 11 has a lower metallicity but with a published N/O abundance ratio excess of $\sim$6 (Bergvall & Östlin 2002). The kinematical maps produced by the IFU observations could also provide insight into their histories - both galaxies are thought result from a merger, with distorted morphologies akin to those seen in UM 462 (Chapter 2). Both galaxies are extended sources and fit well with the $0.52''$/microlens spatial resolution, with the IFU FoV covering 95% of each target (see Figure 6.1)

Observations will be made in the FLAMES low-resolution settings LR1–3 (wavelength range 3620–5078 Å) and LR6 (6438–7184 Å) that will include important diagnostic lines such as [O III] λ4363, λ4959 and λ5007 for the determination of $T_{\rm e}$, [S II] λ6716 and λ6731 to determine $N_{\rm e}$, the Balmer lines Hα, Hβ and Hγ and, most importantly, [O II] λ3727. Detections of this line will enable more accurate calculations of the elemental oxygen abundance when combined with [O III] λ5007, i.e. without the need to employ published long-slit spectra, or the ICF methods that I used for oxygen abundance calculations in Chapter 2 (VIMOS has a minimum wavelength of 4200 Å and O^+ abundances were obtained for Mrk 996 using the detected [O II] λ7320, 7330 lines). With the detection of all these lines, I should be able to create $N_{\rm e}$, $T_{\rm e}$ and ionic and elemental abundance maps.

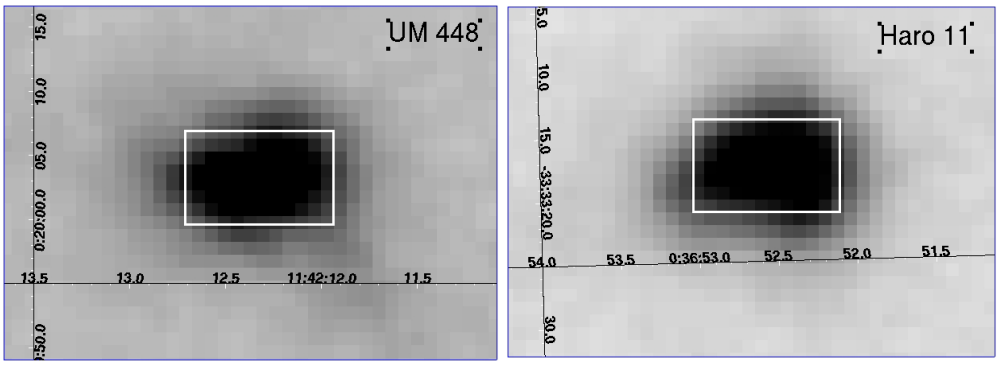

Figure 6.1: Red filter DSS images of UM 448 and Haro 11 with FLAMES-ARGUS $11.5'' \times 7.3''$ IFU overlaid

Both galaxies have shown strong signatures of WR populations, thus I will create 2D maps of the broad WR emission feature at ∼4650 and 5805 Å and comparisons will be made with the SF locations determined from the emission line and excitation maps. Also, following the kinematical analysis of Mrk 996, I will try to determine axes of rotation from the radial velocity maps, and PV diagrams along these axes will be used to derive the dynamical mass as a function of radius.

After obtaining encouraging results from my detailed IFU investigation of UM 420 and Mrk 996 (James *et al.* (2009*b*,*a*)), that yielded more reliable abundances and disposed of their previously anomalous N/O abundance ratios, I hope that these observations will also shed light on the N and O abundances of two more supposedly anomalous BCDs. I believe that these types of high resolution spatial and kinematical studies of low surface brightness galaxies such as BCDs are essential for furthering our understanding of these systems, and are only possible with the use of large integral field units such as VIMOS and FLAMES.

6.2.2 *HST* Imaging of DDO 68

One of the main driving factors behind the study of BCDs is that their relatively chemically unevolved environments offer a means to discover and explore local analogues to the first galaxies. These sought after galaxies, in which stars are now forming for the first time, in the nearby (i.e. present-day) Universe, could be the local analogs of primordial high-redshift galaxies that cannot be observed in detail with current instruments. However, as discussed in Section 1.1.2, resolved stellar photometry of BCDs with *HST* data has revealed an older (>1 Gyr) stellar population in the majority of BCDs, as traced by red giant branch (RGB) stars. One important case study is

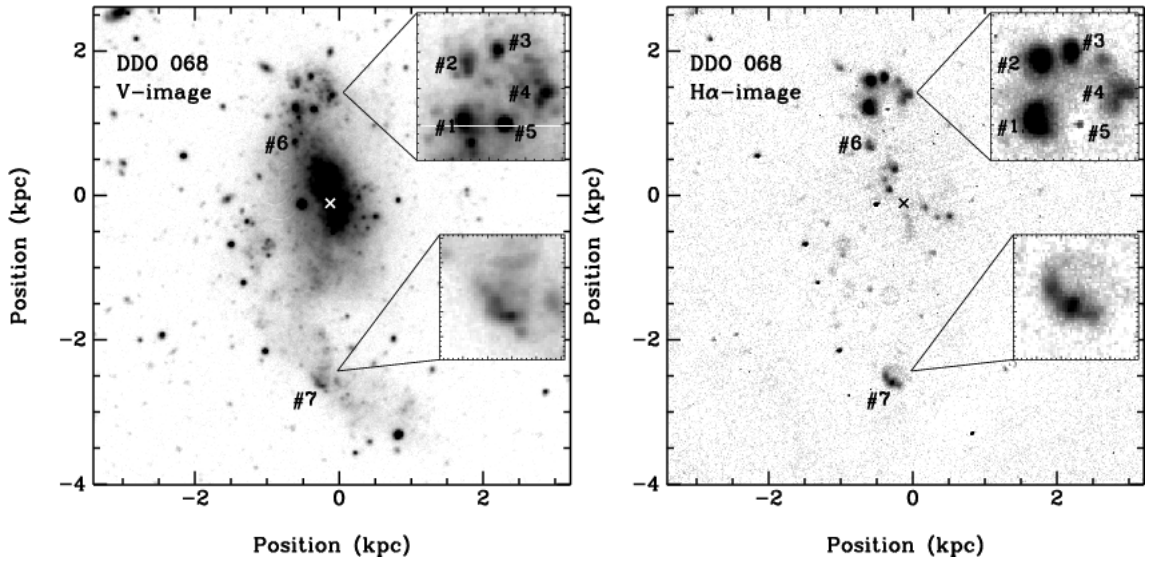

Figure 6.2: V-band and Hα images of DDO 68 from Pustilnik *et al.* (2005) showing its overall morphology and the regions of currently intense star formation. DDO 68 lies at a distance of 6.5 Mpc.

I Zw 18, the most metal-poor galaxy known for over two decades. After an extended controversial exchange between different groups (see Section 1.1.2.1 for details), Aloisi *et al.* (2007) succeeded in detecting an RGB in I Zw 18, although discrepancies exist regarding their adopted distance to I Zw 18. However, the star formation histories of BCDs may vary from galaxy to galaxy and this does not rule out the existence of truly young galaxies in the local Universe.

The exploration of these issues has been revived recently with the discovery of DDO 68, shown in Figure 6.2; an irregular BCD consisting of 5 regions. It is one of the three most metal poor galaxies known (joining SBS 0335-052W and I Zw 18), with an average metallicity of 12+log(O/H)=7.21$\pm$0.03 (Pustilnik *et al.* 2005), more recently revised to 7.15$\pm$0.04, with a lowest metallicity knot at 12+log(O/H)=7.10$\pm$0.06 (Pustilnik *et al.* 2008). The nearby proximity of this galaxy (6.5 Mpc, 2-3 times closer than I Zw 18) allows us to avoid the ambiguities surrounding the studies of I Zw 18. Also, DDO 68 resides in a relative void, making it likely that star-formation has not been contaminated by mergers and/or interactions and has therefore been suppressed for a long time. Stellar age estimations currently lie at 200-900 Myr, from $(V - R)$ colours (Pustilnik *et al.* 2005), although confirmation is needed from photometry of resolved stars.

Hence, one aspect of my future work will involve performing stellar photometry on deep ACS images in order to create deep color-magnitude diagrams (CMDs) for the stellar population of DDO 68 (proposal ID: 11578, PI: A.Aloisi). The data will consist of ACS/WFC images in the F606W and F814W filters, along with F658N filter images to correct the broad F606W images for nebular line contamination. The project will also entail the use of WFC3 data (recently mounted on *HST* during the May 2009 servicing mission), in parallel with the same filters, to study radial population gradients. I will use synthetic CMD fitting routines to construct and interpret CMDs reaching a depth of one magnitude below the predicted RGB tip. It is hoped that this work will determine unambiguously whether DDO 68 has an underlying old stellar population or is forming stars for the first time. Finding just a single nearby 'young' galaxy would have profound implications.

6.2.3 Abundance Determinations in Local SF Galaxies using COS

In Chapters 2 and 3 of this thesis I derived ionic and elemental abundances for three BCDs: UM 420, UM 462 and Mrk 996. As discussed in these chapters, knowledge of the abundances and hence metallicities of BCDs is essential in helping us understand the chemical environments in primordial-like galaxies. The metallicities of galaxies and their evolution with redshift is of paramount importance for understanding galaxy formation. However, the metallicity of a galaxy can differ according to the location (e.g. halo/disk/SF regions) and also the type of gas (e.g. ionised/atomic/molecular) (Kunth & Östlin 2000). The abundances determined in this thesis were obtained via emission line spectroscopy of H II regions within BCDs. However, since the H II regions are associated with recent SF they may not have abundances typical of the galaxy as a whole. This is true in particular for star-forming galaxies (SFGs), in which the bulk of metals may be contained in the neutral gas. One aspect of my future work will involve directly probing the abundances in the neutral gas of SFGs using absorption lines located in the far-UV.

I will build upon previous work using the Far Ultraviolet Spectroscopic Explorer (FUSE) by Grimes *et al.* (2009) in which this technique was applied to a sample of 16 local starburst galaxies. One significant result from previous FUSE observations of I Zw 18 (this object was described in detail in Section 1.1.2.1) suggests that the abundances in the neutral gas may be up to 0.5 dex lower than in the ionised gas (Aloisi *et al.* 2003). However, this work was limited by the very large FUSE aperture (30 $''$), its modest S/N, and the limited selection of species available in the FUSE bandpass.

In May 2009, as part of the Hubble servicing mission 4, the Cosmic Origin Spectrograph

(COS) was successfully mounted on *HST*. It will be the most sensitive UV spectrograph ever flown, with a UV sensitivity specifically designed to "sample the chemical content and physical state of gas in distant galaxy halos, providing important insight into the building processes of early galaxies". My future project involves analysing COS data for the same galaxies sampled by FUSE from a successful *HST* proposal (ID 11579, PI A.Aloisi). The project will involve absorption line spectroscopy with the far-UV G130M grating that will build upon the constraints already obtained from FUSE. Several point-like sources within nine nearby star-forming galaxies (some of which were analysed in this thesis) will be observed in the 1132-1274 Å and 1291-1433 Å ranges. The data will also include ACS images that will be used to select a few optimal bright and compact ($r \leq 0.5''$) target sources in each galaxy, in order to achieve a spectral resolution that will allow the neutral ISM analysis.

It is hoped that the results will provide important new insights into the metallicities of galaxies, and into outstanding problems at high redshifts, such as the observed offset between the metallicities of Lyman-Break Galaxies and Damped Lyman-α systems.

Bibliography

Allamandola, L. J., Tielens, A. G. G. M. & Barker, J. R., 1989, *ApJS*, **71**, 733

Allende Prieto, C., Lambert, D. L. & Asplund, M., 2001, *ApJL*, **556**, L63

Allington-Smith, J. R., Content, R. & Haynes, R., 1998 (SPIE), volume 3355, pp. 196–205
URL: *http://link.aip.org/link/?PSI/3355/196/1*

Alloin, D., Bergeron, J. & Pelat, D., 1978, *A&A*, **70**, 141

Aloisi, A., Annibali, F., Mack, J., Tosi, M., van der Marel, R., Clementini, G., Contreras, R. A., Fiorentino, G., Marconi, M., Musella, I. & Saha, A., 2007, in A. Vazdekis & R. F. Peletier (eds.), *IAU Symposium*, volume 241 of *IAU Symposium*, pp. 310–314

Aloisi, A., Savaglio, S., Heckman, T. M., Hoopes, C. G., Leitherer, C. & Sembach, K. R., 2003, *ApJ*, **595**, 760

Aloisi, A., Tosi, M. & Greggio, L., 1999, *AJ*, **118**, 302

Baker, J. G. & Menzel, D. H., 1938, *ApJ*, **88**, 52

Bakes, E. L. O. & Tielens, A. G. G. M., 1994, *ApJ*, **427**, 822

Baldwin, J. A., Phillips, M. M. & Terlevich, R., 1981, *PASP*, **93**, 5

Bastian, N., Emsellem, E., Kissler-Patig, M. & Maraston, C., 2006, *A&A*, **445**, 471

Begelman, M. C. & Fabian, A. C., 1990, *MNRAS*, **244**, 26P

Beirão, P., Brandl, B. R., Devost, D., Smith, J. D., Hao, L. & Houck, J. R., 2006, *ApJL*, **643**, L1

Benjamin, R. A., Skillman, E. D. & Smits, D. P., 1999, *ApJ*, **514**, 307

Bergvall, N. & Östlin, G., 2002, *A&A*, **390**, 891

Binette, L., Drissen, L., Ubeda, L., Raga, A. C., Robert, C. & Krongold, Y., 2009, *A&A*, **500**, 817

Bradley, W. & Dale, A. O., 1996, *An Introduction to Modern Astrophysics* (Benjamin Cummings)

Brandl, B. R., Bernard-Salas, J., Spoon, H. W. W., Devost, D., Sloan, G. C., Guilles, S., Wu, Y., Houck, J. R., Weedman, D. W., Armus, L., Appleton, P. N., Soifer, B. T., Charmandaris, V., Hao, L., Higdon, J. A. M. S. J. & Herter, T. L., 2006, *ApJ*, **653**, 1129

Brinchmann, J., Kunth, D. & Durret, F., 2008, *A&A*, **485**, 657

Cairós, L. M., Caon, N., Papaderos, P., Noeske, K., Vílchez, J. M., García Lorenzo, B. & Muñoz-Tuñón, C., 2003, *ApJ*, **593**, 312

Cairós, L. M., Caon, N., Vílchez, J. M., González-Pérez, J. N. & Muñoz-Tuñón, C., 2001*a*, *ApJS*, **136**, 393

Cairós, L. M., Vílchez, J. M., González Pérez, J. N., Iglesias-Páramo, J. & Caon, N., 2001*b*, *ApJS*, **133**, 321

Calzetti, D., Harris, J., Gallagher, III, J. S., Smith, D. A., Conselice, C. J., Homeier, N. & Kewley, L., 2004, *AJ*, **127**, 1405

Cerviño, M. & Mas-Hesse, J. M., 1994, *A&A*, **284**, 749

Cesarsky, D., Lequeux, J., Abergel, A., Perault, M., Palazzi, E., Madden, S. & Tran, D., 1996, *A&A*, **315**, L309

Cohen, M., Megeath, S. T., Hammersley, P. L., Martín-Luis, F. & Stauffer, J., 2003, *AJ*, **125**, 2645

Cohen, M. & Volk, K., 1989, *AJ*, **98**, 1563

Conti, P. S. & Underhill, A. B., 1988, *Journal of the British Astronomical Association*, **98**, 374

Cresci, G., Vanzi, L. & Sauvage, M., 2005, *A&A*, **433**, 447

Crowther, P. A., 2007, *ArA&A*, **45**, 177

Crowther, P. A., Beck, S. C., Willis, A. J., Conti, P. S., Morris, P. W. & Sutherland, R. S., 1999, *MNRAS*, **304**, 654

Crowther, P. A. & Hadfield, L. J., 2006, *A&A*, **449**, 711

Dale, D. A., Smith, J. D. T., Schlawin, E. A., Armus, L., Buckalew, B. A., Cohen, S. A., Helou, G., Jarrett, T. H., Johnson, L. C., Moustakas, J., Murphy, E. J., Roussel, H., Sheth, K., Staudaher, S., Bot, C., Calzetti, D., Engelbracht, C. W., Gordon, K. D., Hollenbach, D. J., Kennicutt, R. C. & Malhotra, S., 2009, *ApJ*, **693**, 1821

de Vaucouleurs, G. & de Vaucouleurs, A., 1964, *Reference catalogue of bright galaxies*

DeBernardis, F., Melchiorri, A., Verde, L. & Jimenez, R., 2008, *Journal of Cosmology and Astro-Particle Physics*, **3**, 20

Dimeo, R., 2005, *PAN User Guide*
URL: *ftp://ftp.ncnr.nist.gov/pub/staff/dimeo/pandoc.pdf*

Dopita, M. A., 1978, *ApJS*, **37**, 117

Dopita, M. A., Kewley, L. J., Sutherland, R. S. & Heisler, C. A., 2001, in L. Tacconi & D. Lutz (eds.), *Starburst Galaxies: Near and Far*, p. 225

Doublier, V., Comte, G., Petrosian, A., Surace, C. & Turatto, M., 1997, *A&AS*, **124**, 405

Dufour, R. J., Garnett, D. R., Skillman, E. D. & Shields, G. A., 1996, in C. Leitherer, U. Fritze-von-Alvensleben & J. Huchra (eds.), *From Stars to Galaxies: the Impact of Stellar Physics on Galaxy Evolution*, volume 98 of *Astronomical Society of the Pacific Conference Series*, pp. 358–+

Dwek, E., 2005*a*, in C. C. Popescu & R. J. Tuffs (eds.), *The Spectral Energy Distributions of Gas-Rich Galaxies: Confronting Models with Data*, volume 761 of *American Institute of Physics Conference Series*, pp. 103–+

Dwek, E., 2005*b*, in R. Szczerba, G. Stasinska & S. K. Gorny (eds.), *Planetary Nebulae as Astronomical Tools*, volume 804 of *American Institute of Physics Conference Series*, pp. 197–203

Engelbracht, C. W., Gordon, K. D., Rieke, G. H., Werner, M. W., Dale, D. A. & Latter, W. B., 2005, *ApJL*, **628**, L29

Ercolano, B., Barlow, M. J. & Storey, P. J., 2005, *MNRAS*, **362**, 1038

Ercolano, B., Barlow, M. J., Storey, P. J. & Liu, X.-W., 2003, *MNRAS*, **340**, 1136

Ercolano, B., Young, P. R., Drake, J. J. & Raymond, J. C., 2008, *ApJS*, **175**, 534

Fanelli, M. N., O'Connell, R. W. & Thuan, T. X., 1988, *ApJ*, **334**, 665

Fazio, G. G. *et al.*, 2004, *ApJS*, **154**, 10

Ferland, G. J., 1990, *Hazy, A Brief Introduction to Cloudy 84*

Ferland, G. J., 1993, *Hazy, A Brief Introduction to Cloudy 84*

Fernandes, I. F., de Carvalho, R., Contini, T. & Gal, R. R., 2004, *MNRAS*, **355**, 728

Gallego, J., Zamorano, J., Rego, M. & Vitores, A. G., 1997, *ApJ*, **475**, 502

Galliano, F., 2006, *ArXiv;0610.852*

Galliano, F., Madden, S. C., Jones, A. P., Wilson, C. D. & Bernard, J.-P., 2005, *A&A*, **434**, 867

Galliano, F., Madden, S. C., Jones, A. P., Wilson, C. D., Bernard, J.-P. & Le Peintre, F., 2003, *A&A*, **407**, 159

García-Lorenzo, B., Cairós, L. M., Caon, N., Monreal-Ibero, A. & Kehrig, C., 2008, *ApJ*, **677**, 201

Garcia-Vargas, M. L., Gonzalez-Delgado, R. M., Perez, E., Alloin, D., Diaz, A. & Terlevich, E., 1997, *ApJ*, **478**, 112

Garnett, D. R., Skillman, E. D., Dufour, R. J. & Shields, G. A., 1997, *ApJ*, **481**, 174

Geballe, T. R., Tielens, A. G. G. M., Allamandola, L. J., Moorhouse, A. & Brand, P. W. J. L., 1989, *ApJ*, **341**, 278

Giard, M., Bernard, J. P., Lacombe, F., Normand, P. & Rouan, D., 1994, *A&A*, **291**, 239

Grimes, J. P., Heckman, T., Aloisi, A., Calzetti, D., Leitherer, C., Martin, C. L., Meurer, G., Sembach, K. & Strickland, D., 2009, *ApJS*, **181**, 272

Guseva, N. G., Izotov, Y. I. & Thuan, T. X., 2000, *ApJ*, **531**, 776

Heckman, T. M., Robert, C., Leitherer, C., Garnett, D. R. & van der Rydt, F., 1998, *ApJ*, **503**, 646

Herter, T., Houck, J. R., Shure, M., Gull, G. E. & Graf, P., 1984, *ApJL*, **287**, L15

Higdon, S. J. U., Devost, D., Higdon, J. L., Brandl, B. R., Houck, J. R., Hall, P., Barry, D., Charmandaris, V., Smith, J. D. T., Sloan, G. C. & Green, J., 2004, *PASP*, **116**, 975

Hony, S., Bouwman, J., Keller, L. P. & Waters, L. B. F. M., 2002, *A&A*, **393**, L103

Hopkins, A. M., Schulte-Ladbeck, R. E. & Drozdovsky, I. O., 2002, *AJ*, **124**, 862

Houck, J. R. *et al.*, 2004*a*, *ApJS*, **154**, 18

Houck, J. R., Charmandaris, V., Brandl, B. R., Weedman, D., Herter, T., Armus, L., Soifer, B. T., Bernard-Salas, J., Spoon, H. W. W., Devost, D. & Uchida, K. I., 2004*b*, *ApJS*, **154**, 211

Howarth, I. D., 1983, *MNRAS*, **203**, 301

Huchra, J. P., Geller, M. J., Gallagher, J., Hunter, D., Hartmann, L., Fabbiano, G. & Aaronson, M., 1983, *ApJ*, **274**, 125

Hummer, D. G. & Storey, P. J., 1987, *MNRAS*, **224**, 801

Hunt, L., Bianchi, S. & Maiolino, R., 2005, *A&A*, **434**, 849

Hunt, L. K., Thuan, T. X., Sauvage, M. & Izotov, Y. I., 2006, *ApJ*, **653**, 222

Hunter, D. A. & Thronson, Jr., H. A., 1995, *ApJ*, **452**, 238

Iglesias-Páramo, J. & Vílchez, J. M., 2001, *ApJ*, **550**, 204

Ivezic, Z. & Elitzur, M., 1997, *MNRAS*, **287**, 799

Izotov, I. I., Guseva, N. G., Lipovetskii, V. A., Kniazev, A. I. & Stepanian, J. A., 1990, *Nature*, **343**, 238

Izotov, Y. I., Lipovetsky, V. A., Chaffee, F. H., Foltz, C. B., Guseva, N. G. & Kniazev, A. Y., 1997, *ApJ*, **476**, 698

Izotov, Y. I., Stasińska, G., Meynet, G., Guseva, N. G. & Thuan, T. X., 2006, *A&A*, **448**, 955

Izotov, Y. I. & Thuan, T. X., 1998, *ApJ*, **500**, 188

Izotov, Y. I. & Thuan, T. X., 1999, *ApJ*, **511**, 639

Izotov, Y. I. & Thuan, T. X., 2004, *ApJ*, **616**, 768

Izotov, Y. I. & Thuan, T. X., 2007, *ApJ*, **665**, 1115

Izotov, Y. I. & Thuan, T. X., 2008, *ApJ*, **687**, 133

Izotov, Y. I., Thuan, T. X. & Guseva, N. G., 2005, *ApJ*, **632**, 210

Izotov, Y. I., Thuan, T. X. & Guseva, N. G., 2007*a*, *ApJ*, **671**, 1297

Izotov, Y. I., Thuan, T. X. & Lipovetsky, V. A., 1994, *ApJ*, **435**, 647

Izotov, Y. I., Thuan, T. X. & Stasińska, G., 2007*b*, *ApJ*, **662**, 15

Jackson, D. C., Cannon, J. M., Skillman, E. D., Lee, H., Gehrz, R. D., Woodward, C. E. & Polomski, E., 2006, *ApJ*, **646**, 192

James, B., Tsamis, Y. & Barlow, 2009*a*, *MNRAS Accepted*

James, B. L., Tsamis, Y. G., Barlow, M. J., Westmoquette, M. S., Walsh, J. R., Cuisinier, F. & Exter, K. M., 2009*b*, *MNRAS*, **398**, 2

Keenan, F. P., Aller, L. H., Ryans, R. S. I. & Hyung, S., 2001, *Proceedings of the National Academy of Science*, **98**, 9476

Kehrig, C., Vílchez, J. M., Sánchez, S. F., Telles, E., Pérez-Montero, E. & Martín-Gordón, D., 2008, *A&A*, **477**, 813

Keller, L. P., Hony, S., Bradley, J. P., Molster, F. J., Waters, L. B. F. M., Bouwman, J., de Koter, A., Brownlee, D. E., Flynn, G. J., Henning, T. & Mutschke, H., 2002, *Nature*, **417**, 148

Kennicutt, Jr., R. C., 1984, *ApJ*, **287**, 116

Kennicutt, Jr., R. C., 1998, *ArA&A*, **36**, 189

Kewley, L. J., Dopita, M. A., Sutherland, R. S., Heisler, C. A. & Trevena, J., 2001, *ApJ*, **556**, 121

Kim, H.-S., Wagner, D. R. & Saykally, R. J., 2001, *Physical Review Letters*, **86**, 5691

Kingdon, J. & Ferland, G. J., 1995, *ApJ*, **442**, 714

Kingsburgh, R. L. & Barlow, M. J., 1994, *MNRAS*, **271**, 257

Kinney, A. L., Bohlin, R. C., Calzetti, D., Panagia, N. & Wyse, R. F. G., 1993, *ApJS*, **86**, 5

Kobulnicky, H. A., Kennicutt, Jr., R. C. & Pizagno, J. L., 1999, *ApJ*, **514**, 544

Kodama, T., 1997, Ph.D. thesis, PhD thesis, Institute of Astronomy, Univ. Tokyo , (1997)

Kunth, D., Maurogordato, S. & Vigroux, L., 1988, *A&A*, **204**, 10

Kunth, D. & Östlin, G., 2000, *A&AR*, **10**, 1

Lagos, P., Telles, E., Muñoz-Tuñón, C., Carrasco, E. R., Cuisinier, F. & Tenorio-Tagle, G., 2009, *AJ*, **137**, 5068

Lebouteiller, V., Brandl, B., Bernard-Salas, J., Devost, D. & Houck, J. R., 2007, *ApJ*, **665**, 390

Lebouteiller, V., Kunth, D., Thuan, T. X. & Désert, J. M., 2009, *A&A*, **494**, 915

Lee, J. C., Salzer, J. J., Impey, C., Thuan, T. X. & Gronwall, C., 2002, *AJ*, **124**, 3088

Leger, A. & Puget, J. L., 1984, *A&A*, **137**, L5

Legrand, F., Kunth, D., Mas-Hesse, J. M. & Lequeux, J., 1997, *A&A*, **326**, 929

Leitherer, C., Schaerer, D., Goldader, J. D., Delgado, R. M. G., Robert, C., Kune, D. F., de Mello, D. F., Devost, D. & Heckman, T. M., 1999, *ApJS*, **123**, 3

Lennon, D. J. & Burke, V. M., 1994, *A&AS*, **103**, 273

Lequeux, J., Peimbert, M., Rayo, J. F., Serrano, A. & Torres-Peimbert, S., 1979, *A&A*, **80**, 155

Liu, X.-W., Storey, P. J., Barlow, M. J., Danziger, I. J., Cohen, M. & Bryce, M., 2000, *MNRAS*, **312**, 585

Lodders, K., 2003, *ApJ*, **591**, 1220

Loose, H.-H. & Thuan, T. X., 1985, in D. Kunth, T. X. Thuan & J. Tran Thanh van (eds.), *Star-Forming Dwarf Galaxies and Related Objects*, pp. 73–+

López-Sánchez, Á. R. & Esteban, C., 2008, *A&A*, **491**, 131

Luridiana, V., Peimbert, A., Peimbert, M. & Cerviño, M., 2003, *ApJ*, **592**, 846

Luridiana, V., Peimbert, M. & Leitherer, C., 1999, *ApJ*, **527**, 110

MacAlpine, G. M. & Lewis, D. W., 1978, *ApJS*, **36**, 587

Madden, S. C., 2002, *ApSS*, **281**, 247

Madden, S. C., Galliano, F., Jones, A. P. & Sauvage, M., 2006, *A&A*, **446**, 877

Maeder, A. & Meynet, G., 1987, *A&A*, **182**, 243

Maeder, A. & Meynet, G., 1994, *A&A*, **287**, 803

Mallery, R. P., Kewley, L., Rich, R. M., Salim, S., Charlot, S., Tremonti, C., Seibert, M., Small, T., Wyder, T., Barlow, T. A., Forster, K., Friedman, P. G., Martin, D. C., Morrissey, P., Neff, S. G., Schiminovich, D., Bianchi, L., Donas, J., Heckman, T. M., Lee, Y.-W., Madore, B. F., Milliard, B., Szalay, A. S., Welsh, B. Y. & Yi, S., 2007, *ApJS*, **173**, 482

Markarian, B. E. & Stepanian, D. A., 1983, *Astrofizika*, **19**, 639

Marshall, J. A., Herter, T. L., Armus, L., Charmandaris, V., Spoon, H. W. W., Bernard-Salas, J. & Houck, J. R., 2007, *ApJ*, **670**, 129

Mas-Hesse, J. M. & Kunth, D., 1991, in K. A. van der Hucht & B. Hidayat (eds.), *Wolf-Rayet Stars and Interrelations with Other Massive Stars in Galaxies*, volume 143 of *IAU Symposium*, pp. 613–+

Mas-Hesse, J. M. & Kunth, D., 1999, *A&A*, **349**, 765

Mathis, J. S., Rumpl, W. & Nordsieck, K. H., 1977, *ApJ*, **217**, 425

Melnick, J., Heydari-Malayeri, M. & Leisy, P., 1992, *A&A*, **253**, 16

Méndez, D. I. & Esteban, C., 2000, *A&A*, **359**, 493

Momany, Y., Held, E. V., Saviane, I., Bedin, L. R., Gullieuszik, M., Clemens, M., Rizzi, L., Rich, M. R. & Kuijken, K., 2005, *A&A*, **439**, 111

Moorwood, A. F. M. & Glass, I. S., 1982, *A&A*, **115**, 84

Nazé, Y., Rauw, G., Manfroid, J., Chu, Y.-H. & Vreux, J.-M., 2003, *A&A*, **408**, 171

Nussbaumer, H. & Storey, P. J., 1984, *A&AS*, **56**, 293

O'Halloran, B., Satyapal, S. & Dudik, R. P., 2006, *ApJ*, **641**, 795

Osterbrock, D. E., 1989, *Astrophysics of gaseous nebulae and active galactic nuclei*

Osterbrock, D. E. & Ferland, G. J., 2006, *Astrophysics of Gaseous Nebulae and Active Galactic Nuclei* (University Science Books)

Östlin, G., 2000, *ApJL*, **535**, L99

Östlin, G., 2001, *Astrophysics and Space Science Supplement*, **277**, 345

Padovani, P. & Matteucci, F., 1993, *ApJ*, **416**, 26

Pantelaki, I. & Clayton, D. D., 1987, in T. X. Thuan, T. Montmerle & J. Tran Thanh van (eds.), *Starbursts and Galaxy Evolution*, pp. 145–150

Papaderos, P., Izotov, Y. I., Fricke, K. J., Thuan, T. X. & Guseva, N. G., 1998, *A&A*, **338**, 43

Papaderos, P., Loose, H.-H., Fricke, K. J. & Thuan, T. X., 1996, *A&A*, **314**, 59

Peimbert, M., 2008, *ArXiv;0811.2980*

Peimbert, M. & Torres-Peimbert, S., 1974, *ApJ*, **193**, 327

Péquignot, D., 2008, *A&A*, **478**, 371

Pindao, M., Schaerer, D., González Delgado, R. M. & Stasińska, G., 2002, *A&A*, **394**, 443

Porter, R. L., Bauman, R. P., Ferland, G. J. & MacAdam, K. B., 2005, *ApJL*, **622**, L73

Pustilnik, S., Kniazev, A., Pramskij, A., Izotov, Y., Foltz, C., Brosch, N., Martin, J.-M. & Ugryumov, A., 2004, *A&A*, **419**, 469

Pustilnik, S. A., Brinks, E., Thuan, T. X., Lipovetsky, V. A. & Izotov, Y. I., 2001, *AJ*, **121**, 1413

Pustilnik, S. A., Kniazev, A. Y. & Pramskij, A. G., 2005, *A&A*, **443**, 91

Pustilnik, S. A., Tepliakova, A. L., Kniazev, A. Y. & Burenkov, A. N., 2008, *MNRAS*, **388**, L24

Raimann, D., Bica, E., Storchi-Bergmann, T., Melnick, J. & Schmitt, H., 2000, *MNRAS*, **314**, 295

Reines, A. E., Johnson, K. E. & Hunt, L. K., 2008, *AJ*, **136**, 1415

Rho, J., Kozasa, T., Reach, W. T., Smith, J. D., Rudnick, L., DeLaney, T., Ennis, J. A., Gomez, H. & Tappe, A., 2008, *ApJ*, **673**, 271

Rieke, G. H. *et al.*, 2004, *ApJS*, **154**, 25

Rosenberg, J. L., Ashby, M. L. N., Salzer, J. J. & Huang, J.-S., 2006, *ApJ*, **636**, 742

Roy, J.-R., Aube, M., McCall, M. L. & Dufour, R. J., 1992, *ApJ*, **386**, 498

Roy, J.-R., Boulesteix, J., Joncas, G. & Grundseth, B., 1991, *ApJ*, **367**, 141

Rubin, R. H., 1968, *ApJ*, **153**, 761

Sage, L. J., Salzer, J. J., Loose, H.-H. & Henkel, C., 1992, *A&A*, **265**, 19

Salpeter, E. E., 1955, *ApJ*, **121**, 161

Sandage, A. & Binggeli, B., 1984, *AJ*, **89**, 919

Sandage, A. & Brucato, R., 1979, *AJ*, **84**, 472

Sargent, W. L. W. & Searle, L., 1970, *ApJL*, **162**, L155+

Sawey, P. M. J. & Berrington, K. A., 1993, *Atomic Data and Nuclear Data Tables*, **55**, 81

Schaerer, D., Contini, T. & Kunth, D., 1999*a*, *A&A*, **341**, 399

Schaerer, D., Contini, T., Kunth, D. & Meynet, G., 1997, *ApJL*, **481**, L75+

Schaerer, D., Contini, T. & Pindao, M., 1999*b*, *A&AS*, **136**, 35

Schaerer, D. & Vacca, W. D., 1998, *ApJ*, **497**, 618

Schlegel, D. J., Finkbeiner, D. P. & Davis, M., 1998, *ApJ*, **500**, 525

Scott, P., Asplund, M., Grevesse, N. & Sauval, A. J., 2009, *ApJL*, **691**, L119

Searle, L. & Sargent, W. L. W., 1972, *ApJ*, **173**, 25

Seaton, M. J., 1959, *MNRAS*, **119**, 81

Seaton, M. J., 1968, in D. E. Osterbrock & C. R. O'dell (eds.), *Planetary Nebulae*, volume 34 of *IAU Symposium*, pp. 129–+

Shapley, A. E., Steidel, C. C., Pettini, M. & Adelberger, K. L., 2003, *ApJ*, **588**, 65

Shi, F., Kong, X., Li, C. & Cheng, F. Z., 2005, *A&A*, **437**, 849

Shull, J. M. & McKee, C. F., 1979, *ApJ*, **227**, 131

Skillman, E. D. & Kennicutt, Jr., R. C., 1993, *ApJ*, **411**, 655

Slavin, J. D., Shull, J. M. & Begelman, M. C., 1993, *ApJ*, **407**, 83

Smith, J. D. T., Armus, L., Dale, D. A., Roussel, H., Sheth, K., Buckalew, B. A., Jarrett, T. H., Helou, G. & Kennicutt, Jr., R. C., 2007, *PASP*, **119**, 1133

Smits, D. P., 1996, *MNRAS*, **278**, 683

Spitzer Science Center, 2004, *Spitzer Observer's Manual*, http://ssc.spitzer.caltech.edu/documents/SOM/

Stasińska, G., 1984, *A&AS*, **55**, 15

Stasińska, G., 2000*a*, *New Astronomy Review*, **44**, 275

Stasińska, G., 2000*b*, in S. J. Arthur, N. S. Brickhouse & J. Franco (eds.), *Revista Mexicana de Astronomia y Astrofisica Conference Series*, volume 9 of *Revista Mexicana de Astronomia y Astrofisica Conference Series*, pp. 158–162

Stasińska, G., Cid Fernandes, R., Mateus, A., Sodré, L. & Asari, N. V., 2006, *MNRAS*, **371**, 972

Stasińska, G. & Schaerer, D., 1999, *A&A*, **351**, 72

Steidel, C. C., Giavalisco, M., Dickinson, M. & Adelberger, K. L., 1996, *AJ*, **112**, 352

Storey, P. J. & Hummer, D. G., 1995, *MNRAS*, **272**, 41

Storey, P. J. & Zeippen, C. J., 2000, *MNRAS*, **312**, 813

Strömgren, B., 1939, *ApJ*, **89**, 526

Szczepanski, J. & Vala, M., 1993, *Nature*, **363**, 699

Takase, B. & Miyauchi-Isobe, N., 1986, *Annals of the Tokyo Astronomical Observatory*, **21**, 127

Taylor, C. L., Brinks, E., Grashuis, R. M. & Skillman, E. D., 1995, *ApJS*, **99**, 427

Telles, E. & Terlevich, R., 1995, *MNRAS*, **275**, 1

Telles, J. E., 1995, Ph.D. thesis, , Univ. Cambridge, (1995)

Tenorio-Tagle, G., Munoz-Tunon, C., Perez, E. & Melnick, J., 1997, *ApJL*, **490**, L179+

Thuan, T. X., 1985, *ApJ*, **299**, 881

Thuan, T. X., 2008, in L. K. Hunt, S. Madden & R. Schneider (eds.), *IAU Symposium*, volume 255 of *IAU Symposium*, pp. 348–360

Thuan, T. X., Hibbard, J. E. & Lévrier, F., 2004, *AJ*, **128**, 617

Thuan, T. X., Hunt, L. K. & Izotov, Y. I., 2008, *ApJ*, **689**, 897

Thuan, T. X. & Izotov, Y. I., 2005, *ApJS*, **161**, 240

Thuan, T. X., Izotov, Y. I. & Lipovetsky, V. A., 1995, *ApJ*, **445**, 108

Thuan, T. X., Izotov, Y. I. & Lipovetsky, V. A., 1996, *ApJ*, **463**, 120

Thuan, T. X., Izotov, Y. I. & Lipovetsky, V. A., 1997, *ApJ*, **477**, 661

Thuan, T. X., Lecavelier des Etangs, A. & Izotov, Y. I., 2005, *ApJ*, **621**, 269

Thuan, T. X. & Martin, G. E., 1981, *ApJ*, **247**, 823

Thuan, T. X., Sauvage, M. & Madden, S., 1999, *ApJ*, **516**, 783

Tielens, A. G., 2005, *The Physics and Chemistry of the Interstellar Medium* (Cambridge University Press)

Tran, H. D., Sirianni, M., Ford, H. C., Illingworth, G. D., Clampin, M., Hartig, G., Becker, R. H., White, R. L., Bartko, F., Benítez, N., Blakeslee, J. P., Bouwens, R., Broadhurst, T. J., Brown, R., Burrows, C., Cheng, E., Cross, N., Feldman, P. D., Franx, M., Golimowski, D. A., Gronwall, C., Infante, L., Kimble, R. A., Krist, J., Lesser, M., Magee, D., Martel, A. R., McCann, W. J., Meurer, G. R., Miley, G., Postman, M., Rosati, P., Sparks, W. B. & Tsvetanov, Z., 2003, *ApJ*, **585**, 750

Tsamis, Y. G., Barlow, M. J., Liu, X.-W., Danziger, I. J. & Storey, P. J., 2003, *MNRAS*, **338**, 687

Tsamis, Y. G., Barlow, M. J., Liu, X.-W., Storey, P. J. & Danziger, I. J., 2004, *MNRAS*, **353**, 953

Tsamis, Y. G., Walsh, J. R., Péquignot, D., Barlow, M. J., Danziger, I. J. & Liu, X.-W., 2008, *MNRAS*, **386**, 22

Tsamis, Y. G., Walsh, J. R., Péquignot, D., Barlow, M. J., Liu, X.-W. & Danziger, I. J., 2006, in M. J. Barlow & R. H. Méndez (eds.), *Planetary Nebulae in our Galaxy and Beyond*, volume 234 of *IAU Symposium*, pp. 239–242

Turner, J. L. & Beck, S. C., 2004, *ApJL*, **602**, L85

Turner, J. L., Ho, P. T. P. & Beck, S. C., 1998, *AJ*, **116**, 1212

van Hoof, P. A. M., Weingartner, J. C., Martin, P. G., Volk, K. & Ferland, G. J., 2004, *MNRAS*, **350**, 1330

van Zee, L. & Haynes, M. P., 2006, *ApJ*, **636**, 214

van Zee, L., Salzer, J. J. & Skillman, E. D., 2001, *AJ*, **122**, 121

van Zee, L., Skillman, E. D. & Salzer, J. J., 1998, *AJ*, **116**, 1186

Veilleux, S. & Osterbrock, D. E., 1987, *ApJS*, **63**, 295

Verdes-Montenegro, L., Del Olmo, A., Iglesias-Páramo, J. I., Perea, J., Vílchez, J. M., Yun, M. S. & Huchtmeier, W. K., 2002, *A&A*, **396**, 815

Walsh, J. R. & Roy, J.-R., 1987, *ApJL*, **319**, L57

Walsh, J. R. & Roy, J.-R., 1989, *MNRAS*, **239**, 297

Walsh, J. R. & Roy, J. R., 1990, in D. Baade & P. J. Grosbol (eds.), *ESO Conf. Proc. 34: 2nd ESO/ST-ECF Data Analysis Workshop*, p. 95

Weaver, R., McCray, R., Castor, J., Shapiro, P. & Moore, R., 1977, *ApJ*, **218**, 377

Weedman, D. W., Hao, L., Higdon, S. J. U., Devost, D., Wu, Y., Charmandaris, V., Brandl, B., Bass, E. & Houck, J. R., 2005, *ApJ*, **633**, 706

Werner, M. W. *et al.*, 2004, *ApJS*, **154**, 1

Wesson, R., Barlow, M. J., Liu, X.-W., Storey, P. J., Ercolano, B. & de Marco, O., 2008, *MNRAS*, **383**, 1639

Wesson, R., Liu, X.-W. & Barlow, M. J., 2005, *MNRAS*, **362**, 424

Westmoquette, M. S., Exter, K. M., Smith, L. J. & Gallagher, J. S., 2007*a*, *MNRAS*, **381**, 894

Westmoquette, M. S., Smith, L. J., Gallagher, J. S., Trancho, G., Bastian, N. & Konstantopoulos, I. S., 2009, *ApJ*, **696**, 192

Westmoquette, M. S., Smith, L. J., Gallagher, III, J. S., O'Connell, R. W., Rosario, D. J. & de Grijs, R., 2007*b*, *ApJ*, **671**, 358

White, S. D. M. & Rees, M. J., 1978, *MNRAS*, **183**, 341

Wiese, W. L., Fuhr, J. R. & Deters, T. M., 1996, *Atomic transition probabilities of carbon, nitrogen, and oxygen : a critical data compilation*

Woosley, S. E., Heger, A. & Weaver, T. A., 2002, *Reviews of Modern Physics*, **74**, 1015

Wu, Y., Charmandaris, V., Hao, L., Brandl, B. R., Bernard-Salas, J., Spoon, H. W. W. & Houck, J. R., 2006, *ApJ*, **639**, 157

Wu, Y., Charmandaris, V., Hunt, L. K., Bernard-Salas, J., Brandl, B. R., Marshall, J. A., Lebouteiller, V., Hao, L. & Houck, J. R., 2007, *ApJ*, **662**, 952

Zanichelli, A., Garilli, B., Scodeggio, M., Franzetti, P., Rizzo, D., Maccagni, D., Merighi, R., Picat, J. P., Le Fèvre, O., Foucaud, S., Bottini, D., Le Brun, V., Scaramella, R., Tresse, L., Vettolani, G., Adami, C., Arnaboldi, M., Arnouts, S., Bardelli, S., Bolzonella, M., Cappi, A., Charlot, S., Ciliegi, P., Contini, T., Gavignaud, I., Guzzo, L., Ilbert, O., Iovino, A., McCracken, H. J., Marano, B., Marinoni, C., Mathez, G., Mazure, A., Meneux, B., Paltani, S., Pellò, R., Pollo, A., Pozzetti, L., Radovich, M., Zamorani, G. & Zucca, E., 2005, *PASP*, **117**, 1271

Zwicky, F., 1966, *ApJ*, **143**, 192

Zwicky, F. & Zwicky, M. A., 1971, *Catalogue of selected compact galaxies and of post-eruptive galaxies*

ACKNOWLEDGEMENTS

My first and most sincere thanks are to my supervisor Mike Barlow whose unfaltering wisdom, support and famous red pen have helped me achieve my PhD. You have given me invaluable skills and have helped me build a confidence that will stay with me throughout my career.

I am indebted to my collaborators and work colleagues, in particularly: Barbara Ercolano for her help and encouragement, Jeremy Walsh for his kindness and IRAF expertise, Nate Bastian for his good advice and most importantly Yiannis Tsamis who helped guide me throughout my PhD, introduced me to the world of IFU and entrusted me with that all important data. Endless thanks to my favourite postdocs in the world, Roger Wesson and Mark Westmoquette, for putting up with my incessant pestering and for not laughing (too much) at the 'Questions I can't Ask Mike'.

The friends that I have made at UCL made my PhD-journey not just tolerable but wonderfully pleasurable - in particular those in G15 and my special comrades: Manda my wonderful flat mate and conference-partner, Shaun and his 'angelic' voice, Carolyn and her peanut butter cups. A special thanks goes to Jo Fabbri (my favourite running buddy and life coach), Fab, Dugan, Fiona and Nutan for laughs and late-night Houseman Room sessions. I would also like to thank George and Arnaud 'of the Houseman Room' for endless banter and free sandwiches.

Thank you to my parents and family for the love, guidance and belief that has allowed me to follow and achieve my dreams. A special thanks to my father, for introducing and showing me the vast wonders of the Universe and to my mother, for giving me the opportunities to explore them. Thanks also to my other astrophysics teachers, Mrs Churchman and Dr Everett, for setting me on the path that led me here.

And finally, I would like to thank Jamie. You have put a smile on my face and in my heart every day since we met and always will. I look forward to our next big step over the Atlantic and to a future, holding your hand and facing the wind.